On the edge

On the edge:
Imaging soft interfaces by single-molecule localization microscopy

PROEFSCHRIFT

ter verkrijging van de graad van doctor
aan de Technische Universiteit Eindhoven,
op gezag van de Rector Magnificus, prof. dr. ir. F.P.T. Baaijens
voor een commissie aangewezen door het College voor Promoties
in het openbaar te verdedigen
op donderdag 30 november 2017 om 16.00 uur

door

Antonio Aloi

geboren te Terlizzi, Italië

Dit proefschrift is goedgekeurd door de promotoren en de samenstelling van de promotiecommissie is als volgt:

voorzitter:	prof. dr. K.A.H. van Leeuwen
1^{e} promotor:	prof. dr. O.J. Luiten
2^{e} promotor:	dr. ir. I.K. Voets
leden:	dr. S. Manley (EPFL Lausanne)
	prof. dr. J. Vermant (ETH Zurich)
	prof. dr. E.W. Meijer
adviseurs:	dr. L. Albertazzi (IBEC Barcelona)
	dr. ir. A.M. de Jong

Het onderzoek of onderwerp dat in dit proefschrift wordt beschreven is uitgevoerd in overeenstemming met de TU/e Gedragscode Wetenschapsbeoefening.

A lonely sail is flashing white
Amdist the blue mist of the sea!...
What does it seek in foreign lands?
What did it leave behind at home?..

Waves heave, wind whistles,
The mast, it bends and creaks...
Alas, it seeks not happiness
Nor happiness does it escape!

Below, a current azure bright,
Above, a golden ray of sun...
Rebellious, it seeks out a storm
As if in storms it could find peace!

M.J. Lermontov

A catalogue record is available from the Eindhoven University of Technology Library.
ISBN: 978-90-386-4380-9

Cover Design: Antonio Aloi
Printed by: Gildeprint, Enschede

This project has been financially supported from the European Union (FP7-PEOPLE-2012-ITN SOMATAI contract 316866).


Contents

Chapter 1

Painting soft matter by super-resolution microscopy

Advances in organic and polymer chemistry are now enabling the synthesis of a plethora of increasingly complex small molecules, anisotropic nanoparticles, large polymers and complex colloids with heterogeneous features on sub-μm lengthscales. Conventional imaging tools like (cryo-)TEM and AFM are essential to characterize such samples due to the high spatial resolution achievable. However, they do not resolve any chemical heterogeneity within these materials. Hence, further advances in imaging tools to resolve soft, and multi-component nanostructures are needed. In this context super-resolution microscopy emerged as an attractive tool to visualize with high spatial resolution and chemical specificity, in a minimally invasive manner, both living and man-made hierarchical materials. Its potential is broadly explored in biology and biophysics, but surprisingly received far less attention from the supramolecular chemistry, polymer and colloidal science communities. This thesis explores the utility of super-resolution microscopy to visualize synthetic soft matter, focusing on deformable interfaces and non-aqueous solvents. This introductory chapter has hence, a two-fold aim: give a brief history of the emergence of super-resolution microscopy, and to present an exemplary overview of recent applications.

1.1 Optical microscopy

Vision has always been of extreme importance to humankind. Sight is indeed the first sense we rely on to capture and decode the surrounding environment. But, not everything is within reach of the naked eye. In fact, the most unexpected features of reality can be disclosed only if we look at the ordinary from up close, magnifying each small detail (fig. 1.1). Microscopes thus unleash the hidden dimensions of reality. Looking at the world through a microscope lens sheds light on things never seen before. Recall the discoveries of a Dutch draper on 'little animals' observed in rain, well, sea and snow water in 1677, [1] or the remarkable Hooke's *Micrographia* on illustrated insects, plants and minerals as seen through different lenses in 1665. [2] As centuries passed by, scientists understood that the sub-atomistic scale is essentially the lowest limit how small things can be, and that in such exceedingly small space terabytes of information can be stored. [3] Hence, it is not surprising that the microscope, with its power to magnify and reveal things invisible to the naked eye, has played an essential role in science since the very beginning of its discovery in $\sim$1590.

Figure 1.1: On the left, Caribbean shore. Photo copyright G. Harding (wetravelandblog.com). On the right, sand grains on a glass slide 250 times magnified. Photo copyright Dr. Gary Greenberg (sandgrain.com).

1.2 The diffraction barrier

Microscopy hinges on the use of lenses to magnify objects. This is achieved by bending radiation through the lens in the so-called focal point. This central concept is both its power and limitation. The latter is known as the diffraction limit of light. If we look at radiation as a propagating wave-packet through a lens, geometrically it cannot be focused on a single point, but it will interfere and will be smeared out over a region with a full width at half maximum (FWHM) given by:

$$d = \frac{\lambda}{2n \sin \alpha} \tag{1.1}$$

in the lateral plane, and by:

$$\Delta z = \frac{2\lambda}{n^2 \sin^2 \alpha} \tag{1.2}$$

in the axial direction. [4] The FWHMs are governed by the wavelength of the radiation, λ, and the so-called numerical aperture of the lens, $NA = n \sin \alpha$. Here the semi-aperture angle of the lens, α, and the refractive index of the medium, n, are introduced. The theory describing the diffraction barrier has been formulated for the first time by Ernst Abbe in 1873, [5] and is now engraved in the stone of his memorial in Jena. From eqs. 1.1 and 1.2 it follows that if the wavelengths used are short, as in the case of electrons, the size of the diffracted volume is small enough to resolve nanoscale architectures. For example, an electron beam having kinetic energy of 2 eV and de Broglie wavelength $\lambda \simeq 0.87$ nm will be diffracted on a volume of $\sim$0.7 nm^3 (assuming the same wave optics, with $n = 1$).

Conversely, for radiation in the visible range of the electromagnetic spectrum ($\lambda \simeq 500$ nm), assuming $NA < 1.5$, features closer than 200 nm cannot be distinguished. Notwithstanding $\sim$2 orders of magnitude lower resolution, light microscopy is the most used microscopy technique in life science. This is because light microscopy has a number of advantages compared to electron microscopy: low invasiveness, high penetration depth, chemical specificity, and easier sample handling. The photon energy in the visible range is low enough to look at living biological samples. The redder is the radiation used, the higher is the penetration depth, and hence thicker samples can be investigated. Moreover, multi-colour imaging can be used to easily discern distinct structures labelled with different fluorescent tags. For example, the position of specific proteins can be pinpointed and related to the functions they perform in cells. The direct labelling of single proteins with a specific tag should grant high imaging sensitivity, since each carries a single fluorophore. However, due to diffraction of light, the region over which the light is focused, which is called the point spread function (PSF), illuminates hundreds of proteins, exciting them all at the same time. Their fluorescence emission will thus be roughly simultaneous, which will result in a blurred spot, from which no accurate position of individual proteins can be retrieved.

1.2.1 Pushing the limits of the diffraction of light

To improve the spatial resolution, and hence reducing the distance at which two single emitters can still be discerned, several approaches have been proposed. If the propagation of light emitted by the sample in an unconfined manner (far-field microscopy) undergoes diffraction, the alternative is to stay close to the sample surface and collect the component of non-propagating evanescent light at the surface. This is known as near-field microscopy. Here, the light is confined by a sub-diffraction-sized aperture or tip, and it propagates as an

evanescent wave which exponentially decays within a distance $\ll \lambda/2$. Scanning the surface with the tip at a few nm away from the sample ($\ll \lambda/2$), results in spatial resolution higher than what can be achieved in far-field microscopy ($\ll$ 100 nm). [6] But, near-field microscopy is limited to the investigation of surfaces, hence the exploration of internal structures is not possible with this approach. Total-internal-reflection fluorescence (TIRF) microscopy also relies on an evanescent wave. In TIRF microscopy, only a thin layer of the sample is illuminated, leading to an efficient suppression of background fluorescence, and hence less blurry images. The main drawback is that TIRF is limited to two-dimensional imaging. To overcome these bottlenecks optical tricks to manipulate light and modulate excitation and detection paths have been suggested to increase resolution in far-field microscopy. Structured illumination microscopy (SIM), [7–10] for example exploits light manipulation, ensuring far-field imaging with a two-fold improvement in lateral and axial direction. Conversely a 4Pi microscopy, relying on two mirrored objectives, improves the axial resolution from ∼500 nm to ∼80 nm. [11, 12]

1.3 The "Resolution Revolution"

The advantages described in the previous section successfully achieved 2- to 3-fold improvements in spatial resolution, enabling more precise imaging than before. Yet, the diffraction limit of ∼200 nm remained. This raised the question: how to resolve nanostructures if the diffraction of light prevents the detection of individual emitters spatially separated by less than ∼200 nm?

Clearly, if light diffraction necessitates a minimal distance of ∼200 nm between single emitters for precise localization, while the aim is to image at smaller distances, a possible alternative is to separate the chromophores temporally. Hence, to overcome the bottleneck in spatial resolution, we should exploit the photo-physical properties of dyes to control the density of emitting molecules residing in the illumination volume. Two strategies have been pursued: temporal separation of the emission of fluorophores (coordinate-stochastic methods), [4, 13] and modulation of the effective PSF to shrink the illumination volume (coordinate-targeted methods). [4, 13] In coordinate-stochastic methods, single molecules are forced to emit at a relatively low density such that they are separated by $\gg$ 200 nm in each frame. This enables immediate distinction among molecules within the diffraction limited illumination volume. The term 'stochastic' refers to the random switching between the ON and OFF states of the fluorophores, and ensures that the probability of finding two emitters closer than the diffraction limit at the same time in the ON state is very low. In coordinate-targeted methods, a patterned illumination is engineered, such that the size of the effective PSF is reduced, and only a smaller number of molecules is excited. These advantages have

improved the spatial resolution to tens of nm's, which is a milestone in far-field microscopy, awarded with the Nobel prize in chemistry in 2014 to E.W. Moerner, [14] E. Betzig, [15] and S.W. Hell. [16]

1.3.1 Coordinate-stochastic methods

The central concept in coordinate-stochastic methods is the temporal separation of dyes: the number of emitting dyes at any time point during the experiment is tuned such that the distance, d, between these emitting dyes is larger than the diffraction limit (fig. 1.2). Hence, the dyes are localized when emitting (ON state), but they remain invisible if residing in the dark state (OFF state). Different dyes are thus localized at different time points t_1 and t_2 (fig. 1.2b and 1.2c). This temporal separation enables single molecule localization at high labelling density, such that nanostructures can be visualized with high lateral precision upon reconstruction of the super-resolution image by summation of all localized dyes.

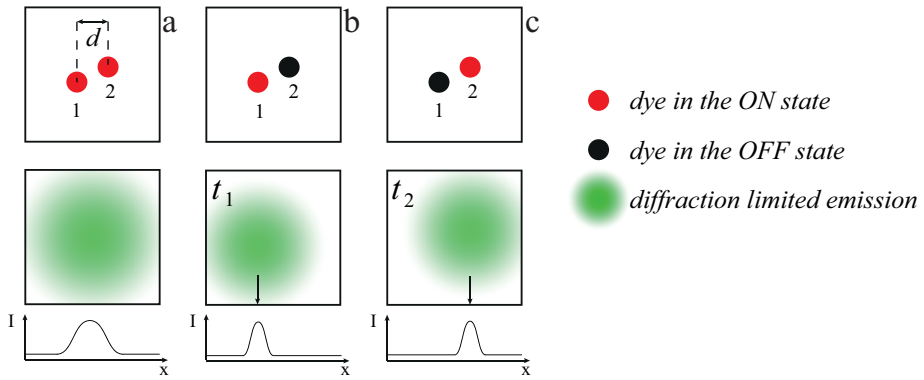

Figure 1.2: Temporal separation of single emitters. (a) Two fluorophores, 1 and 2, emitting light at the same time. Their concomitant emission within the diffraction volume light makes their individual positions indistinguishable. (b) Fluorophore 1 is in the ON state (red dot) and emits a diffraction limited fluorescent signal at time t_1, fluorophore 2 is in the OFF state (black dot) and hence is "invisible". Fluorophore 1 can be identified from its intensity profile and localized (black arrow). (c) Fluorophor 2 is emitting at time t_2, while fluorophore 1 is in the dark state.

Summarizing, if all dyes emit simultaneously, features smaller than ∼200 nm cannot be resolved, and we obtain a classical wide-field diffraction limited image (fig. 1.3a). If the dyes emission are temporally separated (fig. 1.3b), we can resolve features smaller than ∼200 nm. To this end, the profile of the diffraction limited spot of each single molecule (fig. 1.3c and 1.3d) is analyzed. The measured intensity profile (fig. 1.3e) is modeled with a 2D-Gaussian function to obtain its centroid, which corresponds to the most probable location of the molecule (fig. 1.3f). This enables $\geqslant$ 10-fold higher localization precision of emitters compared to the diffraction limited image. In sum, to achieve highly resolved images, the following conditions have to be met: *i)* the distance between the emitting dyes within each

collected frame must be larger than the diffraction limit; *ii)* the emission of the molecules has to last at most one frame before entering a dark non-fluorescent state; *iii)* the emission of a new subset of molecules is collected in the next frame; *iv)* by reiterating these steps, and summing-up all the localizations, a super-resolved image is obtained.

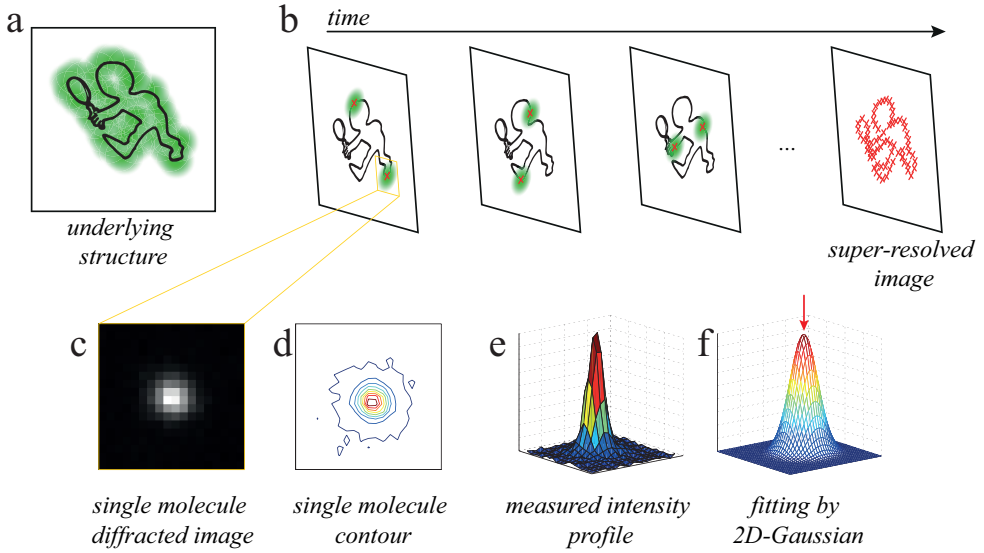

Figure 1.3: Principle of coordinate-stochastic methods. Schematic illustrating (a) wide-field diffraction-limited image and (b) separation in time of single molecule localizations to achieve a super-resolved image. (c) Diffraction limited image of a single molecule and (d) its contour. (e) Intensity profile of the diffraction limited image of a single molecule. (f) 2D Gaussian function fitting the diffraction limited image of a single molecule. The red arrow indicates the most probable location of the emitter.

1.3.1.1 Switching mechanisms in coordinate-stochastic methods

The three main families of coordinate-stochastic methods are (f)PALM, [17,18] (d)STORM, [19–21] and PAINT. [22] Multi-colour and multi-dimensional variants of all of these localization-based methods have been developed and are known under a plethora of different acronyms. To enable the temporal separation of single emitters, and hence to control the switching between the ON and OFF states, there are several mechanisms. In PALM microscopy, photo-activatable fluorescent proteins or organic dyes are used. These emitters reside in a dark state and can be activated to an ON state by an external stimulus (*e.g.*, UV light). The technique requires the majority of fluorophores to be in a stable OFF state. [17,23] (d)STORM employs fluorophores which can be switched reversibly between a fluorescent and a non-fluorescent state (triplet state). The intersystem crossing to bring the fluorophore in the triplet state is typically achieved through an oxygen scavenger and β-mercaptoethylamine. High laser power brings the dyes back in the ON state, forcing the

stochastic blinking of the molecules. [21,24] PAINT exploits transient binding of fluorescent dyes to the structure under investigation, which may be aspecific or specific. Solvochromic dyes, for example, emit fluorescence signals only in specific chemical environments such as hydrophobic domains. [22] The tag may also be temporarily immobilized on the structure through ligand binding to cell membranes, [25] or complementary DNA strands. [26,27] When bound, the dye motion is slowed down sufficiently to be localized, while fast diffusion in the unbound state precludes single-molecule localizations.

1.3.1.2 Advantages and limitations of coordinate-stochastic methods

The spatial resolution in coordinate-stochastic methods depends on the localization accuracy with which each single molecule is localized. The localization accuracy is influenced by the size of the PSF (σ_{PSF}), the signal-to-noise ratio (SNR), and the photon flux of the emitter. All these factors are included in the standard deviation of the distribution function used as fitting model. An analytical expression to calculate the localization accuracy, σ, was proposed by Thompson *et al.*, [28] and successively improved by Mortensen *et al.* (eq. 1.3). [29]

$$\sigma^2 = \frac{\sigma_{PSF}^2 + {}^{a^2}/_{12}}{N_{sig}} \left(\frac{16}{9} + \frac{8\pi N_{bg}(\sigma_{PSF}^2 + {}^{a^2}/_{12})}{N_{sig} a^2} \right), \tag{1.3}$$

where a is the pixel size of the detector, and N the number of photons per pixel collected in the background (N_{bg}) and from each single molecule (N_{sig}). Eq. 1.3 implies that in case of a single molecule located in the focal plane, or closeby, with isotropic fluorescence emission, the intensity distribution over the pixels can be approximated by a 2D-Gaussian profile, with standard deviation σ_{PSF}. [30] In case of high SNR ($^{N_{sig}}/_{N_{bg}}$), *i.e.*, only when shot noise is contributing to the background signal, [31] N_{bg} is negligible and the second term between brackets in eq. 1.3 tends to zero. Assuming ${}^{a^2}/_{12} \ll \sigma_{PSF}^2$, eq. 1.3 can be approximated to:

$$\sigma = \frac{4}{3} \frac{\sigma_{PSF}}{\sqrt{N_{sig}}}, \tag{1.4}$$

demonstrating that an inverse proportionality exists between the accuracy of localization of a dye and the number of photons it emits, N_{sig}. Thus, the spatial resolution of a reconstructed image can be improved after the measurement taking into account only molecules with bright emission. This, however, requires longer acquisition times, because the fluorescence emission is a Poissonian process, and the higher the photon flux the lower is the probability. A possible way to circumvent long imaging acquisition times is to increase the number of activated molecules per frame. However, this would lead to a higher probability of having two molecules ON within the diffraction distance, d. The acquisition time would be shortened, but a careful analysis of the identification of single-molecule fluorescence traces has to be

carried out post-imaging. Many improvements have been sought in the past few years to obtain reliable reconstructions from samples with high label densities beyond d and low SNR, [32–34] in pursuit of high acquisition time rates (∼100 frames/s). [35, 36]

1.3.2 Coordinate-targeted methods

Patterned illumination is the key innovation to enhance spatial resolution in coordinate-targeted approaches. This is achieved either optically or with non-linear manipulation of the electronic states of the fluorescent probes. This family of coordinate-targeted methods is generally referred to as reversible saturable (or switchable) optical fluorescence transitions (RESOLFT), which includes STED, [37] GSD, [38, 39] and SSIM. [7, 8, 40–42]

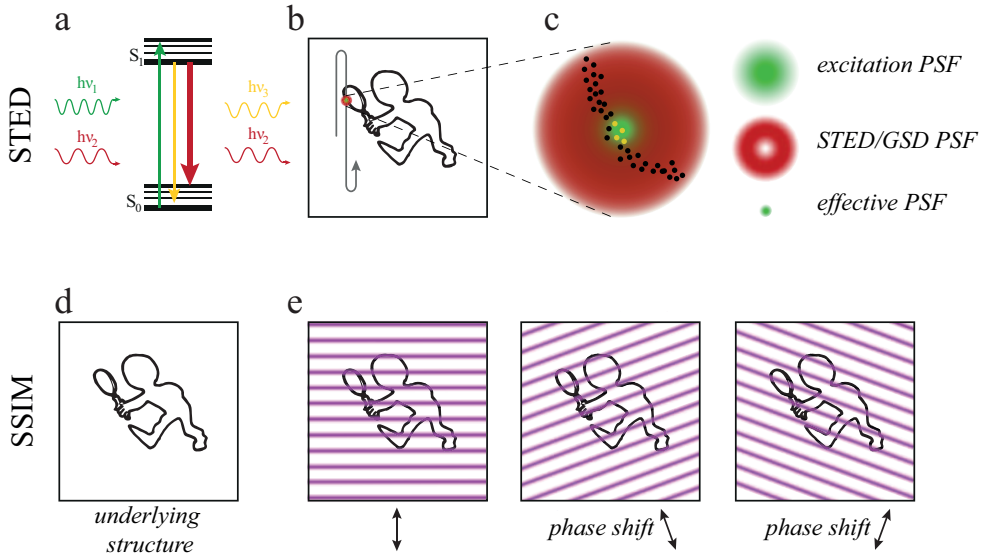

Figure 1.4: Principle of coordinate-targeted methods. (a) Jablonski diagram for a stimulated emission process in STED microscopy. (b) Schematic illustrating the scanning of the structure of interest in STED microscopy. (c) Zoom-in on the coaxial beams focused on the structure, and PSF shapes of the laser beams. (d-e) Schematic illustration of SSIM microscopy concept adapted from [43].

In STED microscopy, [37, 44, 45] Abbe's limit is circumvented by excitation with one laser at $h\nu_1$, and subsequent depletion of the surrounding area with another laser at $h\nu_2$ (fig. 1.4a). The two lasers with $\nu_1 > \nu_2$ are coaxially aligned, such that the excitation laser (a common diffraction limited Gaussian beam) excites in the focal volume the fluorescent molecules ($h\nu_3$ in fig. 1.4a), some of which are switched OFF by the second incoming beam with a donut shape, through a process called stimulated emission. [46] In this process, the electrons populating the excited state of the molecule are forced to decay into a higher vibrational state of the ground non-fluorescent state, thereby emitting a red-shifted radiation

compared to spontaneous fluorescence (red arrow in fig. 1.4a). The red-shifted photons are blocked by a spectral filter, and hence remain undetected. Thus, only the molecules residing in the hole of the donut emit and are subsequently detected. This reduces the effective PSF from which the fluorescent signals are collected. Super-resolved images with a spatial resolution down to tens of nanometers [37] are obtained by scanning the sample (grey arrow in fig. 1.4b). The main drawback of STED microscopy is the high intensity of the depletion beam, which causes photodamage to the sample, and substantially reduces the lifetime of the fluorophores pushed in the OFF-state. Years after the introduction of STED, this limitation has been circumvented through time-gated detection and pulsed excitation to effectively shrink the Gaussian beam and reduce the intensity of the donut beam to $^1/_3$ compared to normal STED. [47]

Stimulated emission is just one of the possible tricks to shrink the PSF. Side by side with STED, ground state depletion (GSD) microscopy is widely applied. In this case the molecules are kept temporally in a non-fluorescent triplet state using a second excitation beam, instead of being forced to the ground state as in STED microscopy. Since the dark triplet state is much longer-lived than the singlet state exploited in STED (μs - s *vs.* ns), GSD necessitates much lower laser intensity than STED, which reduces photodamage significantly.

Saturated structured illumination microscopy (SSIM) exploits the Moiré effect to achieve spatial resolution beyond the diffraction of light (fig. 1.4d and 1.4e). [45] Here, the specimen is illuminated with a striped pattern using an optical grating. Subsequently, the pattern arising from the interference between the fluorescent signal and the striped excitation is recorded in the focal plane. By applying this striped illumination with different orientations (the grating is rotated and the phase shift is varied) diverse beating patterns are collected (fig. 1.4e). A Fourier transform analysis of the superimposed beating patterns reveals fine structures, smaller than the diffraction limit of light. By modulation of the laser in the two orthogonal directions, this strategy enables a two-fold increase in the spatial resolution both in the lateral and axial directions. [7–10, 48]

1.3.2.1 Coordinate-stochastic methods vs. coordinate-targeted methods

Coordinate-stochastic methods are appealing because of two main advantages: *i)* they can be implemented on 'conventional' microscopes, and *ii)* a variety of dedicated fluorescent probes is available, both genetically encoded as well as organic compounds. Care must be taken, however, to exclude artifacts that could arise from numerical data treatment to avoid single-molecule over-counting (*i.e.*, single fluorophores localized multiple times), and to circumvent under-counting, as different fluorophores emit simultaneously within the diffraction limited volume. Furthermore, labelling density is limited and various optical aberrations (chromatic, dipole orientations, drift, *etc.*) might influence the spatial resolution. Conversely, coordinate-

targeted methods realize $\ll$ 100 nm spatial resolution, virtually irrespective of the sample type, the sample environment, and the nature of the dye. Hence, no dedicated dyes, nor specific buffers, are required. The disadvantage of this strategy is the high cost and complexity of the optics required.

1.4 The renaissance of biology

Direct visualization of cells, tissues and entire organisms is essential to understand structure-function relations and their mechanistic origins. This is why imaging technologies have long played an essential role in the development of biology and biomedicine. Light microscopy has been of particular importance due to its widespread use, minimal invasiveness, and chemical specificity. But, the longstanding limit in spatial resolution of several hundreds of nanometers imposed by the diffraction of light in the far-field optics hampered the imaging of smaller nanostrucutures. Complementary imaging tools, often more expensive and complex in use yet offering high spatial resolution, grew in importance. Hence, the advent of super-resolution microscopy generated renewed interest in optical microscopy. By some this has been seen as a renaissance with the potential to 'revolutionize biology and medicine'.[1]

The sub-cellular organization in bacteria can be visualized by super-resolution microscopy, [49] which offered unprecedented insight into local cell dynamics. Several studies shed new light on the binding of proteins to DNA (fig. 1.5a), [50,51] DNA transcription, [52] DNA translation, [53] DNA replication/ repair, [54] the dynamics of cell division (fig. 1.5b), the location of membrane proteins (fig. 1.5c), [55–58] and the organization of proteins in large structures, such as the cytoskeleton, [59] as well as the stoichiometry and the distribution of interacting proteins in subcellular compartments. [60–62]

To understand the complex mechanisms involved in cell signaling and chemotaxis, the counting of the involved players is not the only requirement. Resolving structures and morphologies, along with which proteins are moving, is equally important. Long and linear microtubules served in pioneering studies as model structures to prove the power of super-resolution microscopy in differentiating densely-packed structures. [63] Other researchers addressed the intracellular signaling, and investigated the interactions between compartments. [64,65] For example three-dimensional STORM imaging of mitochondrial network and its connections with microtubules unveiled different stages in the cell growth (fig. 1.6a). [66] Soon after, more complex structures were visualized. In fact, major breakthroughs were achieved in neurosciences, [67] when ordered alternating architectures of actin and spectrin proteins have been resolved within the axons, showing a periodicity of $\sim$200 nm (fig. 1.6 b). [68]

[1] Ehrenberg, M. *Super-resolved fluorescence microscopy* **2014**, The Royal Swedish Academy of Sciences: Stockholm, Sweden.

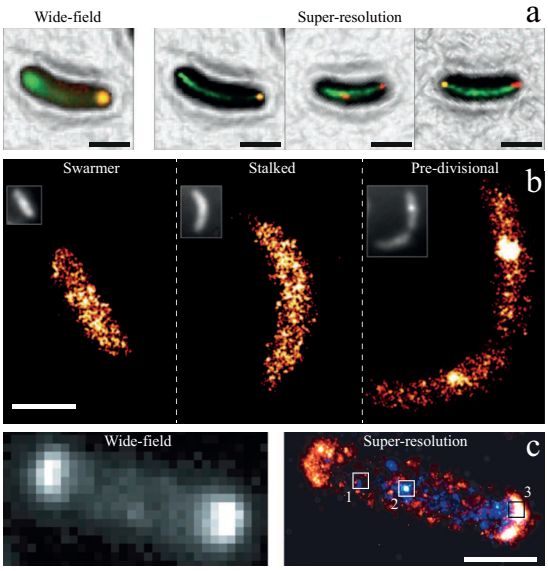

Figure 1.5: Examples of single-molecule super-resolution imaging in biological applications – Structures. (a) Wide-field (left) and super-resolved (right) images of a spindle-like apparatus of ParA in *C. crescentus* bacterial cells, guiding chromosomes during cell division. Figure adapted from [50]. (b) Imaging of the nucleoid-associated protein HU at different cycles (swarmer, stalker, and pre-division stage) of cell division in *C. crescentus* bacteria, by light-induced blinking of enhanced yellow fluorescent protein. Figure adapted from [55]. (c) PALM imaging of the E. coli chemotaxis network looking at the distribution of Tar receptor. Diffraction-limited image of trans-membrane chemoreceptor Tar (left). Superposition of PALM images using TIRF (blue-white localizations) and epi-illumination (yellow-orange localizations) of Tar labeled with mEos2 fluorescent protein (right). Boxes from 1 to 3 represent single proteins, small cluster (241 Tar proteins) and large cluster (722 Tar proteins), respectively. Figure adapted from [57]. The scale bars in all panels indicate 1 μm.

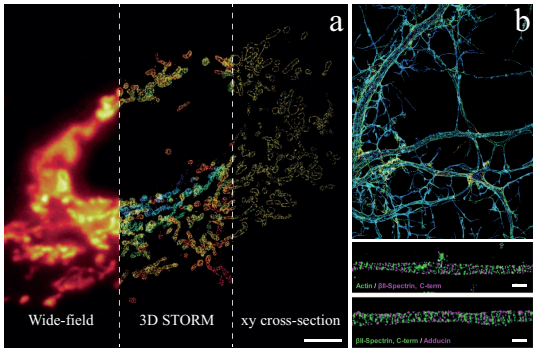

Figure 1.6: Examples of single-molecule super-resolution imaging in biological applications – Morphologies. (a) Conventional vs. 3D STORM image of mitochondria in a cell. Wide-field image (left), 3D STORM image (middle) with colour-coded *z*-dimension, and xy cross-section of the 3D STORM image (right). Figure adapted from [66]. The scale bar indicates 5 μm. (b) STORM imaging unveils a clear organization of actin filaments in the axons and dendrites of neurons. Specifically, actin, spectrin, and adducin are arranged along an uni-dimensional architecture in axons, and distributed in an alternated pattern, elucidating the periodicity in the cytoskeletal structure. The scale bars indicate 500 nm. Figure adapted from [68].

1.5 Breakthroughs in material science and chemistry

Inspired by the diverse functionality of complex nanostructures in Nature, chemists developed a wide array of synthetic self-assembling building blocks to engineer and fabricate hierarchical materials with interesting optical, mechanical and catalytic properties. Further improvements of the performances of these materials requires a detailed understanding of their structure-property relations. While chemists routinely use AFM and EM to image sub-μm architectures, the potential of super-resolution microscopy is far less exploited. Exemplary studies demonstrating the utility of super-resolution microscopy in supramolecular chemistry and material science are presented in the following sections.

1.5.1 Illuminating fibers by super-resolution microscopy

Proteins, peptides and small molecules may assemble into one-dimensional supramolecular fibers due to directional non-covalent interactions between the constituent building blocks. Their assembly pathways and steady-state structures are investigated in detail to understand how these are related to molecular structure and impacted by their physical environment (temperature, concentration, *etc.*). Super-resolution microscopy is an attractive tool to characterize such fibers, since it is minimally invasive and profits from advantages like multicolour imaging and target-specific labelling. Several recent studies therefore, characterized the structure and the dynamics of biological and synthetic supramolecular fibers with super-resolution microscopy.

In a pioneering study, the conformation of single polymeric chains (M_w $\sim 10^6$ Da) was visualized in three dimensions were conducted using PALM microscopy. Poly(butyl methacrylate) (PBMA) labelled with caged rhodamine and mixed with unlabelled poly(butyl methacrylate) was imaged upon spincasting on a glass substrate. The radii of gyration of hundreds of chains were determined with an accuracy of $\sim$3 nm, demonstrating the ability of PALM to resolve the static structure of single polymeric chains (fig. 1.7a). [69] DNA-PAINT has been used to test whether polymers can be forced to adopt a pre-designed conformation, which would pave the way to the realization of specifically designed patterns to be exploited in very compact 3D electronics. To this end, programmable self-assembled oligonucleotides were visualized on DNA-origami scaffolds. [70] Single chains of conjugated (2,5-dialkoxy)paraphenylene vinylene-DNA brush (APPV-DNA) polymers were forced to adopt specific pre-designed configurations (U-shaped, wave, staircase, circular, helical) on $\sim$50 $\times$ 20 nm DNA-origami scaffolds. 3D DNA-PAINT showed single polymer chains wrapped around the scaffold in the desired right-handed helical pattern designed by the authors. In this way they demonstrated that molecular conformations of single polymers can be manipulated at the nanoscale on demand (fig. 1.7b). [70]

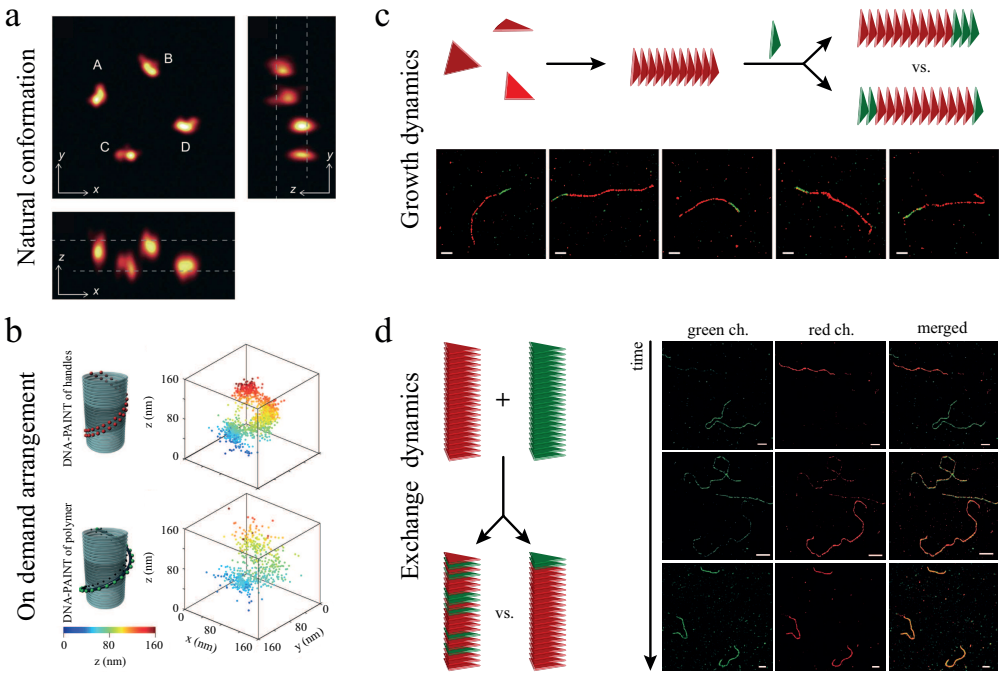

Figure 1.7: Examples of single-molecule super-resolution imaging on 1-dimensional synthetic aggregates. (a) single PBMA polymer chain imaged in three dimensions by PALM showing its natural conformation in a 210 nm thick film (white dashed lines). Figure adapted from [69]. (b) APPV-DNA polymer immobilized on a 3D DNA nanoscaffold, adopting a pre-design conformation. Figure adapted from [70] (c) Unidirectional growth of protein-based nanofibrils probed with two-colours STORM imaging demonstrated by adding green-labelled monomers to already existing red-tagged fibrils. Scale bars represent 2 μm. Figure adapted from [71]. (d) Exchange pathway of supramolecular μm-long fibers unveiled by STORM imaging. Scale bars represent 1 μm. Figure adapted from [75].

It is also possible to study the uni-directional growth of one-dimensional protein-polymer fibers by super-resolution microscopy. [71] To this end, triblock structures with an inner self-assembling silk-like domain, and two lateral water-soluble collagen-like domains, were labelled with Alexa-647, assembled into μm-long fibrils, and imaged by STORM. Aiming to study whether the fiber ends remained 'living' (once polymerization has ceased) and whether growth was uni- or bi-directional, the authors added Alexa-488 labelled triblocks to pre-formed fibers bearing Alexa-647. The added triblocks were found to attach to only one of the two ends of the fibers, resulting in a majority of green-red diblock fibers (fig. 1.7c).

Moreover, the effects of structural differences introduced at the molecular scale in fiber-like aggregates, have been explored by several researchers. The effect of chirality on μm-long and nm-wide 1,3,5-benzenetricarboxamides (BTA) fibers was investigated by STORM microscopy, unveiling small differences in the length of the fibers. [72] The diverse topologies obtainable upon self-assembly of diphenylalanine peptides was studied using Cyanine-5-labelled diphenylalanine monomers in PAINT microscopy. The coexistence of long μm fibers and

small spherical aggregates (∼60 nm in diameter) suggested a step-wise self-assembly of these structures, starting from spherical aggregates hierarchically interacting to form fibers. [73] Finally, self-sorting in a mixed solution of peptide-based hydrogelators containing cationic and anionic head groups, respectively, was observed by STED microscopy. Furthermore, individual supramolecular fibers of 80-100 nm in diameter were resolved in space. The correlation between green and red fibers was analyzed to quantify the degree of self-sorting in the system. [74]

Super-resolution microscopy has also been utilized to study the dynamics of supramolecular systems. The exchange dynamics of BTA based fibers has been studied by STORM. Unexpectedly, BTA monomers were found to migrate homogeneously between fibers stained with different colours (fig. 1.7d). [75] These results highlighted the presence of weak bonds along the fibers offering easy access to free monomers. This inspired further studies to directly visualize monomeric exchange of other supramolecular systems by STORM. Following the same approach, the insertion of a peptide-functionality onto the BTA monomers was studied to understand the impact of introducing bioactivity into a completely synthetic system. Here, they demonstrated that the insertion of peptides acts as catalyst in the monomer exchange. [76]

Monomer exchange rates in ureidopyrimidinone (Upy) based polymers were obtained by Hendrikse *et al.* using STORM microscopy. The authors reported different monomer exchange timescales for differently functionalized Upy polymers. [77] Local heterogeneities were observed along peptide amphiphiles nanofibers. These seemed related to distinct differences in the molecular exchange rates observed for fully and partially mixed supramolecular fibers. Sub-μm long regions where no exchange takes place were observed. [78]

1.5.2 Super-resolution microscopy to visualize nanoparticles, microgels and block co-polymer blends

Super-resolution microscopy has also been applied to study the sub-μm structures of non-fibrous materials, like microgels and block co-polymer blends. For example, the self-assembly, [79] core/shell ratio, [80] and density profile (fig. 1.8a) [81] of core-shell microgels were visualized by dSTORM. STED was used to study the packing and morphology of small particles within large structures. The lamellar morphology poly(2-vinylpyridine) (P2VP) in a polystyrene-P2VP block co-polymer structure was visualized before and after interacting with alcohols, displaying the swelling of the structure (fig. 1.8b). [82]

Yan *et al.* imaged the transition from cylindrical micelles to polymersomes of poly(styrene-*block*-ethylene oxide) (PSt-*b*-PEO). They used the photophysical properties of spiropyrans and the hydrophobicity in solid microphases to induce a stochastic blinking of

the spiropyrans and reconstruct both cylindrical micelles and polymersomes with nanometer resolution (fig. 1.8c). [83] Finally, figure 1.8d shows STORM images of ∼50 nm and ∼150 nm thin films of polymer blend films (polystyrene and polymethyl methacrylate). These reveal morphological differences in the nanoscale domains within the thin films of diffraction limited thickness, with spatial resolution of ∼40 nm. [84]

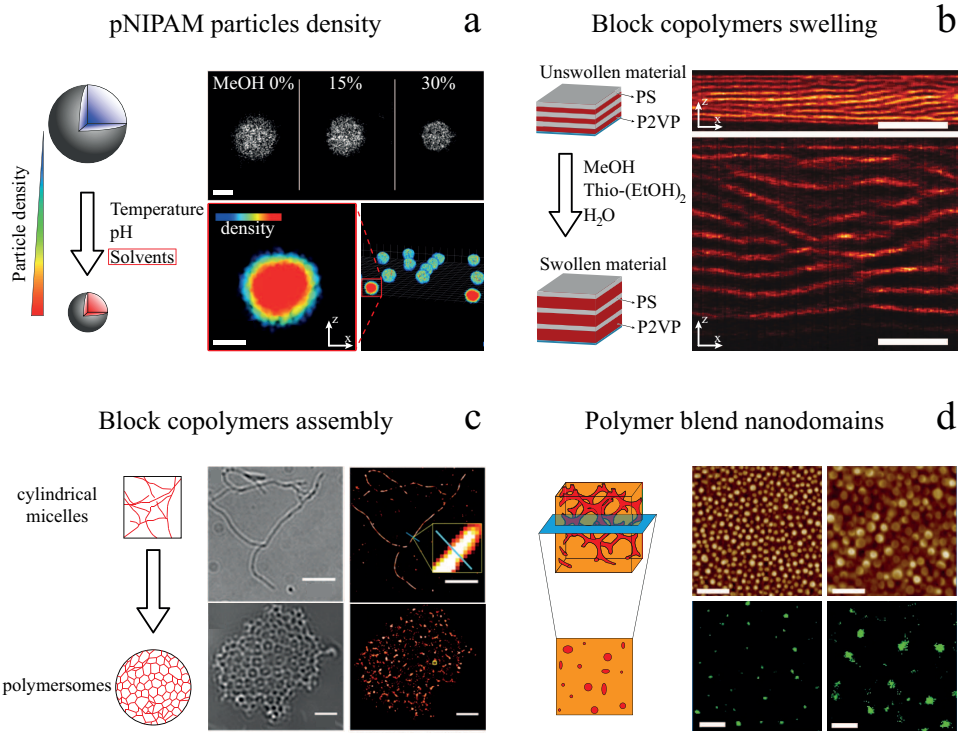

Figure 1.8: Examples of single-molecule super-resolution imaging of 2D and 3D morphologies in synthetic materials. (a) pNIPAM particles imaged by dSTORM in three-dimensions showing the deswelling of microgel particles upon addition of different percentages of methanol (top), and density profile of swollen pNIPAM particles (bottom). Scale bars represent 200 nm. Figure adapted from [81]. (b) Lamellar self-organization of poly(styrene-*block*-2-vinylpyridine) (PS-P2VP) imaged by STED microscopy. The contact with alcohols and water preferentially swells the P2VP phase. Scale bars represent 1 μm. Figure adapted from [82]. (c) Block co-polymer micelles assembled from polystyrene and poly(ethylene oxide), stained with spiropyrans. Upon UV irradiation the spiropyrans exhibit stochastic ON-OFF fluorescence. Scale bars represent 4 μm. Figure adapted from [83]. (d) Thin slices 50 nm (left) and 150 nm (right) thick of polymer blends showing nanoscale domains imaged by STORM. Figure adapted from [84].

1.5.3 New probes for super-resolution microscopy

The first steps super-resolution microscopy made into the fields of supramolecular chemistry and material science required a certain adaptation to the different environmental conditions (*e.g.*, polarity of the solvent, pH) compared to those needed to image biological sam-

ples. This is crucial especially for chromophores with photo-physical properties that depend on the solvent polarity and dielectric constants. This called for the development of new photo-switching and photo-activation approaches. A few examples are highlighted in the following. Diarylethene-based photoswitchers have been used to probe the free volume in block co-polymer structures (polystyrene and polyethylene oxide) on a molecular basis. [85] Rhodamine-lactam dyes are used as an acid-sensitive probe that can be activated either by UV illumination or protonation. They have been used to investigate the photoacid distribution in photoresist masks, providing insights on the interaction between the lithographic beam and the resist. [86] Ideally, one would perform super-resolution microscopy without any manipulation of the sample by exploiting the intrinsic fluorescent properties of synthetic polymers. An illustrative example is a study on poly(methyl methacrylate). The feasibility of this idea was evaluated by Urban *et al.*, who were able to reconstruct super-resolved images of unstained poly(methyl methacrylate) as it exhibits sparse blinking under illumination at $\lambda = 532$ nm illumination. [87]

1.6 Thesis content and aim

The aim of this thesis is to investigate the opportunities and limitations of single-molecule localization microscopy (SMLM) methods to visualize synthetic and supramolecular sub-μm structures in soft materials. To this end, we developed a new SMLM technique and extended the use of photo-activated localization microscopy (PALM) to organic solvents.

In **chapter 2** we report on the development of a new approach in SMLM based on Point Accumulation for Imaging in Nanoscale Topography (PAINT). Herein, we exploit the adsorption of a polymer-conjugated photo-activatable dye to visualize in 3D with high spatial resolution solid-liquid, liquid-liquid and air-liquid interfaces. We coin this method interface Point Accumulation for Imaging in Nanoscale Topography, in short iPAINT. Three exemplary colloidal model systems are studied, all of which are non-covalently labelled with a poly(ethylene oxide)-tagged caged rhodamine. Excellent agreement has been found between the mean values and associated distributions of silica nanoparticles and contact angles of air nanobubbles obtained by SMLM, SEM and AFM, respectively. This validates the applicability of our novel strategy to visualize (deformable) interfaces in a minimally invasive manner through non-covalent labelling with photo-activatable dyes.

Chapter 3 is devoted to the morphological characterization of complex coacervate core micelles (C3Ms) by iPAINT microscopy. These are polymeric micelles formed through electrostatically driven co-assembly of oppositely charged co-polymers. iPAINT enables the direct visualization of PF/P2MVP$_{29}$-*b*-PEO$_{204}$ C3Ms under conditions where conventional methods, like small X-ray scattering, electron microscopy and AFM are unsuccessful due to *e.g.*, high water content, low electron density, and low C3M concentration. We measure the morphology of the micelles as a function of their concentration, which reveals an increase in micellar anisotropy, from spherical to elliptical, with increasing C3M concentration. We attribute this unusual morphological transition to the intrinsic stiffness of the anionic PF within the micellar core.

Next, we study the position and orientation of single spherical (**chapter 4**) and elliptical (**chapter 5**) colloidal particles adsorbed at the interface between immiscible liquids. We show how iPAINT microscopy enables simultaneous visualization of the nanoparticles and the fluid interfaces. This allows for accurate measurements of the contact angle of individual particles, and, further the visualization of interface deformations induced by the particles. We start off by imaging isotropic particles (**chapter 4**) with different surface chemistries (hydrophobic and hydrophilic) at a water-octanol interface. We determine the mean contact angles for both types of particles and the related distributions by one- and two-colour iPAINT experiments. In **chapter 5** we focus on ellipsoidal particles with a $\sim$2μm major axis and a $\sim$400 nm minor axis, adsorbed at water-decane interfaces. Normal, parallel and oblique orientations are observed, while the mean contact angles and their distributions are

subsequently computed. These turn out to be broader for the oblique orientation than for the parallel configuration. Finally, we study by three-dimensional imaging of the particles and the interface, local deformations of the three-phase contact line induced by the adsorbed anisotropic particles.

In **chapter 6** we present the first *in-situ* use of PALM in organic solvents. We investigate the photophysical properties of the two dyes Cage-552 and Cage-635 in several solvents, spanning a wide range of dielectric constants. We clarify the mechanism of photo-activation, and how to enhance the ON-OFF switching of this class of commercially available caged rhodamines. Addition of as little as 2% of alcohol into the organic solvents enables imaging in two colours of two-dimensional colloidal self-assemblies and supramolecular aggregates that are μm-long and nm-wide.

Chapter 7 highlights two new applications of SMLM and the development of a novel class of dyes for SMLM in organic solvents. We report on the formation of supramolecular block co-polymers by two-colour iPAINT imaging, and the interaction between synthetic particles and liposomes. Then, we briefly present the design of a new dye molecule, namely a rhodamine spirothioamide, to facilitate super-resolution microscopy imaging in organic solvents.

In summary, in this Ph.D. research, new approaches in SMLM have been designed and implemented to broaden the scope of super-resolution microscopy and to better understand the structure and dynamics of nanostructured materials. The versatility of iPAINT microscopy makes this method a powerful alternative and a complementary technique for non-invasive, *in-situ* imaging of soft and deformable interfaces with sub-μm spatial resolution.

Bibliography

[1] van Leeuwenhoek A. *Phil. Trans.* **1677**, *12*, 821.

[2] Hooke, R. *Micrographia, or, Some physiological descriptions of minute bodies made by magnifying glasses: with observations and inquiries thereupon* **1665**, London, Printed by J. Martyn and J. Allestry.

[3] Feynman, R.P. *Engineering and Science* **1960**, *23*, 22.

[4] Eggeling, C.; Willig, K.I.; Sahl, S.J.; Hell, S.W. *Q. Rev. Biophys.* **2015**, *48*, 178.

[5] Abbe, E. *Arch. Mikroskop. Anat.* **1873**, *9*, 413.

[6] Betzig, E.; Chichester, R.J.; Lanni, F.; Taylor, D.L. *Bioimaging* **1993**, *1*, 129.

[7] Neil, M.A.; Juskaitis, R.; Wilson, T. *Opt. Lett.* **1997**, *22*, 1905.

[8] Gustafsson, M.G.L. *J. Microsc.* **2000**, *198*, 82.

[9] Gustafsson, M.G.L.; Shao, L.; Carlton, P.M.; Wang, C.J.R.; Golubovskaya, I.N.; Cande, W.Z.; Agard, D.A.; Sedat, J.W. *Biophys. J.* **2008**, *94*, 4957.

[10] Schermelleh, L.; Carlton, P.M.; Haase, S.; Shao, L.; Winoto, L.; Kner, P.; Burke, B.; Cardoso, M.C.; Agard, D.A.; Gustafsson, M.G.L.; Leonhardt, H.; Sedat, J.W. *Science* **2008**, *320*, 1332.

[11] Hell, S.W.; Lindek, S.; Cremer, C.; Stelzer, E.H.K. *Appl. Phys. Lett.* **1994**, *64*, 1335.

[12] Hell, S.W.; Stelzer, E.H.K. *J. Opt. Soc. Am. A Opt. Image Sci. Vis.* **1992**, *9*, 2159.

[13] Fitzpatrick, J.A.J.; Inouye, I.; Manley, S.; Moerner, E.W. *ChemPhysChem* **2014**, *15*, 547.

[14] Moerner, E.W. *Angew. Chem. Int. Ed.* **2015**, *54*, 8067.

[15] Betzig, E. *Angew. Chem. Int. Ed.* **2015**, *54*, 8034.

[16] Hell, S.W. *Angew. Chem. Int. Ed.* **2015**, *54*, 8054.

[17] Betzig, E.; Patterson, G.H.; Sougrat, R.; Lindwasser, O.W.; Olenych, S.; Bonifacino, J.S.; Davidson, M.W.; Lippincott-Schwartz, J.; Hess H.F. *Science* **2006**, *313*, 1642.

[18] Hess, S.T.; Girirajan, T.P.; Mason; M.D. *Biophys. J.* **2006**, *91*, 4258.

[19] Rust, M.J.; Bates, M.; Zhuang, X.W. *Nat. Methods* **2006**, *3*, 793.

[20] van de Linde, S.; Löschberger, A.; Klein, T.; Heidbreder, M.; Wolter, S.; Heilemann, M.; Sauer, M. *Nat. Protocols* **2011**, *6*, 991.

[21] Heilemann, M.; van de Linde, S.; Schüttpelz, M.; Kasper, R.; Seefeldt, B.; Mukherjee, A.; Tinnefeld, P.; Sauer, M. *Angew. Chem. Int. Ed.* **2008**, *47*, 6172.

[22] Sharonov, A.; Hochstrasser, R.M. *Proc. Natl. Acad. Sci. U.S.A.* **2006**, *103*, 18911.

[23] Belov, V.N.; Mitronova, G.Y.; Bossi, M.L.; Boyarskiy, V.P.; Hebisch, E.; Geisler, C.; Kolmakov, K.; Wurm, C.A.; Willig, K.I.; Hell, S.W. *Chem. Eur. J.* **2014**, *20*, 13162.

[24] van de Linde, S.; Kasper, R.; Heilemann, M.; Sauer, M. *Appl. Phys. B* **2008**, *93*, 725.

[25] Giannone, G.; Hosy, E.; Levet, F.; Constals, A.; Schulze, K.; Sobolevsky, A.I.; Rosconi, M.P.; Gouaux, E.; Tampé, R.; Choquet, D.; Cognet, L. *Biophys. J.* **2010**, *99*, 1303.

[26] Jungmann, R.; Steinhauer, C.; Scheible, M.; Kuzyk, A.; Tinnefeld, P.; Simmel, F.C. *Nano Lett.* **2010**, *10*, 4756.

[27] Jungmann, R.; Avendaño, M.S.; Woehrstein, J.B.; Dai, M.; Shih, W.M.; Yin, P. *Nat. Methods* **2014**, *11*, 313.

[28] Thompson, R.E.; Larson, D.R.; Webb, W.W. *Biophys. J.* **2002**, *82*, 2775.

[29] Mortensen, K.I.; Churchman, L.S.; Spudich, J.A.; Flyvbjerg, H. *Nat. Methods* **2010**, *7*, 377.

[30] Zhang, B.; Zerubia, J.; Olivo-Marin, J.C. *Appl. Opt.* **2007**, *46*, 1819.

[31] Ober, R.J.; Ram, S.; Ward, E.S. *Biophys. J.* **2004**, *86*, 1185.

[32] Cox, S.; Rosten, E.; Monypenny, J.; Jovanovic-Talisman,T.; Burnette, D.T.; Lippincott-Schwartz, J.; Jones, G.E.; Heintzmann, R. *Nat. Methods* **2012**, *9*, 195.

[33] Manley, S.; Gillette, J.M.; Patterson, G.H.; Shroff, H.; Hess, H.F.; Betzig, E.; Lippincott-Schwartz, J. *Nat. Methods* **2008**, *5*, 155.

[34] Holden, S.J., Uphoff, S.; Kapanidis, A.N. *Nat. Methods* **2011**, *8*, 279.

[35] Endesfelder, U.; van de Linde, S.; Wolter, S.; Sauer, M.; Heilemann, M. *ChemPhysChem* **2010**, *11*, 836.

[36] Henriques, R.; Lelek, M.; Fornasiero, E.F.; Valtorta, F.; Zimmer, C.; Mhlanga, M.M. *Nat. Methods* **2010**, *7*, 339.

[37] Hell, S.W.; Wichmann, J. *Opt. Lett.* **1994**, *19*, 780.

[38] Hell, S.W.; Kroug, M. *Appl. Phys. B* **1995**, *60*, 495.

[39] Bretschneider, S.; Eggeling, C.; Hell, S.W. *Phys. Rev. Lett.* **2007**, *98*, 218103.

[40] Gustafsson, M.G.L. *Curr. Opin. Struct. Biol.* **1999**, *9*, 627.

[41] Allen, J.R.; Ross, S.T.; Davidson, M.W. *ChemPhysChem* **2014**, *15*, 566.

[42] Ströhl, F.; Kaminski, C.F. *Optica* **2016**, *3*, 667.

[43] Schermelleh, L.; Heintzmann, R.; Leonhardt, H. *J. Cell Biol.* **2010**, *190*, 165.

[44] Klar, T.A.; Jakobs, S.; Dyba, M.; Egner, A.; Hell, S.W. *Proc. Natl. Acad. Sci. U.S.A.* **2000**, *97*, 8206.

[45] Hell, S.W.; Sahl, S.J.; Bates, M.; Zhuang, X.; Heintzmann, R.; Booth, M.J.; Bewersdorf, J.; Shtengel, G.; Hess, H.; Tinnefeld, P.; Honigmann, A.; Jakobs, S.; Testa, I.; Cognet, L.; Lounis, B.; Ewers, H.; Davis, S.J.; Eggeling, C.; Klenerman, D.; Willig, K.I.; Vicidomini, G.; Castello, M.; Diaspro, A.; Cordes, T. *J. Phys. D.: Appl. Phys.* **2015**, *48*, 443001.

[46] Svelto, O. *Principles of lasers* **2010**, 5th ed., Springer, NY.

[47] Vicidomini, G.; Moneron, G.; Han, K.Y.; Westphal, V.; Ta, H.; Reuss, M.; Engelhardt, J.; Eggeling, C.; Hell, S.W. *Nat. Methods* **2011**, *8*, 571.

[48] Gustafsson, M.G.L. *Proc. Natl. Acad. Sci. U.S.A.* **2005**, *102*, 13081.

[49] Cattoni, D.I.; Fiche, J.B.; Nöllmann, M. *Curr. Opin. Microbiol.* **2012**, *15*, 758.

[50] Ptacin, J.L.; Lee, S.F.; Garner, E.C.; Toro, E.; Eckart, M.; Comolli, L.R.; Moerner, W.E.; Shapiro, L. *Nat. Cell Biol.* **2010**, *12*, 791.

[51] Wang, S.; Su, J.-H.; Beliveau, B.J.; Bintu, B.; Moffitt, J.R.; Wu, C.-T.; Zhuang, X. *Science* **2016**, *353*, 598.

[52] Wang, C.; Han, B.; Zhou, R.; Zhuang, X. *Cell* **2016**, *165*, 990.

[53] Uphoff, S.; Reyes-Lamothe, R.; Garza de Leon, F.; Sherratt, D.J.; Kapanidis, A.N. *Proc. Natl. Acad. Sci. U.S.A.* **2013**, *110*, 8063.

[54] Hammar, P.; Walldén, M.; Fange, D.; Persson, F.; Baltekin, O.; Ullman, G.; Leroy, P.; Elf, J. *Nat. Genet.* **2014**, *46*, 405.

[55] Lee, S.F.; Thompson, M.A.; Schwartz, M.A.; Shapiro, L.; Moerner, W.E. *Biophys. J.* **2011**, *100*, L31.

[56] Biteen, J.S.; Thompson, M.A.; Tselentis, N.K.; Bowman, G.R.; Shapiro, L.; Moerner, W.E. *Nat. Methods* **2008**, *5*, 947.

[57] Greenfield, D.; McEvoy, A.L.; Shroff, H.; Crooks, G.E.; Wingreen, N.S.; Betzig, E.; Liphardt, J. *PLoS Biol.* **2009**, *7*, e1000137.

[58] Lew, M.D.; Lee, S.F.; Ptacin, J.L.; Lee, M.K.; Twieg, R.J.; Shapiro, L.; Moerner, W.E. *Proc. Natl. Acad. Sci. U.S.A.* **2011**, *108*, e1102.

[59] Tuson, H.H.; Biteen, J.S. *Anal. Chem.* **2015**, *87*, 42.

[60] Klein, T.; Proppert, S.; Sauer, M. *Histochem. Cell Biol.* **2014**, *141*, 561.

[61] Gunzenhäuser, J.; Olivier, N.; Pengo, T.; Manley, S. *Nano Lett.* **2012**, *12*, 4705.

[62] Gunzenhäuser, J.; Wyss, R.; Manley, S. *PLoS One* **2014**, *9*, e115095.

[63] Bates, M.; Huang, B.; Dempsey, G.T.; Zhuang, X. *Science* **2007**, *317*, 1749.

[64] French, J.B.; Jones, S.A.; Deng, H.; Pedley, A.M.; Kim, D.; Chan, C.Y.; Hu, H.; Pugh, R.J.; Zhao, H.; Zhang, Y.; Huang, T.J.; Fang, Y.; Zhuang, X.; Benkovic, S.J. *Science* **2016**, *351*, 733.

[65] Godin, A.G.; Lounis, B.; Cognet, L. *Biophys. J.* **2014**, *107*, 1777.

[66] Huang, B.; Jones, S.A.; Brandenburg, B.; Zhuang, X. *Nat. Methods* **2008**, *5*, 1047.

[67] Maglione, M.; Sigrist, S.J. *Nat. Neurosci.* **2013**, *16*, 790.

[68] Xu, K.; Zhong, G.; Zhuang, X. *Science* **2013**, *339*, 425.

[69] Aoki, H.; Mori, K.; Ito, S. *Soft Matter* **2012**, *8*, 4390.

[70] Knudsen, J.K.; Liu, L.; Bank Kodal, A.L.; Madsen, M.; Li, Q.; Song, J.; Woehrstein, J.B.; Wickham, S.F.J.; Strauss, M.T.; Schueder, F.; Vinther, J.; Krissanaprasit, A.; Gudnason, D.; Abbotsford Smith, A.A.; Ogaki, R.; Zelikin, A.N.; Besenbacher, F.; Birkedal, V.; Yin, P.; Shih, W.M.; Jungmann, R.; Dong, M.; Gothelf, K.V. *Nat. Nanotech.* **2015**, *10*, 892.

[71] Beun, L.H.; Albertazzi, L.; van der Zwaag, D.; de Vries, R.; Cohen Stuart, M.A. *ACS Nano* **2016**, *10*, 4973.

[72] Baker, M.B.; Albertazzi, L.; Voets, I.k.; Leenders, C.M.A.; Palmans, A.R.A.; Pavan, G.M.; Meijer, E.W. *Nat. Commun.* **2015**, *6*, 6234.

[73] Pujals, S.; Tao, K.; Terradellas, A.; Gazit, E.; Albertazzi, L. *Chem. Commun.* **2017**, *53*, 7294.

[74] Onogi, S.; Shigemitsu, H.; Yoshii, T.; Tanida, T.; Ikeda, M.; Kubota, R.; Hamachi, I. *Nat. Chem.* **2016**, *8*, 743.

[75] Albertazzi, L.; van der Zwaag, D.; Leenders, C.M.A.; Fitzner, R.; van der Hofstad, R.W.; Meijer, E.W. *Science* **2014**, *344*, 491.

[76] Baker, M.B.; Gosens, R.P.J.; Albertazzi, L.; Matsumoto, N.M.; Palmans, A.R.A.; Meijer, E.W. *ChemBioChem* **2016**, *17*, 207.

[77] Hendrikse, S.I.S.; Wijnands, S.P.W.; Lafleur, R.P.M.; Pouderoijen, M.J.; Janssen, H.M.; Dankers, P.Y.W.; Meijer, E.W. *Chem. Commun.* **2017**, *53*, 2279.

[78] da Silva, R.P.M.; van der Zwaag, D.; Albertazzi, L.; Lee, S.S.; Meijer, E.W.; Stupp, S.I. *Nat. Commun.* **2016**, *7*, 11561.

[79] Tian, Z.; Li, A.D.Q.; Hu, D. *Chem. Commun.* **2011**, *47*, 1258.

[80] Gelissen, A.P.H.; Oppermann, A.; Caumanns, J.T.; Hebbeker, P.; Turnhoff, S.; Tiwari, R.; Eisold, S.; Simon, U.; Lu, Y.; Mayer, J.; Richtering, W.; Walther, A.; Wöll, D. *Nano Lett.* **2016**, *16*, 7295.

[81] Conley, G.M.; Nöjd, S.; Braibanti, M.; Schurtenberger, P.; Scheffold, F. *Colloids Surf. A: Physicochem. Eng. Aspects* **2016**, *499*, 18.

[82] Ullal, C.K.; Primpke, S.; Schmidt, R.; Böhm, U.; Egner, A.; Vana, P.; Hell, S.W. *Macromol.* **2011**, *44*, 7508.

[83] Yan, J.; Zhao, L.-X.; Li, C.; Hu, Z.; Zhang, G.-F.; Chen, Z.-Q.; Chen, T.; Huang, Z.-L.; Zhu, J.; Zhu, M.-Q. *J. Am. Chem. Soc.* **2015**, *137*, 2436.

[84] Gramlich, M.W.; Bae, J.; Hayward, R.C.; Ross, J.L. *Opt. Express* **2014**, *22*, 8438.

[85] Nevskyi, O.; Sysoiev, D.; Oppermann, A.; Huhn, T.; Wöll, D. *Angew. Chem. Int. Ed.* **2016**, *55*, 12698.

[86] Berro, A.J.; Berglund, A.;J.; Carmichael, P.T.; Seung Kim, J.; Liddle, J.A. *ACS Nano* **2012**, *6*, 9496.

[87] Urban, B.E.; Dong, B.; Nguyen, T.-Q.; Backman, V.; Sun, C.; Zhang, H.F. *Sci. Rep.* **2016**, *6*, 28156.

Chapter 2

iPAINT: a general approach tailored to image the topology of interfaces with nanometer resolution

Understanding interfacial phenomena in soft materials such as wetting, colloidal stability, coalescence, and friction warrants non-invasive imaging with nanometer resolution. Super-resolution microscopy has emerged as an attractive method to visualize nanostructures labelled covalently with fluorescent tags, but this is not amenable to all interfaces. Inspired by PAINT we developed a simple and general strategy to overcome this limitation, which we coin 'iPAINT: interface Point Accumulation for Imaging in Nanoscale Topography'. It enables three-dimensional, sub-diffraction imaging of interfaces irrespective of their nature *via* reversible adsorption of polymer chains end-functionalized with photo-activatable moieties. We visualize model dispersions, emulsions, and foams with $\sim$20 nm and $\sim3^{\circ}$ accuracy demonstrating the general applicability of iPAINT to study solid-liquid, liquid-liquid and air-liquid interfaces. iPAINT thus broadens the scope of super-resolution microscopy paving the way for non-invasive, high-resolution imaging of complex soft materials.

Part of this work has been published as: Aloi, A.; Vilanova, N.; Albertazzi, L.; Voets, I.K. *Nanoscale* **2016**, *8*, 8712.

2.1 Introduction

Interfaces play an essential role in physical, biological and chemical processes, ranging from colloidal stability, energy conversion, and phase-transfer catalysis to signal-transduction, molecular recognition, and molecular transport across membranes. This is a direct consequence of their ubiquitous presence, especially in nanostructured materials with high surface-to-volume ratios due to the small dimensions of the building blocks. In the last decade super-resolution microscopy emerged as an attractive technique complementary to X-ray diffraction, electron microscopy (EM), and atomic force microscopy (AFM) to study interfaces with nanometer resolution in 3D. [1–4] It is particularly suited for dynamic, soft materials where minimal sample perturbation is essential and differences in electron density are small. Nowadays, point accumulation for imaging in nanoscale topography (PAINT), [5] photo-activated localization microscopy (PALM), [2] stochastic optical reconstruction microscopy (STORM), [4] and other single-molecule localization methods [6] are fundamental techniques to study the morphology and dynamics of living matter. [7] Recent STORM experiments unravelling the self-assembly mechanism and architecture of complex synthetic molecular systems [8, 9] demonstrate that super-resolution microscopy also offers unique insights into man-made materials. Most sub-diffraction imaging methods rely on covalent labelling with fluorescent markers that can be photo-activated or blink stochastically. Dyes with suitable photophysical properties equipped with a functional group for direct coupling to the object under consideration are selected and subsequently the label density is tuned to optimize object reconstruction. [2] PAINT on the other hand relies on non-covalent labelling, exploiting a continuous and reversible targeting of the object by freely diffusing fluorophores. [5] In a pioneering study, Sharanov *et al.* imaged lipid vesicles by PAINT using Nile red, which fluoresces only in hydrophobic environments. [5] Thus, probes immobilized on the lipid bilayer start to fluoresce, a diffraction-limited single-molecule image is acquired, and eventually fluorescence drops to zero as the dyes photobleach and/or dissociate from the vesicle. Subsequently, Giannone and coworkers developed uPAINT to study the structure and dynamics of membranes via labelling of specific membrane-bound biomolecules with a fluorescently tagged ligand. [10] Shortly after, DNA-PAINT was developed to realize three-dimensional, multi-colour, sub-10 nm imaging of DNA nanostructures and proteins with better control over the binding specificity and dissociation kinetics of the probes. [11, 12] PAINT-based techniques have been rapidly adopted as an essential research tool throughout biology and biophysics, but still remain scarcely applied in soft matter and materials science. A major hurdle for the widespread application in colloid and interface science are the stringent requirements of having hydrophobic domains (PAINT) or incorporation of specific ligand/receptor pairs (uPAINT, DNA-PAINT). To overcome these limitations, we develop PAINT further into what we coin 'iPAINT', which is short for interface Point Accumulation

for Imaging in Nanoscale Topography. This new approach enables visualization of solid-liquid, liquid-liquid, and air-liquid interfaces with nanometer resolution in 3D irrespective of their surface chemistry via continuous noncovalent labelling during imaging. The latter is essential for complex interfaces that cannot be labelled directly through site-specific covalent coupling of a dye, such as emulsions, foams, and crystals like ice.

2.2 Results and discussion

2.2.1 The iPAINT method

A flow chart of a typical iPAINT experiment is given in figure 2.1. The crucial element is the presence of a large reservoir of polymers end-functionalized with photo-activatable probes (PEG-552). While most of these macromolecules freely diffuse in solution, some adsorb at and desorb from the interface, allowing prolonged non-covalent labelling of the interface during imaging. PEG-552 consists of a photo-activatable rhodamine analogue [13] coupled to a poly(ethylene glycol) chain, which is well-known for reversible, non-specific adsorption onto a wide range of interfaces. [14] At the onset of the iPAINT experiment, no fluorescence signal is collected as the probes are in the dark state (fig. 2.1b). Next, low-power UV laser light ($\lambda = 405$ nm) photo-activates a small number of probes, while a full-power readout beam ($\lambda = 561$ nm) excites the activated probes (fig. 2.1c).

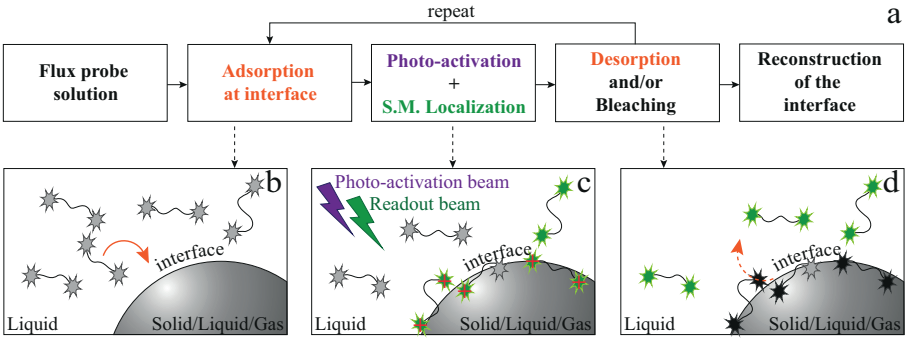

Figure 2.1: Flow chart of iPAINT super-resolution microscopy. (a) A typical iPAINT experiment commences with probe injection followed by probe adsorption, photo-activation, excitation, single-molecule (S.M.) localization, bleaching, and desorption until the object of interest is reconstructed in a final step of image analysis. (b) Upon injection of a PEG-552 solution into the chamber, probes (all in the dark state) accumulate at the interface. (c) UV laser light photo-activates a limited amount of probes all of which are subsequently excited by visible laser light. Individual excited dyes immobilized at the interface are localized (red crosses). (d) Immobilized dyes bleach and/or exchange with probes in the reservoir. This repetitive sequence of events (b–d) results in continuous non-covalent labelling of the interface.

The number of fluorescent dyes in the bright state is controlled by the power of the UV laser, aiming for a probe density of several tens of excited dyes per frame of $\sim$1900 μm^2.

Single-molecule localization of dyes occurs solely at the interface (red crosses in fig. 2.1c), since freely diffusing probes move too fast relative to the EMCCD camera acquisition frame rate. Continuous iteration of these steps allows reconstructing the interface with nanometer accuracy. In the following, figure 2.2 describes the accumulation of the single-molecule localizations in time in a typical iPAINT experiment. It can be clearly seen how the sparse set of localizations is constantly increasing in density at the interfaces (fig. 2.2a-c). After a time lapse of ∼30 min the objects are completely reconstructed as shown in figure 2.2d.

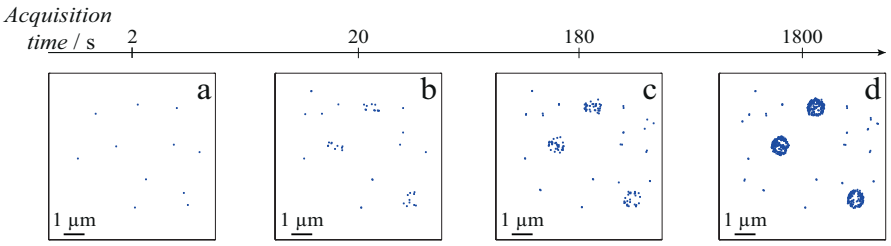

Figure 2.2: iPAINT single-molecule localization accumulation in time. iPAINT images at different time lapses after (a) 10^2, (b) 10^3, (c) 10^4, and (d) 5×10^4 acquired frames. Blue dots correspond to individual fluorescent probes localized at the silica surface, building up the reconstructed images in time of colloidal particles.

2.2.1.1 Image analysis

The image analysis procedure for iPAINT is outlined in figure 2.3. First, the raw image (fig. 2.3a) is corrected for the background signal from fluorescent probes adsorbed on the glass coverslip. The background signal removal (implemented in the NIS element Nikon software) is density-based: the algorithm looks for datapoints having at least *n* other datapoints within a certain range δ, and removes those localizations which do not fulfill the set parameters ($n = 10$, $\delta = 150$ nm in fig. 2.3b). Next, single beads and clustered beads are identified by eye (fig. 2.3c). The single molecule localizations corresponding to each single bead are saved in a separate file for further analysis of particle size and size distribution (fig. 2.3d). Mean particle sizes are determined using freeware exchange Matlab files for two- and three-dimensional fitting routines. The 2D routine utilizes the single molecule localizations corresponding to the midplane of the bead, taken as $\frac{z_{max}-z_{bg}}{2}$, where z_{max} is the highest *z*-plane with localized single molecules, and z_{bg} is the *z*-position of the localizations on the background. The distribution of points in this plane is fitted to a circle (Matlab exchange file 'Circle Fit') as shown in figure 2.3e, which outputs the center coordinates and the circle radius. The algorithm minimizes $\sum(x^2 + y^2 - R^2)^2$, with *x* and *y* being the coordinates of the localizations and R the radius of the circle.

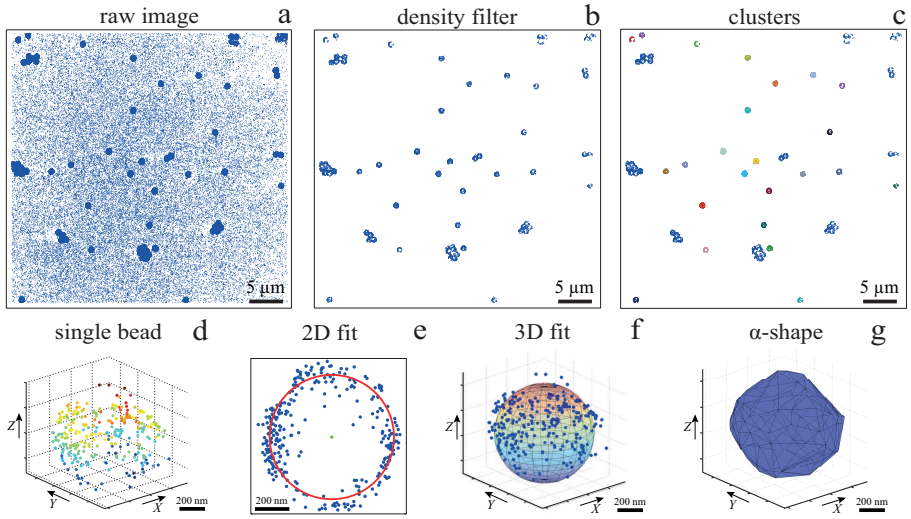

Figure 2.3: iPAINT data analysis routines. Representative iPAINT image of hydrophilic silica beads of ∼330 nm radius (a) prior, and (b) after background removal. (c) Identification of singlets; clustered beads are not taken into account in further data analysis steps. (d) Three dimensional iPAINT image of a single bead. (e) Circular fit of localizations in the mid-plane of the bead shown in panel (d) to find the bead center and radius. (f) Three-dimensional fit of a sphere to all single molecule localizations of the entire bead shown in (d) to find the bead center and radius. (g) α-shape triangulation of the localizations shown in (d)

The 3D fitting routine uses the entire three-dimensional data set collected for each single bead that is identified. The localization pointcloud is fit with a Matlab exchange file 'Sphere Fit' that again computes the center coordinates (x_c, y_c, z_c) and the sphere radius, R (fig. 2.3f). Here, $\sum[(x^2 - x_c^2)^2 + (y^2 - y_c^2)^2 - (z^2 - z_c^2) - R^2]^2$ is minimized. To further reconstruct the surfaces of the beads we employ a convex hull algorithm called α-shape, operated in Matlab. [15] The α-shape algorithm is based on the use of an α-ball of radius R_α which rolls over the pointcloud of the iPAINT localizations. To use the α-shape the experimental resolution of the iPAINT measurements has to be taken into account to fix the radius of the α-ball, in this case to $R_\alpha = 80$ nm. If operated on a three-dimensional set of localizations, it gives back the volume of the object as shown in figure 2.3g. The α-shape algorithm can also be used on a two-dimensional set of localizations to identify only the boundaries of the object. This is useful for the air-liquid interface (section 2.2.4 to define the size of the air nanobubbles).

2.2.1.2 Enhanced localization accuracy

In a typical iPAINT measurement, μM concentration of dye molecules are used to perform the imaging. In such a way iPAINT enables long acquisition times – roughly five times longer than regular super-resolution microscopy – due to continuous exchange of dyes between the interface and the solution. The latter serves as a large reservoir of photo-activatable, non-bleached fluorescent probes in solution. To demonstrate the impact of dye exchange, a long acquisition time-lapse of 10^5 frames is collected in the presence of freely diffusing PEG-552 chains in the sample chamber (5×10^{-5} M). Figure 2.4 shows the average number of localizations, normalized per bead and per acquired frame as a function of the acquisition time. After a short equilibration period of few minutes, the number of localizations remains constant as a steady state is reached due to the balance between adsorption, desorption and bleaching of the fluorescent probes.

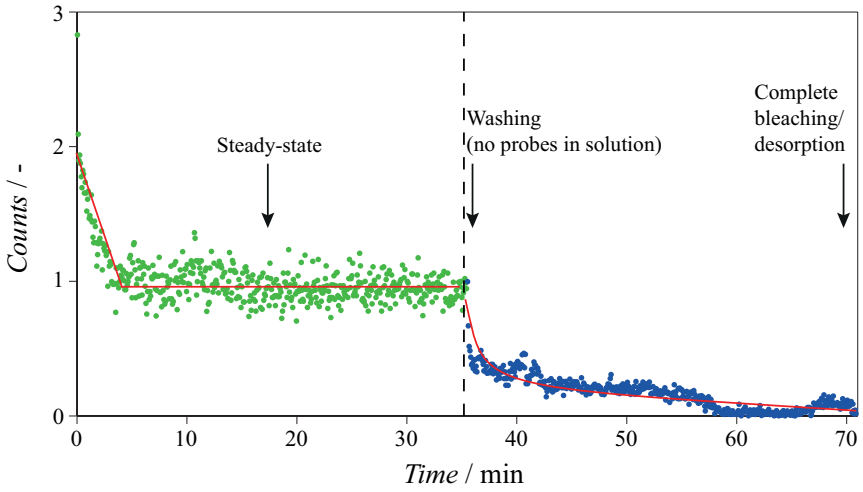

Figure 2.4: Continuous exchange of photo-activatable probes enables long acquisition times in iPAINT. Number of single molecule localizations per bead and per frame N during a long acquisition time-lapse of 10^5 frames in total. In the presence of a large reservoir of PEG-552, N rapidly plateaus at a constant value as a steady state is reached due to a balance between adsorption, desorption and photobleaching. After 35 min, the PEG-552 solution is replaced by MilliQ-water. By doing this, continuous exchange of dyes during imaging is prevented, and thus a rapid decrease in the number of localizations is observed, until all dyes are bleached. Lines are drawn to guide the eye.

During this period, the density of fluorescent probes at the interface is essentially constant and photobleaching hardly reduces the number of excited probes at the interface since bleached dyes are rapidly replenished by photo-activatable dyes from the large reservoir. This enables localization of a large number of individual probes which improves the resolution of the experiment. Upon replacing the PEG-552 solution by flushing MilliQ-water into the chamber (vertical dashed line in fig. 2.4), which prevents the exchange during imaging, the number of localizations per bead and per frame rapidly reduces until finally all probes are

bleached. This demonstrates that reversible exchange of dyes between the interface and the large reservoir of dyes in solution is essential to reach long acquisition times in iPAINT.

The accuracy in the reconstruction of the object depends on the total number of localizations used for reconstruction, as well as the accuracy of the individual single molecule localizations. The theoretical accuracy of each single molecule localization is given by: [16]

$$\sigma_{\mu_i} = \sqrt{\left(\frac{{s_i}^2}{N}\right) + \left(\frac{a^2/12}{N}\right) + \left(\frac{8\pi {s_i}^4 b^2}{a^2 N^2}\right)} \propto \frac{s_i}{\sqrt{N}} \tag{2.1}$$

where σ is the standard error to the mean in the photon distribution ($\mu = x_0;\ y_0$), a is the pixel size of the imaging CCD detector, b is the standard deviation of the background (including the background fluorescence emission combined with detector noise), s_i is the standard deviation of the localization distribution (in direction i, with $i = x$ or y), and N is the number of photons gathered. The first term in equation 2.1 refers to the photon noise, the second term takes into account the finite size of the pixels of the detector, and the third term defines the background noise. Typically the noise term due to pixelation $\frac{a^2/12}{N}$, and the background noise $\frac{8\pi {s_i}^4 b^2}{a^2 N^2}$ are negligible compared to the main noise contribution which is given by the point-spread function width of the microscope, hence equation 2.1 can be simplified by omitting the second and the third term.

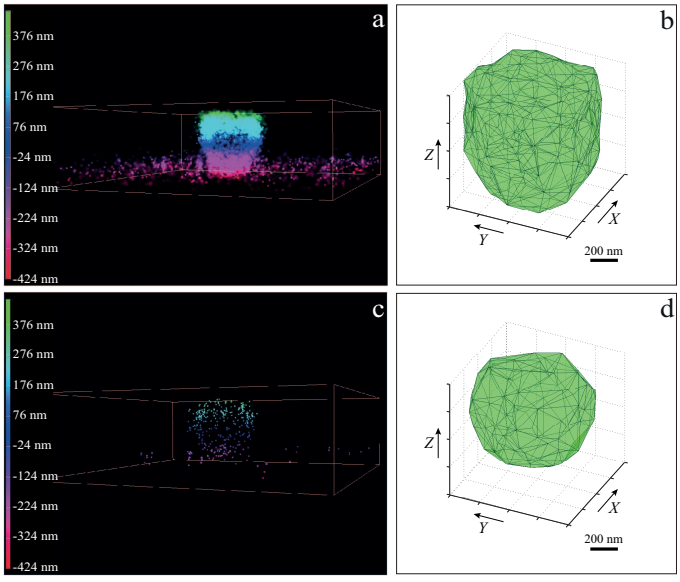

Figure 2.5: Enhanced localization accuracy in iPAINT. 3D iPAINT reconstructed images of hydrophilic silica beads, ~330 nm in radius, with a photon threshold set to (a) 1000 and (c) 11000, corresponding to theoretical accuracies of 10 and 1-2 nm, respectively. (b) and (d) α-shape triangulation of the localizations shown in (a) and (c), respectively.

In iPAINT imaging, the presence of a large reservoir of fluorescent probes enables long acquisition times, which increases the total number of localized single molecules at the interface ($>10^6$). This offers the possibility to not use all localizations for reconstruction, but instead to select the localizations from dyes that emit a large number of photons. Figure 2.5 shows a reconstruction of hydrophilic silica colloids using all localizations (fig. 2.5a) and selected localizations only (fig. 2.5c). The fluorescent tags emit at least 1000 (fig. 2.5a) or 11000 (fig. 2.5c) photons, which gives a theoretical accuracy for each single molecule localization of 10 nm and 1-2 nm, respectively. By α-shaping we obtain a 3D reconstruction of the object (fig. 2.5b, fig. 2.5d). Clearly, increasing the photon threshold improves the 3D reconstruction. The lower threshold of 1000 photons yields a shape that is not perfectly spherical, particularly the top of the bead is flat and enlarged. This is because the diameter of the bead approaches the maximum height that can be probed in our microscope. Gratifyingly, the higher photon threshold of 11000 photons does enable accurate reconstruction of the entire bead.

2.2.2 Solid-liquid interface: colloidal dispersions

To evaluate the possibilities and limitations of iPAINT as a complementary tool to visualize interfaces with high precision, we start off by imaging aqueous dispersions of monodisperse, spherical hydrophilic silica nanoparticles, which are broadly applied as biomaterials and in food formulations, photonics, coatings, and responsive materials. [17,18] Silica particles of low polydispersity are synthesized using a Stöber-based method. [19–21] Particles of $\sim$110 nm adn $\sim$330 nm in radius are obtained. The suspension is washed and stored in ethanol. To investigate the impact of different surface chemistry on the iPAINT imaging, hydrophobic colloidal particles are synthesized as well. Hydrophobic silica beads are prepared by simply functionalizing plain silica beads with stearyl alcohol. [22] The particles are characterized by SEM (section 2.4.2), showing a $\langle R \rangle = 332 \pm 18$ nm for the big colloids, and $\langle R \rangle = 115 \pm 14$ nm for the small particles. For the iPAINT experiments, few droplets of silica colloids dispersed in ethanol are placed on a microscope coverslip and dried under a flow of N_2. After the assembly of a sample chamber to run the imaging (section 2.4.4), a solution containing the iPAINT probes is injected. Upon injection, the processes described in section 2.2.1 takes place, leading to the super-resolved image of colloidal particles.

2.2.2.1 iPAINT imaging of colloidal particles

After a time lapse of ∼30 minutes of acquisition, the final reconstructed 3D iPAINT images of beads of ∼330 and ∼110 nm in radius are obtained as summation of localizations of more than 10^6 single molecules collected in 5×10^4 frames. The projection on the *x*–*y* plane of each single-molecule localization on the bead surface is depicted in figure 2.6a and 2.6d. The size and shape of individual nanoparticles are clearly resolved in three dimensions (fig. 2.6b and 2.6e), even though their dimensions are below the diffraction limit (∼250 nm). For benchmarking purposes, we compare the particle size distributions of >100 colloids obtained by 3D iPAINT and SEM in figure 2.6c and f. We find excellent agreement for both particle sizes with mean radii differing only by less than 5%: $\langle R_{iPAINT} \rangle = 350 \pm 15$ nm vs. $\langle R_{SEM} \rangle = 332 \pm 18$ nm and $\langle R_{iPAINT} \rangle = 118 \pm 26$ nm vs. $\langle R_{SEM} \rangle = 115 \pm 14$ nm.

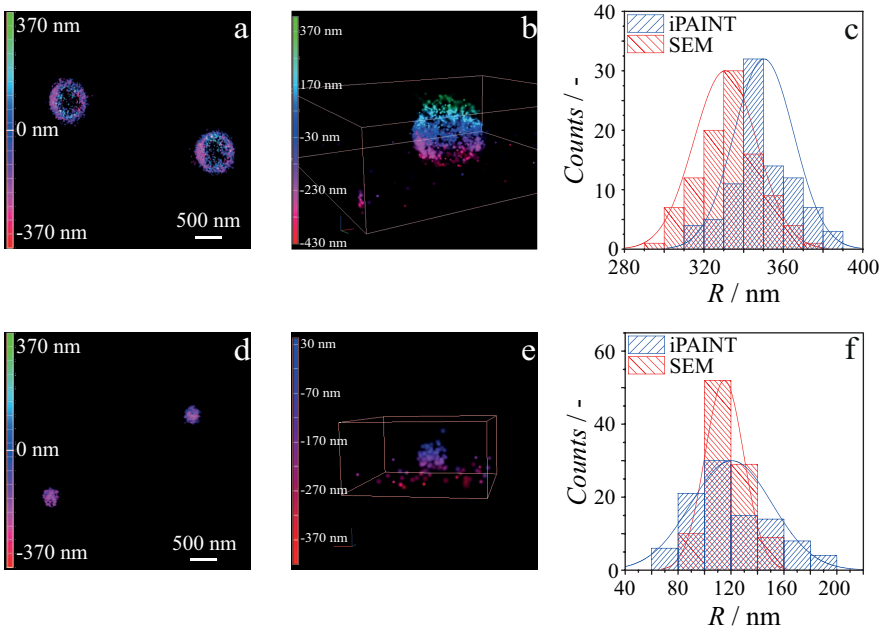

Figure 2.6: iPAINT imaging of colloidal dispersions. 2D projection of reconstructed images in time of silica beads of (a) ∼330 nm and (d) ∼110 nm in radius. Colour bars indicate the z-position ranging from 400 nm below (pink) to 400 nm above (green) the focal plane. (b) and (e) 3D image of reconstructed beads of ∼330 nm and ∼110 nm in radius, respectively. (c) and (f) Distribution of particle radii obtained by iPAINT and SEM for particles of ∼330 and ∼110 in radius, respectively.

2.2.2.2 iPAINT imaging of hydrophilic and hydrophobic colloids

Hydrophilic (plain) and hydrophobic (stearyl-coated) silica beads are imaged by iPAINT microscopy to investigate whether iPAINT can be applied to image both hydrophilic and hydrophobic solid-liquid interfaces. Both hydrophilic (fig. 2.7a) and hydrophobic (fig. 2.7c) silica nanoparticles are imaged in three-dimensions with ∼20 nm accuracy. The particle size distributions are computed for both hydrophilic (fig. 2.7b) and hydrophobic (fig. 2.7d) silica colloids using 2D and 3D fitting routines on the pointcloud localizations. For the hydrophilic nanoparticles we obtain $\langle R_{2D} \rangle = 349 \pm 16$ nm and $\langle R_{3D} \rangle = 358 \pm 18$ nm and for the hydrophobic colloids we found $\langle R_{2D} \rangle = 346 \pm 15$ nm and $\langle R_{3D} \rangle = 351 \pm 17$ nm.

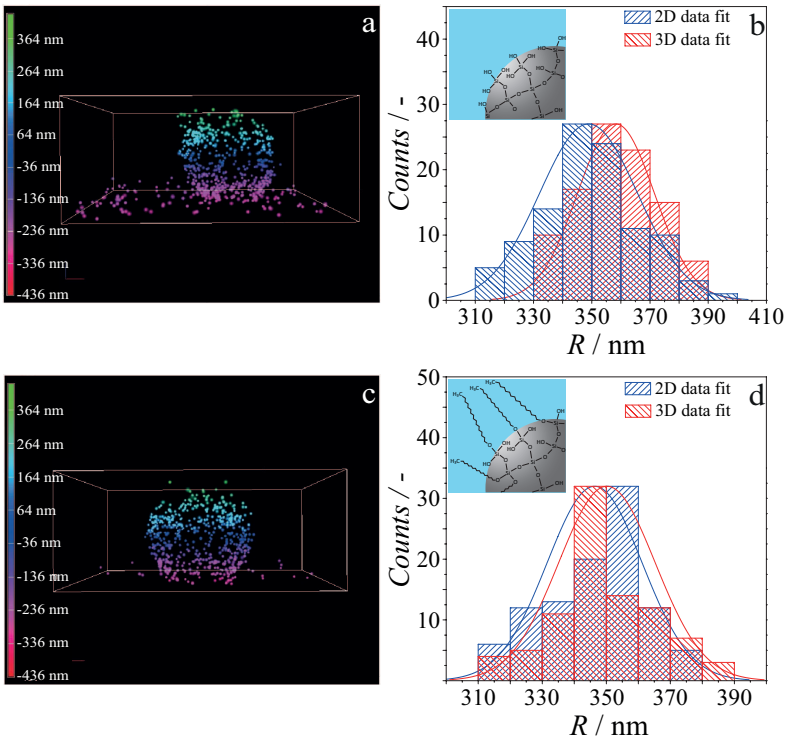

Figure 2.7: 3D iPAINT imaging of hydrophilic and hydrophobic nanoparticles. (a) and (c) 3D iPAINT reconstruction of a plain (hydrophilic) and stearyl alcohol-coated (hydrophobic) silica bead, respectively. (b) and (d) Colloid size distributions from two- (blue) and three-dimensional (red) fitting routines of the localization pointcloud, reconstructing the hydrophilic and hydrophobic surface of silica beads. Insets: cartoons representing the surface chemistry of a hydrophilic and hydrophobic silica bead, respectively.

2.2.3 Liquid-liquid interface: emulsions

Next, we turn to three-dimensional, non-invasive, high-resolution imaging of emulsions, which is a challenging task since droplets are dynamic and their interface is deformable under applied pressure. To this end, we prepare model water-in-oil (W/O) and oil-in-water (O/W) emulsions from 1-octanol and water, which are used as a model to study the partitioning of species from water into soil, [23] and to mimic the adsorption of molecules into living tissues. [24] To circumvent Gaussian blurring due to diffusion, droplets need to be immobilized onto glass coverslips. Figure 2.8 shows a comparison between wide-field and iPAINT imaging of W/O (fig. 2.8a–d) and O/W (fig. 2.8e–h) emulsions. The oil phase in figure 2.8b and f appears dark, whereas the aqueous phase is bright, since PEG-552 adsorbs onto the oil-water and coverslip-water interfaces. Only large droplets are clearly distinguishable by wide-field microscopy, while iPAINT resolves nanometer- to micrometer-sized oil and water droplets. The reservoir with PEG-552 probes in the W/O emulsion ($\sim 10^4$ molecules in a 1 μm diameter droplet) is too small for a neat reconstruction of the interface of sub-diffraction-sized nanodroplets, but it is sufficient to identify them (fig. 2.8d). By contrast, the larger aqueous reservoir in O/W emulsions contains sufficient PEG-552 for full reconstruction of the oil-water interface of small droplets.

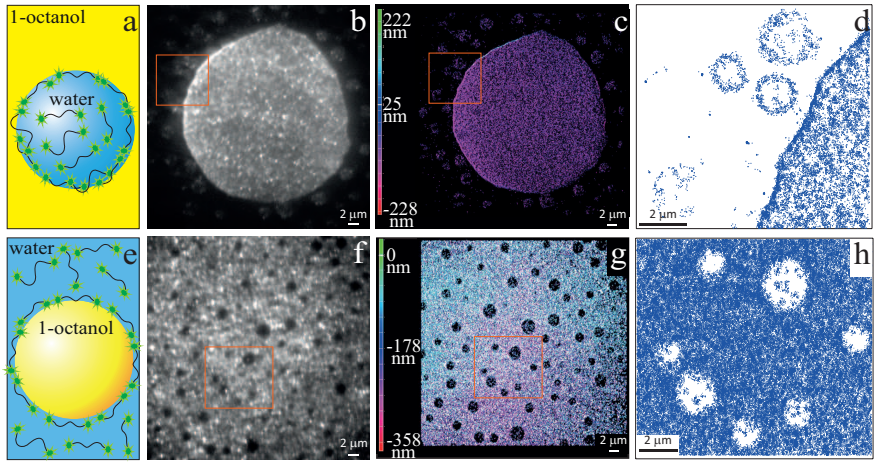

Figure 2.8: Imaging of emulsions by iPAINT microscopy. (a) Cartoon of a water droplet with PEG-552 dispersed in 1-octanol. (b) Wide-field and (c) iPAINT images of a W/O emulsion (scale bar 2 μm). (d) Zoom-in of iPAINT image in (c) depicts three aqueous nanodroplets which are less than 300 nm apart. (e) Cartoon of an 1-octanol droplet dispersed in a PEG-552 solution. (f) Wide-field and (g) iPAINT images of an O/W emulsion (scale bar 2 μm). (h) Zoom-in of iPAINT image in (g) depicts oil nanodroplets with $R <$ 600 nm.

2.2.4 Air-liquid interface: nanobubbles

As a final test for the general applicability of iPAINT for interface imaging we aim to visualize air-liquid interfaces. We opt to investigate air nanobubbles, so far imaged by fluorescence microscopy at the microscale, [25] and only by AFM, [26] and cryo-SEM [27] at the nanoscale. Nanobubbles are an active area of physico-chemical research as they impact a range of interfacial phenomena including molecular adsorption, thin film rupture, and surface corrosion. [28,29] We nucleate air nanobubbles through a well-established protocol based on alcohol-water exchange, [26] on a microscope glass coverslip at 37 °C. Figure 2.9a shows the brightfield image of air nanobubbles obtained in such way.

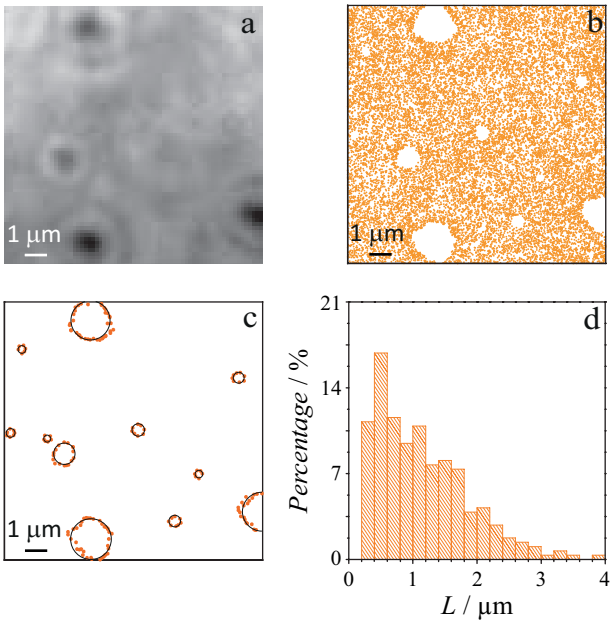

Figure 2.9: Identification of individual nanobubbles by iPAINT microscopy. (a) Brightfield imaging of air bubbles nucleated on a glass coverslip by solvent-exchange. [26] (b) iPAINT imaging of the same region as in (a) reveals air nanobubbles smaller than the diffraction limit. (c) Identification of the contours of single air nanobubbles (orange dots) by α-shaping, $R_\alpha = 20$nm, and subsequent circular fit (black solid line). (d) Lateral size distribution of nanobubbles shown in (c).

Microbubbles are visible in the brightfield image in figure 2.9a, but their size cannot be determined accurately, merely based on the values of the gray scale of the bubbles and the background. Conversely, the distribution of lateral bubble sizes L is readily determined from the bubble contours identified by iPAINT imaging (fig. 2.9b), unveiling subdiffraction-sized air bubbles. Analogous to the O/W emulsions, PEG-552 adsorbs at the relevant interface as well as on the glass coverslip in contact with water, which means that the air bubbles are the areas without single-molecule localizations in the iPAINT image (fig. 2.9b). Recurring at the 2D α-shaping algorithm, we retrieve the boundaries of the nanobubbles as depicted in figure

2.9c. Through the same fitting procedure described for colloidal particles in 2D, we compute the lateral size of single air nanobubbles, leading to the size distribution presented in figure 2.9d. From the 3D iPAINT image, the height of a nanobubble can be determined as well (fig. 2.10a). To this end we utilize the 3D α-shaping algorithm. First, the complete surface of the nanobubble is identified by triangulation of the coordinates of the single molecule localizations (fig. 2.10b). The lateral size L is then easily computed from the boundaries of the air nanobubble on the cover slip (fig. 2.9c). Next, the three-dimensional profile is divided into 80 nm thick slices, since this thickness is slightly bigger than the achieved resolution in the *z*-direction (fig. 2.10c-f). This allows to compute the height of the nanobubbles from the difference in *z*-position between the lower (fig. 2.10c) and the upper planes (fig. 2.10f) containing single molecule localizations, such that $h = z_{max} - z_{min}$.

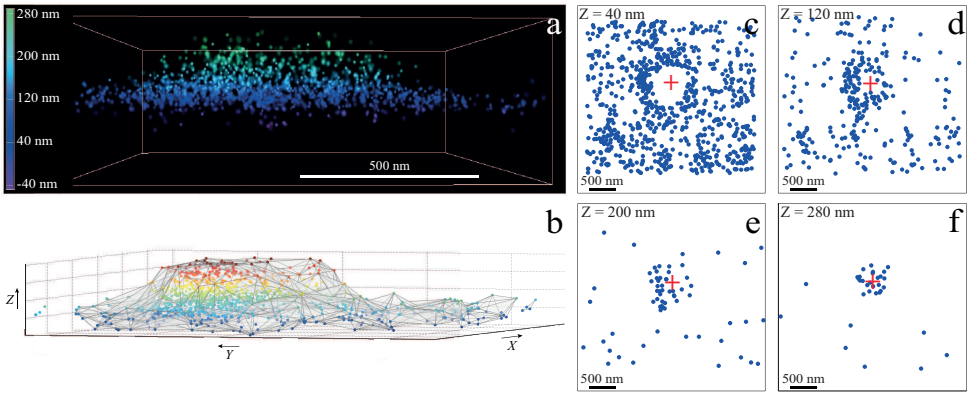

Figure 2.10: Z-stack of a nanobubble. (a) iPAINT image of an air nanobubble in three dimensions. (b) α-shaping of the bubble surface. To compute bubble height, the image is sectioned in the z-direction into four planes of 80 nm in thickness. The lateral size of the air nanobubble is determined from the lower slice (c). The hollow cavity corresponding to the bubble shrinks with increasing distance away from the coverslip (c-f). The bubble height h is taken as $h = z_{max} - z_{min}$. The red cross in (c-f) identifies the center of mass of the nanobubble.

Once the height h and lateral size $L = 2R_b$ of the nanobubbles are determined from 3D iPAINT images (fig. 2.11a), the contact angle of single nanobubbles can be calculated. Figure 2.11b depicts a schematic illustration of the cross-section of an immobilized nanobubble on a glass coverslip. Here, the principal dimensions accessible by an iPAINT experiment are shown, *i.e.*, the contact angle, θ, the bubble height, h, the base radius, R_b, the radius of curvature, R, and the lateral size, L. For a nucleation process carried out at 37 °C, the distribution in lateral size can vary from few hundreds of nanometers to several microns, as illustrated in figure 2.11c.

The plot in figure 2.11d shows the height of nanobubbles *vs.* their lateral size. The data can be fitted with a linear dependency, assuming that all bubbles are similar in shape. [30] According to equation 2.2, the mean contact angle of the analyzed nanobubbles can be

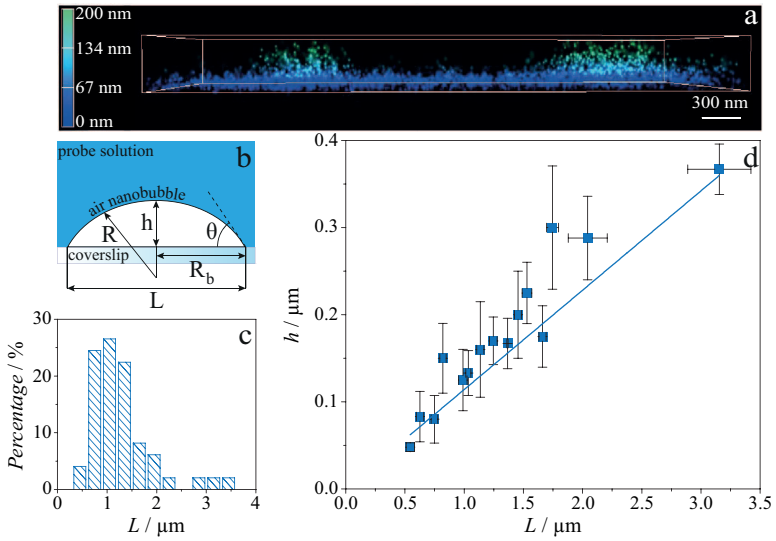

Figure 2.11: Contact angle measurements of individual nanobubbles by iPAINT. (a) 3D iPAINT imaging of two nanobubbles. Single-molecule localizations at the air-water interface are colour-coded according to their distance relative to the coverslip from blue (0 nm) to green (200 nm); adsorption at the water/coverslip interface is visible as a non-negligible background of localizations throughout the coverslip at ∼0 nm. (b) Cartoon of an immobilized air bubble indicating the contact angle, θ, the bubble height, h, the base radius, R_b, the radius of curvature, R, and the lateral size, L. (c) Lateral size distributions of air nanobubbles nucleated at 37 °C. (d) Bubble height as a function of lateral size for 37 °C. The error bars represent the standard deviation.

determined from the slope of the linear fit:

$$tan\theta = \frac{R_b}{R-h} = \frac{2\frac{h}{R_b}}{1-\left(\frac{h}{R_b}\right)^2}. \tag{2.2}$$

We find the mean non-equilibrium contact angles $\langle\theta\rangle = 13° \pm 0.7°$. The contact angles computed are spanning between $\theta_{min} = 10°$ and $\theta_{max} = 21°$, depending on the lateral size of the bubbles and their heights. The obtained values result in excellent agreement with the contact angles computed by AFM measurements on nanobubbles nucleated at 37 °C ($11° < \theta_{ref} < 23°$, $\langle\theta_{ref}\rangle = 20°$). [30]

2.2.4.1 The influence of nucleation temperature on nanobubbles morphology

It is well-known that nanobubbles reduce their lateral size upon increasing the temperature of the substrate during the nucleation process. [31] Hence, to further evaluate if iPAINT microscopy is able to investigate small changes in the interfacial topology, we decide to look at the influence of the nucleation temperature on the morphology of nanobubbles. We choose to carry out the iPAINT imaging on nanobubbles nucleated at two different temperatures, namely 37 °C and 50 °C, and compare our measurements directly with AFM data from others. [31] In accordance with previous work by others, we obtain smaller mean lateral sizes and lateral size distributions for bubbles nucleated at 50 °C (fig. 2.12b), compared to those nucleated at 37 °C (fig. 2.12a).

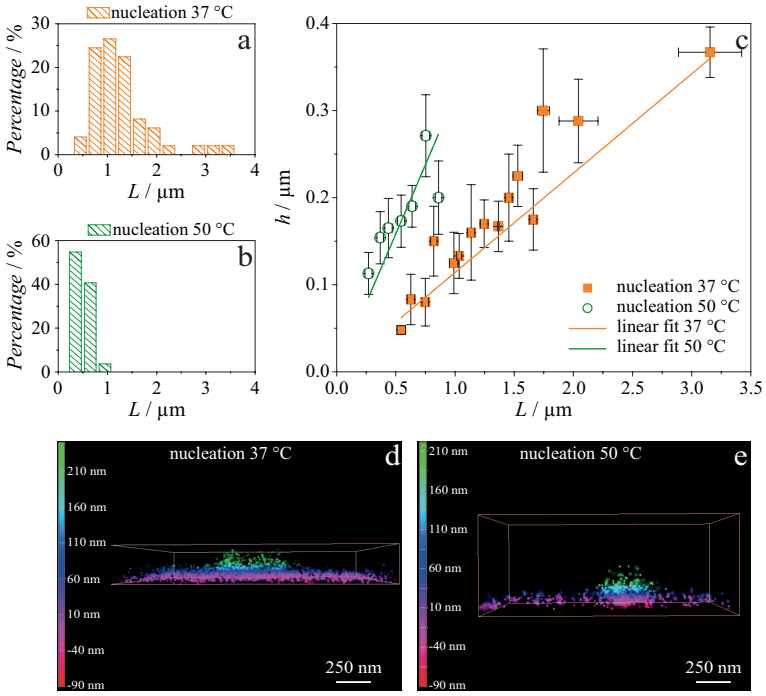

Figure 2.12: Temperature effect on the nanobubbles morphology. Lateral size distributions of air nanobubbles nucleated at (a) 37 °C and (b) 50 °C. (c) Bubbles height as a function of their lateral size after nucleation at 37 °C (closed squares) and 50 °C (open circles). The error bars represent the standard deviation. 3D iPAINT images of nanobubbles nucleated at (d) 37 °C and (e) 50 °C.

This is presumably due to an increased mobility of gas molecules at elevated temperatures. [31] The non-equilibrium contact angles computed from the slopes of the linear fitting curves in figure 2.12c are: $\langle\theta_{37°C}\rangle = 13° \pm 0.7°$ and $\langle\theta_{50°C}\rangle = 35° \pm 2.6°$. The difference in the wettability of the substrate by the nanobubble, and hence in their contact angles, is also appreciable from the 3D images presented in figure 2.12d and 2.12e. Here, the bubbles

nucleated at 37 °C show a larger base radius compared to the bubbles obtained at 50 °C, but their heights are still comparable. Our findings clearly confirm the influence of the substrate temperature during nucleation on bubble morphology. [32–34] Gratifyingly, iPAINT thus offers a complementary non-invasive method to investigate the morphology and contact angle of individual air nanobubbles. This enables an independent verification of AFM results, which has been long sought-after since perturbation of the nanobubbles by the AFM tip could lead to an underestimation of the actual contact angles. [35]

2.3 Conclusions

In summary, we have introduced a powerful new super-resolution approach called iPAINT, tailored to investigate interfaces of different nature through continuous non-covalent labelling during imaging. iPAINT is a generic method able to super-resolve interfaces in three-dimensions in complex soft materials, such as dispersions, emulsions, and foams. The key innovation is simple: a continuous exchange at the interface between surface-bound and freely diffusing polymer chains end-functionalized with a photo-activatable moiety. This novel approach broadens the scope of PAINT to colloid and interface science, food science, soft matter physics, and nanotechnology. We anticipate that iPAINT will find widespread use in these areas, particularly for non-invasive 3D imaging of the topology of soft and dynamic interfaces, such as droplets, bubbles, and ice crystals.

2.4 Experimental

2.4.1 Synthesis and characterization of polymer chains labelled with a photo-activatable moiety

Poly(ethylene glycol) bis(amine) MW 20 kDa (PEG) is purchased from Sigma Aldrich; an N-hydroxysuccinimide ester activated rhodamine analogue (Cage-552) designed for photo-activation localization microscopy is purchased from Abberior®. 1 mg of PEG is dispersed in 1 mL of 0.1 M sodium bicarbonate buffer at pH 8.5 to which 20 μL of a 10 mM solution of Cage-552 in DMSO is added. The reaction mixture is stirred overnight in the dark at room temperature and subsequently purified by dialysis (Spectra/Por®7 dialysis membrane, pre-treated RC tubing, molecular weight cutoff: 8 kDa) to remove unreacted dye molecules, which is confirmed by gel permeation chromatography (GPC). Figure 2.13 shows the chromatogram of the photo-activatable probe (PEG-552) in blue, and the one of the free dye (Cage-552) in red. The latter elutes at 11.5 min. The absence of a peak at 11.5 min in the PEG-552 spectrum demonstrates the absence of free dye in the dye solution for iPAINT imaging.

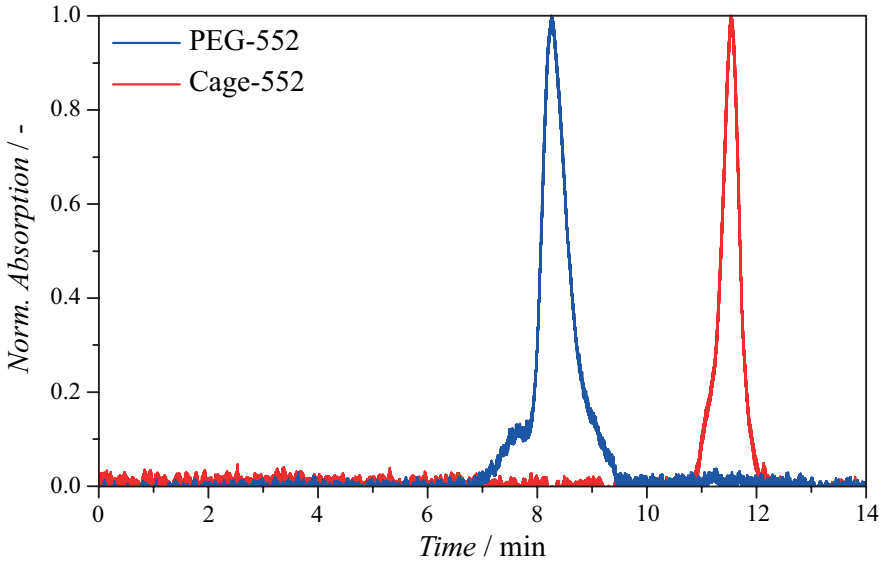

Figure 2.13: Characterization of photo-activatable probes for iPAINT microscopy. GPC chromatograms of aqueous solutions of PEG-552 (5 $\times 10^{-5}$ M) and the free dye Cage-552 (10^{-6} M) depicted in blue and red, respectively.

2.4.2 Synthesis and characterization of silica particles

The synthesis of silica particles, and SEM imaging has been carried out by dr. N. Vilanova.

Silica colloids of low polydispersity are synthetized using a Stöber-based method. [19–21] Briefly, 6.4 μL of (3-aminopropyl)triethoxysilane (APTES) are mixed with 33.5 mL of ethanol and 2.8 mL of ammonia (25% in water). 2.5 mL of this solution are added to a mixture of 25 mL of ammonia (25% in water) and 250 mL of ethanol. 1.6 mL of tetraethylortosilicate (TEOS) are then added all at once and the final mixture is stirred for 5 hours. Subsequently, 1.75 mL of TEOS are added and the reaction mixture is stirred overnight under an argon atmosphere. Following this procedure, particles of $\sim$110 nm in radius are obtained. Such particles are further used as seeds to synthesize bigger particles by means of growing a silica shell onto them. To do so, in a round-bottom flask equipped with 2 inlets, 51 mL of ethanol, 17 mL of water, 3.4 mL ammonia (25% in water) and 4 mL of the seed suspension (solid content 0.0136g seeds/mL of suspension) are mixed. Through one of the inlets, a mixture of 5 mL of TEOS with 10 mL of ethanol is pumped with a peristaltic pump at 1.7 mL/hour. Through the other inlet a second mixture consisting of 1.34 mL ammonia (25% in water), 10.25 mL of ethanol and 3.4 mL of water is also pumped with the same flow rate. After all the reactants are added, the resulting suspension of silica colloids (of $\sim$330 nm in radius approximately) is washed and stored in ethanol. Following the same protocol, particles of $\sim$110 nm in radius are synthesized by merely changing the time of the reaction. To investigate the impact of different surface chemistry on the iPAINT imaging, hydrophobic colloidal particles are synthesized. Hydrophobic silica beads are prepared by functionalizing plain silica colloids with stearyl alcohol. [22] 10 mg of dried plain silica colloids are dispersed by sonication in 1 mL of ethanol together with 40 mg of stearyl alcohol. Afterwards, the ethanol is totally evaporated with a steady stream of argon. The flask, equipped with a magnetic stirrer, is heated up to 180 °C for 6 hours under continuous stirring and in an argon atmosphere. The resulting particles are thoroughly washed with chloroform and dried overnight at 70 °C in vacuum. For the iPAINT experiments, hydrophobic silica colloids are finely re-suspended in ethanol using a sonication bath. The particles are characterized by SEM using a FEI Quanta 600F ESEM. Figure 7.17 shows the SEM images of the big and small colloids. The insets depict the size distribution obtained from image analysis of more than 100 particles, using Image J: $\langle R \rangle = 332 \pm 18$ nm for the big colloids, and $\langle R \rangle = 115 \pm 14$ nm for the small one.

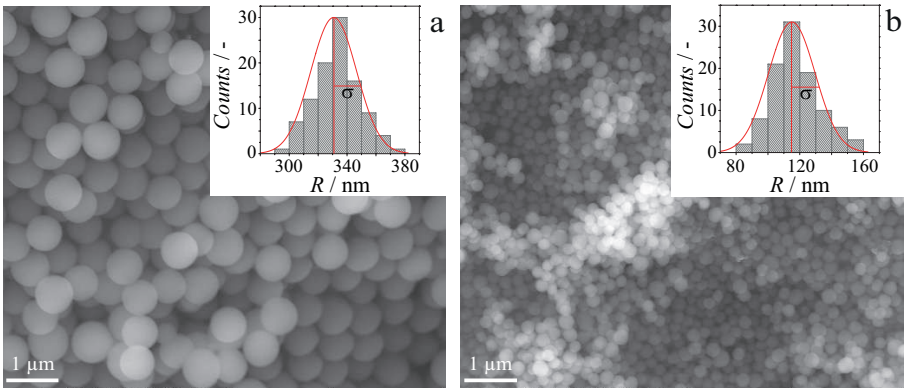

Figure 2.14: Characterization of silica colloids. (a) and (b) SEM pictures of plain silica beads of ∼330 nm and ∼110 nm in radius, respectively. The insets illustrate the size distribution of the two batches measured for over 100 beads.

2.4.3 Microscopy

iPAINT images are acquired using a Nikon N-STORM system equipped with ∼488.0 mW/cm^2 (λ = 561 nm) and ∼160.0 mW/cm^2 (λ = 405 nm) laser lines configured for total internal reflection fluorescence (TIRF) imaging. The excitation inclination is tuned to maximize the signal-to-noise ratio. Fluorescence is collected by means of a Nikon 100×, 1.4 NA oil immersion objective and passed through a quad-band pass dichroic filter (97335 Nikon). All time-lapses are recorded onto a 128 × 128 pixel region (pixel size 170 nm) of an EMCCD camera (ixon3, Andor) at a rate of 97 frames/s. Unless stated otherwise, 2 × 10^4 frames are acquired in each experiment, while the Cage-552 moieties are photo-activated with a 405 nm UV laser (0.5% power) and excited with a 561 nm laser (100% power). Single molecule localization movies are analyzed with NIS-element Nikon software. 3D iPAINT measurements are performed using the astigmatism method. [36] The *z*-position in 3D iPAINT experiments on dispersions and bubbles is computed using a calibration curve made with fluorescent TetraSpeck™ microspheres (R = 50 nm, Lifetechnologies, Molecular Probes®) that relates the ellipticity of the fluorescence signal of single molecules to their *z*-position.

2.4.4 Sample preparation

Sample chambers consist of a coverslide (Menzel Gläser, 76 × 26 mm, thickness 1 mm) onto which a coverslip (Menzel Gläser, no. 1.5, 24 × 24 mm, thickness 170 μm) is glued with double-sided tape. Prior to assembly of the chamber, the coverslip is cleaned to remove impurities and reduce background fluorescence as follows: it is consecutively immersed and sonicated for 10 minutes in acetone, isopropanol and MilliQ-water (18.2 MΩ) after which it

is dried with a N_2 stream.

2.4.4.1 Colloidal dispersion

iPAINT samples are prepared by application of a few drops of the colloidal dispersion on a coverslip, followed by drying in N_2 stream prior to closure of the sample chamber, after which a freshly prepared 50 μM PEG-552 solution is fluxed into it.

2.4.4.2 Emulsions

Water-in-oil and oil-in-water emulsions (10 wt% dispersed phase) are prepared by direct mixing of a 50 μM PEG-552 solution with chromatographic grade 1-octanol from Sigma-Aldrich, followed by 5 minutes sonication. Hydrophobic coverslips are made for iPAINT experiments on O/W emulsions to immobilize the oil droplets. To this end, hydrophilic coverslips are first cleaned by piranha etching and extensively rinsed with MilliQ-water, and subsequently silanized as follows: coverslips are first incubated for 15 minutes in 5% dimethyldichlorosilane in heptane (Sigma Aldrich), then cleaned with heptane, blow-dried under N_2 flow and finally dried at 60 °C for two hours.

2.4.4.3 Nanobubbles

Air bubbles are nucleated at 37 °C and 50 °C using the solvent exchange protocol. [30] First, the sample chamber is assembled and heated to 37 °C or 50 °C. Then, 2-propanol is injected and subsequently replaced by an aqueous PEG-552 solution, which induces nanobubble nucleation. Imaging is carried out at room temperature to avoid water evaporation. [30]

Bibliography

[1] Whelan, D.R.; Bell, T.D.M. *J. Phys. Chem. Lett.* **2015**, *6*, 374.

[2] Betzig, E.; Patterson, G.H.; Sougrat, R.; Lindwasser, O.W.; Olenych, S.; Bonifacino, J.S.; Davidson, M.W.; Lippincott-Schwartz, J.; Hess, H. F. *Science* **2006**, *313*, 1642.

[3] Willig, K.I.; Kellner, R.R.; Medda, R.; Hein, B.; Jakobs, S.; Hell, S.W. *Nat. Methods* **2006**, *3*, 721.

[4] Rust, M.J.; Bates, M.; Zhuang, X. *Nat. Methods* **2006**, *3*, 793.

[5] Sharanov, A.; Hochstrasser, R.M. *Proc. Natl. Acad. Sci. U.S.A.* **2006**, *103*, 18911.

[6] Westphal, V.; Hess, S.W. *Phys. Rev. Lett.* **2005**, *94*, 143903.

[7] Xu, K.; Zhong, G.; Zhuang, X. *Science* **2013**, *339*, 6118.

[8] Albertazzi, L.; van der Zwaag, D.; Leenders, C.M.A.; Fitzner, R.; van der Hofstad, R.W.; Meijer, E.W. *Science* **2014**, *344*, 491.

[9] Aoki, H.; Mori, K.; Ito, S. *Soft Matter* **2012**, *8*, 4390.

[10] Giannone, G.; Hosy, E.; Levet, F.; Constals, A.; Schulze, K.; Sobolevsky, A.I.; Rosconi, M.P.; Gouaux, E.; Tampé, R.; Choquet, D.; Cognet, L. *Biophys. J.* **2010**, *99*, 1303.

[11] Jungmann, R.; Steinhauer, C.; Scheible, M.; Kuzyk, A.; Tinnefeld, P.; Simmel, F.C. *Nano Lett.* **2010**, *10*, 4756.

[12] Jungmann, R.; Avendaño, M.S.; Woehrstein, J.B.; Dai, M.; Shih, W.M.; Yin, P. *Nat. Methods* **2014**, *11*, 313.

[13] Belov, V.N.; Mitronova, G.Y.; Bossi, M.L.; Boyarskiy, V.P.; Hebisch, E.; Geisler, C.; Kolmakov, K.; Wurm, C.A.; Willig, K.I.; Hell, S.W. *Chem. Eur. J.* **2014**, *20*, 13162.

[14] Cooper, S.L.; Bamford, C.H.; Tsuruta, T. *J. Biomed. Mater. Res.* **1996**, *30*, 171.

[15] Lou, S.; Jiang, X.; Scott, P.J. *Proc. R. Soc. A* **2013**, *469*, 20130150.

[16] Deschout, H.; Cella Zanacchi, F.; Mlodzianoski, M.; Diaspro, A.; Bewersdorf, J.; Hess, S.T.; Braeckmans, K. *Nat. Methods* **2014**, *11*, 253.

[17] de Feijter, I.; Albertazzi, L.; Palmans, A.R.A.; Voets, I.K. *Langmuir* **2015**, *31*, 57.

[18] Xia, Y.; Bates, B.; Yin, Y.; Lu, Y. *Adv. Mater.* **2000**, *12*, 693.

[19] Stöber, W.; Fink, A.; Bohn, E. *J. Colloid Interface Sci.* **1968**, *26*, 62.

[20] Giesche, H. *J. Eur. Ceram. Soc.* **1994**, *14*, 189.

[21] Wu, H. *Chem. Phys.* **2010**, *367*, 44.

[22] van Helden, A.K.; Jansen, J.W.; Vrij, A.*J. Colloid Interface Sci.* **1981**, *81*, 354.

[23] Wick, C.D.; Chang, T.M. *J. Phys. Chem. B* **2014**, *118*, 7785.

[24] Cramb, D.T.; Wallace, S.C. *J. Phys. Chem. B* **1997**, *101*, 2741.

[25] Dong-Jin, S.; German, S.R.; Mega, T.L.; Ducker, W. A. *J. Phys. Chem. C* **2015**, *119*,14262.

[26] Seddon, J.R.T.; Lohse, D. *J. Phys. Condens. Matter* **2011**, *23*, 133001.

[27] Ohgaki, K.; Khanh, N.Q.; Joden, Y.; Tsuji, A.; Nakagawa, T. *Chem. Eng. Sci.* **2010**, *65*, 1296.

[28] Zhang, X.; Winnik, F.M. *Langmuir* **2016**, *32*, 11071.

[29] Zhang, X.; Lhuissier, H.; Enríquez, O.R.; Sun, C.; Lohse, D. *Langmuir* **2013**, *29*, 9979.

[30] Xu, C.; Peng, S.; Qiao, G.G.; Gutowski, V.; Lohse, D.; Zhang, X. *Soft Matter* **2014**, *10*, 7857.

[31] Petsev, N.D.; Shell, M.S.; Leal, L.G. *Phys. Rev. E: Stat. Phys., Plasmas, Fluids, Relat. Interdiscip. Top.* **2013**, *88*, 010402.

[32] Berkelaar, R.P.; Seddon, J.R.T.; Zandvliet, H.J.W.; Lohse, D. *ChemPhysChem* **2012**, *13*, 2213.

[33] Seddon, J.R.T.; Kooij, E.S.; Poelsema, B.; Zandvliet, H.J.W.; Lohse, D. *Phys. Rev. Lett.* **2011**, *106*, 056101.

[34] Zhang, X.H.; Li, G.; Wu, Z.H.; Zhang, X.D.; Hu, J. *Chin. Phys.* **2005**, *14*, 1774.

[35] Walczyk, W.; Schönherr, H. *Langmuir* **2014**, *30*, 11955.

[36] Huang, B.; Wang, W.; Bates, M.; Zhuang, X. *Science* **2008**, *319*, 810.

Chapter 3

Morphological evolution of complex coacervate core micelles revealed by iPAINT microscopy

Structural characterization of polymeric micelles is important to understand the relation between micellar structure and properties for application in *e.g.*, drug delivery, catalysis, and sensing. In this chapter we demonstrate the potential of iPAINT super-resolution microscopy for the imaging of complex coacervate core micelles (C3Ms). C3Ms are formed out of the flexible cationic diblock copolymer poly(Nmethyl-2-vinyl pyridinium chloride)-*b*-poly(ethylene oxide) (P2MVP$_{29}$-*b*-PEO$_{204}$) and a stiff anionic polyfluorene derivative (PF$_{22}$). We use iPAINT to 'stain' the C3Ms in a simple, non-covalent fashion to image the morphology of individual micelles. Spherical architectures are detected at low concentrations ($<$0.07 mM), while more elongated, non-spherical structures with axial ratios $\nu \leq$2.3 are adopted at higher concentrations ($>$0.14 mM). The observed ellipsoid-like morphology is unusual and furthermore unexpected for C3Ms of copolymers with a considerably longer corona-forming hydrophilic block than the core-forming ionic block. We attribute the observed morphological transition from spherical to ellipsoidal micelles as concentration rises to the stiffness of the conjugated polyfluorene.

Part of this work has been published as: Aloi, A.; Guibert, C.; Olijve, L.L.C.; Voets, I.K. *Polymer* **2016**, *107*, 450.

3.1 Introduction

Complex coacervate core micelles (C3Ms) are nanostructures that form upon co-assembly in water of neutral-ionic block copolymers with oppositely charged species. C3Ms can offer a versatile route to encapsulation of hydrophilic (macro)molecules in water through direct inclusion upon complexation. The C3M core comprises the oppositely charged moieties, which is surrounded by a shell of the hydrophilic blocks of the copolymer. A broad range of ionic compounds – like DNA, RNA, multivalent ions, dendrimers, nanoparticle precursors and inorganic particles – has been incorporated in C3Ms out of fundamental interest and for application in *e.g.*, catalysis, sensing, controlled delivery, *in vivo* imaging, particle synthesis and in various other areas. [1–12] An important determinant of functionality is the architecture of the polymer micelle. Wormlike structures are highly effective thickeners for example. [13] In biomedical applications, both micellar size and shape impact drug efficiency as these affect cellular uptake, circulation times, transport, retention, intracellular trafficking and tissue-specific delivery. [9, 10, 14, 15] In equilibrium, the morphology of polymeric micelles like C3Ms is determined by the relative free energies of the potential morphologies with contributions from the micellar core, corona, and interface between the two. By far most abundant are spherical micelles with core-shell architectures. For high molecular weight amphiphilic polymers, it has been shown that other morphologies become thermodynamically stable when micelles have a crew-cut structure with a corona thickness H smaller than the core radius R_{core}. [16] Similarly, electrostatically driven complexation of ionic-neutral copolymers with relatively long ionic and short neutral blocks yields wormlike and vesicular structures. [12, 17] Various groups demonstrated that unusual micellar morphologies may also appear upon self-assembly of stiff amphiphilic copolymers [18–20] and oppositely charged dendritic peptides, [21–23] but fairly little is known about electrostatically driven co-assembly involving stiff polymers. Co-aggregation of poly(-ethylene oxide) based comb polymers and sodium dodecylsulfate resulted in aggregate morphologies determined largely by the structure of the comb polymer. [24] Needle-like particles were reported by Müller *et al.* upon complexation under nonstoichiometric conditions of stiff, α-helical poly(L-lysine) with sodium poly(maleic acid-co-propylene). [25] Rod-like C3Ms have been observed in aqueous mixtures of PEG-poly(L-lysine) copolymer and plasmid DNA (pDNA) at charge stoichiometric compositions, [10, 26] and in case of stoichiometric mixing of iron-coordination polymers. [27] Here we focus on complex coacervate core micelles formed upon complexation of a stiff, conjugated anionic derivative of polyfluorene (PF_{22}, fig. 3.1a) with the flexible ionic-neutral copolymer poly(N-methyl-2-vinyl pyridinium chloride)-*b*-poly(ethylene oxide) ($P2MVP_{29}$-*b*-PEO_{204}, fig. 3.1b).

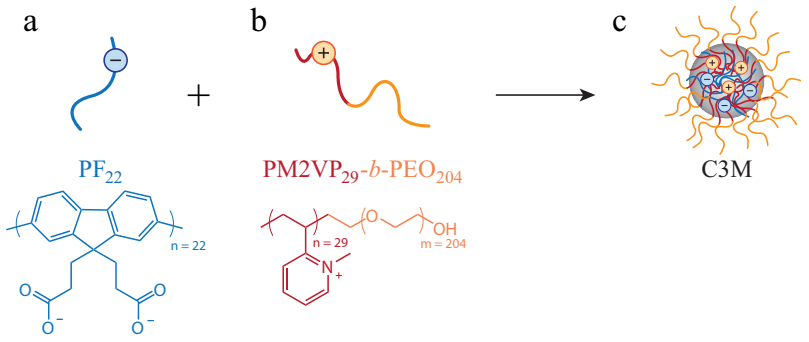

Figure 3.1: Illustration of co-assembly of oppositely charged copolymers into complex coacervate core micelles (C3Ms). (a) The polyanion is a carboxylated polyfluorene derivative (PF_{22}); (b) the cationic-neutral diblock copolymer is poly(N-methyl-2-vinyl pyridinium chloride)-*b*-poly(ethylene oxide) ($P2MVP_{29}$-*b*-PEO_{204}). Subscripts denote the degree of polymerization. (c) The ionic blocks of the polymers associate to form the core of the micelle, whereas the neutral blocks of the block copolymers form the micelle corona.

Conjugated polyelectrolytes like PF are polymeric chains with a conjugated backbone that bears chargeable groups. Their optical properties, such as fluorescence and UV-vis absorption, are dependent on the composition and conformation of the polymer chain (*i.e.*, planarised or twisted backbone) [28, 29] and can thus be modulated by their charge and complexation state. [30] This makes conjugated ionomers interesting candidates for sensing of biopolymers, such as proteins [31] and DNA. [32] Recently, Cingil *et al.* demonstrated that the optical response of PF undergoing coassembly with capsid proteins [33] or polyelectrolytes [34] can be taken as a quantitative measure of PF chain stretching due to the mechanical forces associated with complexation. The mechanochromic properties of this carboxylated polyfluorene thus allow to independently detect binding to and stretching of the polymer. C3Ms often pose a considerable challenge to powerful methods for detailed structural characterization like small angle X-ray and neutron scattering (SAXS, SANS), cryogenic transmission electron microscopy (cryo-TEM) and atomic force microscopy (AFM), since the micelles are small and dynamic, aggregation numbers are relatively low and both the core and corona are highly penetrated by solvent. SAXS and cryo-TEM reflect local differences in electron density, which tend to be small in C3M solutions due to the aforementioned characteristics resulting in electron micrographs with low contrast and precluding SAXS experiments in a broad concentration range. [1, 2, 35] AFM does not suffer from these drawbacks, but perturbations of the structure of the easily deformable, dynamic micelles due to *e.g.*, the presence of a solid substrate and the applied load cannot be ruled out unambiguously. Single molecule localization microscopy (SMLM) has recently gained ground as an alternative, complementary imaging technology enabling non-invasive *in-situ* visualization at room temperature with $\sim$20 nm and $\sim$80 nm resolution in the lateral and axial direction, respectively. [36–39] Encouraged by earlier work from our laboratory and others on the structure and dynamics of

synthetic, self-assembled architectures by SMLM, [40–42] we decided to explore the potential of SMLM for imaging of complex coacervate core micelles. In this chapter we present single molecule localization microscopy experiments enabling direct imaging of the morphology of C3Ms in a broad concentration range inaccessible to small angle scattering methods. To this end we adopt the newly developed approach iPAINT (abbreviation of 'interface Point Accumulation for Imaging at Nanoscale Topography') [43] (*vide infra*) to 'stain' C3Ms in a facile, non-covalent manner. Furthermore, the intrinsic fluorescence of the carboxylated polyfluorene derivative (PF_{22}) within the micellar core allows for unambiguous discrimination between micelles and background fluorescence from adsorbed dyes, facilitating the identification of regions of interest as well as data analysis. We find that the PF_{22} C3Ms undergo a morphological transition from micelles with a low to intermediate axial ratio (ν = 1.06-2.34) as the C3M concentration is raised from 0.04 to 2.83 mM. In analogy to previous experimental and theoretical work by others on surfactants and amphiphilic copolymers, we attribute the emergence of these non-spherical architectures at elevated concentrations to the intrinsic stiffness of the PF_{22} backbone, which is characterized by a Kuhn segment length of 17 nm. [44]

3.2 Results and discussion

3.2.1 Spectroscopic characterization of C3M

Complex coacervate core micelles are prepared upon mixing of a stiff, conjugated anionic derivative of polyfluorene (PF_{22}, fig. 3.1a) with the flexible ionic-neutral copolymer poly(Nmethyl-2-vinyl pyridinium chloride)-*b*-poly(ethylene oxide) ($P2MVP_{29}$-*b*-PEO_{204}, fig. 3.1b) in 30 mM $NaNO_3$ aqueous solutions (unless stated otherwise) at room temperature. The concentrations in the various systems are expressed using the concentration of the monomers of carboxylated polyfluorene, C_{CF}, as a reference. The pH of all the solutions is set to 9 by addition of 0.1 or 1.0 M NaOH solutions to ensure complete deprotonation of PF_{22}. Details on polyelectrolyte synthesis, characterization, instrumentation and experimental procedures are described in section 3.4. Typically, C3Ms form in a narrow compositional window close to charge stoichiometry where the concentrations of anionic and cationic monomers in the mixed solution are equal. [2] The preferred micellar composition (PMC) then corresponds to a mixing fraction $f_+ = 0.5$, with

$$f_+ = \frac{[+]}{([+]+[-])}, \tag{3.1}$$

where $[+]$ and $[-]$ are the monomer concentrations of the cationic and anionic species in solution.

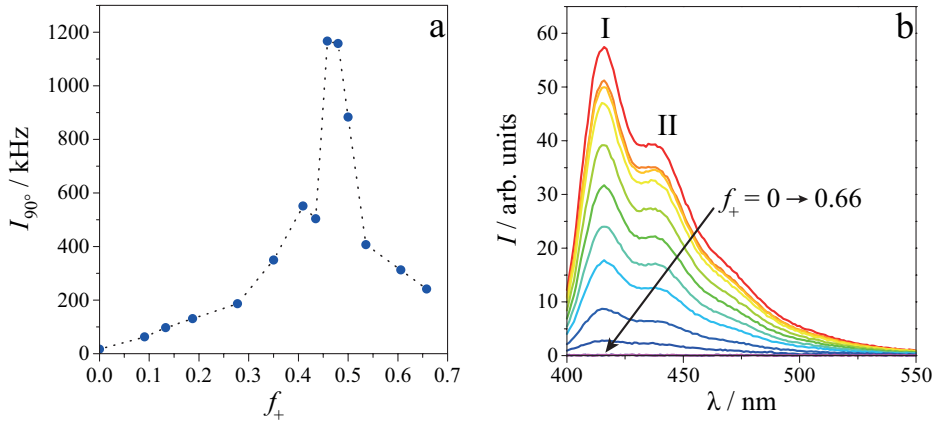

Figure 3.2: Formation and characterization of complex coacervate core micelles of a carboxylated polyfluorene (PF_{22}) derivative and poly(N-methyl-2-vinyl pyridinium chloride)-bpoly(ethylene oxide) ($P2MVP_{29}$-*b*-PEO_{204}) by light scattering and fluorescence spectroscopy at a constant concentration, $C_{CF} = 1.3$ mM and without added background salt. (a) A light-scattering titration (LS-T) is performed to monitor the mean scattering intensity as a function of mixing fraction f_+ upon addition of $P2MVP_{29}$-*b*-PEO_{204} to PF_{22}. A preferred micellar composition PMC $= f_+ = 0.47$ is obtained, which corresponds to the composition at which the scattering intensity displays a maximum. (b) Fluorescence spectra acquired during the titration, showing the superquenching of fluorescence of the polyfluorene due to the assembly into micelles ($\lambda_{ex} =$ 383 nm). The two maxima identified by I and II are the 1-0 and 2-0 vibronic transitions in the polyfluorene, respectively.

Experimentally, the PMC is readily determined as the f_+ corresponding to the maximum in light scattering intensity obtained in a static light scattering titration (LS-T) experiment. Here the composition-dependent mean scattering intensity is monitored as one polymer solution is titrated into the other (fig. 3.2a) (without added background salt). We obtain $f_+ = 0.47 \pm 0.01$, which is close to the expected value of $f_+ = 0.50$ and in agreement with previous reports on PF and P2MVP-*b*-PEO containing C3Ms. [34] Since the optical properties of PF_{22} are conformation-dependent, co-assembly into C3Ms can also be monitored spectroscopically. Fluorescence spectra are collected as a function of mixing fraction at a fixed excitation wavelength $\lambda_{ex} = 383$ nm (fig. 3.2b), and at a fixed concentration $C_{CF} = 1.3$ mM (without added background salt). A strong decay of the overall fluorescence intensity is observed and can be attributed to the complexation of PF_{22} with $P2MVP_{29}$-*b*-PEO_{204}. A similar trend is also reported in the literature [33] and referred to as superquenching. [45–47] The local maxima I ($\lambda = 416$ nm) and II ($\lambda = 438$ nm), shown in figure 3.2b, are vibronic bands, corresponding respectively to 1-0 and 2-0 vibronic transitions. Interestingly, the ratio between the intensities of these two bands remains constant upon $P2MVP_{29}$-*b*-PEO_{204} addition, which indicates that the PF_{22} chains are not stretched nor twisted when forming micelles with $P2MVP_{29}$-*b*-PEO_{204}. [33]

3.2.2 iPAINT microscopy of C3Ms

Having established PMC = $f_+ = 0.47 \pm 0.01$ by LS-T, we now fix the composition to this value to study the morphology of the micelles as a function of overall concentration. For this purpose we select iPAINT, [43] a novel methodology which we recently developed to image soft and deformable nanostructures with dimensions smaller than the Rayleigh criterion by single molecule localization microscopy (SMLM). iPAINT is based on the SMLM method PAINT, originally designed by Sharanov *et al.* to image cellular membranes, organelles and other (intracellular) biological structures. [48] In a typical iPAINT experiment, the object of interest is continuously labelled *in-situ*, in a non-invasive and non-covalent manner, through aspecific adsorption of short poly(ethylene oxide) chains (M_w = 20 kDa) carrying a photo-activatable moiety at both chain ends. This dye is stochastically switched from a dark to a bright, fluorescent state upon UV light irradiation enabling single molecule detection upon repetitive cycles of photo-activation, excitation, localization and photobleaching. [49] As such, iPAINT constitutes a facile non-covalent labelling method to 'stain' nanostructures such as polyelectrolytes for visualization by SMLM. [43]

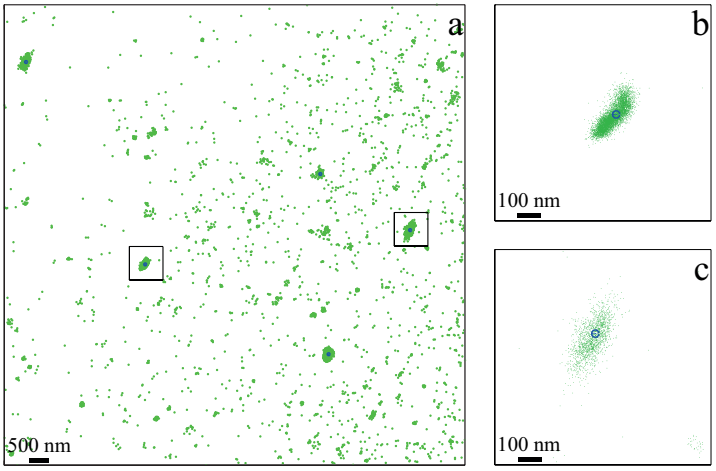

Figure 3.3: iPAINT imaging of complex coacervate core micelles. (a) Super-resolved image of complex coacervate core micelles at C_{CF} = 0.57 mM and $f_+ = 0.47$. The green dots are the single-molecule localizations obtained through the physisorption of the iPAINT probe onto the micelles. The blue dots denote the fluorescent core in each micelle. (b-c) Zoom-ins on two micelles highlighted by black squares in (a).

For the iPAINT experiments we first prepare a pristine solution of C3Ms by direct mixing of two polyelectrolyte stock solutions to obtain $C_{CF} = 1.13$ mM and $f_+ = 0.47$. Subsequently, the micellar solution is mixed with an equal volume of a 5×10^{-5} M solution of poly(ethylene oxide) end-functionalized with a rhodamine derivative, hereafter referred to as PEG-552. This simple strategy allows for super-resolution imaging on the one hand through reversible adsorption and desorption of PEG-552 onto the C3Ms, while PF_{22} fluorescence within the

micellar core [34] enables on the other hand unambiguous identification of the micelles and facile selection of the region of interest by application of a low power blue laser (λ = 488 nm, ~48.1 mW/cm^2). Once a suitable spot is identified, the blue laser is turned off and a combination of UV (λ = 405 nm, ~1.6 mW/cm^2) and visible (λ = 561 nm, ~488 mW/cm^2) lasers is used instead. In this way, only a small number of PEG-552 probes is photo-activated, selectively excited, and localized to generate upon prolonged acquisition a super-resolved image with a lateral resolution of <20 nm upon summation of all single molecule localizations collected within ~15 $\times$ 10^3 frames during a typical acquisition of ~3 min. Figure 3.3 displays exemplary results of iPAINT imaging of C3Ms at a concentration C_{CF} = 0.57 mM. The polyfluorene chains detected by excitation at λ = 488 nm are represented by a single dot corresponding to the maximum of the Gaussian intensity distribution. As expected, these coincide with areas of high PEG-552 localization density enabling visualization of C3M morphology by iPAINT. Zooming-in on the enclosed areas in figure 3.3a reveals elongated, quasi worm-like structures that are roughly ~300 nm long and ~150 nm wide (fig. 3.3b and 3.3c). Quantitative image analysis of iPAINT reconstructions over tens of micelles yields an axial ratio ν = 1.99 $\pm$ 0.29.

3.2.2.1 The nature of the iPAINT probe does not impact C3Ms morphology

To image the morphology of complex coacervate core micelles made of a rigid anionic polyfluorene and a cationic-neutral copolymer poly(N-methyl-2-vinyl pyridinium chloride)-bethylene oxide, we stain the micelles with the photo-activatable dye Cage-552 coupled to a poly(ethylene oxide) chain. To ensure that this non-covalent labelling strategy does not impact C3M morphology, we performed iPAINT imaging at a fixed concentration C_{CF} = 0.57 mM with two different probes: PEG-552 and Cage-552.

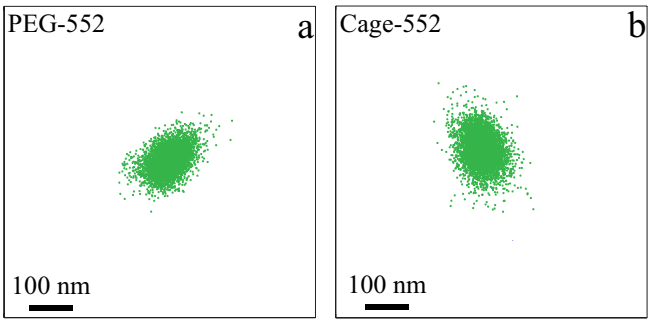

Figure 3.4: iPAINT imaging of coacervate core micelles (C_{CF} = 0.57 mM, f_+ = 0.47) using (a) PEG-552, which is poly(ethylene oxide) functionalized Cage-552 (M_{PEG}= 20kDa) and (b) the bare dye Cage-552 as iPAINT probe.

Figure 3.4 shows that both the poly(ethylene oxide) Cage-552-functionalized, and the bare

photo-activatable dye Cage-552, successfully stain the coacervate core micelles enabling iPAINT imaging. Furthermore, the two iPAINT experiments are in excellent agreement, since micellar morphology, axial ratio, and surface area as well as the number of single molecule localizations are comparable, as shown in table 3.1. This demonstrates that the utilized iPAINT probes do not affect the morphology of the micelles.

Table 3.1: Comparison between iPAINT experiments on the same C3Ms utilizing two different iPAINT probes. Tabulated are the axial ratio, ν, surface area, A, and number of single molecule localizations per micelle ($C_{CF} = 0.57$ mM) for iPAINT imaging using (Cage-552) the bare rhodamine derivative and (PEG-552) the poly(ethylene oxide) functionalized dye.

probe	$\boldsymbol{\nu}$	***A*** (nm^2)	***# of localizations***
PEG-552	1.99 ± 0.3	52640 ± 7432	3390 ± 281
Cage-552	1.94 ± 0.4	54318 ± 6549	3363 ± 259

3.2.3 Morphological transition in C3Ms

Next, we collected iPAINT images of C3Ms at concentrations ranging from $0.04 < C_{CF} < 2.83$ mM, *ceteris paribus* (fig. 3.5a-e). A gradual increase in micellar anisotropy and concomitant axial ratio is observed as the concentration rises (fig. 3.5e) from $\nu \simeq 1$ for spherical core-shell structures at 0.04 mM to $\nu \simeq 2.3$ for ellipsoidal micelles at 2.83 mM. The transition from spherical to ellipsoidal C3Ms seemingly spans a rather narrow range of concentrations in which the axial ratio steeply increases with increasing concentration after which it appears to level off at a plateau value $\nu \simeq 2.1$ for concentrations of 0.28 mM and higher.

To corroborate these results, we decide to further quantify the surface area of the C3Ms as a function of concentration (fig. 3.6). To quantify the surface area of the C3Ms as a function of concentration we employ a convex hull algorithm (α-shape). [50] The α-shape algorithm relies on the use of an α-ball of radius R_α which rolls over the pointcloud of iPAINT localizations, representing the super-resolved image of the micelles, to identify their boundaries and therewith their surface area (fig. 3.6b). The experimental resolution of the iPAINT measurements is taken as a suitable criterion to fix the radius of the α-ball for

analysis, which corresponds in this case to $R_\alpha = 20$ nm.

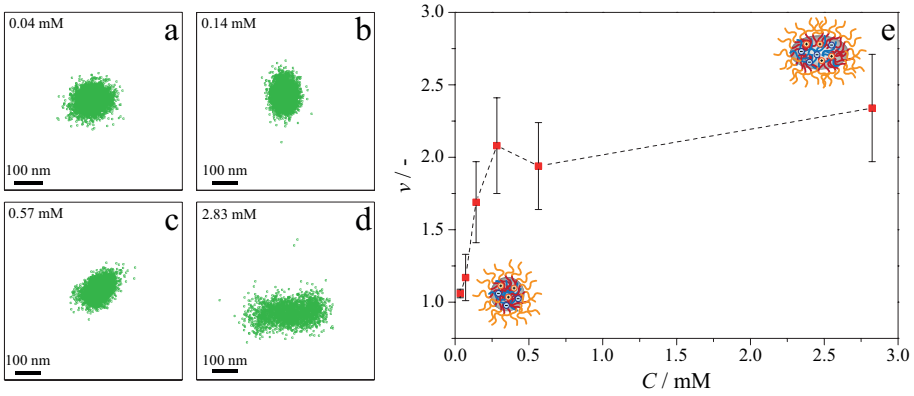

Figure 3.5: Concentration-induced morphological transition of PF-containing C3Ms. (a-d) Super-resolved images of C3Ms acquired at four different concentrations: $C_{CF} = 0.04$ mM, 0.14 mM, 0.57 mM and 2.83 mM, respectively. (e) Corresponding axial ratios of C3Ms at 0.04 mM $\leq C_{CF} \leq$ 2.83 mM.

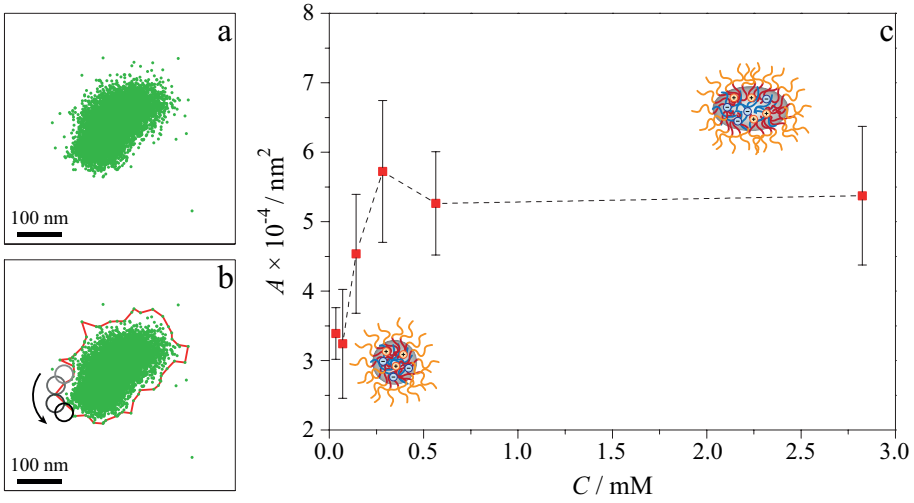

Figure 3.6: Concentration-dependent surface area of C3Ms. An α-shape algorithm is used to determine the boundaries of C3Ms imaged by iPAINT at 0.04 mM $\leq C_{CF} \leq$ 2.83 mM. (a) Pointcloud representing a C3M imaged by iPAINT at $C_{CF} = 0.57$ mM (b) An α-ball radius $R_\alpha = 20$ nm (circles from grey to black) is selected for α-shaping in accordance with the iPAINT resolution. (c) Mean C3M surface areas calculated by the α-shape algorithm as function of $C_{CF} = 0.04$ mM, 0.07 mM, 0.14 mM, 0.28 mM, 0.57 mM and 2.83 mM.

The surface area of the micelles exhibits a steep increase at concentrations below 0.28 mM, after which it reaches a plateau, leveling off to a value twice larger than at low concentrations. Hence, the concentration-dependent axial ratio and surface area reflect the morphological transition from spherical to ellipsoidal micelles in a highly similar fashion. Although it is well-known that an increase in concentration may lead to a morphological

transition from spherical to elongated structures, it has been rarely observed. [51–54] Deviations from the common spherical core-shell architecture have been reported for complex coacervate core micelles containing poly(ethylene oxide) based comb polymers, [24] α-helical poly(L-lysine), [25] and pDNA. [9, 10, 26] Particularly interesting is a previous study on the stability and structure of C3Ms of P2MVP-b-PEO with the same block length ratio N_{core}/N_{corona} = 0.2 and poly(acrylic acid) (PAA) of varying molecular weight. [55] While spherical C3Ms are observed at salt concentrations <100 mM NaCl in all cases, worm-like structures emerge at higher salt concentrations in micellar solutions with sufficiently short PAA (*i.e.*, N_{PAA} = 13, 20 and 47). Notably, these worm-like structures are also found to grow in size upon an increase in polymer concentration. By contrast, for the PF_{22}-containing micelles studied here, non-spherical core-shell architectures are already present at low salt concentration (C_{NaNO_3} = 30 mM) when the poly(ethylene oxide) chains are well-solvated. We therefore attribute the ellipsoidal shape to the intrinsic stiffness of the carboxylated polyfluorene. Indeed, previous work by others demonstrates that stiff polymer chains may result in unusual micellar morphologies. [10, 24–26]

3.2.3.1 Micellar axial ratio and surface area distributions

Finally, we decide to take a closer look at the morphological transition aiming to evaluate whether there is coexistence of two well-defined morphologies or whether the spherical micelles gradually adopt, as the concentration rises, a more elongated morphology. SMLM experiments offer direct access to structural information on the level of individual micelles, which enables detailed insight into the mean and distribution of micellar axial ratios and surface areas, which is not easily attainable from ensemble measurements. Quantitative image analysis of over tens of micelles per concentration yields the distributions in axial ratio and surface area shown in figure 3.7 and in figure 3.8, respectively, corresponding to the concentration-dependent mean values given in figures 3.5e and figure 3.6c. As expected for a monomodal distribution of well-defined spherical micelles, a narrow distribution in micellar axial ratio ν and surface area A_{C3M} is observed at the lowest concentration studied C_{CF} = 0.04 mM (fig. 3.7a, fig. 3.8a), with a mean axial ratio $\nu \simeq 1$.

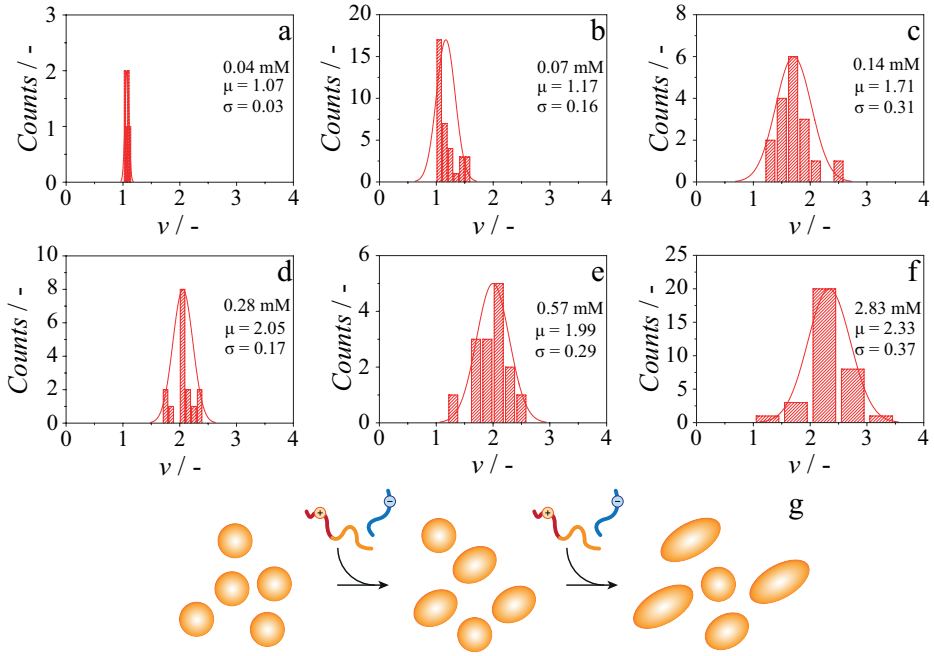

Figure 3.7: Distribution of axial ratios obtained by iPAINT imaging at 0.04 mM $\leq C_{CF} \leq$ 2.83 mM. Histograms of axial ratios at C_{CF} = (a) 0.04 mM, (b) 0.07 mM, (c) 0.14 mM, (d) 0.28 mM, (e) 0.57 mM and (f) 2.83 mM. Both the mean and standard deviation of the axial ratio distribution increase as C_{CF} increases, as C3Ms adopt larger morphologies of varying elongation upon increasing concentration. (g) Scheme illustrating the concentration-induced increase in micellar anisotropy and polydispersity.

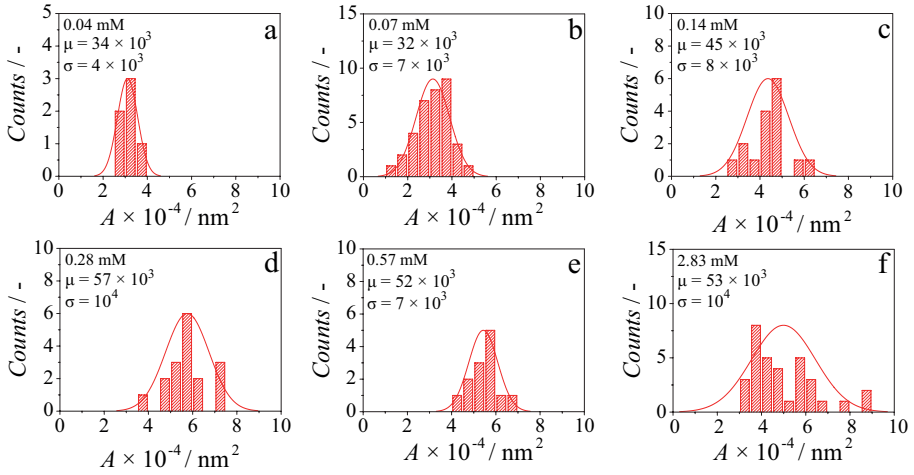

Figure 3.8: Surface area distribution of single C3Ms. (a-f) Surface area histograms of single C3Ms computed at concentrations C_{CF} = 0.04 mM, 0.07 mM, 0.14 mM, 0.28 mM, 0.57 mM and 2.83 mM, respectively. A concentration-induced increase in the mean surface area and standard deviation suggest a progressive micellar growth into more elongated and polydisperse architectures.

Both distributions significantly broaden upon increasing C_{CF}, but remain peaked around a central value which increases as C_{CF} increases. The abundance of spherical micelles becomes progressively smaller, while aggregates with varying degrees of elongation occur at the same overall concentration (fig. 3.7g). Hence, the C3Ms appear to gradually transform from spherical core-shell structures into the preferred, ellipsoidal architectures, due to the stiffness of the carboxylated polyfluorene backbone within the micellar core.

3.3 Conclusions

In summary, we have investigated the morphology of complex coacervate core micelles comprising a stiff, conjugated anionic derivative of polyfluorene (PF_{22}) and a flexible ionic-neutral copolymer poly(N-methyl-2-vinyl pyridinium chloride)–*b*-poly(-ethylene oxide) ($P2MVP_{29}$-*b*-PEO_{204}) in 30 mM $NaNO_3$ aqueous solutions at room temperature by super-resolution microscopy. To this end, we label the C3Ms in a simple, non-covalent fashion with a PEO-conjugated photo-activatable dye. We monitor C3M morphology in a broad range of concentrations $0.04 < C_{CF} < 2.83$ mM, of which the lower end is inaccessible by conventional methods for structural elucidation such as *e.g.*, small angle X-ray scattering. iPAINT reveals a concentration-induced morphological transition from spherical structures at low concentrations (C_{CF} <0.07 mM) to more elongated architectures at higher C_{CF}. The transformation appears gradual as both the mean and width of the micellar axial ratio and surface area distributions progressively increase with increasing concentration, while remaining peaked around a single value at all investigated concentrations. We attribute this concentration-induced micellar elongation for C3Ms from copolymers with a rather low block length ratio $N_{core}/N_{corona} = 0.2$ to the stiffness of the polyfluorene backbone.

3.4 Experimental

All commercial reagents are purchased from Sigma Aldrich and used as received without further purification, unless stated otherwise. Pd_2dba_3 is purchased from Strem Chemicals. Poly(2-vinyl pyridine-*b*-ethylene oxide) (M_n: 3000 g/mol -*b*- 9000 g/mol) is purchased from Polymer Source, GPC (DMF, PEO standards): M_n = 6840 g/mol, M_w = 8110 g/mol, $Đ$ = 1.19. PPh_3 is recrystallized from hot ethanol. The 20 kDa poly(ethylene glycol) bis(amine) is purchased from Sigma Aldrich. The N-hydroxysuccinimide activated ester rhodamine analogue (Cage-552) is purchased from Abberior®. Deuterated solvents are obtained from Cambridge Isotope Laboratories and dried over molsieves. All solvents are of AR quality and purchased from Biosolve. Reactions are followed by thin-layer chromatography (precoated 0.25 mm, 60-F254 silica gel plates from Merck).

3.4.1 Synthesis of polyelectrolytes

The synthesis of monomers follows the procedure of Wu *et al.*, [56] while the procedure of Hendriks *et al.* is used for the Suzuki polymerization. [57] The synthesis of the polyelectrolytes has been carried out by dr. C. Guibert. The synthesis steps are depicted in figure 3.9.

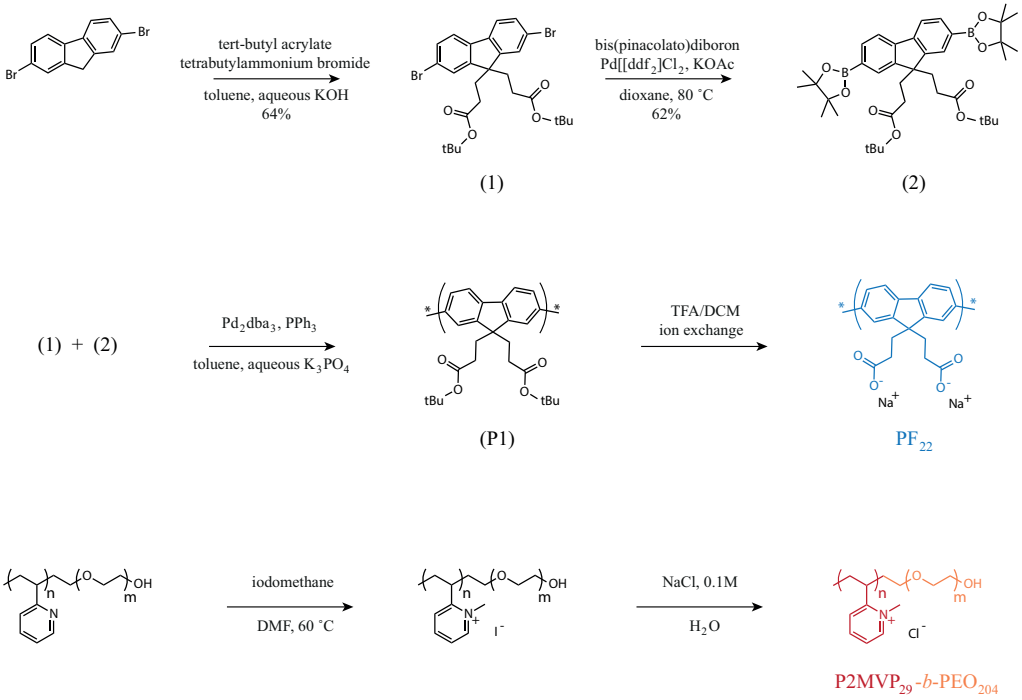

Figure 3.9: Synthesis of the rigid carboxylated polyfluorene derivative (PF_{22}) and the flexible diblock copolymer poly(N-methyl-2-vinyl pyridinium chloride)-*b*-poly(ethylene oxide) ($P2MVP_{29}$-*b*-PEO_{204}).

3.4.1.1 Synthesis of negatively charged polyelectrolytes

2,7-Dibromo-9,9-bis(3-(tert-butyl propanoate))fluorene, (**1**):
Aqueous KOH (50 wt%, 5 mL) is added dropwise to a solution of 2,7-dibromofluorene (3.3 g, 10.2 mmol) and tetrabutylammonium bromide (250 mg, 0.78 mmol) in toluene (25 mL). The solution is stirred for 20 min at room temperature. tert-butyl acrylate (5.25 g, 41 mmol) is added dropwise, and the mixture is stirred at room temperature for 5 h. The mixture is diluted with dichloromethane (15 mL) and washed with water (20 mL). The organic layer is collected and dried over anhydrous $MgSO_4$. After the solvent is removed, the residue is purified by column chromatography (ethyl acetate / heptane = 1 : 15, R_f = 0.34) to give the product as an off-white powder (3.8 g, 64 %). ^{1}H NMR ($CDCl_3$, 400 MHz): δ 7.54-7.48 (m, 6H, Ar-H), 2.33-2.28 (m, 4H, CH_2), 1.49-1.45 (m, 4H, CH_2), 1.33 (s, 18H, CH_3); ^{13}C NMR ($CDCl_3$, 100 MHz): δ 172.2, 149.9, 139.1, 126.5, 122.0, 121.4, 80.4, 54.0, 34.4, 29.9, 28.0; IR (ATR, cm^{-1}) ν_{max}: 2977, 2931, 1724, 1451, 1366, 1146; MALDI-TOF: calcd. for $C_{27}H_{32}Br_2O_4$ 580.35, found 580.07 (M^+).

2,7-[Bis(4,4,5,5-tetramethyl-1,3,2-dioxaborolan-2-yl)-9,9-bis(3-(tert-butyl-propanoate))] fluorene, (**2**):
Under argon, a mixture of (**1**) (1.8 g, 3.1 mmol), KOAc (0.91 g, 9.3 mmol), and bis(pinacolato)diboron (1.7 g, 6.5 mmol) in dioxane (30 mL) is placed in a 100 mL flask. After the mixture is stirred for 10 min, $Pd(dppf)_2Cl_2$ (5 mol%, 0.155 mmol, 113 mg) is added. The mixture is stirred at 80 °C overnight. After cooling to room temperature, water and dichloromethane are added, the aqueous phase is extracted with dichloromethane, and the organic layer is dried over $MgSO_4$. After the solvent is removed, the residue is purified by column chromatography (ethyl acetate / heptane = 1 : 4, R_f = 0.44) to give the product as an off-white solid (1.3 g, 62 %). ^{1}H NMR ($CDCl_3$, 400 MHz): δ 7.83 (d, 2H, J = 7.67 Hz, Ar-H), 7.78 (s, 2H, Ar-H), 7.72 (d, 2H, J = 7.67 Hz, Ar-H), 2.38 (t, 4H, J = 8.94 Hz, CH_2), 1.44-1.34 (m, 4H, CH_2, 24H, CH_3), 1.30 (s, 18H, CH_3). ^{13}C NMR ($CDCl_3$, 100 MHz): δ 172.8, 147.9, 143.8, 134.3, 129.0, 119.7, 83.9, 79.9, 53.5, 34.4, 28.0; IR (ATR, cm^{-1}) ν_{max}: 2978, 2932, 1729, 1349, 1144; MALDI-TOF: calcd. for $C_{38}H_{54}B_2O_8$ 660.40, found 697.41 (M^+Na).

Bis(phenyl)poly[9,9-bis(3-(tert-butyl propanoate))-fluorene-2,7-diyl], (**P1**):
PPh_3 (0.04 mmol, 10.5 mg), Pd_2dba_3 (0.01 mmol, 9.2 mg) and monomers (**1**) (0.5 mmol, 290 mg) and (**2**) (0.5 mmol, 337 mg) are placed in a 10 mL two-necked flask (Chemglass) under argon atmosphere. Toluene (10 mL) and few drops of aliquote 336 (phase transfer catalyst) is degassed using argon and added to the reaction flask. A 2 M solution of K_3PO_4 is degassed using argon and 1.25 mL is added to the toluene mixture. The reaction mixture

is stirred for two days at 90 °C. After the reaction mixture is cooled to room temperature, it is added to a large excess of methanol. The precipitate is redissolved in dichloromethane, passed through a silica column and reprecipitated in methanol. The product is obtained via filtration as green solid (340 mg, 81%). ^{1}H NMR ($CDCl_3$, 400 MHz): δ 7.86-7.72 (b, 6H, Ar-H), 2.53 (b, 4H, CH-2), 1.62 (b, 4H, CH_2), 1.30 (s, 18H, tBu). GPC ($CHCl_3$, PS standards): M_n = 9260 g/mol, M_w = 12233 g/mol (after correction, see below), $Đ$ = 1.33.

Bis(phenyl)poly[9,9-bis(3-propanoate)-fluorene-2,7-diyl] sodium salt, (**PF_{22}**):
(**P1**) (250 mg) is dissolved in dichloromethane (10 mL) and trifluoroacetic acid (2 mL) is added dropwise. The reaction mixture is stirred overnight at room temperature. The solvent is removed under reduced pressure, and the residue redissolved in 20 mL solution of Na_2CO_3 0.1 M, and stirred at room temperature for 5 h. The solution is dialyzed in deionized water and product is obtained by lyophilization. ^{1}H NMR (D_O, 400 MHz): δ (D_2O, 400 MHz): δ 7.99-7.90 (b, 6H, Ar-H), 2.53 (b, 4H, CH_2), 1.54 (b, 4H, CH_2).

3.4.1.2 Synthesis of positively charged polyelectrolytes

Poly(N-methyl-2-vinyl pyridine-b-ethylene oxide), (**$P2MVP_{29}$-*b*-PEO_{204}**):
Poly(2-vinyl pyridine-*b*-ethylene oxide) (0.5 g) is dissolved in N,N-dimethylformamide (10 mL) and large excess of iodomethane (1.5 mL, 20 equivalents per vinyl pyridine unit) is added. The reaction mixture is stirred overnight at 60 °C. The mixture is added to large excess of diethyl ether, the precipitate redissolved in 50 mL 0.1 M NaCl solution and stirred for 5 h. The mixture is extensively dialyzed in deionized water and the product lyophilized. ^{1}H NMR (D_2O, 400 MHz): δ 7-8.5 (b, Ar-H), 3.69 (s, EO units), 2.71 (s, N-CH_3), 2.2 (b, 2VP units).

3.4.2 Synthesis of PEG-552 probes

1 mg of poly(ethylene glycol) bis(amine) is dispersed in 1 mL of 0.1 M sodium bicarbonate buffer at pH 8.5. 20 μL of Cage-552 in DMSO (10 mM) is added to the solution. The reaction mixture is stirred overnight in the dark at room temperature, and subsequently purified by dialysis (Spectra/Por®7 dialysis membrane, pretreated RC tubing, molecular weight cutoff: 8 kDa) to remove the unreacted dye molecules.

3.4.3 Instrumentation

The chromatography, spectroscopy and light scattering measurements have been carried out by dr. C. Guibert.

3.4.3.1 Chromatography

Flash chromatography.
Flash cromatograpy is performed using an automatic flash chromatography instrument Biotage Isolera One equipped with biotage SNAP KP-Sil silica cartridges.

Gel Permeation Chromatography.
$CHCl_3$-GPC measurements are performed on aShimadzu-system (Prominence i LC-2030C 3D) equipped with a Agilent Technology Resipore column [200-400.000 Da], a RI detector and a PDA detector, with $CHCl_3$ as eluent at 40 °C and a constant flow rate of 1 mL/min. The system is calibrated with polystyrene (PS) samples with a range of 92-371.000 Da (Polymer Laboratories). According to Grell *et al.*, the molecular weight of (**P1**) is corrected by a factor of 2.7 to take into account the stiffness of (**P1**) compared to the PS standards. [44]
DMF-GPC measurements are carried out on a PL-GPC-50 plus from Polymer Laboratories (Agilent Tech.) with refractive index detector working in DMF containing 10 mM LiBr at 50 °C at a constant flow rate of 1 mL/min on a Shodex GPC-KD-804 column (exclusion limit = 400 kDa; 0.8 cm i.d. × 300 mL), which is calibrated with polyethyleneoxide (PEO) standards with a range from 282-77350 Da (Polymer Laboratories, Agilent Tech.).

3.4.3.2 Spectroscopy

NMR spectroscopy.
NMR spectroscopy is performed on a Varian Mercury Vx 400 MHz and/or Varian 400MR, operating at 400 MHz for ^{1}H and 100 MHz for ^{13}C. Chemical shifts are reported in ppm (δ) values relative to tetramethylsilane (TMS) or residual solvent. Splitting patterns are labelled as s, singlet; d, doublet; dd, double doublet; t, triplet; q, quartet; q, quintet; m, multiplet and b stands for broad.

Matrix assisted laser desorption/ionisation (MALDI).
Mass spectra are obtained on a PerSeptive Biosystems Voyager DE-PRO spectrometer or Bruker autoflex speed spectrometer using α-cyano-4-hydroxycinnamic acid (CHCA) and trans-2-[3-(4-tert-butylphenyl)-2-methyl-2-propenylidene]malononitrile (DCTB) as matrices.

IR spectoscopy.

IR spectra are recorded on a Perkin-Elmer FTIR Spectrum 2 spectrometer equipped with a Perkin-Elmer Universal ATR Sampler Accessory.

Fluorescence spectroscopy.
Fluorescent emission spectra are recorded on a Varian Cary Eclipse fluorometer using a quartz cuvette with a pathlength of l = 3 mm and the following parameters: λ_{ex} = 383 nm, excitation slit 5 nm, emission slit 5 nm, scan rate 120 nm/min, data interval 1 nm, averaging time 0.5 s. The measurements are performed in MilliQ-water at pH 9 (adjusted using 1 M NaOH).

3.4.3.3 Light scattering

Light scattering (LS) experiments are performed using an ALV/CGS-3 MD-4 compact goniometer system equipped with a Multiple Tau digital real time correlator (ALV-7004) and a solid-state laser (λ_{max} = 532 nm; 40 mW). The measurements are performed at 90° in milli-Q water at pH 9 (adjusted using 1 or 0.1 M NaOH). To prevent dust contamination, the solvent is prefiltered (PVDF 0.2 μm), and glass cuvettes are rinsed with filtered (PVDF 0.2 μm) acetone and left to dry inverted. The polymer samples are not filtered.

3.4.3.4 Microscopy

Super-resolution iPAINT microscopy is carried out on a Nikon NSTORM system in total internal reflection fluorescence (TIRF) configuration. A low power (∼48.1 mW/cm^2) blue laser (λ = 488 nm) was used to localize the complex coacervate core micelles in the field of view. Subsequently, a 1% power (∼1.6 mW/cm^2) UV laser (λ = 405 nm) is used to photo-activate a small number of PEG-552 molecules, to stochastically ensure a distance larger than the diffraction limit among photo-activated molecules. At the same time, a 100% power (∼488 mW/cm^2) visible laser (λ = 561 nm) is used to excite and successively bleach the photo-activated molecules. The fluorescence signal is collected by a Nikon objective 100×, oil immersion, 1.4 NA, and filtered by a quad-band pass dichroic filter (97335 Nikon), embedded in the microscope. The iPAINT images are recorded on a field of view of 128 × 128 pixels (pixel size 170 nm) of an EMCCD camera (ixon3, Andor). Over 15 × 10^3 frames are collected, at a rate of 97 frames/s. The single molecule localizations are analyzed using the Nikon software 'NIS elements'. iPAINT imaging is performed on samples kept in a sample chamber made from a coverslide and a coverslip held together by double-side tape. Prior to chamber assembly, the coverslip is cleaned by piranha etching, followed by rinsing and sonication in acetone, isopropanol, MilliQ-water (18.2 MΩ) and finally blow drying in a nitrogen flow.

Bibliography

[1] Voets, I.K.; de Keizer, A.; de Waard, P.; Frederik, P.M.; Bomans, P.H.H.; Schmalz, H.; Walther, A.; King, S.M.; Leermakers, F.A.M.; Cohen Stuart, M.A. *Angew. Chem. Int. Ed.* **2006**, *45*, 6673.

[2] Voets, I.K.; de Keizer, A.; Cohen Stuart, M.A. *Adv. Colloid Interface Sci.* **2009**, *147*, 300.

[3] Wang, J.; Voets, I.K.; Fokkink, R.; van der Gucht, J.; Velders, A. *Soft Matter* **2014**, *10*, 7337.

[4] Berret, J.F.; Vigolo, B.; Eng, R.; Herve, P.; Grillo, I.; Yang, Y. *Macromolecules* **2004**, *37*, 4922.

[5] Lee, Y.; Ishii, T.; Kim, H.J.; Nishiyama, N.; Hayakawa, Y.; Itaka, K.; Kataoka, K. *Angew. Chem. Int. Ed.* **2010**, *49*, 2552.

[6] Uchman, M.; Štěpànek M.; Prèvost, S.; Angelov, B.; Bednár, J.; Appavou, M.S.; Gradzielski, M.; Procházka, K. *Macromolecules* **2012**, *45*, 6471.

[7] Christie, R.J.; Miyata, K.; Matsumoto, Y.; Nomoto, T.; Menasco, D.; Lai, T.C.; Pennisi, M.; Osada, K.; Fukushima, S.; Nishiyama, N.; Yamasaki, Y.; Kataoka, K. *Biomacromolecules* **2011**, *12*, 3174.

[8] Bronstein, L.M.; Sidorov, S.N.; Zhirov, V.; Zhirov, D.; Kabachii, Y.A.; Kochev, S.Y.; Valetsky, P.M.; Stein, B.; Kiseleva, O.I.; Polyakov, S.N.; Shtykova, E.V.; Nikulina, E.V.; Svergun, D.I.; Khokhlov, A.R. *J. Phys. Chem. B* **2005**, *109*,18786.

[9] Dirisala, A.; Osada, K.; Chen, Q.; Tockary, T.A.; Machitani, K.; Osawa, S.; Liu, X.; Ishii, T.; Miyata, K.; Oba, M.; Uchida, S.; Itaka, K.; Kataoka, K. *Biomaterials* **2014**, *35*, 5359.

[10] Tockary, T.A.; Osada, K.; Chen, Q.; Machitani, K.; Dirisala, A.; Uchida, S.; Nomoto, T.; Toh, K.; Matsumoto, Y.; Itaka, K.; Nitta, K.; Nagayama, K.; Kataoka, K. *Macromolecules* **2013**, *46*, 6585.

[11] Kishimura, A.; Koide, A.; Osada, K.; Yamasaki, Y.; Kataoka, K. *Angew. Chem. Int. Ed.* **2007**, *47*, 6085.

[12] Stepanek, M.; Škvarla, J.; Uchman, M.; Procházka, K.; Angelov, B.; Kováčik, L.; Garamus, V.M.; Mantzaridis, C.; Pispas, S. *Soft Matter* **2012**, *8*, 9412.

[13] Dreiss, C.A. *Soft Matter* **2007**, *3*, 956.

[14] Williford, J.M.; Santos, J.L.; Shyam, R.; Mao, H.Q. *Biomater. Sci.* **2015**, *3*, 894.

[15] Kamaly, N.; Xiao, Z.; Valencia, P.M.; Radovic-Moreno, A.F.; Farokhzad, O.C. *Chem. Soc. Rev.* **2012**, *41*, 2971.

[16] Zhulina, E.B.; Adam, M.; LaRue, I.; Sheiko, S.S.; Rubinstein, M. *Macromolecules* **2005**, *38*, 5330.

[17] Koide, A.; Kishimura, A.; Osada, K.; Jang, W.D.; Yamasaki, Y.; Kataoka, K. *J. Am. Chem. Soc.* **2006**, *128*, 5988.

[18] Klok, H.A.; Lecommandoux, S. *Adv. Mater.* **2001**, *13*, 1217.

[19] Tu, G.; Li, H.; Forster, M.; Heiderhoff, R.; Balk, L.J.; Sigel, R.; Scherf, U. *Small* **2007**, *3*, 1001.

[20] Gutacker, A.; Lin, C.Y.; Ying, L.; Nguyen, T.Q.; Scherf, U.; Bazan, G.C. *Macromolecules* **2012**, *45*, 4441.

[21] Ahlers, P.; Frisch, H.; Besenius, P. *Polym. Chem.* **2015**, *6*, 7245.

[22] Frisch, H.; Unsleber, J.P.; Lüdeker, D.; Peterlechner, M.; Brunklaus, G.; Waller, M.; Besenius, P. *Angew. Chem. Int. Ed.* **2013**, *52*, 10097.

[23] Frisch, H.; Nie, Y.; Raunser, S.; Besenius, P. *Chem. Eur. J.* **2015**, *21*, 3304.

[24] Bastardo, L.A.; Iruthayaraj, J.; Lundin, M.; Dedinaite, A.; Vareikis, A.; Makuška, R.; van der Wal, A.; Furò, I.; Garamus, V.M.; Claesson, P.M. *J. Coll. Interf. Sci.* **2007**, *312*, 21.

[25] Müller, M.; Reihs, T.; Ouyang, W. *Langmuir* **2005**, *21*, 465.

[26] Tockary, T.A.; Osada, K.; Motoda, Y.; Hiki, S.; Chen, Q.; Takeda, K.M.; Dirisala, A.; Osawa, S.; Kataoka, K. *Small* **2016**, *12*, 1193.

[27] Ding, Y.; Yang, Y.; Yang, L.; Yan, Y.; Huang, J.; Cohen Stuart, A.M. *ACS Nano* **2012**, *2*, 1004.

[28] Nilsson, K.P.R.; Herland, A.; Hammarström, P.; Inganäs, O. *Biochemistry* **2005**, *44*, 3718.

[29] Yoon, B.; Lee, S.; Kim, J.M. *Chem. Soc. Rev.* **2009**, *38*, 1958.

[30] Levitsky, I.A.; Kim, J.; Swager, T.M. *J. Am. Chem. Soc.* **1999**, *121*, 1466.

[31] Yu, D.; Zhang, Y.; Liu, B. *Macromolecules* **2008**, *41*, 4003.

[32] Pu, K.Y.; Cai, L.; Liu, B. *Macromolecules* **2009**, *42*, 5933.

[33] Cingil, H.E.; Storm, I.M.; Yorulmaz, Y.; te Brake, D.W.; de Vries, R.; Cohen Stuart, M.A.; Sprakel, J. *J. Am. Chem. Soc.* **2015**, *137*, 9800.

[34] Cingil, H.E.; Boz, E.B.; Wang, J.; Cohen Stuart, M.A.; Sprakel, J. *Adv. Funct. Mater.* **2016**, *26*, 1420.

[35] Voets, I.K.; de Vries, R.; Fokkink, R.; Sprakel, J.; May, R.P.; de Keizer, A.; Cohen Stuart, M.A. *Eur. Phys. J. E* **2009**, *30*, 351.

[36] Hell, S.W. *Science* **2007**, *316*, 1153.

[37] Betzig, E.; Patterson, G.H.; Sougrat, R.; Lindwasser, O.W.; Olenych, S.; Bonifacino, J.S.; Davidson, M.W.; Lippincott-Schwartz, J.; Hess, H.F. *Science* **2006**, *313*, 1642.

[38] Willig, K.I.; Kellner, R.R.; Medda, R.; Hein, B.; Jakobs, S.; Hell, S.W. *Nat. Methods* **2006**, *3*, 721.

[39] Rust, M.J.; Bates, M.; Zhuang, X. *Nat. Methods* **2006**, *3*, 793.

[40] Albertazzi, L.; van der Zwaag, D.; Leenders, C.M.A.; Fitzner, R.; van der Hofstad, R.W.; Meijer, E.W. *Science* **2014**, *344*, 491.

[41] Aloi, A.; Vargas Jentzsch, A.; Vilanova, N.; Albertazzi, L.; Meijer, E.W.; Voets, I.K. *J. Am. Chem. Soc.* **2016**, *138*, 2953.

[42] Boott, C.E.; Laine, R.F.; Mahou, P.; Finnegan, J.R.; Leitao, E.M.; Webb, S.E.D.; Kaminski, C.F.; Manners, I. *Chem. Eur. J.* **2015**, *21*, 18539.

[43] Aloi, A.; Vilanova, N.; Albertazzi, L.; Voets, I.K. *Nanoscale* **2016**, *8*, 8712.

[44] Grell, M.; Bradley, D.D.C.; Long, X.; Chamberlain, T.; Inbasekaran, M.; Woo, E.P.; Soliman, M. *Acta Polym.* **1998**, *49*, 439.

[45] Chen, L.; McBranch, D.W.; Wang, H.L.; Helgeson, R.; Wudl, F.; Whitten, D.G. *Proc. Nat. Am. Soc. U.S.A.* **1999**, *96*, 12287.

[46] Chen, L.; Xu, S.; McBranch, D.; Whitten, D.G. *J. Am. Chem. Soc.* **2000**, *122*, 9302.

[47] Jones, R.M.; Bergstedt, T.S.; Buscher, C.T.; McBranch, D.; Whitten, D.G. *Langmuir* **2001**, *17*, 2568.

[48] Sharanov, A.; Hochstrasser, R.M. *Proc. Natl. Acad. Sci. U.S.A.* **2006**, *103*, 18911.

[49] Belov, N.V.; Mitronova, G.Y.; Bossi, M.L.; Boyarskiy, V.P.; Hebisch, E.; Geisler, C.; Kolmakov, K.; Wurm, C.A.; Willig, K.I.; Hell, S.W. *Chem. Eur. J.* **2014**, *20*, 13162.

[50] Lou, S.; Jiang, X.; Scott, P.J. *Proc. R. Soc. A* **2013**, *469*, 20130150.

[51] Danino, D.; Abezgauz, L.; Portnaya, I.; Dan, N. *J. Phys. Chem. Lett.* **2016**, *7*, 1434.

[52] Schillen, K.; Brown, W.; Johnsen, R.M. *Macromolecules* **1994**, *27*, 4825.

[53] Ohlendorf, D.; Interthal, W.; Hoffmann, H. *Rheol. Acta* **1986**, *25*, 468.

[54] Molina-Bolívar, J.A.; Aguiar, J.; Peula-García, J.M.; Ruiz, C.C. *J. Phys. Chem. B* **2004**, *108*, 12813.

[55] van der Kooij, H.M.; Spruijt, E.; Voets, I.K.; Fokkink, R.; Cohen Stuart, A.M.; van der Gucht, J. *Langmuir* **2012**, *28*, 14180.

[56] Wu, C.S.; Su, H.C.; Chen, Y. *Org. Biomol. Chem.* **2014**, *12*, 5682.

[57] Hendriks, K.H.; Heintges, G.H.L.; Gevaerts, V.S.; Wienk, M.M.; Janssen, R.A.J. *Angew. Chem. Int. Ed.* **2013**, *52*, 8341.

Chapter 4

In-situ visualization of nanoparticles adsorbed at fluid interfaces by single-molecule localization microscopy

Colloidal particles adsorbed at droplet interfaces are crucial for the mechanical stability and thus protection against coalescence of Pickering emulsions. The key parameter which determines the kinetic and thermodynamic properties of these systems is the contact angle θ. At the nanoscale, morphological and chemical heterogeneities of particles can affect the value of θ significantly. Many methods have therefore been developed to measure the contact angle of individual particles when adsorbed at interfaces. However, none of these methods enables a simultaneous visualization of nanoparticles and liquid-liquid interfaces, *in-situ*. To tackle this challenge, we utilize a newly developed super-resolution microscopy method, called iPAINT, which relies on non-covalent and continuous labelling of interfaces through photo-activatable fluorescent probes. Here we image individual, hydrophobic and hydrophilic colloidal nanoparticles ($R \sim$300 nm) adsorbed at a water-octanol interface, while simultaneously visualizing the position of this interface with nanometric accuracy. From the iPAINT reconstructions, we obtain contact angle distributions, which are narrow and centered at $\langle\theta\rangle = 111.5° \pm 2.3°$, and $\langle\theta\rangle = 59.5° \pm 5.5°$ for the hydrophobic and hydrophilic particles, respectively. We further find a non-negligible dependency of $\langle\theta\rangle$ on particle size, from which we estimate the magnitude of the line tension, τ. We obtain $\tau = 1.13 \pm 0.22$ nN (hydrophobic particles) and $\tau =$ -3.36 $\pm$ 0.31 nN (hydrophilic particles). Our findings suggest that the broad distributions reported by others for sub-μm-sized particles may be due to sample preparation methods (*e.g.*, co-solvent effects, *etc.*) rather than chemical heterogeneities.

4.1 Introduction

Fine mixtures of two immiscible liquids are ubiquitous in everyday life, even though they are thermodynamically unstable. Over time, these will therefore separate into two macroscopic liquid phases to minimize the total interfacial area. [1] It is possible to kinetically stabilize (emulsify) such fine mixtures using surface-active agents. Their adsorption at the liquid-liquid interface lowers its interfacial energy and thus the overall free energy of the system. Alternatively, liquid-liquid interfaces can be stabilized by colloidal particles to reduce the total interfacial area, resulting in so-called Pickering emulsions. [2] These particles confer to the system an extreme stability as their high adsorption energy, ΔF, far exceeds the thermal energy, k_BT, when the particle radius, R, and interfacial tension, $\gamma_{o/w}$, are large and/or $\theta \sim \frac{\pi}{2}$, according to:

$$\Delta F = \gamma_{o/w} R^2 \pi (1 - |\cos\theta|)^2. \tag{4.1}$$

Since the early reports on particle-stabilized emulsions, [2, 3] various groups have demonstrated their enhanced mechanical properties, robustness, long-term stability, and adequate protection against coalescence, [4–6] all of which are paramount in technologies like drug delivery [7], catalysis, [8] and nanocapsule stabilization. [9, 10] Hence, particle-laden interfaces have been at the forefront of colloidal science for more than a century. [2, 3] Only recently, however, wetting phenomena have been examined at the single colloid level. [11, 12] Several elegant methods with high spatial resolution and image contrast, like FreSCa, [13] digital holography, [14] and Bessel beam microscopy, [15] have been recently developed for this purpose. These technological advances have revealed how particle heterogeneities (*e.g.*, chemical or shape anisotropy, surface functionalization, roughness) impact the stabilization of liquid-liquid interfaces. [16] Local differences in contact angles and consequentially adsorption energies are observed, [15, 17] which may lead to local detachment, faster dynamics, [18–20] and large capillary forces [21, 22] resulting in mechanical instabilities. [23] None of the newly developed methods, however, allows to simultaneously localize the particles and the interface *in-situ*. Instead, all these techniques require fixation of the (particles at the) interface to perform *ex-situ* SEM or AFM imaging. To do so, the interface is vitrified, [13, 24–26] fluid phases are gelled, [27, 28] and/or chemical reactions are performed to mark the position of the three-phase contact line. [29]

Here, we present a complementary method based on single-molecule localization microscopy (SMLM) that instead allows *in-situ* and simultaneous visualization of both the individual particles and the interface to which they are adsorbed. In SMLM, fluorescence signals from single molecules (typically thousands of photons per dye) closer than the diffraction limit of light (∼200 nm) are temporally separated from one another. The position of

individual dyes is subsequently determined with nanometric precision from the centroid of a 2D-Gaussian distribution fit to the experimental fluorescence intensity profile. Next, all localizations are combined to yield a super-resolved image. As such, SMLM enables *in-situ* imaging with chemical specificity and high spatial resolution. Recently, we introduced a new approach to SMLM which is coined interface Point Accumulation for Imaging in Nanoscale Topography (iPAINT). In iPAINT, interfaces are continuously and non-covalently labelled through physical adsorption of photo-activatable dyes to image soft materials with < 20 nm resolution. [30, 31] Here we utilize iPAINT super-resolution microscopy to visualize hundreds of hydrophobic and hydrophilic silica nanoparticles adsorbed at the water-octanol interface. From these images, we determine their mean contact angles, $\langle\theta\rangle$, and associated distributions. We find a non-negligible dependence of $\langle\theta\rangle$ on particle size, which we attribute to line tension effects. Finally, we discuss the width of the experimentally obtained contact angle distributions, with mean values in line with theoretical predictions. While we find narrow distributions with $\sigma \simeq 7°$, others reported much broader distributions for (supposedly) the same particles. In view of the differences between these methods and the low invasiveness of iPAINT, we tentatively attribute the broadening observed by others to sample preparation methods (vitrification, co-solvent effects, *etc.*) rather than chemical heterogeneities.

4.2 Results and discussion

4.2.1 In-situ visualization of individual nanoparticles at fluid interfaces

An accurate measurement of the contact angle of individual particles at liquid-liquid interfaces requires a precise localization of both the particles and the interface to which they are adsorbed (details in section 4.4.7). To critically evaluate whether iPAINT can be utilized for this purpose, we set out to determine the contact angles of surface-functionalized hydrophobic and hydrophilic silica particles ($R = 332 \pm 14$ nm, further details in section 4.4.1) at the water-octanol interface. Particle-laden water-octanol interfaces are prepared normal to the coverslip, to profit from the heightened spatial resolution in the lateral plane ($\sim$17 nm) compared to the axial direction ($\sim$80 nm). [32] We use the photo-activatable dye Cage-552 end-attached to the water-soluble polymer polyethylene glycol (PEG-552), to ensure interfacial adsorption and to tune the fraction of emitting dyes (further details in section 4.4). Conveniently, Brownian blurring precludes PEG-552 localization in solution, while the labels are readily identified when adsorbed at the interfaces where their motion is restricted. [30] Thus, we anticipate that PEG-552 'stains' the oil-water interface, the coverslip exposed to the water phase, and the surface of the particles.

Figure 4.1 displays exemplary results of iPAINT experiments on water-octanol interfaces onto which hydrophilic (fig. 4.1a) and hydrophobic (fig. 4.1b) particles are adsorbed (details in section 4.4.4). These reconstructions are based on $>10^6$ localizations of PEG-552 ($\sim$20 localizations per frame) acquired over $\sim$18 min, approximately 1 hour after sample preparation, to ensure steady-state conditions (details in section 4.4.7). Clearly, both the particles and the liquid-liquid interface can be simultaneously visualized. The oil phase appears dark and the water phase bright, as PEG-552 is preferentially distributed at the interfaces and in the aqueous phase. The hydrophilic particles are uniformly covered by PEG-552 probes as these are initially dispersed in the aqueous phase with the dye (fig. 4.1a). By contrast, only the portion of the hydrophobic particles exposed to the water phase is labelled (fig. 4.1b).

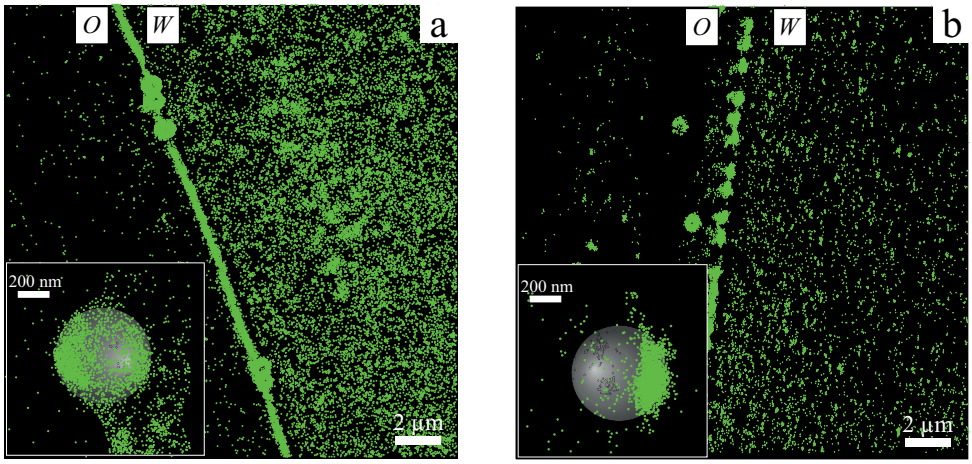

Figure 4.1: iPAINT enables simultaneous and *in-situ* visualization of particles at fluid interfaces. (a) Plain silica (hydrophilic) and (b) stearyl-alcohol coated (hydrophobic) silica particles adsorbed at the water-octanol interface. The oil phase appears dark and the water phase bright as PEG-552 is water-soluble. The hydrophilic particles are uniformly covered by PEG-552 while only the hemisphere wet by the water phase is labelled in hydrophobic particles. Insets: zoom of a representative hydrophobic and hydrophilic colloidal particle. The grey sphere is a representation of a sphere with radius $R = 660$ nm, localizing the particle at the interface.

To unambiguously identify the position of the particles and the interface we rely on the single-molecule counts per μm^2. In fact, the different interaction of PEG-552 with the various interfaces causes a stark contrast among the single-molecule localization densities of oil, water phases, interface and particle surfaces (section 4.4.7 for details).

4.2.2 Contact angle of single-particles at deformable interfaces

To determine the contact angle of hydrophobic ($\langle R_{SEM} \rangle = 346$ nm $\pm$ 15 nm) and hydrophilic ($\langle R_{SEM} \rangle = 349$ nm $\pm$ 16 nm) particles, we calculate the particle radius, R (details in section 4.4.6), and measure the height of the spherical cap, h, of each individual adsorbed particle, as schematically outlined in figure 4.2.

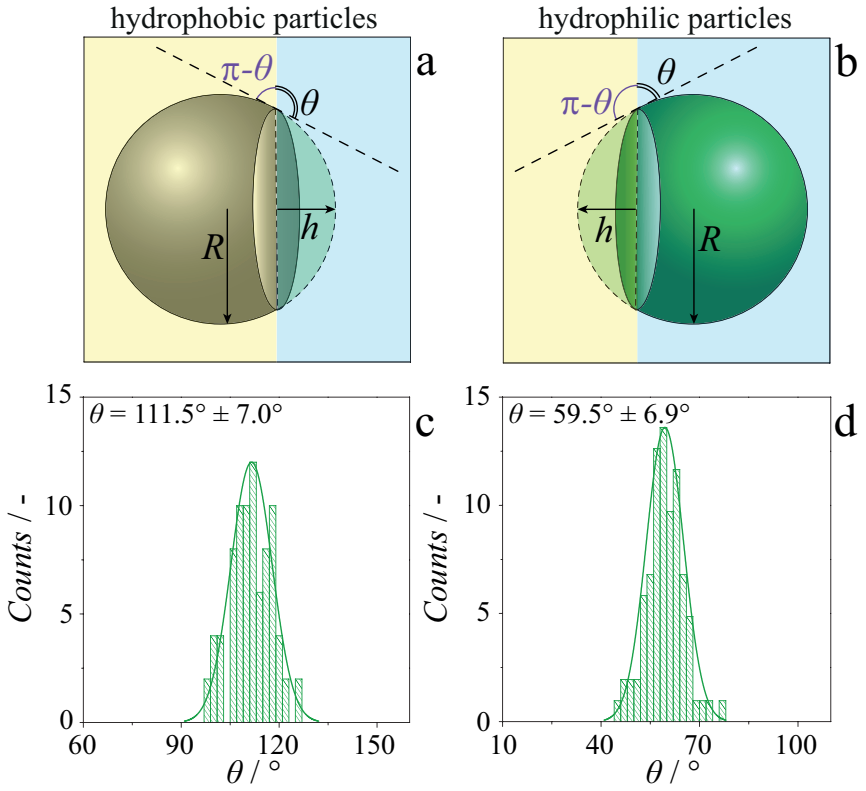

Figure 4.2: Contact angle measurement of individual particles at a fluid interface. (a-b) Representation of a hydrophobic and hydrophilic colloidal particle of radius R at an oil-water interface. The schematic highlights the three-phase contact angle θ, and the height of the bead relative to the interface h. (c-d) Distribution of contact angles of hydrophobic and hydrophilic colloids, respectively.

The spherical cap height corresponds to the distance between the interface and the outermost localization on the particle surface (vector h in fig. 4.2a). Using the values of R and h for each individual particle, we can compute the contact angle of hydrophobic particles at the water-octanol interface as:

$$\theta = \cos^{-1}\left(\frac{h-R}{R}\right), \tag{4.2}$$

and θ of the hydrophilic particles as follows:

$$\theta = \cos^{-1}\left(\frac{R-h}{R}\right). \tag{4.3}$$

As expected, we find much larger values for the hydrophobic particles ($\langle\theta\rangle = 111.5° \pm 7.0°$, fig. 4.2c) than for hydrophilic particles ($\langle\theta\rangle = 59.5° \pm 6.9°$, fig. 4.2d). Furthermore, these values are in the same ballpark as values reported for the equilibrium contact angles of μm-sized silica beads at water-octanol interfaces obtained from ensemble measurements ($\langle\theta\rangle = 148° \pm 5°$, $\langle\theta\rangle = 68° \pm 6°$). [33] Using eq. 4.1, an estimated interfacial fluid tension $\gamma_{(o/w)} = 0.00852$ N/m (water-octanol interface at 20 °C), [34] and particle radii R, we calculate the corresponding adsorption energies $\Delta F = 1.16 \pm 0.07 \times 10^{-15}$ J ($= 0.28 \pm 0.02 \times 10^6$ k_BT), and $\Delta F = 0.69 \pm 0.08 \times 10^{-15}$ J ($= 0.17 \pm 0.02 \times 10^6$ k_BT), for hydrophobic and hydrophilic particles, respectively. Clearly, $\Delta F \gg k_BT$, hence both kinds of particles are irreversibly adsorbed.

4.2.3 Narrow single-particle contact angle distribution

Various groups studied the contact angles distributions obtained by single particle measurements for (sub-)μm-sized colloidal particles, reporting distributions (FreSCa: $\pm 12°$, Bessel beam microscopy: $\pm 19°$) broader than those obtained by iPAINT microscopy ($\pm 7°$). Taking a closer look at the contact angle distributions obtained by iPAINT (fig. 4.2) is therefore of interest. Multiple factors may cause broadening of the contact angle distribution, some of which are related to the colloidal particles, $\sigma_{\theta,p}$ (chemical heterogeneities, size polydispersity), [35] and others to the liquid-liquid interface (aging of the three-phase contact line, thermal motion of the particle within the oil-water interfacial plane, $\sigma_{\theta,B}$). [13, 36, 37] In addition, the limited experimental resolution of iPAINT, $\sigma_{\theta,res,i}$, should be taken into account.

Aiming first to critically evaluate whether aging effects can safely be neglected as measurements are performed under steady-state conditions, we investigate the measured contact angles $\langle\theta\rangle$ for both particle types as a function of time (fig. 4.3). The contact angle remains fairly constant during the course of several hours, aside from small fluctuations which are within the experimental uncertainty. Hence, aging can be ruled out as a significant contribution to the contact angle distributions.

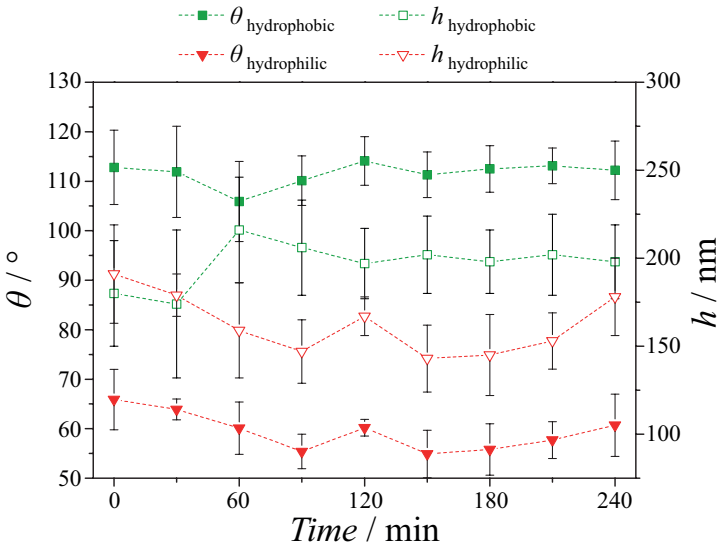

Figure 4.3: Variation in time, of the total population of the contact angle, θ, (close symbols) and the height, h, (open symbols) of the particles relative to the position of the interface for hydrophobic (green symbols) and hydrophilic (red symbols) particles. The graph suggests no aging of the contact line occurs.

We now focus on the three remaining factors. The quantity of interest is $\sigma_{\theta,p}$, as this variability in particle position is related to differences in particle size and surface functionalization. The factors affecting the total broadening of the contact angle distribution in iPAINT can be described by the following equation:

$$\sigma_{\theta,total,i} = \sqrt{\sigma^2_{\theta,res,i} + \sigma^2_{\theta,p} + \sigma^2_{\theta,B}}. \tag{4.4}$$

Since $\Delta F \gg k_B T$, and the particles are gently immobilized at the coverslip, Brownian motion can safely be neglected ($\sigma_{\theta,B} \ll \sigma_{\theta,res,i}$, $\sigma_{\theta,p}$). Hence, $\sigma_{\theta,p}$ can be calculated from eq. 4.4 and the measured $\sigma_{\theta,total,i}$, once $\sigma_{\theta,res,i}$ is computed.

$\sigma_{\theta,res,i}$ is determined by the accuracy of the single-molecule localizations from which the radius, R, and the height of the spherical cap, h are obtained, since these are the quantities needed to calculate the contact angle, according to eqs. 4.2 and 4.3. We refer to these two quantities as $\sigma_{R,res,i}$, and $\sigma_{h,res,i}$. First, we determine $\sigma_{R,res,i}$. To do so, we measure the size distribution of particles calculated by SEM imaging (blue curves in fig. 4.4a and 4.4c) and its standard deviation ($\sigma_{R,p,e}$). Here we assume that the SEM distribution is given only by the polydispersity of the particles ($\sigma_{R,p}$), *i.e.*, the resolution of the method does not broaden the width of the distribution ($\sigma_{R,p,e} = \sigma_{R,p}$).
Conversely, the particle size distribution ($\sigma_{R,p,i}$) obtained by iPAINT imaging of the same particles (red curved in fig. 4.4a and 4.4c) are broadened by the polydispersity of the particles ($\sigma_{R,p}$) and by the accuracy of the single-molecule localizations ($\sigma_{R,res,i}$). Hence, we can

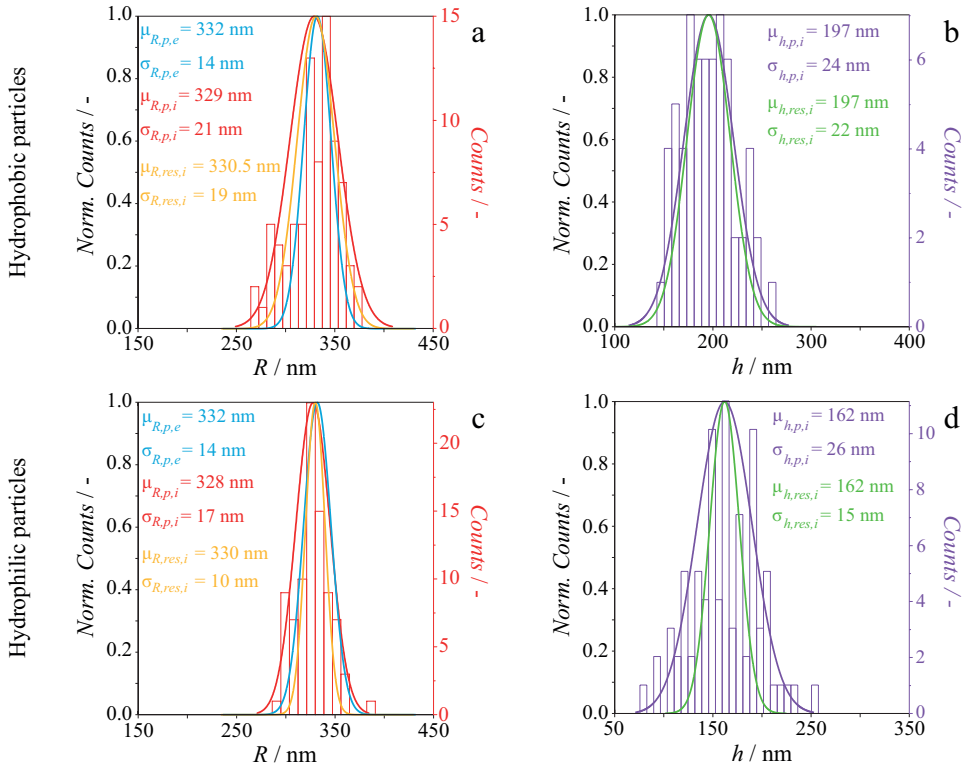

Figure 4.4: Influence of iPAINT resolution on estimating size distributions. (a, c) Size distribution of colloidal particles imaged by SEM (blue curve), and by iPAINT (red curve and histogram data). The yellow curve is given by deconvolution between the blue and the red curve, and illustrates the distribution in sizes of particles only affected by iPAINT resolution. (b, d) Size distribution of heights of the spherical cap of colloidal particles adsorbed at the liquid-liquid interface, before (purple curve and histogram data) and after (green curve) deconvolution.

calculate $\sigma_{R,res,i}$ from the deconvolution of $\sigma_{R,p,e}$ (blue distributions in fig. 4.4) and $\sigma_{R,p,i}$ (red distributions in fig. 4.4):

$$\sigma_{R,res,i} = \sqrt{\sigma^2_{R,p,i} - \sigma^2_{R,p,e}}. \tag{4.5}$$

This gives $\sigma_{R,res,i} = 19$ nm for the hydrophobic particles, $\sigma_{R,res,i} = 10$ nm for the hydrophilic particles. Now that $\sigma_{R,res,i}$ is determined, we compute how the resolution in iPAINT affects the distribution of heights of the spherical caps (green curve in fig. 4.4b and 4.4d), and its width ($\sigma_{h,res,i}$). To do so, we rescale $\sigma_{R,res,i}$ to the experimental data of h (purple curve in fig. 4.4b and 4.4d). The results of the radii and the heights are summarized in table 4.1:

Table 4.1: Mean (μ_R) and standard deviations (σ_R) of the radii distribution of hydrophobic and hydrophilic colloidal particles obtained by SEM, iPAINT and from their deconvolution. Mean (μ_h) and standard deviations (σ_h) of the distribution of the spherical cap height of hydrophobic and hydrophilic colloidal particles, obtained by iPAINT and their deconvolution with the iPAINT resolution.

	Particle Radii			Spherical Cap Heights		
Particle	*Distribution*	$\boldsymbol{\mu_R}$ (nm)	$\boldsymbol{\sigma_R}$ (nm)	*Distribution*	$\boldsymbol{\mu_h}$ (nm)	$\boldsymbol{\sigma_h}$ (nm)
Hydrophobic	R,p,e	332	14	h,p,i	197	24
	R,p,i	329	21	h,res,i	197	22
	R,res,i	330.5	19			
Hydrophilic	R,p,e	332	14	h,p,i	162	26
	R,p,i	328	17	h,res,i	162	15
	R,res,i	330	10			

Now that both $\sigma_{R,res,i}$ and $\sigma_{h,res,i}$ are known, we can finally compute $\sigma_{\theta,res,i}$ as:

$$\begin{aligned}\sigma_{\theta,res,i} &= \sqrt{\left(\left|\frac{\partial\theta}{\partial R}\right|\partial R\right)^2 + \left(\left|\frac{\partial\theta}{\partial h}\right|\partial h\right)^2} = \\ &= \sqrt{\left(\frac{|h-R|^2 + R(h-R)}{R^2|h-R|\sqrt{1-\frac{|h-R|^2}{R^2}}}\partial R\right)^2 + \left(\frac{R-h}{R|h-R|\sqrt{1-\frac{|h-R|^2}{R^2}}}\partial h\right)^2}\end{aligned} \tag{4.6}$$

where ∂R and ∂h are the standard deviation on the radii ($\sigma_{R,res,i}$) and heights ($\sigma_{h,res,i}$) affected by the iPAINT resolution, as calculated from the distributions in figure 4.4. We obtain $\sigma_{\theta,res,i} = 6.6°$ for the hydrophobic particles and $\sigma_{\theta,res} = 4.2°$ for the hydrophilic ones.

Using these computed values and the standard deviations of the measured distributions of contact angles shown in figure 4.2 ($\sigma_{\theta,total,i} = 7.0°$ for the hydrophobic particles, and $\sigma_{\theta,total,i} = 6.9°$ for the hydrophilic ones), we can determine the effect of the particle variability ($\sigma_{\theta,p}$) on the broadening of the contact angle distributions. To do so, we compute $\sigma_{\theta,p}$ from eq. 4.4, which gives $\sigma_{\theta,p} = 2.3°$ for the hydrophobic particles (red curve in fig. 4.5a), and $\sigma_{\theta,p} = 5.5°$ for the hydrophilic ones (red curve in fig. 4.5b).

Our experimental values can now be directly compared to the theoretical broadening. In absence of chemical inhomogeneities and neglecting the line tension effects, the full width at

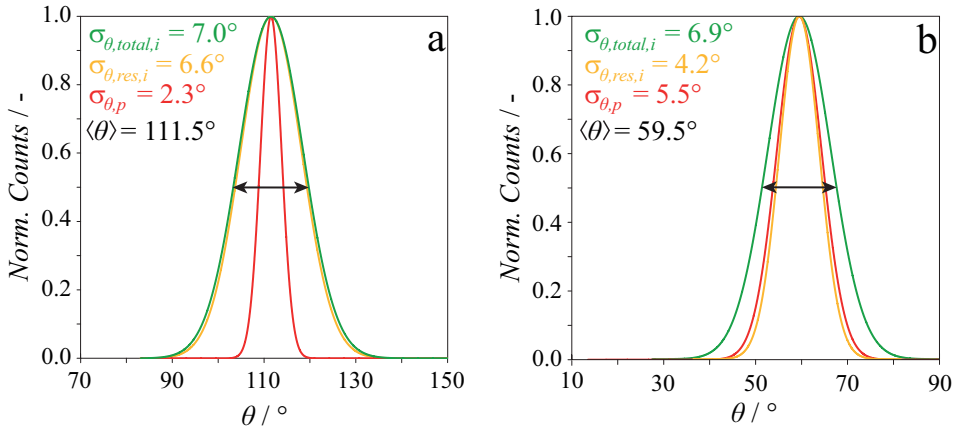

Figure 4.5: Influence of the iPAINT resolution ($\sigma_{\theta,res,i}$), and the variability of the particle position relative to the interface ($\sigma_{\theta,p}$) on determining the contact angle distributions for (a) hydrophobic and (b) hydrophilic particles.

half maximum (FWHM) of the particle position distribution of monodisperse particles with ~300 nm radius is given by FWHM $= 2\sqrt{\ln 2/\beta} = 3\%$, where $\beta = 4\pi R^2\gamma_{o/w}/k_BT$. [23] This translates into a theoretical broadening of the contact angle distributions $\sigma_{\theta,th} = 2°$, which equals $\sigma_{\theta,p}$ for hydrophobic particles after deconvolution of $\sigma_{\theta,total,i}$ (eq. 4.4). By contrast, we have a mismatch between the theoretical and experimental values $\Delta\sigma = \sigma_{\theta,p} - \sigma_{\theta,th} = 3.5°$ for hydrophilic beads. We attribute this discrepancy to the higher affinity of PEG-552 for the hydrophilic silica particles.

4.2.3.1 Two-colour iPAINT imaging

To further improve the accuracy with which $\langle\theta\rangle$ is determined, we decide to utilize multi-colour imaging, using a combination of covalent and non-covalent labelling of the particles and the interface, respectively. To this end, we use amino-functionalized polystyrene particles (R ~250 nm), which are subsequently labelled with a photo-activatable moiety (Cage-635, Abberior®, further details in section 4.4.3). Thus, Cage-635, a red emitting dye, used side by side with PEG-552 provides two-colour imaging as showed in figure 4.6a. From analysis carried out on these particles we retrieve a mean contact angle $\langle\theta\rangle = 47.1° \pm 4.2°$, which corresponds to an adsorption energy $\Delta F = 0.170 \pm 0.01 \times 10^{-15}$ J ($= 0.41 \pm 0.04 \times 10^5$ k_BT). The distribution of contact angles computed results 2.8° narrower than in the single-colour imaging (fig. 4.2). This is because the two-colour imaging makes the ascription of single-molecule localizations either to the beads or to the interface unambiguous.

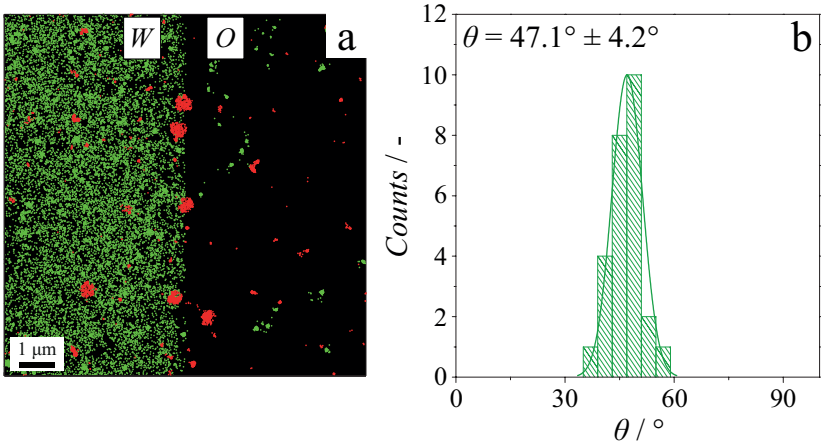

Figure 4.6: Tow-colour imaging of particles at liquid-liquid interface. (a) Polystyrene particles of ~500 nm adsorbed at the water-decane interface. The particles are covalently labelled with a red-emitting photo-activatable dye (Cage-635, $\lambda_{max} = 635$ nm, Abberior®). The iPAINT probes (green dots) are confined in the water phase, and hence used to readily discriminate between the two phases.

4.2.4 Impact of the iPAINT probe on the single-particle contact angle measurement

As a probe in our iPAINT experiments, we utilize a polymer-conjugated photo-activable dye. Its adsorption at the interface reduces the interfacial tension, [38] which in turn affects the measured single-particle contact angle values. To assess the extent of this effect, we perform a number of experiments which are described in the following.

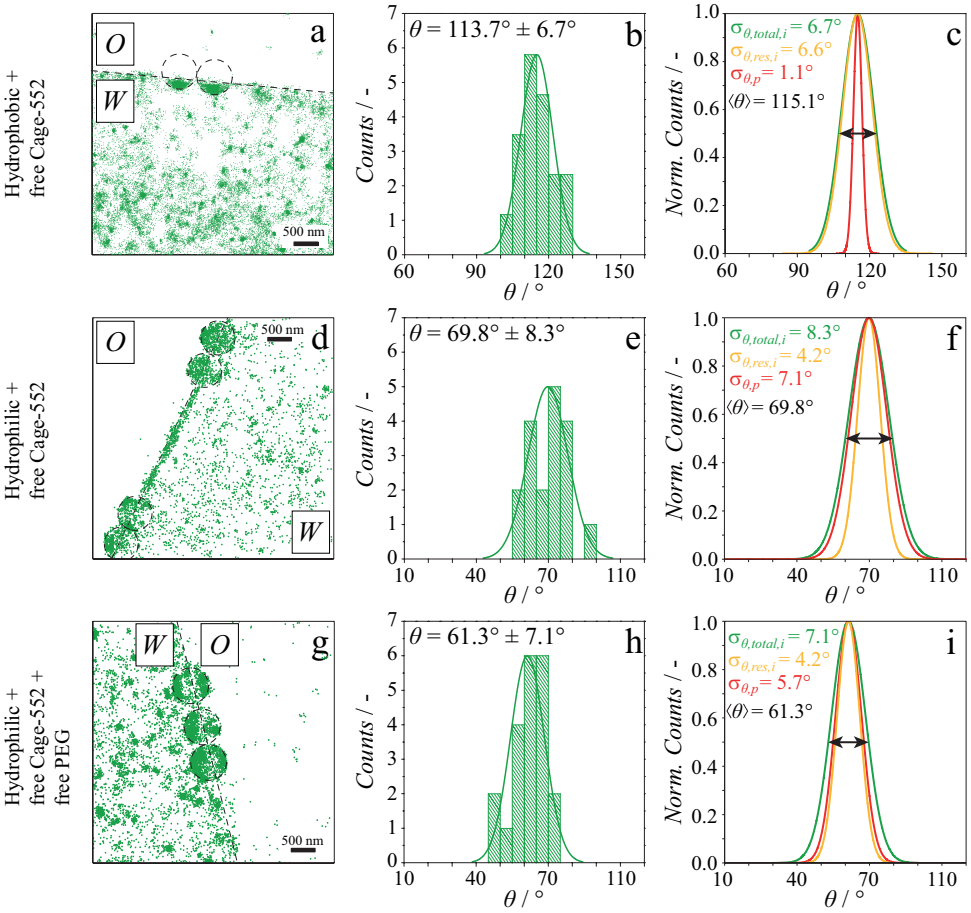

Figure 4.7: Quantification of the effect of iPAINT probes on particles contact angles. iPAINT imaging of hydrophobic (a), hydrophilic (d) particles (black dashed circles) adsorbed at the fluid interface (black dashed line) by using freely diffusing Cage-552 dye. Contact angle distribution of ∼20 hydrophobic (b), and hydrophilic (e) particles adsorbed at the water-octanol interface, and deconvolution of the imaging resolution ($\sigma_{\theta,res,i}$) and particle variability ($\sigma_{\theta,p}$) in the contact angle distribution on hydrophobic (c), and hydrophilic (f) particles. (g) iPAINT imaging by freely diffusing Cage-552 dye of hydrophilic particles in presence of polyethylene glycol (PEG) at the water-octanol interface. (h) Related contact angle distribution of ∼ 20 hydrophilic particles, and (i) subsequent deconvolution of the imaging resolution ($\sigma_{\theta,res,i}$) and particle variability ($\sigma_{\theta,p}$) in the contact angle distribution.

We start off by iPAINT experiments on hydrophobic (fig. 4.7a) and hydrophilic (fig. 4.7d) particles using as a probe the dye itself, Cage-552, instead of the polymer-conjugated dye, PEG-552. As before, the particles can be located with high accuracy at a fluid interface. We determine a mean contact angle for the hydrophobic colloids is $\langle\theta\rangle = 113.7° \pm 6.7°$, which is 2.2° higher than the one reported when using the PEG-552 as a probe ($\langle\theta\rangle = 111.5° \pm 7.0°$). This means that the presence of the polymer slightly affects the system. An even larger difference is observed for the hydrophilic particles: $\langle\theta\rangle = 69.8° \pm 8.3°$ (Cage-552) *vs.* $\langle\theta\rangle = 59.5° \pm 6.9°$ (PEG-552). To test whether this effect originates from the presence of the PEG chains, we image the hydrophilic particles by iPAINT using free Cage-552 and free PEG chains in solution (fig. 4.7g). If the presence of PEG is the key factor, we should retrieve the same contact angle calculated in figure 4.2d. From iPAINT experiments on hydrophilic particles in the presence of Cage-552 and free PEG in solution we obtain $\langle\theta\rangle = 61.3° \pm 7.1°$ (fig. 4.7h). This value is ∼9° lower than the values obtained for Cage-552 (fig. 4.7e, $\langle\theta\rangle = 69.8° \pm 8.3°$) and comparable to that obtained using PEG-552 (fig. 4.2d), suggesting that the difference is due to the interfacial adsorption of PEG.

Since the presence of PEG influences the measured contact angles, it would be better to image with Cage552 instead of PEG552. However, the identification of the two phases is not as neat as when PEG-552 is utilized. In fact, the presence of the polymer as carrier of the photo-activatable moieties confines the probes to diffuse solely in the aqueous phase (∼85 localizations per μm^2 in the water phase *vs.* ∼15 localizations per μm^2 in the oil phase, fig. 4.14d), allowing for a clear identification of the two phases. Conversely, the hydrophobicity of the Cage-552 dye alone reduces its partitioning between the two phases, resulting in similar single-molecule localization densities (∼75 and ∼53 localizations per μm^2 for water *vs.* oil, respectively). This necessitates the application of more stringent density filters to ensure precise visualization of both the interface and the particle positions. Unfortunately, this leads in turn to less localizations per particle, losing their full reconstruction.

4.2.5 Size-dependent contact angles

The advantage of single-particle contact angle measurements is that both the mean and the distribution of the contact angle can be measured accurately. In figure 4.8 we present the contact angle as a function of diameter for hydrophobic (fig. 4.8a) and hydrophilic (fig. 4.8b) particles at the water-octanol interface as determined by iPAINT. For clarity, θ values are averaged for particles differing less than 5 nm in mean diameter (*i.e.*, $\Delta D_{bin} \leq$ 5 nm). We find that θ increases with increasing particle diameter for hydrophobic in the range between 620 nm and 720 nm, and conversely, θ decreases with increasing size for hydrophilic. This is a clear violation of Young's law, which states that contact angles are size-independent.

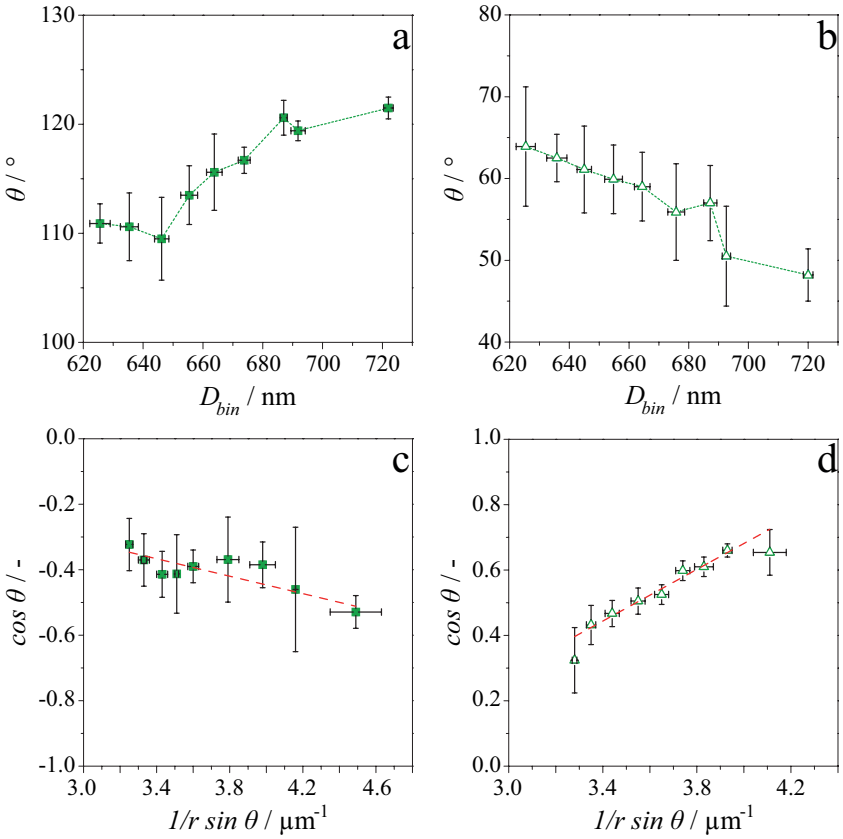

Figure 4.8: Contact angle θ as function of averaged diameters D_{bin} of hydrophobic (closed squares) and hydrophilic (open triangles) particles. The diameters were binned over 5 nm range. (c, d) Line tension evaluation for single particles. $\cos\theta$ vs. $(r\sin\theta)^{-1}$ of single hydrophobic (closed squares) and hydrophilic (open triangles) particles adsorbed at water-octanol interface are plotted. The slopes of the linear fit (0.113 $\pm$ 0.026 for hydrophobic particles, 0.395 $\pm$ 0.036 for hydrophilic particles) are related to the line tension through eq. 4.7.

We attribute these trends for $\langle D_{bin}\rangle$ between 620 nm and 720 nm to non-negligible line tension effects, which can taken into account using the modified Young-Dupré equation:

$$\cos\theta = \cos\theta_{Young} - \frac{\tau}{\gamma_{o/w} r \sin\theta}, \tag{4.7}$$

where, θ_{Young} is the contact angle at the three-phase contact line from the Young equation, and τ is the line tension. In accord with theory, [39,40] we find a linear dependence for both types of particles (fig. 4.8c and 4.8d), from which we obtain values for the line tension τ. This yields τ = 1.13 $\pm$ 0.22 nN for the hydrophobic colloids, and τ = -3.36 $\pm$ 0.31 nN for the hydrophilic colloids, which is well within the range of reported values for τ of 10^{-12} N $< \tau < 10^{-9}$ N for μm-sized particles, as recently reviewed by Bresme and Ottel. [23]

4.3 Conclusions

The single-molecule localization microscopy based method iPAINT is applied to investigate particle-laden liquid-liquid interfaces by simultaneous and *in-situ* imaging of both the interface and the particles through continuous, non-covalent labelling with a polymer-conjugated photo-activatable dye. iPAINT images of hydrophilic and hydrophobic nanoparticles of $\sim$300 nm in radius are obtained with high spatial resolution ($\sim$20 nm) from which mean contact angles and their distributions are determined. The contact angle of both particle types is found to be size-dependent yielding values for the line tension $\tau \sim 10^{-9}$ N in accordance with previous work by others. Furthermore, narrow contact angle distributions are obtained for both hydrophilic and hydrophobic particles after deconvolution. These are in line with theoretical predictions, and less broad than what observed by other experimental single-particle methods, because of the *in-situ* imaging procedure. Therefore, iPAINT greatly simplifies sample handling and experimentation, and it reduces the impact on the broadening of contact angle distributions observed when immobilization techniques (*e.g.*, gel trapping, vitrification) and spreading agents are used.

4.4 Experimental

4.4.1 Synthesis and characterization of silica particles

The synthesis of silica particles, and the SEM imaging has been carried out by dr. N. Vilanova.

Hydrophilic silica beads of ∼300 nm in radius are synthesized using a two-step Stöber-based method. [41] Silica particles with intermediate hydrophobicity are obtained by partially functionalizing them with stearyl alcohol through a modified van Helden method. [42] Briefly, 0.25 g of hydrophilic particles are dispersed by sonication in ethanol together with 0.07 mg of stearyl alcohol and 0.70 g octadecane. Subsequent evaporation of ethanol is achieved under a stream of air. The system is then heated up to 180 °C for 6 hours under an inert atmosphere. Because of the high temperature, the octadecane melts and acts as solvent allowing the stearyl alcohol chains to react with the silanol groups onto the silica colloids. The applied 1:10 ratio alcohol:octadecane ensures incomplete hydrophobization of the particles. The resulting particles are thoroughly washed with chloroform and dried overnight at 70 °C in vacuum. All chemicals are purchased from Sigma-Aldrich and used without further purification.

A FEI Quanta 600F ESEM scanning electron microscope (SEM) is used to image the silica particles. Figure 7.17 shows a SEM image of the colloids, where the inset illustrates the size distribution obtained from image analysis of more than 100 particles. The image analysis is run using Image-J; a mean radius $\langle R \rangle = 332 \pm 14$ nm is computed.

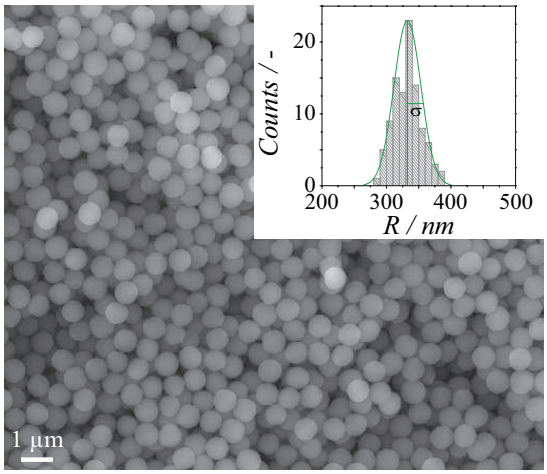

Figure 4.9: Characterization of silica colloids. SEM pictures of plain silica beads of ∼330 nm in radius. In the inset the radii distribution of silica colloids measured for over 100 beads is shown.

4.4.2 Synthesis of PEG-552 probes

1.1 mg of poly(ethylene glycol) bis(amine) (M_W 20 kDa, Sigma Aldrich) is set to react with 20 μL of 10 mM solution of N-hydroxysuccinimide ester activated rhodamine (Cage-552, Abberior®) in 1 mL of 0.1 M sodium bicarbonate buffer at pH 8.5. The reaction mixture is stirred overnight, in the dark, and at room temperature. Subsequently the product is purified by dialysis (Spectra/Por®7 dialysis membrane, pre-treated RC tubing, molecular weight cutoff: 8 kDa) to remove unreacted dye molecules.

4.4.3 Labelling of polystyrene particles

62.5 μL of polystyrene particles 5% w/v (R ∼250 nm) amino-funtionalized (Sperotech®) is diluted in 2.5 ml of 0.1 M sodium bicarbonate buffer at pH 8.5 to which 2.5 μL of 10 mM solution of Cage-635 in DMSO is added. The system is kept under stirring overnight and at room temperature. The reaction mixture is subsequently purified by dialysis (Spectra/Por®7 dialysis membrane, pre-treated RC tubing, molecular weight cutoff: 8 kDa) to remove unreacted dye molecules. The particles are stored in MilliQ-water (18.2 MΩ).

4.4.4 Sample preparation

Stock solutions of 0.6 mg/mL hydrophilic and hydrophobic particles are prepared by dispersion in 10^{-5} M aqueous solution of the iPAINT dye PEG-552 and octanol, respectively. For iPAINT imaging on the hydrophobic particles, a 15 μL droplet of the particle stock solution is placed onto a coverglass (Menzel Gläser, 76 × 26 mm, thickness 1 mm) next to a 15 μL droplet of aqueous solution of the iPAINT dye PEG-552 (10^{-5} M). The sample is sandwiched between the coverglass and a coverslip (Menzel Gläser, No. 1.5, 24 × 24 mm, thickness 170 μm) using double-sided tape (∼90 μm) as depicted in figure 4.10a. iPAINT imaging on hydrophilic beads is carried out similarly by placing a 15 μL droplet of pure octanol side by side to a 15 μL droplet of the hydrophilic silica beads dispersed in the iPAINT dye PEG-552 solution. Prior to sample preparation, the coverslips are treated beforehand with piranha etching to remove impurities, which reduces background fluorescence. Solvent evaporation is not encountered during image acquisition due to the short imaging time-lapses (∼20 min for a 256 × 256 pixels field of view).

Being normal to the focal plane, and squeezed between two surfaces, the oil-water interface appears μm-wide, depending on the angle of the *quasi*-TIRF illumination adopted in the experiment. This is because the interfacial plane is not perfectly normal to the coverglass along the entire thickness of the spacers used. In other words, the interface is somewhat curved on $\gg \mu$m lengthscales. However, the angle in the *quasi*-TIRF is set to illuminate the

first μm's of the interface in contact with the coverslip. In this small penetration depth of the laser, we can assume that the interface is normal to the coverslip (fig. 4.10).

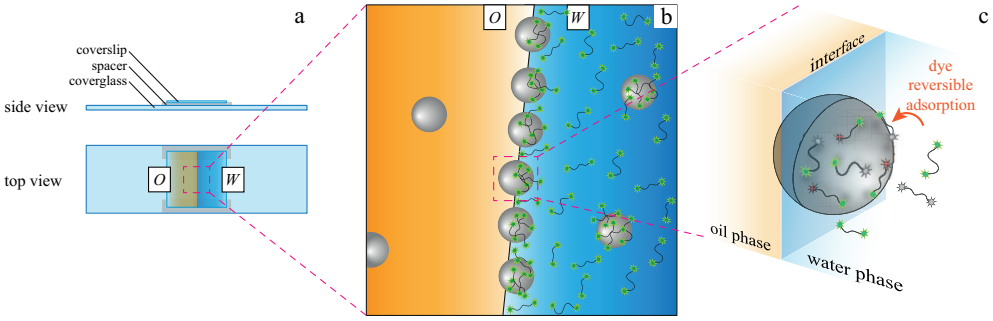

Figure 4.10: Schematic illustration of a fluid cell for iPAINT imaging of particles at a fluid interface. (a) Side and top view of the assembled chamber made out of a coverglass, double-sided tape and a coverslip. The two liquids are put into contact to create an interfacial plane normal to the coverglass. (b) Cartoon depicting colloidal particles adsorbed at the fluid interface between the water phase, rich in PEG-552 (green probes), and the oil phase. (c) Zoom-in on a particle adsorbed at the fluid interface in 3D.

4.4.5 Microscopy

iPAINT images are acquired using a Nikon Eclipse Ti-E N-STORM system supplied by ~488.0 mW/cm^2 (λ = 561 nm) and ~160.0 mW/cm^2 (λ = 405 nm) laser lines set for *quasi*-total internal reflection fluorescence (TIRF) imaging. The TIRF angle is adjusted to maximize the signal-to-noise ratio. The fluorescence signal is collected through a Nikon 100×, 1.4 NA oil immersion objective and filtered by a quad-band pass dichroic mirror (97335 Nikon). The region of interest used to acquire the time-lapses is set to 256 × 256 pixels of an ixon3, Andor EMCCD camera (pixel size 170 nm) at a frame rate of 47 frames/s. The adsorption of the iPAINT probes at the fluid interfaces is collected over 5 × 10^4 frames in each acquisition; the PEG-552 probes are continuously photo-activated with a low power UV laser (405 nm, 0.5% power), excited and subsequently bleached using a 561 nm laser (100% power). Single-molecule localization movies are analysed with NIS-element Nikon software.

4.4.6 Calculation of contact angle of individual spherical particles

We use two different strategies to compute the contact angle, θ, for the hydrophobic and hydrophilic particles. In the case of hydrophobic particles, only the hemisphere exposed to the water phase is labelled by PEG-552 probes, and hence visible. Here, the principal dimensions which can be determined from iPAINT images are the height, h, and the lateral size, $2a$ (fig. 5.12). We can calculate from trigonometry the radius of the particle, R, according to eq. 4.8.

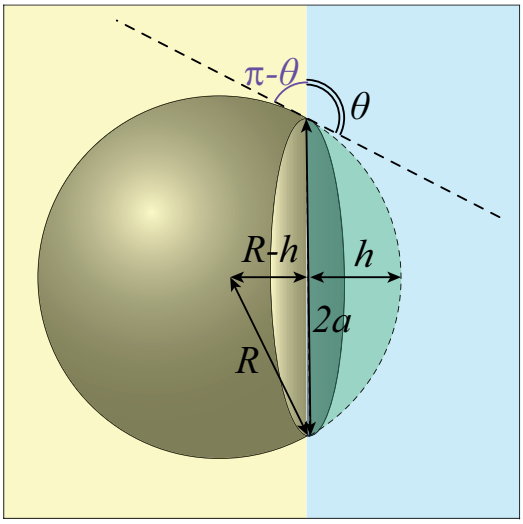

Figure 4.11: Representative cartoon of an hydrophobic spherical particle at a fluid interface. The dimensions needed to calculate the contact angle are illustrated by the double-arrowed segments in black and summarized in eq. 4.8.

$$(R-h)^2 = R^2 - a^2. \tag{4.8}$$

The measured h and the calculated radii, R, are then used in eq. 4.2 to compute the contact angle for each single hydrophobic particle.

Conversely, the hydrophilic particles are completely labelled since they are dispersed in the water phase along with the PEG-552. In this case, we isolate the particles based on the density of single-molecule localization (further details in section 4.4.7.2, fig. 4.14), and proceed to fit the particle to a circle (Matlab exchange file 'Circle Fit') as previously described in chapter 2. The fit gives the (*x*,*y*) coordinates of the center of the particle, and its radius. To determine the position of the particle compared to the interface we first select the single-molecule localizations which belong to the interface (further details in section 4.4.7.2, fig.

4.14). By sectioning across the interface (fig. 4.12a red rectangles), the localizations appear to follow a Gaussian profile (fig. 4.12b), and its mean value is taken as the most probable location of the interface. This procedure is applied all along the interface (every ∼20 nm interval) to determine its profile. By overlapping the profile of the interface with the position of the particles (fig. 4.12c) we can calculate h, the height of the hydrophilic particles in the oil phase. The computed values of h, and the radii of the particles obtained from the 2D fit are subsequently used in eq. 4.3 to calculate the contact angle, θ.

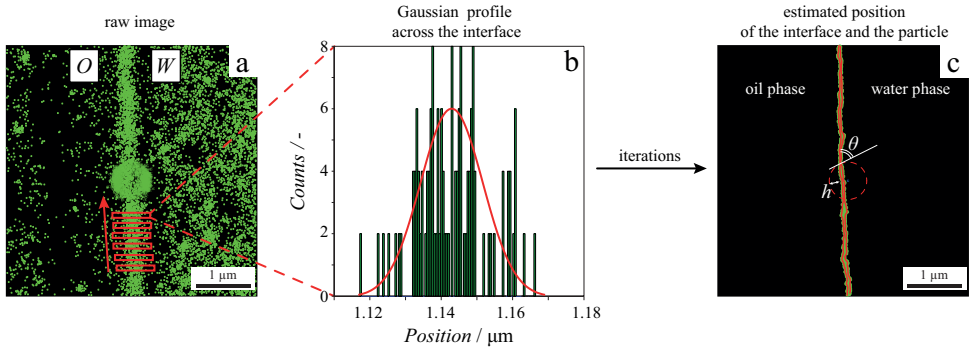

Figure 4.12: Analysis routine to compute the contact angle of hydrophilic particles at a fluid interface. (a) Representative iPAINT image of an hydrophilic particle adsorbed at a fluid interface. The red rectangles illustrates the sectioning across the interface, along the red arrow, to determine its location. (b) Distribution of localizations in one of the red rectangles presented in (a); the mean value gives the most probable location of the interface. (c) Reconstructed interface, and placement of the circle fitting the particle. From (c) the height, h, of the particle in the oil phase is calculated, giving in turn the contact angle, θ.

In the case of hydrophobic particles the error on the size distribution of the radius of the particles is higher than the one computed for the hydrophilic particles due to the method used to calculate R. In fact, for the hydrophobic particles we have to consider the errors on the determination of h and $2a$. Whereas, for the hydrophilic particles the error comes from the fitting routine run in Matlab.

4.4.7 Precise localization of the position of the interface and the particles

4.4.7.1 Monitoring the sliding of the interface towards the steady-state

Accurate particle and interface localization necessitates imaging under stable conditions. To this end, we first determine the position of the interface by wide-field imaging, after which we monitor the sliding of the interface during the transition towards the steady-state. This serves as a test of potential pinning of the interface on the coverslip due to particle adsorption and enables us to determine the time it takes to reach steady-state conditions. We prepare a

sample by bringing into contact a droplet of the aqueous solution of particles and PEG-552 and an oil droplet. The location of the interface is determined from an intensity profile of a wide-field image of the two liquids in contact (fig. 4.13).

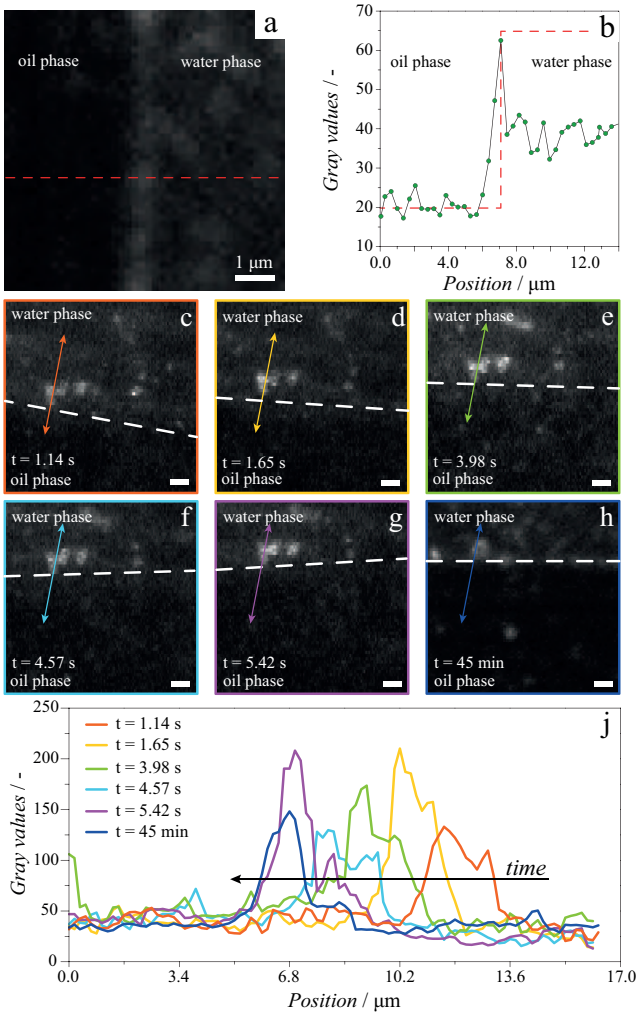

Figure 4.13: Identification of the fluid interface and its sliding. (a) Wide-field image of the oil-water interface. The water phase is rich in PEG-552 probes and hence fluorescent; the oil phase appears darker. (b) Intensity profile along the dashed red line in (a); from the gray values the position of the interface can be defined. (c-h) Wide-field images of hydrophilic colloidal particles adsorbed at the water-octanol interface visualized over ∼45 min. The dashed white line indicates the position of the fluid interface, between the aqueous and the octanol phases. The double-arrowed line indicates the direction along which the fluorescence intensity traces presented in (j) have been recorded. (j) Fluorescence intensity signal along the double-arrowed line as a function of pixel position.

The aqueous phase, oil phase, and interface, can be distinguished in the fluorescence intensity profile based on their grayscale values (fig. 4.13b), which is maximal at the interface ($\sim$60) and lower in the respective bulk phases, water ($\sim$40) and oil ($\sim$20). This method enables interface localization with a $\sim$1 μm accuracy (fig. 4.13b). Next, we collect the time-lapse images of the particles and interface in wide-field (fig. 4.13c-h), and monitor the sliding of the interface (greyscale value $\sim$60) and adsorbed particles (greyscale value $\sim$150-200) during 45 minutes. We observe the motion of the interface (white dashed line in fig. 4.13c-h) and the particles thereby adsorbed moving in the same direction in time. To trace the correlated motion of the interface and the particles thereby adsorbed, we measure the fluorescence intensity profiles along the double-arrowed lines shown in figure 4.13c-h, and plot them as function of their position (fig. 4.13j). The uni-directional motion of interface and particles demonstrates that the interface is not pinned. Instead, both the particles and the interface can adjust their position and transition towards a stead-state condition. We monitor the sliding of the interface and the particles during 45 minutes to determine how long it takes to reach steady-state. we find the interface at similar positions at $t = 5.42$ s and $t = 45$ min, suggesting that steady-state is reached within a few seconds after sample preparation. To be certain iPAINT imaging is performed under steady-state conditions, we nevertheless initiate image acquisition 1 hour after sample preparation.

4.4.7.2 Precise identification of the fluid interface, particles and liquid phases

Once the system has reached the steady-state, we can determine the precise position of the fluid interface and the single particles from an iPAINT image, based on the number of localized single molecules. An exemplary iPAINT image is shown in figure 4.14a. First, we calculate the density of single-molecule localizations for the particles, the interface and the liquid phases. Then, we sort them applying density filters based on these values. Subsequently, we save each subset of single-molecule localizations to define the precise positions of the particles and the interface.

To this end, an area (red dashed area in fig. 4.14a) as wide as one particle ($\sim$700 nm) and $\sim$10 μm long, extending up to $\sim$5 μm into the oil and the water phase, respectively, is considered. Then the overall density of localizations is plotted (fig. 4.14b). From hundreds of these data sets, we compute the mean density of single-molecule localizations for particles, interface, water and oil phase. We report a density of $\sim$2500 localizations per μm^2 for the particles (fig. 4.14c, red bar), $\sim$160 localizations per μm^2 for the interface (fig. 4.14c, green bar), $\sim$85 localizations per μm^2 in the water phase (fig. 4.14c, blue bar), and as low as $\sim$15 localizations per μm^2 in the oil phase (fig. 4.14c, yellow bar).

We can use these density parameters to display only the localizations with $> n$ neighbours within a certain range δ. We then remove those localizations which do not fulfill the set

parameters. In this way we first visualize only the dye molecules adsorbed onto the particle surfaces (fig. 4.14d, top row), since are the most densely labelled. We use this set of localizations to precisely determine the position of the particles. Then, we continue with less dense localizations to identify the position of the interface (fig. 4.14d, second row), the water phase (fig. 4.14d, third row) and finally the oil phase (fig. 4.14d, bottom row). We are now able to locate the position of the interface with ∼20 nm accuracy, which is 50-fold better than the 1 μm localization accuracy obtained in wide-field.

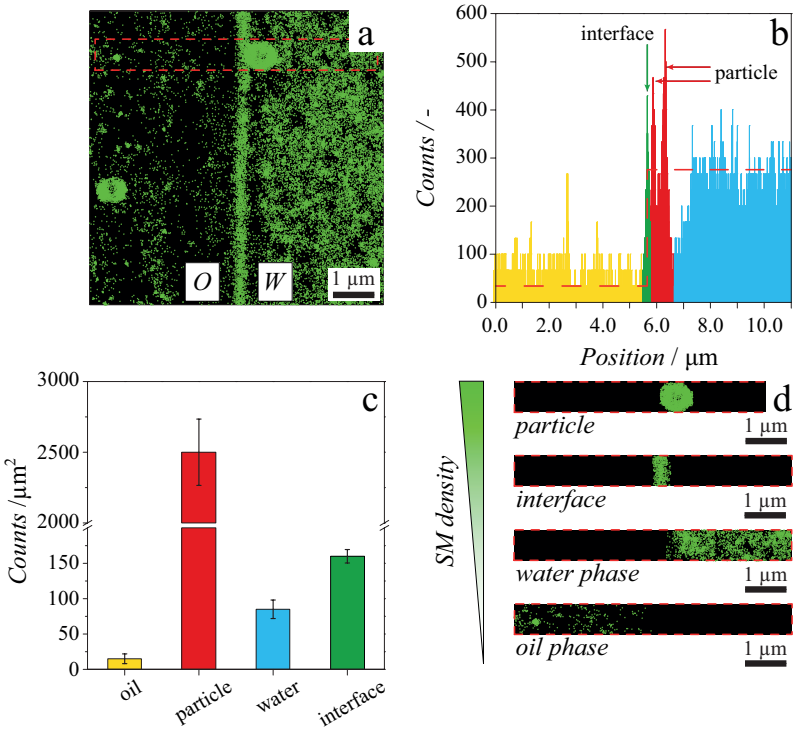

Figure 4.14: Counts-based identification of interface and particles' positions. (a) Super-resolved image of an oil-water interface. The water phase is rich in PEG-552 probes and hence fluorescent (green localizations); the oil phase appears darker. The silica beads are initially dispersed in the water phase and consequently labelled by PEG-552. (b) Number of single-molecule localizations along the dashed red line in (a) showing clear differences in PEG-552 localizations collected in the oil (yellow) and water (blue) phases, at the interface (green), and finally on the particle surfaces (red). (c) Single-molecule localizations identified in the red dashed area in (a) after applying different density filters and sorting of localizations. (d) Quantification of the counts for the oil phase, the interface, the water phase and the particle based on the separated datapoints displayed in (c).

Bibliography

[1] Cosgrove, T. *Colloid Science: Principles, Methods and Applications* **2010**, 2nd ed., Wiley, UK.

[2] Pickering, S.U. *J. Chem. Soc. Trans.* **1907**, *91*, 2001.

[3] Ramsden, W. *Proc. R. Soc.* **1903**, 72, 156.

[4] Dinsmore, A.D.; Hsu, M.F.; Nikolaides, M.G.; Bausch, A.R.; Marquez, M.; Weitz, D.A. *Science* **2002**, *298*, 1006.

[5] Bormashenko, E. *Curr. Opin. Colloid Interface Sci.* **2011**, *16*, 266.

[6] Herzig, E.M.; White, K.A.; Schofield, A.B.; Poon, W.C.K.; Clegg, P.S. *Nat. Mater.* **2007**, *6*, 966.

[7] Barratt, G. *Cell. Mol. Life Sci.* **2003**, *60*, 21.

[8] Pera-Titus, M.; Leclercq, L.; Clacens, J.-M.; De Campo, F.; Nardello-Rataj, V. *Angew. Chem. Int. Ed.* **2015**, *54*, 2006.

[9] Silva, B.F.B.; Rodrìguez-Abreu, C.; Vilanova, N. *Curr. Opin. Colloid Interface Sci.* **2016**, *25*, 98.

[10] Miller, R.; Liggieri, L. *Interfacial rheology* **2009**, Brill, Leiden.

[11] Preuss, M.; Butt, H.J. *J. Colloid Interface Sci.* **1998**, *208*, 468.

[12] Horozov, T.S.; Braz, D.A.; Fletcher, P.D.I.; Binks, B.P.; Clint, J.H. *Langmuir* **2008**, *24*, 1678.

[13] Isa, L.; Lucas, F.; Wepf, R.; Reimhult, E. *Nat. Commun.* **2011**, *2*, 1.

[14] Fung, J.; Perry, R.W.; Dimiduk, T.G.; Manoharan, V.N. *J. Quant. Spectrosc. Radiat. Trans.* **2012**, *113*, 212.

[15] Snoeyink, C.; Barman, S.; Christopher, G.F. *Langmuir* **2015**, *31*, 891.

[16] Mable, C.J.; Warren, N.J.; Thompson, K.L.; Mykhaylyk, O.O.; Armes, S.P. *Chem. Sci.* **2015**, *6*, 6179.

[17] Pieranski, P.I. *Phys. Rev. Lett.* **1980**, *45*, 569.

[18] Squires, T.M.; Mason, T.G. *Annu. Rev. Fluid Mech.* **2010**, *42*, 413.

[19] Peng, Y.; Chen, W.; Fischer, T.M.; Weitz, D.A.; Tong, P. *J. Fluid Mech.* **2009**, *618*, 243.

[20] Fischer, T.M.; Dhar, P.; Heinig, P. *J. Fluid Mech.* **2006**, *558*, 451.

[21] Cubaud, T.; Mason, T.G. *Phys. Fluids* **2008**, *20*, 053302.

[22] Anna, S.L. *Annu. Rev. Fluid Mech.* **2016**, *48*, 285.

[23] Bresme, F.; Ottel, M. *J. Phys.: Condens. Matter* **2007**, *17*, 413101.

[24] Binks, B.P.; Isa, L.; Tyowua, A.T. *Langmuir* **2013**, *29*, 4923.

[25] van Rijssel, J.; van der Linden, M.; Meeldijk, J.D.; van Dijk-Moes, R.J.A. *Phys. Rev. Lett.* **2013**, *111*, 108302.

[26] Vogel, N.; Ally, J.; Bley, K.; Kappl, M.; Landfester, K.; Weiss, C.K. *Nanoscale* **2014**, *6*, 6879.

[27] Paunov, V.N. *Langmuir* **2003**, *19*, 7970.

[28] McBride, S.P.; Law, B.M. *Phys. Rev. Lett.* **2012**, *109*, 196101.

[29] Sabapathy, M.; Kollabattula, V.; Basavaraj, M.G.; Mani, E. *Nanoscale* **2015**, *7*, 13868.

[30] Aloi, A.; Vilanova, N.; Albertazzi, L.; Voets, I.K. *Nanoscale* **2016**, *8*, 8712.

[31] Aloi, A.; Guibert, C.; Olijve, L.L.C.; Voets, I.K. *Polymer* **2016**, *107*, 450.

[32] Huang, B.; Wang, W.; Bates, M.; Zhuang, X. *Science* **2008**, *319*, 810.

[33] Maestro, A.; Bonales, L.J.; Ritacco, H.; Rubio, R.G.; Ortega, F. *Phys. Chem. Chem. Phys.* **2010**, *12*, 14115.

[34] Demond, A.H.; Lindner, A.S. *Environ. Sci. Technol.* **1993**, *27*, 2318.

[35] Zanini, M.; Isa, L. *J. Phys.: Condens. Matter* **2016**, *28*, 313002.

[36] Kaz, D.M.; McGorty, R.; Mani, M.; Brenner, M.P.; Manoharan, V.N. *Nat. Mater.* **2012**, *11*, 138.

[37] Hogg, R.V.; McKean, J.W.; Craig, A.T. *Introduction to Mathematical Statistics* **2006**, 6th ed., Pearson, UK.

[38] Cohen Stuart, M.A.; de Vos, W.M.; Leermakers, F.A.M. *Langmuir* **2006**, *22*, 1722.

[39] Aveyard, R.; Clint, J.H. *J. Chem. Soc. Faraday Trans.* **1996**, *92*, 85.

[40] Good, R.J.; Koo, M.N. *J. Colloid Interface Sci.* **1979**, *71*, 283.

[41] Vilanova, N.; de Feijter, I.; Voets, I.K. *J. Vis. Exp.* **2016**, *110*, e53934.

[42] van Helden, A.K.; Jansen, J.W.; Vrij, A. *J. Colloid Interf. Sci.* **1981**, *81*, 354.

Chapter 5

Ellipsoidal nanoparticles at fluid interfaces: interfacial deformations revealed by iPAINT microscopy

Anisotropic particles straddling two immiscible liquids deform the fluid interface by pulling the liquid upward along the major axis and downward at the particle tips. The induced deformations create an excess of interfacial area, which can be minimized if the particles assemble, such that their deformations overlap. This is the origin of capillary forces, which are widely exploited in particle self-assembly. To date, however, methods to simultaneously visualize adsorbed ellipsoidal particles and the associated interfacial deformations were unavailable. Here we employ the newly-developed method iPAINT to 'stain' the ellipsoidal particles and the interface. This allows us to, for the first time, image the position of the particles, the interface onto which they adsorb, and the interfacial deformations thereby induced, simultaneously and *in-situ*.

5.1 Introduction

Anisotropic geometries are ubiquitous. Examples spanning order of magnitude in length-scales range from planets spinning in the solar system following elliptical orbits, to wood fibers with properties strongly dependent on the grain orientation, till the elusive interaction of molecular dipoles with polarized light. As a consequence of the broken symmetry, behaviour is often more diverse and complex. In the colloidal domain, anisotropy may refer to shape and/or surface chemistry, *i.e.*, a non-uniform distribution of *e.g.*, tethered moieties on the particle surface. [1] Various consequences of anisotropic particle shapes in the colloidal domain have been reported. Elliptical particles assemble into different lattices than spherical particles at fluid interfaces. [2, 3] This is of potential interest in coating technologies and ink-jet printing. [4, 5] Furthermore, anisotropic particle enhance the stability of Pickering-Ramsden emulsions [6, 7] compared to spherical particles of similar dimensions. [3] Dispersions of ellipsoids, and mixed dispersions with ellipsoidal and spherical particles can suppress undesired phenomena which occur during drying processes, such as the coffee-ring effect. [8–10] This is due to a more loose packing, with more open and aggregated structures. [11–13]

In this chapter we study the orientation and the position of ellipsoidal particles at a liquid-liquid interface, focusing specifically on the interfacial deformations they induce. Indeed, it is well-known that anisotropic particles must bend the fluid interface to which they are adsorbed to locally satisfy the Young's equation as the particle's curvature is not uniform. [14, 15] Hence, ellipsoidal particles should pull up the liquid along the major axis, and push it down at their tips, as schematically drown in figure 5.1. [11, 14, 16]

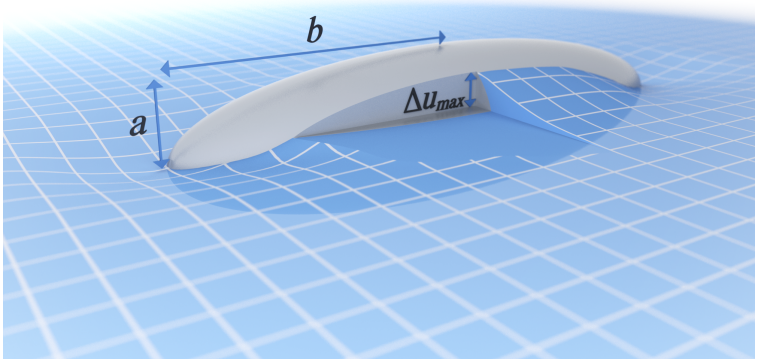

Figure 5.1: Schematic of deformations induced by an ellipsoidal particle at a fluid interface. The three-phase contact line around the ellipsoid is pulled down at the tips and lifted up along the major axis. Δu_{max} is the maximum displacement of the three-phase contact line.

Theory further predicts how these interfacial deformations give rise to capillary

interactions, [14,17] and are related to the extent of particle anisotropy, [18] and particle orientation at the interface. [19–21]

Aiming to stringently test the newly developed theories and understand the macroscopic behaviour of Pickering emulsions, various technologies were developed to measure single-particle contact angles at liquid-liquid interfaces, visualize interfacial deformations, and measure pair-interaction potentials between particles. Among these are interferometric microscopy, [22,23] gel-trapping (GTT) in combination with electron microscopy, [24] or AFM, [25] freeze-fracture shadow-casting (FreSCa), [26,27] and intra-pair magnetophoresis. [28,29] Some of these are suitable for small colloids, including nanoparticles, while others necessitates large particles sizes. Interferometric microscopy, for example, enables measurements of the deformation of the interface induced by single ellipsoids of several tens of μm's in length. GTT and FreSCa allows to determine with high spatial resolution the position of single ellipsoidal particles of $\sim\mu$m in length. None of these methods, however, monitors the interfacial deformations, [22,23] particle position, [24–27] orientation and assembly [16] simultaneously and *in-situ*. Instead, either the interface cannot be localized *in-situ* or the sample should be treated for further analysis.

To overcome these drawbacks, we utilize iPAINT (interface Point Accumulation for Imaging in Nanoscale Topography) microscopy, a newly-developed method in super-resolution imaging. [30] In iPAINT, interfaces are reversibly 'stained' through the physisorption of photo-activatable probes. Here we use poly-ethylene glycol funtionalized with a photo-activatable moiety (PEG-552). Upon UV-light exposure, these probes can be selectively switched from a dark to a bright state, [31] allowing for single-molecule localization with $<$ 20 nm spatial accuracy. In stark contrast with other experimental techniques, iPAINT enables simultaneous visualization of the fluid interface and the adsorbed ellipsoidal particles, such that local deformations can be imaged directly *in-situ* without manipulation of the interface.

In this chapter, we measure the contact angle (θ) of $>$ 30 ellipsoidal particles laying flat at the decane-water interface by iPAINT. We also observe $>$ 20 particles in an 'arrested' configuration, namely oblique to the interface, which we characterize by their polar angles (φ). These measurements of the wetting behaviour and orientation of individual particles reveals pivoting of the ellipsoids, which we attribute to pinning of the three-phase contact line. Next, we visualize the interface deformations induced by the adsorbed particles, which depend on their orientations in the near- and far-field. Finally, the snapshots taken by iPAINT of the 'arrested' configuration adopted by the particles allows to compute the pair-potential interaction between two particles in a particular 'arrested' configuration (*e.g.*, tip-to-tip or side-by-side relative orientation at a given 'arrested' interparticle separation).

5.2 Results and discussion

5.2.1 Visualization of ellipsoidal particles at fluid interfaces by iPAINT microscopy

To test whether iPAINT microscopy can be used to characterize the wetting behaviour of anisotropic particles at fluid interfaces, we attempt to image prolate ellipsoids at decane-water interface. The μm-sized, polystyrene ellipsoids have a semi-major axis $b = 1043 \pm 71$ nm and semi-minor axis $a = 215 \pm 16$ nm (fig. 5.1), and an aspect ratio $AR = 4.9 \pm 0.5$ (see section 5.4.1 for details). A computation of the Bond number ($Bo \sim 4 \times 10^{-4}$), and capillary length ($L_c = 20$ μm) for the selected experimental system reveals that gravitational forces can be neglected and the adsorbed particles interact through capillary forces (see section 5.4.5).

To benefit from the higher spatial resolution in the later plane ($\sim$17 nm) than in the axial direction ($\sim$80 nm), [32] we prepare the sample such that the decane-water interface is oriented normal to the focal plane. To this end, sample are prepared as follows. First, the ellipsoidal particles and the PEG-552 probes are dispersed in the water phase, and contacted with the decane phase on top of a microscope coverslip (details in section 5.4.3). Image acquisition commences once the particles have adsorbed at the interface, and settled onto the glass coverslip. As such, the iPAINT images represent a snapshot of the system under scrutiny.

In an iPAINT experiment, the PEG-552 probes are localized only when bound to interfaces. This is because, in comparison to the acquisition rate of the camera ($\sim$50 frames/s), their fast diffusion in bulk aqueous solution precludes their detection. Therefore, the surface of the ellipsoidal particles and coverslip in contact with the water phase are 'stained' with PEG-552. These show up in the exemplary iPAINT images in figure 5.2 as regions of dense single-molecule localizations. Since the oil phase is virtually devoid of water-soluble PEG-552, it appears dark.

iPAINT images of > 50 particles adsorbed at a decane-water interface are collected at room temperature. Illustrative reconstructions are shown in figure 5.2. We take a similar approach as described in chapter 4 to identify the ellipsoids position respect to the interface, and use the α-shape reconstruction algorithm [33] to determine the perimeters of both the interface and the particles. We observe ellipsoids laying parallel to the interface (fig. 5.2a), as well as normal and oblique orientations (fig. 5.2b). The anisotropic particles oriented with their major axis parallel to the interface are considered in the equilibrium configuration. [14, 34] Indeed, it is well-known that gravitational forces are negligible when the surface free energies dominate the overall free energy of the system, and a reduction in oil-water interfacial area

is favourable. [35] This has been observed experimentally in FreSCa images, where all the ellipsoids are laying flat at the interface. [27] Conversely, the ellipsoids observed oblique to the interface are captured in an 'arrested' configuration, forced by the settling of the particles on the coverslip while reaching the interface from the water phase. To better characterize these configurations, we take a close look at the particles orientations.

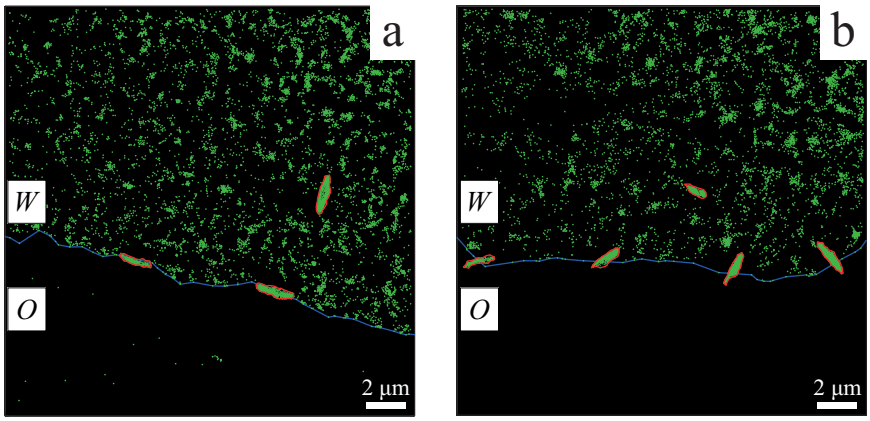

Figure 5.2: Ellipsoids at fluid interfaces imaged by iPAINT. (a) Polystyrene ellipsoidal particles laying parallel and (b) obliquely at the water-decane interface. Both iPAINT probes and ellipsoids are dispersed in the aqueous phase, therefore the entire colloids are homogeneously labelled (green dots). The red line along the ellipsoids perimeter and the blue line to define the interface are obtained by α-shaping. [33]

5.2.2 Quantifying the orientation of ellipsoids at the liquid-liquid interface

First, we set out to unambiguously define the orientation of the ellipsoids at the fluid interface using the polar angle, φ. This corresponds to the angle between the interface and the major axis of the particle (fig. 5.3a-c). For particles laying flat at the interface we can also define a contact angle, θ, as the angle between the liquid-liquid interface and the tangent to the particle surface at the three-phase contact line position (fig. 5.4a).

We consider particles with -5° $< \varphi <$ 5° to be oriented parallel to the interface (fig. 5.3a and 5.3d), while 85° $< \varphi <$ 95° are taken as normal to the interface (fig. 5.3b and 5.3e). All the φ values not included in the intervals mentioned before are considered oblique (fig. 5.3c and 5.3f). Note that we use a minimal interval of 10° in view of the experimental resolution of ∼3° due to the ∼20 nm lateral resolution in iPAINT.

Applying the above described classification on iPAINT images of ellipsoidal particles at decane-water interface, it reveals that most ellipsoids ($>$ 30 examples) lay parallel, as expected. Roughly 9% is aligned normal ($<$ 5 cases), while ∼36% is in the 'arrested' oblique

orientation (20 particles). The distribution of polar angles for each orientation is also of interest (fig. 5.3g). The parallel ellipsoids display a narrow distribution with a standard deviation of $\pm 2.2°$ around a mean value $\langle\varphi\rangle = 2.8°$. The polar angle distribution of particles normal to the interface is peaked at $91.4° \pm 2.6°$. The oblique particles, on the other hand, exhibit a broad distribution of polar angles spanning from $99° < \varphi < 153°$.

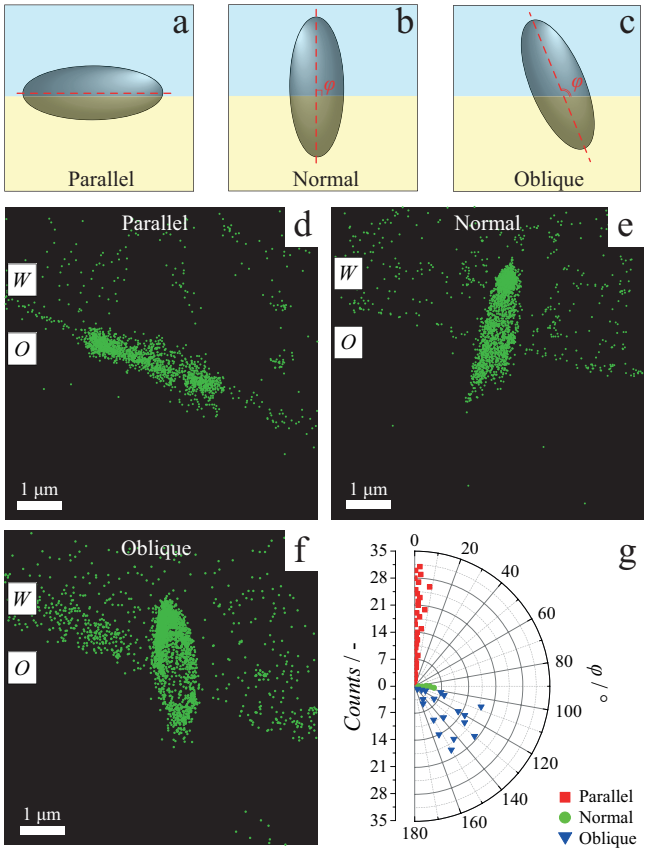

Figure 5.3: Orientation of ellipsoidal particles at the fluid interface. (a-c) Schematic illustrations of ellipsoids oriented parallel, normal and oblique to the oil-water interface. (d-f) Exemplary iPAINT images of ellipsoids oriented parallel, normal and oblique to the water-decane interface. The long axis of the ellipsoids gives the orientation respect to the interface; within a range of $\pm 5°$ (larger than the resolution of the iPAINT method) we discriminate among different orientations. (g) Quantification of the parallel (red closed squares), normal (green closed circles) and oblique (blue closed triangles) ellipsoids as a function of their orientation φ. The absolute value of φ is displayed for the parallel ellipsoids.

The results of the iPAINT experiments on particles laying flat at the interface can be directly compared to FreSCa measurements previously reported by Coertjens *et al.*. We obtain a mean contact angle $\langle\theta\rangle = 42.7° \pm 6.1°$ (fig. 5.4b) for ellipsoids parallel to the fluid interface with the same surface chemistry and aspect ratio, which is somewhat lower than the values from FreSca ($\langle\theta\rangle = 66° \pm 12°$). [27] Interestingly, oblique particles have been

already observed in FreSCa measurements, [36] but their polar angle was not quantified as their dimensions and orientation could not be determined. In fact, in FreSCa images part of the particles is submerged in the vitrified phase (water phase), preventing to determine the full dimensions of the particle. This in turn leads to the impossibility of quantify their polar angle. *Vice versa*, iPAINT microscopy allows for full visualization of the particles across the interface, since the latter is normal to the focal plane. This grants the precise quantification of each dimension of the particles. Since the ellipsoidal particles with an oblique orientation are 'arrested' at the interface at different times, we can compile all the orientations observed to qualitatively describe how the particles reach the interface, and compare it to theoretical studies on their approaching.

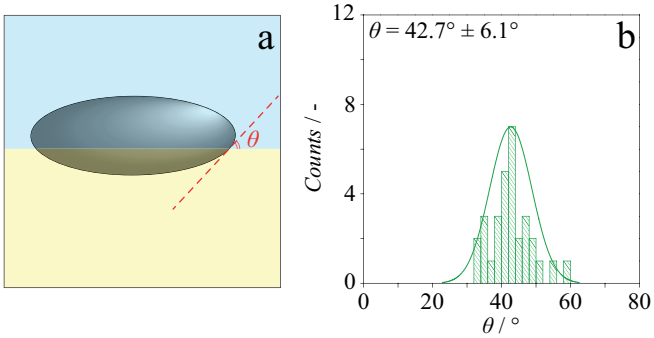

Figure 5.4: Contact angle θ measurements of individual ellipsoids laying flat at a fluid interface. (a) Schematic representation of a parallel ellipsoid at an oil- water interface. The schematic highlights the three-phase contact angle θ. Partial wetting of the ellipsoid by water occurs when $\theta < 90°$ and the center of the mass of the particle resides in the water phase. (b) Distribution of contact angles of oblique and parallel ellipsoids. A full description of the computation of θ from iPAINT images is reported in section 5.4.6.

5.2.3 Pivoting of ellipsoidal particles at the interface

In the previous sections we explained that iPAINT offers a unique vista into the adsorption behaviour of anisotropic particles at liquid-liquid interfaces. For the first time, we have been able to quantify the single-particle polar angles of ellipsoids in the 'arrested' oblique orientation at a decane-water interface with high precision. Since parallel orietations are energetically favoured, we now take a look at the distribution of polar angles, φ, aiming to elucidate the reason for the occurrence of the oblique orientations. It is conceivable that these result from pinning and reflect the trajectory that ellipsoids travel before reaching their equilibrium position parallel to the fluid interface (fig. 5.5a). To test this idea, we plot φ *vs.* the distance to the interface of the center of mass, z_{CM}. These quantities are related to the translational (z_{CM}) and rotational (φ) motion of the particles. Interestingly, we find a linear relation between φ and z_{CM} (fig. 5.5b), as predicted for particles that pivot at the interface

due to pinning of the three-phase contact line which exerts a tangential force on the particle. Wang *et al.* previously observed such pivoting of ellipsoids at a fluid interface by holographic microscopy. [37] The authors attributed the linear dependence of φ on z_{CM} to the pinning of the interface on defects on the surface of rough sulfate-functionalized polystyrene particles of $\sim$2 μm in length. [38–40]

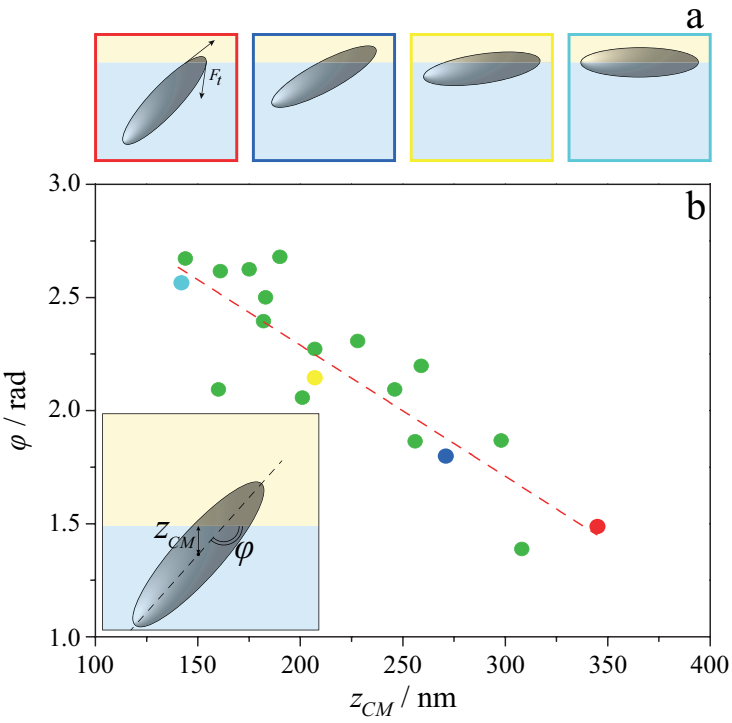

Figure 5.5: Polar angle φ of oblique ellipsoids *vs.* the height of the center of mass, z_{CM}. (a) Schematic of an ellipsoidal particle breaching the fluid interface showing a monotonic decrease in height of the center of mass and polar angle, adapted from [37]. Each panel in (a) is related to a datapoint in the graph showed in (b). (b) The height of the center of mass of ellipsoids oriented oblique to the fluid interface evolves linearly with the polar angles, implying translation and rotation of the particle at the fluid interface.

5.2.4 Interfacial deformation around single ellipsoids

Anisotropic particles distort the liquid-liquid interface to which they are adsorbed. With iPAINT, we can visualize the deformation of the interface around individual ellipsoids, which is what we focus on next. We first image the interfacial profiles around ellipsoids in both oblique and parallel orientations. Subsequently, we compare our results with simulations. We find that the data computed from the profile observed in the 'arrested' oblique orientation obey to a dipolar deformation, while those collected from ellipsoids in equilibrium follow a quadrupolar deformation. Then, in section 5.2.5 we use these values to compute the capillary interactions two particles would experience in the far-field for the specific configuration adopted.

5.2.4.1 Dipolar interfacial deformations

Anisotropic particles oriented in an oblique fashion at the interface induce dipolar deformations, depressing the interface on one side and elevating it on the other (fig. 5.6a). Such particle orientations are unexpected, since the parallel orientation is most stable. But it has been shown previously they can be induced by a magnetic field when applied normal to the fluid interface laden with magnetic ellipsoids, with dipole moment aligned with the major axis. [20,41] Here, we exploit the 'arrested' oblique orientation adopted by the particles at the fluid interface to visualize such deformations. We image and trace the shape (fig. 5.6b and 5.6c) of the interface around the ellipsoids by α-shaping. [33] We measure the maximum deformation that the interface can adopt, Δu, as schematically illustrated in figure 5.6a. We take Δu as the distance along the surface normal between the outermost single-molecule localizations on the interface, close to the tips of the ellipsoidal particle in the oil and in the water phase, respectively. We plot Δu divided by half of the minor axis of the ellipsoid, *a*, as a function of $180° - \varphi$ in figure 5.6d. Note that we include both parallel ellipsoids ($\varphi < 27°$) and oblique ellipsoids ($30° < \varphi < 75°$). For clarity, the iPAINT data are binned over 5° range of polar angles. For $\varphi < 20°$, we find that the dipolar deformation is proportional with φ as $\Delta u/a = 0.0105\ \varphi$. The deformations reach a maximal value at $\varphi = 38.7°$, and decrease to zero at $\varphi \sim 90°$. These experimental findings are in good agreement with the computational results of Davies *et al.*, [17] which present a scaling behaviour with slope of 0.0133 for polar angles $\varphi < 20°$. From this dependence, they derive a simple equation applicable to small tilting angles ($\varphi < 20°$), where the pair potential, ΔE, scales inversely to the distance between particles (d_{cc}^2) squared:

$$\Delta E/\gamma a^2 \propto \frac{\varphi^2}{d_{cc}^2}. \tag{5.1}$$

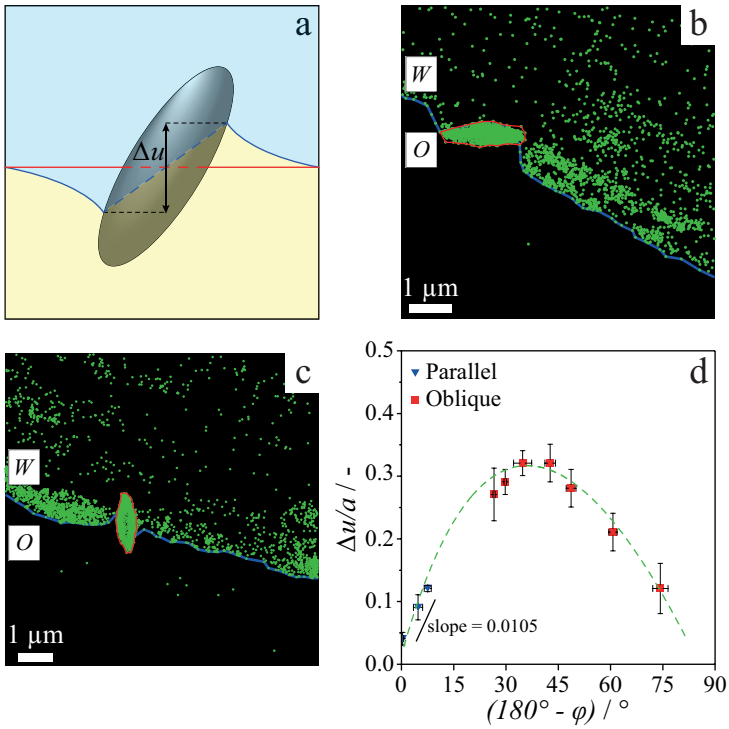

Figure 5.6: Deformation of the fluid interface due to the presence of anisotropic particles. (a) Schematic showing how the interfacial deformation (blue line) increases the wettability of the particles by maximizing the ellipsoid surface area in between the two phases, if compared to an unperturbed interface (red line). Δu represents the maximum difference in the contact line height. (b-c) Two exemplary iPAINT images of deformed interfaces in presence of oblique ellipsoidal particles adsorbed at the fluid interface. The red line along the ellipsoids perimeter and the blue line to define the interface are obtained by α-shaping. [33] (d) Maximum difference in the contact line height, Δu, as a function of the polar angle, φ. The red closed squares are data points collected from ellipsoids in the oblique configuration, the closed blue triangles, instead, are ellipsoids laying flat at the interface. The green dashed line is meant to guide the eyes. The error bars represent the standard deviation.

5.2.4.2 Quadrupolar interfacial deformations

We now attempt to characterize the deformation of the three-phase contact line along the major axis of an ellipsoidal particle laying flat at the interface. In simulations, this deformation is measured by calculating the contact angle along the major axis of a single ellipsoidal particle as a function of Δu. It appears that Δu decreases while moving from the center to the tip of the particle, showing a profile similar to the one depicted in figure 5.1. [42] In a single-colour iPAINT experiment, we cannot follow the profile of the interface along the major axis of the particle, but we can quantify its maximal deformation at the tips Δu_{max} (fig. 5.7a and the zoom-in 5.7b). We measure Δu_{max} for all ellipsoids oriented parallel to the interface as function of their contact angles, θ. Each value of Δu_{max} is normalized by the semi-minor axis of each ellipsoid, *a*, and averaged over $\theta = 5°$ intervals (5.7c). For comparison with

theoretical values, the deformation along the major axis of ellipsoids with aspect ratio $AR = 4$ and $AR = 5$ (blue and green line in fig. 5.7c, respectively) are shown. [42]

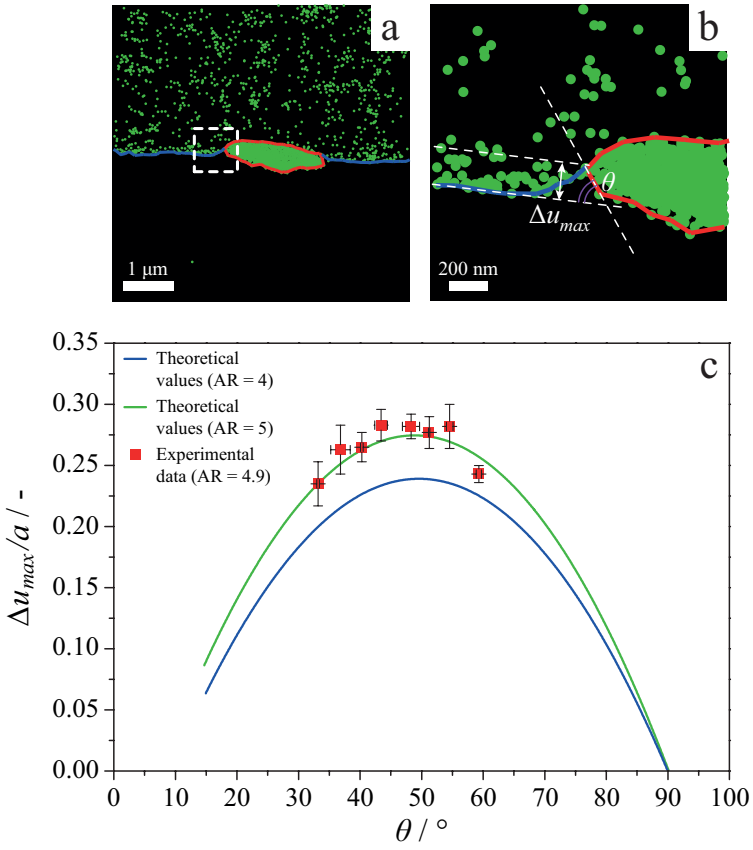

Figure 5.7: Maximal height difference Δu_{max} of the contact line for a single ellipsoidal particle laying parallel to the interface. (a) iPAINT images of the deformation of the interface in presence of an ellipsoidal particle. (b) Zoom-in of the region highlighted in (a) by the dashed white square, showing the height of Δu_{max}, and the contact angle θ. (c) The green and the blue lines are numerical data for ellipsoids with aspect ratio $b/a = 5$ and $b/a = 4$, respectively, taken from [42]. The red squares are iPAINT experimental data collected for ellipsoidal particles laying parallel to the interface with aspect ratio $b/a = 4.9$. The error bars represent the standard deviation.

Since every ellipsoid has different contact angles and sizes, combining the Δu_{max} of each one of them gives the deformation profile of an ellipsoidal particle having size equal to the averaged size of the particles investigated, and aspect ratio $AR = \overline{AR}$. The trend displayed illustrates that Δu_{max} increases non-monotonically with the contact angle, and decreases to zero at $\theta = 90°$. From the iPAINT data we find that Δu is maximum at $\theta_{AR=4.9} = 43.4°$, which is well in line with theoretical predictions of Dasgupta *et al.* ($\theta_{AR=5} = 48.5°$), [42] and Lehle *et al.* ($\theta_{AR=5} \simeq 46°$). [14] Furthermore, we report a value of $\Delta u_{max} = 0.29$, which is in excellent agreement with the theoretical value of $\simeq 0.28$ reported in literature. [42]

5.2.5 Quantification of pair-interaction potential from interfacial deformations

For the specific 'arrested' configuration of the particle pairs observed we now attempt to quantify the interaction potential between two particles adopting a specific reciprocal orientation, at a well-determined distance.

To compute the capillary forces between pairs of ellipsoids from Δu, we first distinguish the two possible reciprocal orientations of the particles: tip-to-tip and side-by-side (fig. 5.8a and 5.8b). These appear to be equally abundant (fig. 5.8c). Particles in the tip-to-tip configuration are further apart than particles arranged side-by-side. We find mean values for the distance between their center of mass, d_{cc}, of $d_{TT} \sim 2.1$ μm *vs.* $d_{SS} \sim 1.1$ μm for tip-to-tip and side-by-side, respectively (fig. 5.8d).

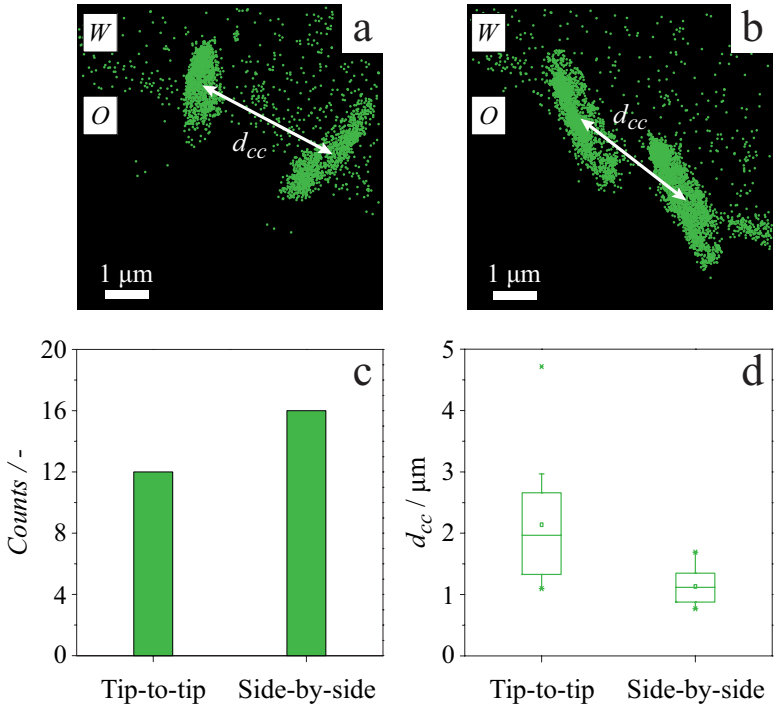

Figure 5.8: Reciprocal orientation of ellipsoids at a fluid interface. Examples of oblique ellipsoids oriented (a) tip-to-tip and (b) side-by-side. (c) quantification of ellipsoids in the different reciprocal orientation. (d) center to center distance, d_{cc}, of the ellipsoids for both reciprocal orientations. Dots indicate the mean, the horizontal line within the box is the median, the boxes are the 25^{th} and 75^{th} percentiles, the whiskers denote the 5^{th} and 95^{th} percentiles.

The smaller d_{cc} for SS *vs.* TT suggests that the side-by-side configuration is likely the more stable one. Simulations by Davies *et al.* indeed show that the tip-to-tip is a metastable state, while the side-by-side bound state is a free energy minimum. [17] This is because the

magnitude of the deformation per unit area is larger around the tip than along the side. The overlap between the deformations at the tips is therefore less favourable.

To compute the pair-interaction potential between two ellipsoidal particles, we use eq. 5.2, developed by Loudet *et al.* [16] and Stamou *et al.* [43] to describe the the capillary interactions in the far-field, assuming quadrupolar interface deformations. We input the experimental quantities determined from iPAINT imaging of an 'arrested' configuration to calculate $\Delta E/\gamma a^2$ as a function of the center-to-center distance, d_{cc}, between two ellipsoids (1 and 2): [13, 14, 43]

$$\Delta E/\gamma a^2 = -3\pi \cos(\, 2\varphi_1 + 2\varphi_2\,)\left(\frac{\Delta u}{a}\right)^2\left(\frac{d_{cc}}{a}\right)^{-4}. \tag{5.2}$$

In eq. 5.2, φ_1 and φ_2 are the polar angles of the two ellipsoids, and γ is the interfacial tension. The $\Delta u/a$ value is averaged for each pair of ellipsoids investigated. The experimental values of $\Delta E/\gamma a^2$ here calculated represent the pair-interaction potential between two particles for the particular distances and orientations observed in the iPAINT snapshot.

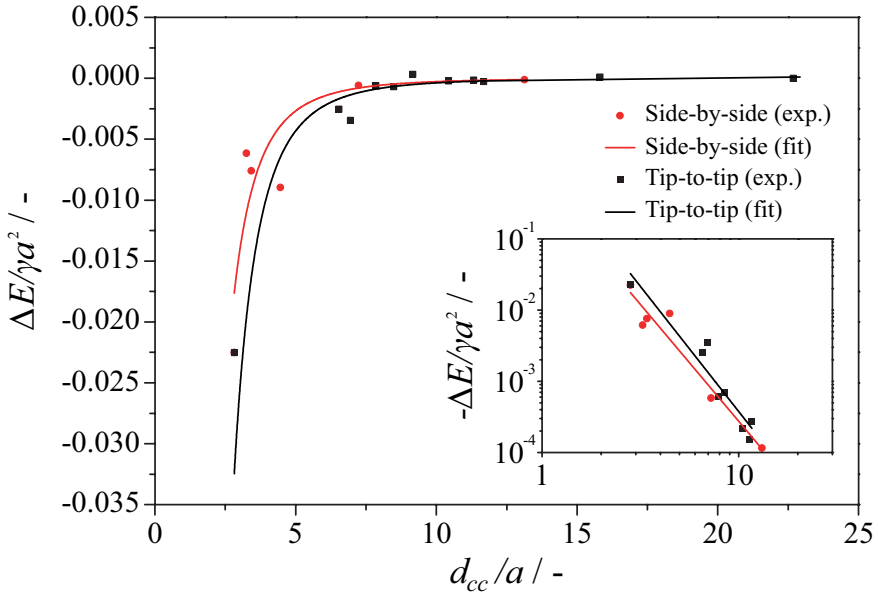

Figure 5.9: Capillary interactions calculated in the quadrupole approximation between two ellipsoids with aspect ratio $b/a = 4$ oriented side-by-side (red closed circles) and tip-to-tip (black closed squares). For both orientations the interaction is attractive ($\Delta E/\gamma a^2 < 0$). The side-by-side configuration is energetically more stable than the tip-to-tip configuration, since is shifted to smaller d_{cc}/a. The fit of the experimental data are calculated through eq. 5.3 on a linear (main graph) on a log-log scale (inset).

In agreement with theoretical predictions, [42] we find that the interparticle forces are attractive for both orientations, with the side-by-side configuration being slightly more attractive than the tip-to-tip orientation (fig. 5.9). As a self-consistent check, we fit the experimental

data obtained in the quadrupolar approximation using eq. 5.2 to eq. 5.3. We do not recover $m = 4$, instead we find $m = 3.5 \pm 0.4$ for the tip-to-tip configuration, and $m = 3.2 \pm 0.4$ for the side-by-side orientation. Our findings show the same dependence as previously reported by Loudet *et al.* by holographic microscopy on polystyrene ellipsoidal particles of $\sim$10 μm in length. [16]

$$\Delta E/\gamma a^2 = k\left(\frac{d_{cc}}{a}\right)^{-m}. \tag{5.3}$$

From the pair-interaction potential we obtain the capillary forces as $F_{cap} = {}^{\partial \Delta E}/_{\partial d_{cc}}$, hence from eq. 5.3 we have $F_{cap} \sim ({}^{d_{cc}}/_{a})^{-(m+1)}$. This gives $F_{cap} \sim ({}^{d_{cc}}/_{a})^{-4.2}$ for the side-by-side configuration and $F_{cap} \sim ({}^{d_{cc}}/_{a})^{-4.5}$ for the tip-to-tip coupled state. These values are in reasonable agreement with the aforementioned holographic microscopy experiments calculating attractive forces $F_{cap} \propto d^{-4.1}$, and $F_{cap} \propto d^{-5}$ for the side-by-side and the tip-to-tip configurations, respectively. [16] Hence, for both configurations the capillary interactions calculated between ellipsoids (far-field) are not quantitatively described by the quadrupolar approximation of the deformations around the single particle (near-field). This mismatch has been explained by Lehle *et al.* through theoretical calculations which predict capillary forces $F_{cap} \propto d^{-5}$ if elliptical quadrupole deformations are used instead of polar quadrupoles. [14, 42, 44] In elliptical quadrupoles the deformations are focused more at the tip of the particle, and the contribution from polar multipoles higher than the quadrupole is substantial. [14]

5.3 Conclusions

The single-molecule microscopy approach iPAINT is used to investigate the orientation of anisotropic particles at liquid-liquid interfaces. Contrary to other single particle methods, in iPAINT the ellipsoids and the fluid interface can be visualized simultaneously and *in-situ*, minimizing sample manipulation. We observe ellipsoids parallel ($\varphi = 2.8° \pm 2.2°$), oblique ($\varphi = 124.9° \pm 21.7°$) and normal ($\varphi = 91.4° \pm 2.6°$) to the interface. We calculate also the contact angle θ for the ellipsoids parallel to the interface ($\theta = 42.7° \pm 6.1°$). Through an in-depth study of particles 'arrested' in an oblique configuration at the interface, we deduce the path of approach to the fluid interface. The linear behaviour of φ *vs.* z_{CM} suggests a close relationship between translational and rotational motions of the ellipsoids while adsorbing at the interface, and finds its origin in the pinning of the three-phase contact line. iPAINT also enables us to investigate the interfacial deformations induced by particles. The data computed from particle in the oblique configuration suggest the presence of dipolar deformations, whereas, those calculated from particles flat at the interface hints at quadrupolar deformations. Finally, we calculate the capillary interactions corresponding to the imaged 'arrested' states between pairs of ellipsoids at given distances and orientations, and for specific deformations, showing pair-interaction potentials slightly more attractive for particles arranged side-by-side than tip-to-tip. The scaling deviates from predictions for polar quadrupoles, suggesting that the ellipsoids studied here induce deformations somewhat in between polar and elliptical quadrupoles.

5.4 Experimental

5.4.1 Synthesis and characterization of ellipsoidal particles

Prolate ellipsoidal particles are kindly provided by prof. J. Vermant and prof. L. Isa, from the Department of Materials at ETH, Zurich. TEM imaging has been carried out by D. Atkins. Briefly, monodisperse sulfate latex spheres of 1 μm in diameter (Invitrogen) are embedded into a poly(vynil alcohol) (PVA) matrix and subsequently put in a silicon bath at a temperature above the glass transition temperature but below the melting temperature of the material. The film undergoes to an uniaxial stretching as reported in literature. [45] All spheres are exposed to a controlled plastic deformation to prolate ellipsoids with a given aspect ratio. [27] The ellipsoids here used present an aspect ratio of 4.9 $\pm$ 0.5 (fig. 5.10c). Data reported by Coertjens *et al.* demonstrates a constant volume deformation of the particles under stretch, and that they keep an ideal prolate shape. [27] Afterwards, the film strips are kept under stretching and cooled down by air flow. Several washing steps involving isopropanol-water mixture and MilliQ-water, followed by an heating step at 50 °C and subsequent ultrasonication are needed to clean the ellipsoids, after the PVA film is dissolved. [27, 45]

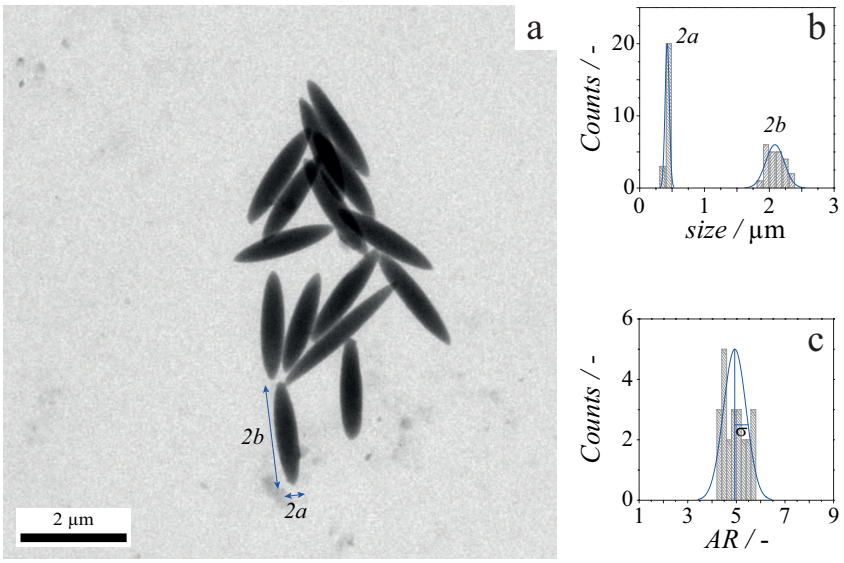

Figure 5.10: Characterization of polystyrene ellipsoids. (a) TEM picture of ellipsoidal particle with major axis 2b = 2087 $\pm$ 142 nm, and minor axis 2a = 425 $\pm$ 32 nm. The aspect ratio $AR = b/a = 4.9 \pm 0.5$. (b-c) Distributions of major and minor axis and aspect ratio of the ellipsoidal particles.

TEM images of the prolate ellipsoids with aspect ratio of 4.9 $\pm$ 0.5 are conducted on a FEI Tecnai 20, type Sphera TEM instrument operating at 200 kV (LaB_6 filament) with a

bottom mounted 1024 × 1024 Gatan msc 794^{TM} CCD camera. Samples are prepared using carbon-coated 200 mesh copper grids.

5.4.2 Synthesis of PEG-552 probes

∼1 mg of poly(ethylene glycol) bis(amine) with molecular weight M_W = 20 kDa, purchased from Sigma Aldrich, is dissolved in 1 mL of sodium bicarbonate buffer (0.1 M, pH 8.5). 20 μL of 10 mM solution of N-hydroxysuccinimide ester activated rhodamine (Cage-552) purchased from Abberior® is added to the reaction mixture and set to stir overnight, in the dark, and at room temperature. The product is purified by dialysis with a Spectra/Por®7 dialysis membrane, pre-treated RC tubing, and molecular weight cutoff of 8 kDa, to remove unreacted dye molecules.

5.4.3 Sample preparation

50 μL of the aqueous solution of the ellipsoidal particles are added to 50 μL of the aqueous solution of the iPAINT dye PEG-552 (10^{-4} M). For iPAINT imaging, 15 μL droplet of the aforementioned solution is placed onto a coverglass (Menzel Gläser, 76 × 26 mm, thickness 1 mm) next to a 15 μL droplet of decane (fig. 5.11).

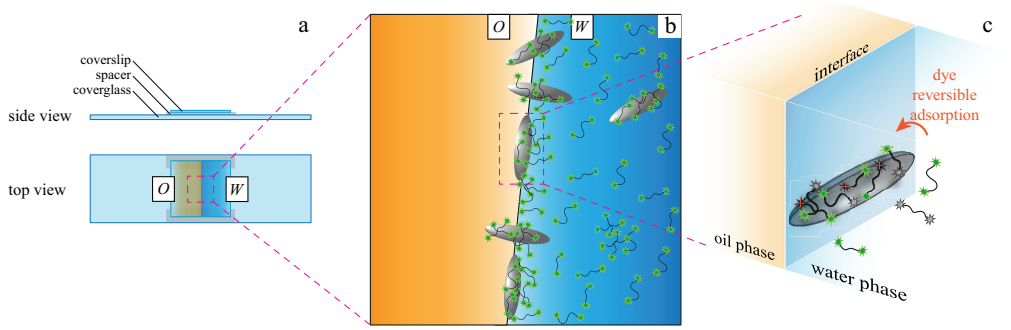

Figure 5.11: Schematic illustration of a fluid cell for iPAINT imaging of anisotropic particles at a fluid interface. (a) Side and top view of the assembled chamber made out of a coverglass, double-sided tape and a coverslip. Water and decane phases are put into contact to create an interfacial plane normal to the coverglass. (b) Cartoon depicting ellipsoidal particles adsorbed at the fluid interface between the water phase, rich in PEG-552 (green probes), and the oil phase. (c) Zoom-in on a ellipsoidal particle adsorbed at the fluid interface in 3D.

The sample is sandwiched between the coverglass and a coverslip (Menzel Gläser, No. 1.5, 24 × 24 mm, thickness 170 μm) using double-sided tape (∼90 μm). The coverslips are treated beforehand with piranha etching to remove impurities, hence reducing background fluorescence. As reported for other measurements of particles at fluid interface, solvent

evaporation is negligible during image acquisition due to the short imaging time-lapses (∼20 min for a 256 × 256 pixels field of view).

5.4.4 Microscopy

iPAINT images are acquired using a Nikon Eclipse Ti-E N-STORM system supplied by $\lambda =$ 561 nm (∼488.0 mW/cm^2), and $\lambda =$ 405 nm (∼158.3 mW/cm^2) laser lines set for *quasi*-total internal reflection fluorescence (TIRF) imaging, maximizing the signal-to-noise ratio. A Nikon 100×, 1.4 NA oil immersion objective is used to collect the fluorescence signal, while a quad-band pass dichroic mirror (97335 Nikon) filters out the excitation laser lines. The fluorescence signal is recorded on an Andor EMCCD camera (ixon3) with pixel size of 170 nm, at a frame rate of 47 frames/s for a region of interest of 256 × 256 pixels. A continuous photo-activation with a low power UV laser (405 nm, 0.5% power) of the iPAINT probes is performed followed by excitation and subsequent bleaching by 561 nm laser (100% power). Single-molecule localization movies are analyzed with NIS-element Nikon software over 2 × 10^4 frames collected for each acquisition.

5.4.5 Bond number and capillary length calculations

To rule out possible gravitational forces exerted on the particles, we calculate the Bond number, Bo (eq. 5.4), which defines the balance between surface tension forces and gravitational forces:

$$Bo = \frac{(\rho_1 - \rho_2) g R_p^2}{\gamma}, \tag{5.4}$$

where R_p is the characteristic size of the particle, g the gravitational acceleration, ρ_i the density of each phase, and γ the interfacial tension. The Bond number can also be expressed in units of capillary length, L_c, which is given by eq. 5.5:

$$L_c = \sqrt{\frac{\gamma}{(\rho_1 - \rho_2) g}}. \tag{5.5}$$

This is the length over which the interfacial deformations propagate. Inserting eq. 5.5 into eq. 5.4 gives $Bo = R_p^2/L_c^2$. For the decane-water interface ($\gamma =$ 0.05233 N/m at 20 °C) [46] herein investigated, we compute a capillary length of $L_c = 20$ μm, and a Bond number of $Bo \sim 4 \times 10^{-4}$. Since $L_c \gg R_p$, the Bond number is negligible ($Bo \ll 1$), thus we can safely neglect the contribution of gravitational forces on the particle in the deformation of the interface. [14] Furthermore, L_c is larger than the distance between particles (d_{cc}, *vide infra* section 5.2.5), which means that the particles experience significant capillary forces. [47]

5.4.6 Calculation of contact angle of individual ellipsoidal particles

Here we present how to calculate the polar angle (φ) for ellipsoidal particles 'arrested' oblique to the interface, and the contact angle (θ) for those oriented parallel to the interface from iPAINT measurements.

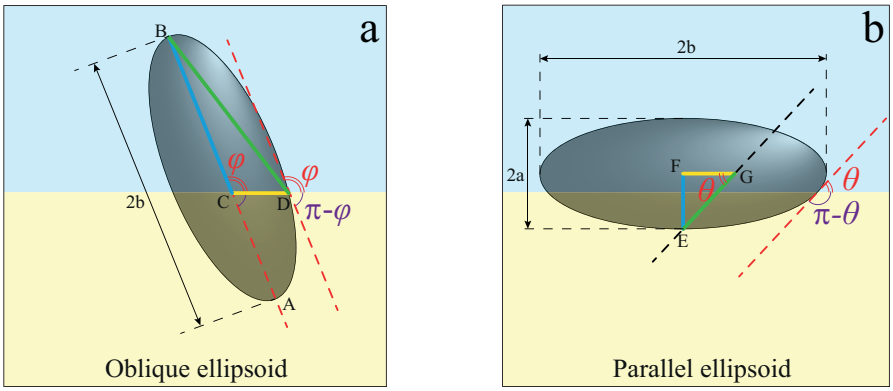

Figure 5.12: Representative cartoon of a ellipsoidal particles at a fluid interface. The schematics illustrate the relevant dimensions $\overline{BC}$, $\overline{CD}$, and $\overline{BD}$ to calculate φ (eq. 5.6), and $\overline{EF}$, $\overline{FG}$ and $\overline{EG}$ to measure θ (eq. 5.7).

Aiming to obtain φ for the particles with an oblique orientation, we measure in the iPAINT image the length of the segments $\overline{BC}$, $\overline{CD}$, and $\overline{BD}$, as depicted in figure 5.12a. For the oblique configuration, the polar angle is given by the orientation of the major axis respect to the fluid interface. Hence, we draw the major axis ($2b$) of the particle as the segment $\overline{AB}$ in figure 5.12a. Along the segment $\overline{AB}$ we define the segment $\overline{BC}$ as the segment which goes from the tip of the ellipsoid in the water phase till the position of the interface (blue line in fig. 5.12a). We determine the segment $\overline{CD}$ (yellow line in fig. 5.12a) following the interface from the point C till the contour of the particle (point D). Then we join point D and point B in the segment $\overline{BD}$ (green line in fig. 5.12a). The angle in $\widehat{C}$ is the polar angle φ, and it can be calculated from trigonometry as:

$$\cos(\varphi) = \frac{\overline{BC}^2 + \overline{CD}^2 - \overline{BD}^2}{2\,\overline{BC}\,\overline{CD}}. \tag{5.6}$$

To calculate the contact angel θ of an ellipsoid oriented flat at the interface we proceed to the determination of segments $\overline{EF}$, $\overline{FG}$ and $\overline{EG}$ (fig. 5.12b). We start off with drawing the tangent to the particle at the three phase contact line (red dashed line in fig. 5.12b), which defines the contact angle θ. Then we translate the tangent till it intersects the contour of the particle in its minor axis $2a$ (black dashed line in fig. 5.12b). The semi minor axis will

be defined as the segment $\overline{EF}$ (blue line in fig. 5.12b). We then highlight the major axis of the particle and from its intersection with the tangent we define the point G (yellow line in fig. 5.12b). Then we connect point G and point E to define the segment $\overline{EG}$ (green line in fig. 5.12b). The angle in $\widehat{G}$ is the contact angle θ, and it can be computed as:

$$\cos(\theta) = \frac{\overline{EG}^2 + \overline{FG}^2 - \overline{EF}^2}{2\,\overline{EG}\,\overline{FG}}. \tag{5.7}$$

Bibliography

[1] Xia, Y. *Farad. Discuss.* **2016**, *191*, 597.

[2] Madivala, B.; Fransaer, J.; Vermant, J. *Langmuir* **2009**, *25*, 2718.

[3] Madivala, B.; Vandebril, S.; Fransaer, J.; Vermant, J. *Soft Matter* **2009**, *5*, 1717.

[4] de Gans, B.J.; Duineveld, P.C.; Schubert, U.S. *Adv. Mater.* **2004**, *16*, 203.

[5] Park, J.; Moon, J. *Langmuir* **2006**, *22*, 3506.

[6] Pickering, S.U. *J. Chem. Soc. Trans.* **1907**, *91*, 2001.

[7] Ramsden, W. *Proc. R. Soc.* **1903**, 72, 156.

[8] Deegan, R.D.; Bakajin, O.; Dupont, T.F.; Huber, G.; Nagel, S.R.; Witten, T.A. *Nature* **1997**, *389*, 827.

[9] Denkov, N.D.; Velev, O.D.; Kralchevsky, P.A.; Ivanov, I.B.; Yoshimura, H.; Nagayama, K. *Nature* **1993**, *361*, 26.

[10] Hu, H.; Larson, R.G. *J. Phys. Chem. B* **2002**, *106*, 1334.

[11] Vermant, J. *Nature* **2011**, *476*, 286.

[12] Yunker, P.J.; Still, T.; Lohr, M.A.; Yodh, A.G. *Nature* **2011**, *476*, 308.

[13] Fournier, J.B.; Galatola, P. *Phys. Rev. E* **2002**, *65*, 031601.

[14] Lehle, H.; Noruzifar, E.; Ottel, M. *Eur. Phys. J.* **2008**, *26*, 151.

[15] Oettel, M.; Dietrich, S. *Langmuir* **2008**, *24*, 1425.

[16] Loudet, J.C.; Alsayed, A.M.; Zhang, J.; Yodh, A.G. *Phys. Rev. Lett.*, **2005**, *94*, 018301.

[17] Davies, G.B.; Botto, L. *Soft Matter* **2015**, *11*, 7969.

[18] Morris, G.; Neethling, S.J.; Cilliers, J.J. *J. Colloid Interface Sci.* **2011**, *354*, 380.

[19] Park, B.J.; Lee, D. *ACS Nano* **2012**, *6*, 782.

[20] Davies, G.B.; Krüger, T.; Coveney, P.V.; Harting, J.; Bresme, F. *Soft Matter* **2014**, *10*, 6742.

[21] Botto, L.; Lewandowski, E.P.; Cavallaro, Jr.M.; Stebe, K.J. *Soft Matter* **2012**, *8*, 9957.

[22] Loudet, J.C.; Pouligny, B. *Europhys. Lett.* **2009**, *85*, 28003.

[23] Loudet, J.C.; Yodh, A.G.; Pouligny, B. *Phys. Rev. Lett.* **2006**, *97*, 018304.

[24] Paunov, V.N. *Langmuir* **2003**, *19*, 7970.

[25] Arnaudov, L.N.; Cayre, O.J.; Stuart, M.A.C.; Stoyanov, S.D.; Paunov, V.N. *Phys. Chem. Chem. Phys.* **2010**, *12*, 328.

[26] Isa, L.; Lucas, F.; Wepf, R.; Reimhult, E. *Nat. Commun.* **2011**, *2*, 438.

[27] Coertjens, S.; Moldenaers, P.; Vermant, J.; Isa, L. *Langmuir* **2014**, *30*, 4289.

[28] Cappelli, S.; de Jong, A.M.; Baudry, J.; Prins, M.W.J. *Soft Matter* **2016**, *12*, 5551.

[29] Cappelli, S.; de Jong, A.M.; Baudry, J.; Prins, M.W.J. *Langmuir* **2017**, *33*, 696.

[30] Aloi, A.; Vilanova, N.; Albertazzi, L.; Voets, I.K. *Nanoscale* **2016**, *8*, 8712.

[31] Belov, V.N.; Mitronova, G.Y.; Bossi, M.L.; Boyarskiy, V.P.; Hebisch, E.; Geisler, C.; Kolmakov, K.; Wurm, C.A.; Willig, K.I.; Hell, S.W. *Chem. - Eur. J.* **2014**, *20*, 13162.

[32] Huang, B.; Wang, W.; Bates, M.; Zhuang, X. *Science* **2008**, *319*, 810.

[33] Lou, S.; Jiang, X.; Scott, P.J. *Proc. R. Soc. A* **2013**, *469*, 20130150.

[34] Faraudo, J.; Bresme, F. *J. Phys. Chem.* **2003**, *118*, 6518.

[35] Zanini, M.; Isa, L. *J. Phys.: Condens. Matter* **2016**, *28*, 313002.

[36] Coertjens, S.; De Dier, R.; Moldenaers, P.; Isa, L.; Vermant, J. *Langmuir* **2017**, *33*, 2689.

[37] Wang, A.; Rogers, W.B.; Manoharan, V.N. preprint [arXiv:cond-mat.soft/1607.08167] **2016**.

[38] Manoharan, V.N. *Nat. Mater.* **2015**, *14*, 869.

[39] Boniello, G.; Blanc, C.; Fedorenko, D.; Medfai, M.; Mbarek, N.B.; In, M.; Gross, M.; Stocco, A.; Nobili, M. *Nat. Mater.* **2015**, *14*, 908.

[40] Kaz, D.M.; McGorty, R.; Mani, M.; Brenner, M.P.; Manoharan, V.N. *Nat. Mater.* **2012**, *11*, 138.

[41] Davies, G.B.; Krüger, T.; Coveney, P.V.; Harting, J.; Bresme, F. *Adv. Mater.* **2014**, *26*, 6715.

[42] Dasgupta, S.; Katava, M.; Faraj, M.; Auth, T.; Gompper, G. *Lamgmuir* **2014**, *30*, 11873

[43] Stamou, D.; Duschl, C.; Johannsmann, D. *Phys. Rev. E* **2000**, *62*, 5263.

[44] Lewandowski, E.P.; Cavallaro, M.; Botto, L.; Bernate, J.C.; Garbin, V.; Stebe, K.J. *Langmuir* **2010**, *26*, 15142.

[45] Keville, K.M.; Franses, E.I.; Caruthers, J.M. *J. Colloid Interface Sci.* **1991**, *144*, 103.

[46] Demond, A.H.; Lindner, A.S. *Environ. Sci. Technol.* **1993**, *27*, 2318.

[47] Bresme, F.; Ottel, M. *J. Phys.: Condens. Matter* **2007**, *19*, 413101.

Chapter 6

Imaging nanostructures by single-molecule localization microscopy in organic solvents

The introduction of super-resolution fluorescence microscopy (SRM) opened an unprecedented vista into nanoscopic length scales, unveiling a new degree of complexity in biological systems in aqueous environments. Regrettably, supramolecular chemistry and material science benefited far less from these recent developments. Here we expand the scope of SRM to photo-activated localization microscopy (PALM) imaging of synthetic nanostructures that are highly dynamic in organic solvents. Furthermore, we characterize the photophysical properties of commonly used photo-activatable dyes in a wide range of solvents, which is made possible by the addition of a tiny amount of an alcohol. As proof-of-principle, we use PALM to image silica beads with radii close to Abbe's diffraction limit. Individual nanoparticles are readily identified and reliably sized in multicolor mixtures of large and small beads. We further use SRM to visualize nm-thin yet μm-long dynamic, supramolecular polymers, which are among the most challenging molecular systems to image.

Part of this work has been published as: Aloi, A.; Vargas Jentzsch, A; Vilanova, N.; Albertazzi, L.; Meijer, E.W.; Voets, I.K. *J. Am. Chem. Soc.* **2016**, *138*, 2953.

6.1 Introduction

The introduction and use of super-resolution optical fluorescent microscopy (SRM) has opened the door to a better understanding of living cells and organisms. SRM gave access to length scales otherwise inaccessible to optical microscopy shedding new light on structure-function relationships of living matter with unprecedented detail. [1–6]

SRM circumnavigates the diffraction barrier while profiting from many of the advantages inherent to optical microscopy, like multicolor and target-specific labeling. This is what makes SRM a powerful tool to study biological systems and complementary to well-established characterization methods such as X-ray crystallography, nuclear magnetic resonance (NMR), and electron microscopy (EM). [7–9] Numerous practical applications of SRM have been demonstrated in recent years. Illustrative examples include the mapping of neurons, [10] protein-driven chromosome organization, [11] and the periodic structure of actin and spectrin in axons. [12] Small molecules that self-assemble to form long unidimensional structures reminiscent of natural systems also represent a fascinating class of supramolecular organization. [13] Since widespread interest in biomaterials has catalyzed the design of molecular motifs for assembly into such supramolecular polymers in aqueous media, [14] some of us revealed the structure and exchange dynamics of supramolecular polymers in water using single-molecule localization microscopy (SMLM). [15] However, the majority of these synthetic systems are only soluble in organic, nonprotic media, like alkanes or chlorinated solvents. Preliminary steps toward super-resolution imaging in organic solvents have been taken to map living crystallization-driven block copolymer self-assembly in cyclohexane [16] and colloidal nanostructures in material science. [17,18] Inspired hereby, we decided to investigate the exciting possibility of expanding the scope of SMLM to several organic solvents.

To this end, we screen among the several SMLM techniques available the most feasible candidate to pursue the imaging in organic solvents. On the one hand there are techniques that rely on the use of patterned illumination (SSIM, STED, RESOLFT), on the other hand on photo-switchable fluorescent dyes (STORM, PALM). [19,20] In this chapter, we focus on the latter class of SMLM methods, since these are attractive candidates for widespread application of SMLM in organic solvents in supramolecular chemistry and material science, as they are easier to operate and rely only on the usage of suitable dyes. Stochastic optical reconstruction microscopy (STORM) [21] employs fluorophores which can be switched reversibly between a fluorescent and a non-fluorescent state. This is typically achieved in the presence of an oxygen scavenger and β-mercaptoethylamine. [22] In this way the fluorescent signal from fluorophores spatially closer than the diffraction limit can be temporally separated, thus achieving sub-diffraction imaging. [23] Photo-activated localization microscopy (PALM) [1] uses dyes that start in an OFF state and can be activated to an ON state by an external stimulus (*e.g.*, 405 nm light). The technique requires the majority of fluorophores

to be in a stable OFF state. Stochastically, a subset of fluorophores is switched to the ON state by application of low 405 nm laser power (photo-activation). Finally, a readout beam can selectively excite, and subsequently photobleach the photo-activated fluorophores. The iterative routine of photo-activation, excitation and bleaching leads to a super-resolved image. [24]

We decide not to use STORM, since herein the switching of the dye is driven by a chemical reaction, which is highly sensitive to the composition of the medium. Conversely, we turn to PALM since the essential switching of the dye is intrinsic; *i.e.*, encoded in the chemical structure of the dye. First, we report on the photophysical properties of commercially available PALM dyes in organic solvents. We next discuss the photo-activation of the dye in organic solvents. Finally, we focus on SRM imaging of assembly of nanoparticles and synthetic supramolecular systems in organic media.

6.2 Results and discussion

6.2.1 Photophysical properties of caged dyes in water

We first report on the switching behaviour of two photo-activatable dyes in aqueous solvents, and show the chemical reaction needed to transform the non-fluorescent compound into a bright, fluorescent structure. We then highlight why the same reaction cannot be carried out in organic solvents. Finally, we propose a method to circumvent this limitation and prove that single-molecule imaging can be performed in organic solvents with this expedient.

Essential for PALM (as for any SMLM technique) is the choice of the most suitable fluorophore. Among the various PALM dyes reported in the literature, there are only a few which chemistry is not necessarily affected by the solvent. [25, 26] These, however, have important limitations, such as the colorful and potentially toxic nature of the byproducts (*e.g.*, nitrobenzyl derivatives). At present, PALM dyes based on diazoketo chemistry are commercially available (*e.g.*, Cage-552, Cage-635). These are well-known and commonly used on commercial and custom microscopes.

First, we characterize the switching behaviour of two caged dyes in aqueous solvents. The spectra of Cage-552 (fig. 6.1a) and Cage-635 (fig. 6.1b) in saline phosphate buffer (PBS), pH $= 7.4$, are presented in figure 6.1. In the caged-dark state, the rhodamines have a strong absorption in the UV region, at wavelengths $\lambda < 400$ nm. Upon UV light absorption, the compound is uncaged, and a distinctive and intense absorption in the visible region is recorded. Finally the fluorescence emission can be collected by exciting the bright, uncaged form of the photo-activated dyes.

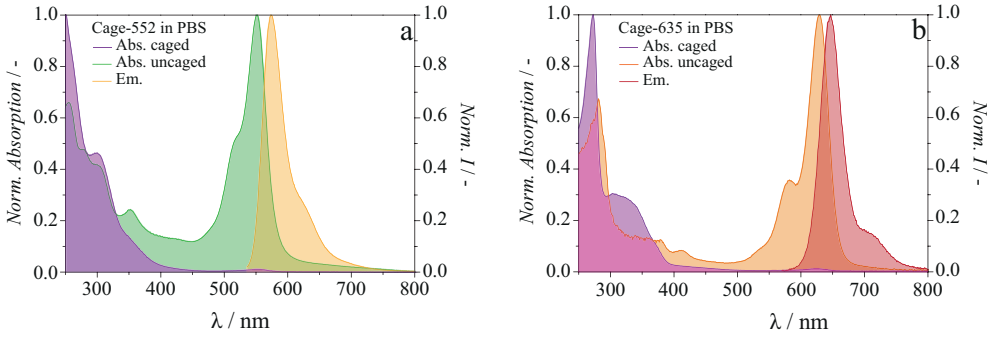

Figure 6.1: Spectra of caged rhodamines in saline phosphate buffer (PBS), pH = 7.4. (a) Absorption spectra of Cage-552 in the caged state (purple), and after photo-activation (green); the emission spectrum is denoted in yellow. (b) Absorption spectra of Cage-635 in the caged state (purple), and after photo-activation (orange); the emission spectrum is shown in deep-red. The spectra are normalized to their maximum values.

Next, we look at the photo-activation mechanism of this class of caged rhodamines (fig. 6.2). While the photoreaction and the subsequent Wolff rearrangement of the caged dyes likely proceed in most solvents, the last step in the reaction mechanism that leads to the fluorescent form requires fails in non-protic solvents. This is because a nucleophilic attack on the formed ketene is needed, limiting its use to nucleophilic solvents like methanol or water. [24] In fact, photolysis of Cage-552 in typical organic solvents such as chloroform, toluene, or acetonitrile resulted almost exclusively in nonfluorescent products (as it will be shown in the following section). To circumvent this limitation, we decide to simply add small amounts of alcohol to the organic solvents. Gratifyingly, addition of tiny percentages already recovers significant fluorescence in every solvent tested, as it will be discussed in the next section.

6.2.2 Volumetric effect of methanol on fluorescence emission

To investigate the percentage of methanol needed to obtain the fluorescent species of the caged rhodamine, emission spectra of the compounds after UV irradiation are acquired. Four solutions of 10^{-7} M of Cage-552, containing 0%, 0.1%, 1% and 2% in volume of methanol in each of the studied solvents are prepared and exposed to UV-A light (λ_{max} = 354 nm, 7.0 ± 0.5 mW/cm^2) for 30 min (fig. 6.3).

The maximum percentage of methanol added is 2% to not alter significantly the polarity of the overall solution. The emission spectra of Cage-552 in acetonitrile, chloroform and toluene with the described methanol % v/v are acquired, and are shown in figure 6.3a, 6.3b and 6.3c, respectively. As reported in figure 6.3, the compound is barely fluorescent if methanol is not present in solution. A small fluorescent signal is collected in the case of chloroform, but the structure obtained is highly unstable and particularly susceptible to photobleaching.

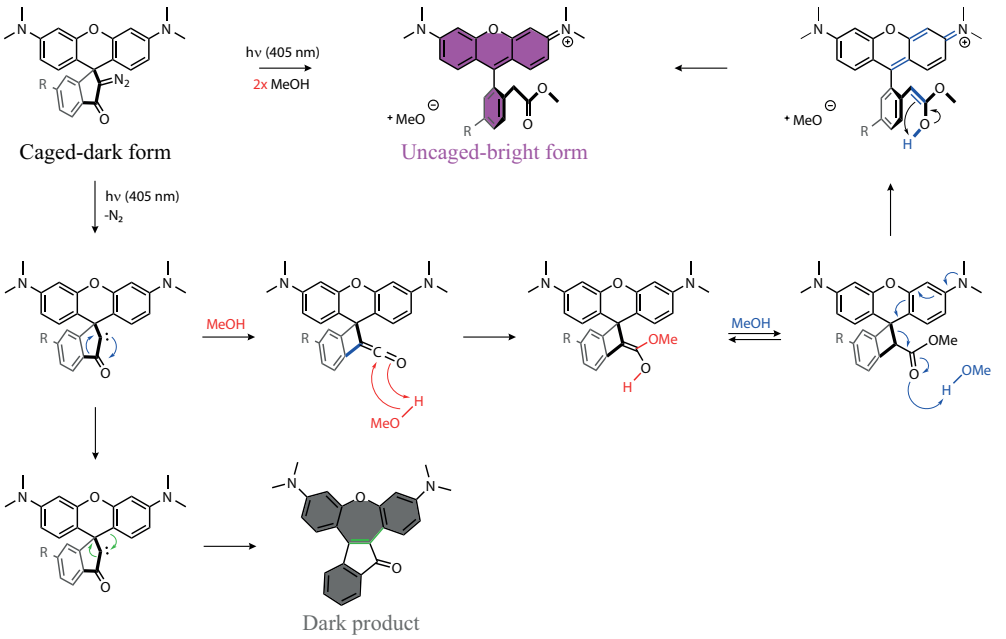

Figure 6.2: Photolysis of caged rhodamine performed in methanol upon UV light exposure. The highly fluorescent ester ('uncaged-bright form') is obtained by a Wolff rearrangement of the carbene to ketene, with the following addition of methanol to the reactive ketene group. Upon UV irradiation a minor non-fluorescent product will be formed in minor concentration ('dark product').

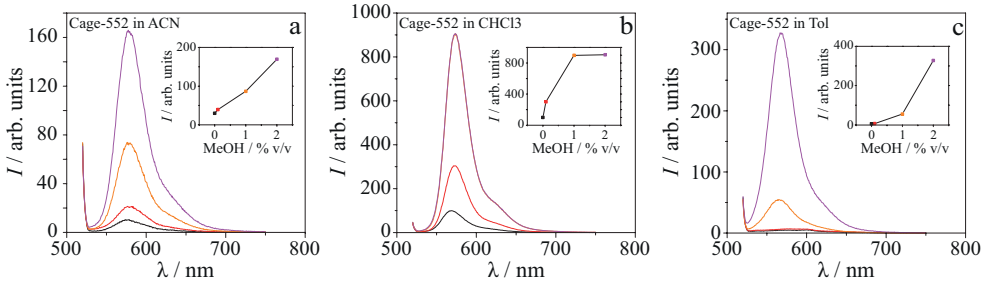

Figure 6.3: Influence of methanol content on the fluorescence intensity of the uncaged dye. Fluorescence spectra of the open form of Cage-552 10^{-7} M in acetonitrile (a), chloroform (b) and toluene (c), respectively, at different methanol concentrations. The UV light exposure was set to 30 min (λ_{max} = 354 nm); λ_{ex} = 510 nm, emission slit 10 nm, scan rate 200 nm/min, data interval 0.6 nm, averaging time 0.2 s. The insets show the evolution of the fluorescence maxima as function of the volume percentage of methanol added to the organic solvents.

Adding increasing percentages of methanol, leads to a raise of the fluorescence signal in all solvents (48-325% relative to water). A plateau in the fluorescence intensity is reached upon switching from 1% to 2% of methanol, (fig. 6.3b). The substantial increase of the fluorescence intensity of the compounds with 2% of added methanol is sufficient to perform PALM imaging (as it will be shown later in this chapter). Since cyclohexane is immiscible

with methanol, we use iso-propanol instead. Unfortunately, due to the poor solubility of the dyes in the mixture cyclohexane/iso-propanol, UV-vis spectra could not be collected, mainly due to the dominance of scattering processes. Nonetheless, PALM imaging carried out in cyclohexane with 2% v/v of iso-propanol leads to comparable results as will be shown in further on in the text, proving that a stable fluorescent structure is formed after the Wolff rearrangement in this mixture.

6.2.2.1 The kinetics of uncaging in organic solvents

To investigate the photobleaching rates of Cage-552 and Cage-635 in organic solvents, emission spectra are collected after different UV light exposure time lapses. We select several solvents covering the main families (*i.e.*, chlorinated, alcohols, aromatics, aliphatic) of common organic solvents while spanning a wide range of dielectric constants, ε, varying between 2.38 (toluene) and 80.1 (water). Individual solutions of 10^{-7} M of the dye in acetonitrile, chloroform, water, methanol and toluene are prepared in high quality glass vials (cut-off $\sim$340 nm) and placed together in a UV-oven. The solutions are simultaneously irradiated with UV-A light (λ_{max} = 354 nm, 7.0 $\pm$ 0.5 mW/cm^2). At a given time, t_{PA}, the corresponding sample is removed from the oven and its fluorescence spectrum is measured immediately. The spectra collected in the different solvents are reported in figure 6.4. The insets display the intensity of the fluorescence maximum as a function of the UV exposure time (t_{PA}) to monitor the uncaging kinetics in each solvent. We find out that the exposure time needed to obtain the maximum amount of uncaged dyes $t_{PA,M}$ is solvent dependent: $t_{PA,M}$ = 20 min for both dyes in ACN; $t_{PA,M}$ = 20 min for Cage-552 and $t_{PA,M}$ = 6 min for Cage-635 in $CHCl_3$; $t_{PA,M}$ = 60 min for Cage-552 and $t_{PA,M}$ = 30 min for Cage-635 in H_2O; $t_{PA,M}$ = 20 min for both dyes in methanol; $t_{PA,M}$ = 20 min for Cage-552 and $t_{PA,M}$ = 6 min for Cage-635 in toluene. We find that 20 min UV-A irradiation of a 10^{-7} M solution suffices in most of organic solvents to react all the uncaged molecules to either the dark [27] or fluorescent product.

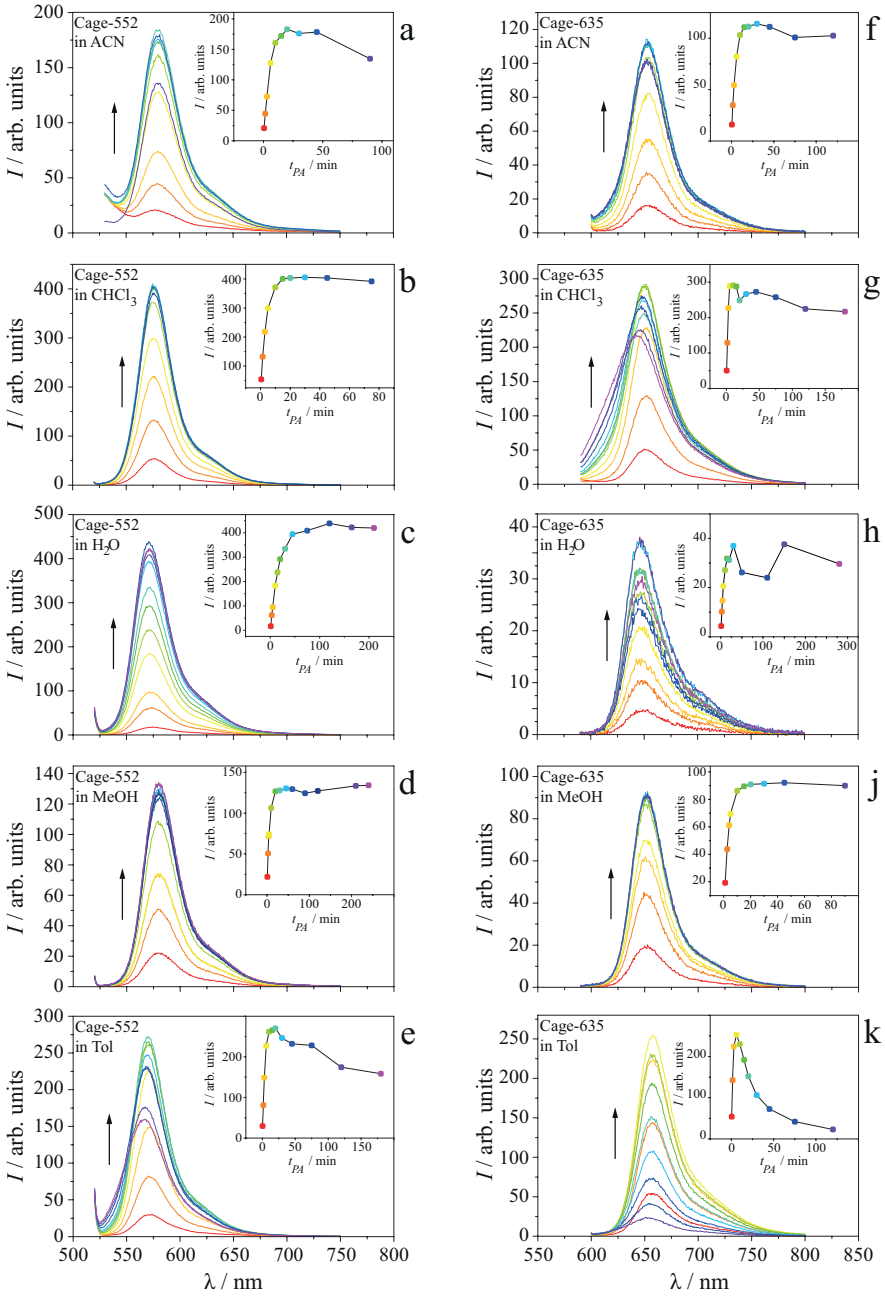

Figure 6.4: Fluorescence spectra of the open form of Cage-552 (left column) and Cage-635 (right column) 10^{-7} M at different UV light exposure times t_{PA}, in (a-f) acetonitrile, (b-g) chloroform, (c-h) water, (d-j) methanol and (e-k) toluene. For Cage-552 $\lambda_{ex} = 510$ nm, while for Cage-635 $\lambda_{ex} = 585$ nm. The spectra were acquired with emission slit 5 nm, scan rate 200 nm/min, data interval 0.6 nm, averaging time 0.2 s. The insets show the fluorescence intensity as a function of UV light exposure time, t_{PA}, for the emission maxima of Cage-552 and Cage-635 in the respective solvents.

6.2.2.2 Absorption and emission spectra, and fluorescence quantum yield of cage-dyes in organic solvents

Next, absorption and emission spectra of the (un)caged state of both dyes are collected at the appropriate UV light exposure time lapses as determined from the experiments on the uncaging kinetics in figure 6.4. The spectra are reported in figure 6.5, clearly showing that the uncaging mechanism takes place in each solvent upon addition of 2% v/v methanol. In agreement with published literature, [27] both caged compounds show a large absorption band in the region $\lambda < 350$ nm (ε = 14-24 $\times$ 10^3 M^{-1} cm^{-1}) and a long and low intensity tail extending up to $\lambda = 450$ nm ($\varepsilon \sim 7 \times 10^2$ M^{-1} cm^{-1}) in all solvents (for the numerical values refer to table 6.1). Upon irradiation with UV-A light (λ = 354 nm, 7.0 $\pm$ 0.5 mW/cm^2), a strong absorption band appears (Cage-552: $\lambda \sim$ 555 nm; Cage-635: $\sim$ 635 nm), confirming the formation of the uncaged and fluorescent adduct (fig. 6.5). The corresponding fluorescent emission (Cage-552: $\lambda \sim$ 580 nm; Cage-635: $\sim$ 650 nm) shows small yet consistent shifts that are attributed to excited-state stabilization. [28] All the spectral features related to the fluorescent product are included in table 6.2

Table 6.1: Photophysical features of Cage-552 and Cage-635 in the caged, non-fluorescent form in the selected organic solvents and water.

Caged Form (CF)			
dye	***solvents***	***Abs. max*** (nm)	ε (M^{-1} cm^{-1})
Cage-552	Tol	309	14000
	MeOH	301	24000
	ACN	307	16000
	$CHCl_3$	310	15000
	H_2O	324	19000
Cage-635	Tol	317	10000
	MeOH	318	12000
	ACN	316	10000
	$CHCl_3$	317	11000
	H_2O	323	16000

Table 6.2: Photophysical features of Cage-552 and Cage-635 in the open, fluorescent state upon UV photoactivation (6-60 min, according to the kinetic data in figure 6.4) in the selected organic solvents and water.

		Fluorescent Product (FP)		
dye	***solvents***	***Abs. max*** (nm)	ε (M^{-1} cm^{-1})	***Em. max*** (nm)
Cage-552	Tol	551	17000	587
	MeOH	558	33000	581
	ACN	555	42000	583
	$CHCl_3$	562	54000	574
	H_2O	551	38000	571
Cage-635	Tol	643	42000	655
	MeOH	636	75000	652
	ACN	637	39000	654
	$CHCl_3$	638	43000	649
	H_2O	630	38000	647

From the absorption and emission spectra in figure 6.5 it is possible to compute the fluorescent quantum yield (ϕ_f) of the caged rhodamines. [29] The fluorescence quantum yield of Cage-552 and Cage-635 is measured in all solvents (except cyclohexane) using the quantum yield of both dyes dissolved in methanol reported in literature as reference. [27] Additionally, the reported quantum yields are confirmed by using rhodamine 6G as a reference (see table 6.3). All compounds are illuminated by UV-A light (λ_{max} = 354 nm, 7.0 $\pm$ 0.5 mW/cm^2) during an exposure time $t_{PA,M}$ based on the measurements of the uncaging kinetics. The fluorescence spectra are corrected for the instrumental response function before the quantum yield is calculated. The following formula is used to estimate the quantum yield:

$$\phi_f(S) = \phi_f(R) \cdot \frac{1 - 10^{-A_R}}{1 - 10^{-A_S}} \cdot \frac{n_S^2}{n_R^2} \cdot \frac{\int I_S(\tilde{\nu}) d\tilde{\nu}}{\int I_R(\tilde{\nu}) d\tilde{\nu}} \tag{6.1}$$

where A_i is half of the absorbance measured at the excitation wavelength (λ_{ex} = 510 nm for Cage-552, λ_{ex} = 585 nm for Cage-635), I_i is the spectral fluorescence intensity, while the refractive index of the medium is denoted as n_i. The subscripts *S* and *R* refer to the sample and the reference, respectively. The integration of the spectra was performed in OriginLab, with spectra represented in wavenumbers ($I_{\tilde{\nu}} \propto {}^{I_\lambda(\lambda)}/_{\tilde{\nu}^2}$).

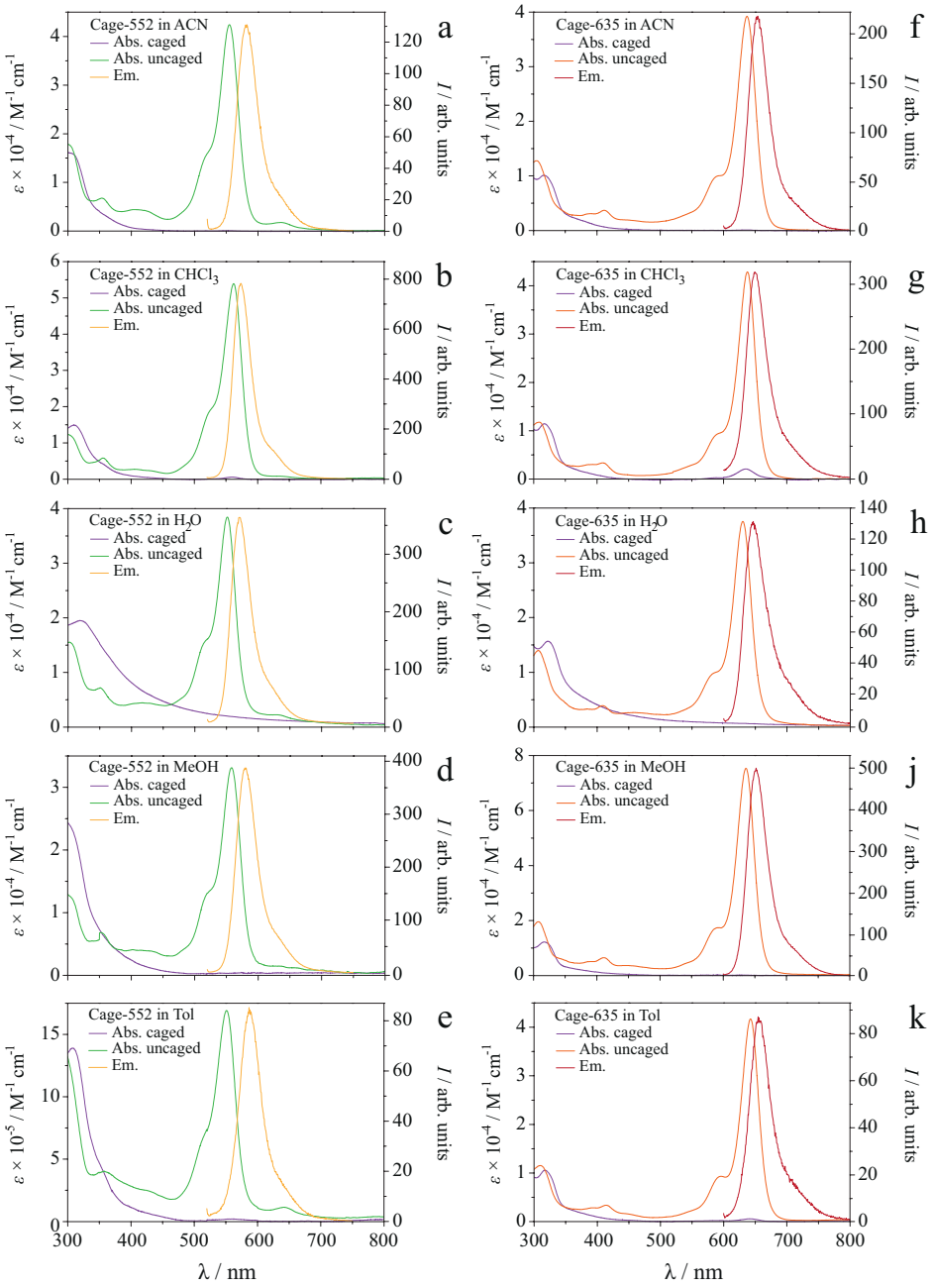

Figure 6.5: Absorption spectra of the closed and open form and emission spectra of Cage-552 (left column) and Cage-635 (right column) in (a-f) acetonitrile, (b-g) chloroform, (c-h) water, (d-j) methanol and (e-k) toluene. The spectra were collected after a UV light exposure times, t_{PA}, of maximum fluorescence emission $t_{PA,M}$ observed in the experiments on the uncaging kinetics (figure 6.4). For the fluorescence emission: λ_{ex} = 510 nm (Cage-552), λ_{ex} = 585 nm (Cage-635), emission slit 5 nm, scan rate 200 nm/min, data interval 0.6 nm, averaging time 0.2 s.

Table 6.3 summarizes the values obtained. Remarkably, the relative quantum yield in some organic solvents is significantly higher (up to 3-fold increase compared to the values calculated in water - $\phi_f = 0.23$), which should improve the localization accuracy. [30]

Table 6.3: Fluorescence quantum yield determination. [a]Relative quantum yield using the same dyes in methanol corresponding to the reaction mixture after photolysis. [27] [b]Literature value. [27]

dye	***solvents***	$^1/_2$ ***Abs.*** $\times 10^4$	n_i	***Peak area***	$\phi_f{}^a$
Cage-552	Tol	2.074	1.497	256251.1	0.161 ± 0.026
	ACN	4.193	1.344	100938.9	0.111 ± 0.005
	$CHCl_3$	3.628	1.444	513192.7	0.755 ± 0.006
	H_2O	4.899	1.333	58356.6	0.237 ± 0.009
	MeOH	-	-	-	0.40^b
Cage-635	Tol	3.174	1.497	91945	0.269 ± 0.020
	ACN	3.813	1.344	215672.3	0.424 ± 0.009
	$CHCl_3$	3.490	1.444	321207.7	0.799 ± 0.009
	H_2O	3.957	1.333	143106	0.267 ± 0.011
	MeOH	-	-	-	0.54^b
Rhodamine 6G	EtOH	4.017	1.362	656021.5	0.919 ± 0.007

6.2.3 Colloidal particles as model system

Having established the photophysical features of the dyes, we set out to image nanoparticles with radii R close to Abbe's diffraction limit by PALM in organic solvents. To this end, we synthesize monodisperse (for further details refer to section 6.4.2), spherical hydrophilic silica nanoparticles that are subsequently cofunctionalized with stearyl alcohol and either Cage-552 ($R \sim 220$ nm) or Cage-635 ($R \sim 110$ nm).

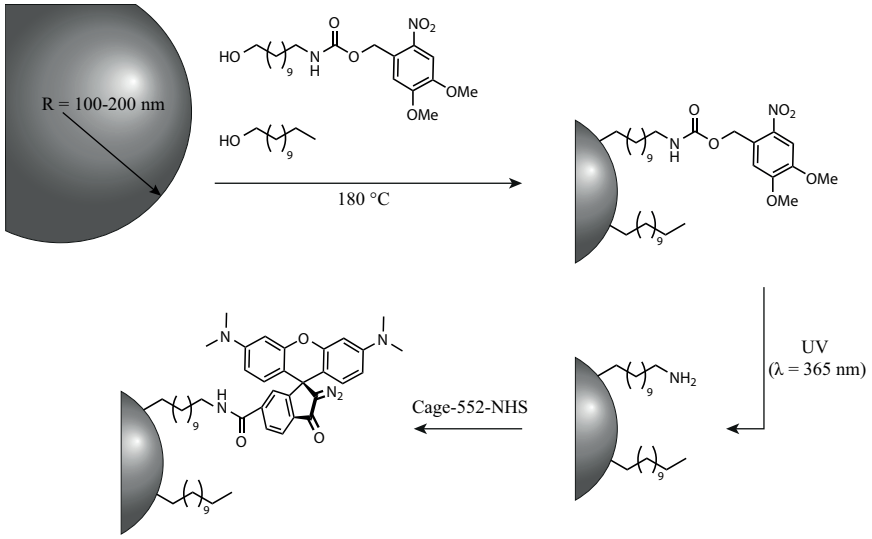

Figure 6.6: Schematic overview of the functionalization of silica beads with stearyl alcohol, and following labelling with Cage-552 dye molecule.

6.2.3.1 PALM imaging on colloidal particles in organic solvents

PALM images are collected in the above-mentioned organic solvents with 2% v/v methanol, as well as in cyclohexane with an addition of 2% v/v isopropanol. Note that the caged-dyes are not soluble in cyclohexane, precluding the photophysical characterization in this solvent. Exemplary images in figure 6.7 show that both shape and size of the silica beads labelled with Cage-552 (fig. 6.7a-e) and Cage-635 (fig. 6.7l-p) are clearly resolved in each solvent. Moreover, we report narrow radii distributions for big (fig. 6.7f-k) and small (fig. 6.7q-u) particles. The mean radii obtained by PALM imaging differ by $<$6% (see fig. 6.15 in section 6.4.2) compared to the mean radii calculated from scanning electron microscopy (SEM) images.

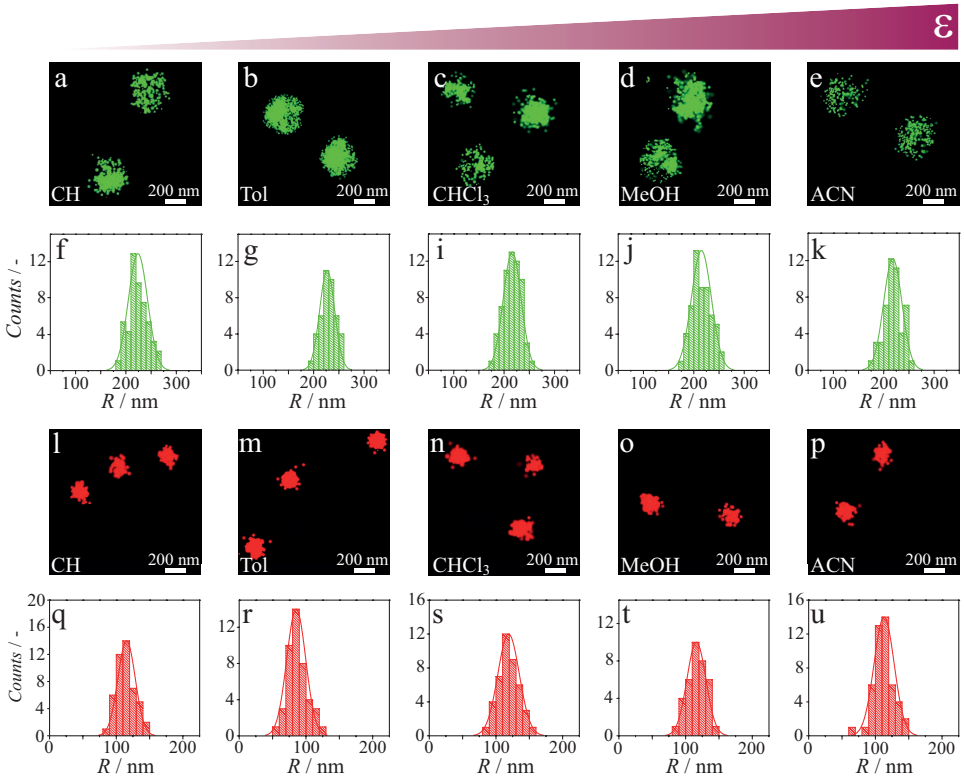

Figure 6.7: Super-resolved images of silica colloids ($R \sim 220$ nm) labelled with Cage-552 (a-e) and silica colloids ($R \sim 110$ nm) labelled with Cage-635 (l-p), respectively. The images were collected in different organic solvents (as indicated), covering a wide range of dielectric constant (ε). Scale bar 200 nm. (f-k) and (q-u) Corresponding distributions of the radii of the nanoparticles obtained by PALM image analysis.

6.2.3.2 Dispersed beads

To test whether two populations of small and large beads differing in $\langle R \rangle$ by a factor $\leq$2 can be distinguished in a mixture, we image in cyclohexane a sample with well-dispersed small and large dye-functionalized nanoparticles (fig. 6.8). As a reference, figure 6.8a shows the wide-field image obtained by summation of all frames acquired in the two channels. Clearly, individual red beads of $R_{red} \sim 110$ nm, and green beads of $R_{green} \sim 220$ nm cannot be singularly resolved. The corresponding super-resolved image, wherein all the single molecules localized in each frame are presented as small dots, is given in panel b, along with a cartoon to guide the eye in panel d, which offers a schematic representation of the arrangement of the identified silica beads in panel b. The individual small and large beads are readily identified and reconstructed. The size distributions are obtained as described in section 6.4.4 (fig. 6.8c), which yields to two well-defined peaks centered on $\langle R_{red} \rangle = 116 \pm 13$ nm and

$\langle R_{green} \rangle = 224 \pm 19$ nm. These values are in excellent agreement with those obtained from PALM imaging of the separate dispersions (fig. 6.15), demonstrating that PALM is able to accurately resolve structural features differing by less than 100 nm in dimension in organic media.

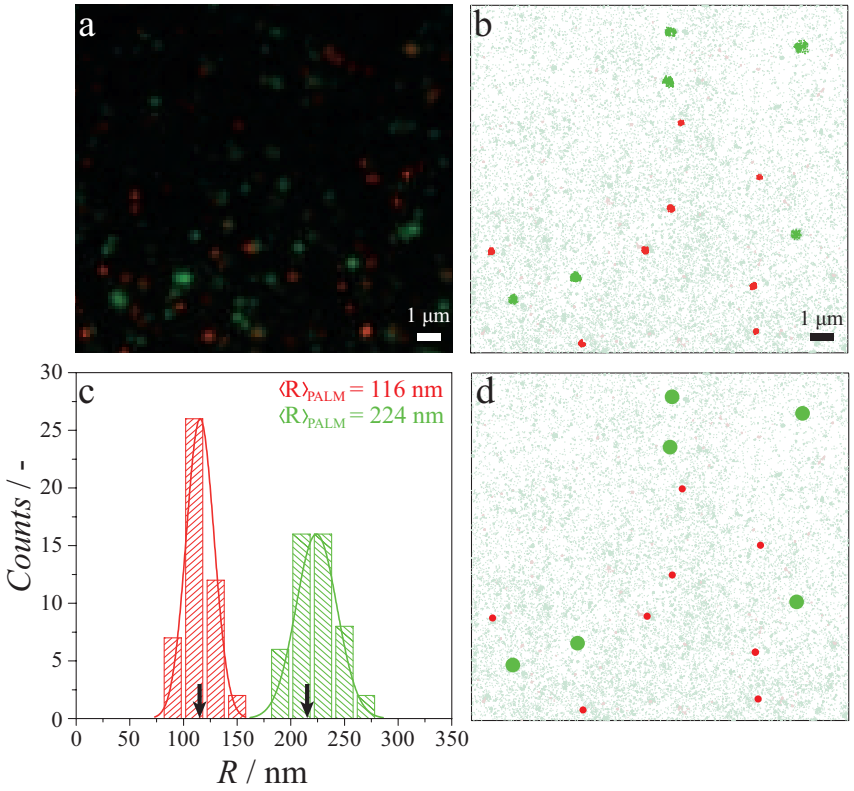

Figure 6.8: (a) Two-colour wide-field image acquired in cyclohexane with 2% v/v isopropanol of well-dispersed mixtures of silica nanoparticles of $R \sim 110$ nm labeled with Cage-635 (red dots) and $R \sim 220$ nm labeled with Cage-552 (green dots). (b) Super-resolved image of the field of view shown in a. Scale bar 1 μm. (c) Corresponding distributions of radii of the identified and reconstructed colloidal particles in the mixture; black arrows indicate the mean radii determined by SEM. (d) Schematic representation of the beads identified in b.

6.2.3.3 Clustered beads

Aiming to visualize a more complex multicomponent nanostructured material, we prepare composite aggregates of both colloids by evaporative self-assembly (fig. 6.9). The wide-field image in figure 6.9a confirms colocalization of the Cage-552 and Cage-635 tagged beads within the clusters, but is unable to resolve the individual nanoparticles. By contrast, PALM microscopy (fig. 6.9b) reveals the disordered internal structure of the aggregate, resolves individual colloids, as represented by the cartoon in figure 6.9d to guide the eye, and

recovers the narrow size distributions of both particles centered on $\langle R_{red} \rangle = 104 \pm 18$ nm and $\langle R_{green} \rangle = 225 \pm 19$ nm (fig. 6.9c). The single-molecule localizations in figure 6.9b that do not belong to a reconstructed particle are attributed to beads that are out-of-focus, as the evaporative self-assembly is not strictly 2D.

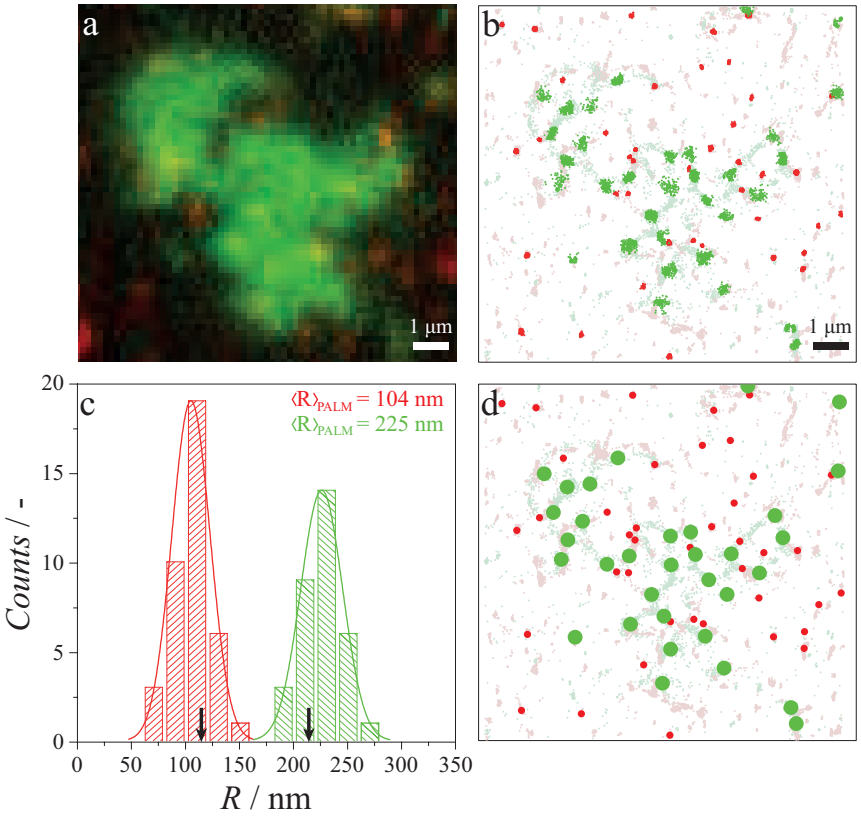

Figure 6.9: (a) Two-color wide-field image acquired in cyclohexane with 2% v/v isopropanol of a mixed cluster of colloidal particles of $R \sim 110$ nm labeled with Cage-635 and $R \sim 220$ nm labeled with Cage-552. (b) Super-resolved image of the field of view shown in a. Scale bar 1 μm. (c) Radii distribution of the nanoparticles identified and reconstructed in the mixed sample; black arrows indicate the mean radii determined by SEM. (d) Schematic representation of the beads identified in b.

6.2.4 1D supra-molecular aggregates visualized in their native environment

Encouraged by these promising results, we turn to an elusive system for standard imaging techniques due to their dynamic nature, size, and low imaging contrast: nm-thin yet μm-long, dynamic supramolecular polymers, so far studied mainly by spectroscopy and scanning-probe techniques. [31–33] For this purpose we select benzene 1,3,5-tricarboxamides (BTA). These small molecules are known to self-assemble by three-fold hydrogen bonding into nanometer-sized, one-dimensional (1D) supramolecular polymers (fig. 6.10) and have found a panoply of applications in material science. [34]

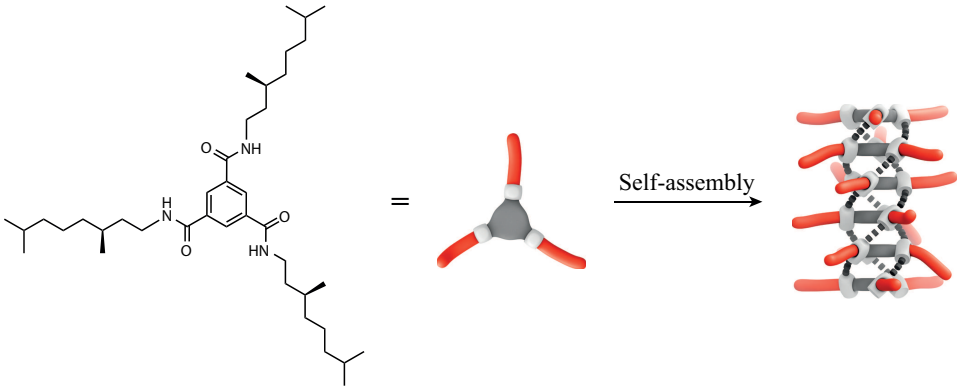

Figure 6.10: Schematic representation of benzene-1,3,5-tricarboxamides (BTA) self-assembly upon three-fold hydrogen bonding.

Figure 6.11a shows the wide-field image of a BTA aggregate containing a small amount (<5%) of monofunctionalized BTA with Cage-552 (structure 2 in fig. 6.12). Since the aggregates are 0.7-1.0 μm long and several nm's wide, the 1D morphology of fibers cannot be observed in the wide-field image. Conversely, the super-resolved image (fig. 6.11b) shows clearly the supramolecular aggregates. The sizes retrieved in figure 6.11b are in perfect agreement with the data obtained previously on similar BTA supramolecular polymers by depolarized light scattering, [35] and atomic force microscopy. [36]

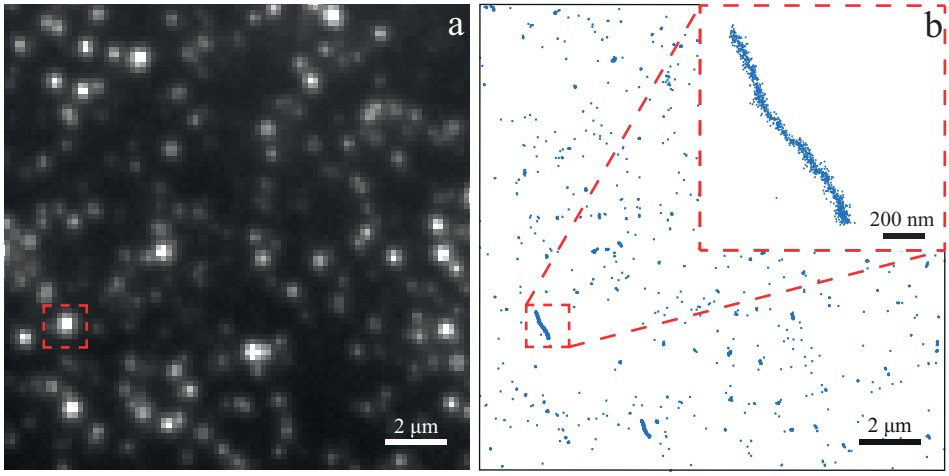

Figure 6.11: (a) Wide-field image of BTA fibers containing 5% Cage-552 labeled BTA acquired in cyclohexane with 2% v/v isopropanol. (b) Super-resolved image of the same field of view depicted in a. The inset is a zoom-in on one of the fibers.

6.3 Conclusions

In summary, we demonstrate the possibility to perform super-resolution microscopy in a wide range of organic solvents with high accuracy. Narrow-size distributions and accurate mean radii are obtained by PALM for (mixed) nanoparticle dispersions even if the nanoparticles with radii close to Abbe's diffraction limit are in close contact. While the addition of an auxiliary nucleophile is essential in the experiments reported here, we foresee integration of the nucleophile into the dye structure in future work. Furthermore, we successfully visualize the morphology of dynamic, 1D supramolecular polymers composed of hydrogen-bonded small molecules, which are elusive to other imaging techniques. We expect that *in-situ* visualization by SMLM of the structure and exchange dynamics of such supramolecular polymers in organic media will shed new light on their structure-function relations and complex polymerization pathways.

6.4 Experimental

The synthesis and characterization of BTA has been carried out by dr. A. Vargas Jentzsch. The synthesis and SEM imaging of silica particles has been carried out by dr. N. Vilanova.

6.4.1 Synthesis and characterization of BTA

Compound (**1**) reported in figure 6.12 is prepared following the reported synthetic procedure in reference. [37] The NMR and mass spectra are in agreement with those reported. ^{1}H-NMR (400 MHz, $CDCl_3$): δ = 8.35 (s, 3H, aromatic), 6.63 (m, 3H, NH), 3,48 (m, 6H, NH-CH_2), 2.67 (m, 2H, NH_2-CH_2), 1.78 ∼0.85 (m, 56H, CH_2, CH_3). ^{13}C-NMR (400 MHz, $CDCl_3$): δ =165.7, 139.4, 135.2, 135.2, 127.9, 40.3, 39.2, 38.5, 37.1, 36.6, 30.7, 29.4, 27.9, 26.9, 24.6, 22.7, 22.6, 19.5. Maldi-TOF Calcd. $[M+H]^+$= 657.56, Obs. $[M+H]^+$= 657.63. Cage-552-NHS (20 μL, 10 mM in DMSO), NH_2-C_{11}-BTA (400 μL, 200 μM in dry $CHCl_3$), and dry TEA (5 μL) (this represents a 1:2.5 ratio Cage-552 to NH_2-C_{11}-BTA) are mixed in a 1 mL Eppendorf vial to label compound (**1**) with the photo-activatable moiety and obtain compound (**2**). The reaction mixture is shaken at 500 rpm for 24 h at room temperature under protection from light. The reaction mixture is directly loaded on a SiO_2 column chromatography and eluted first with MeOH/DCM 1:9 and then MeOH/DCM 1.5:8.5. The purity of the compound is inferred from the TLC, indeed Cage-552-NHS has an R_f = 0.9 (MeOH/DCM 1:9) and Cage-552-BTA has an R_f = 0.1 (MeOH/DCM 1:9).

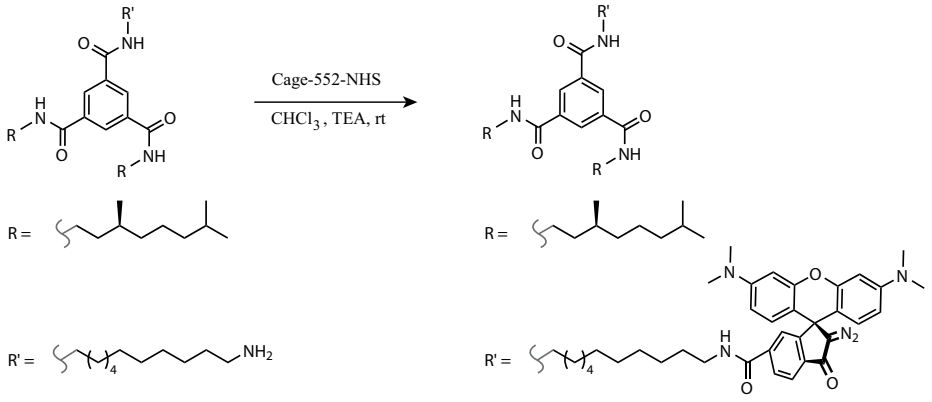

Figure 6.12: Preparation of the Cage-552 mono-functionalized BTA.

6.4.2 Synthesis and characterization of silica particles

Silica colloids of low polydispersity are synthesized using a Stöber-based method. [38–40] Briefly, 6.4 μL of (3-Aminopropyl)triethoxysilane (APTES) are mixed with 33.5 mL of ethanol and 2.8 mL of ammonia (25% in water). 2.5 mL of this solution are added to a mixture of 25 mL of ammonia (25% in water) and 250 mL of ethanol. 1.6 mL of tetraethylortosilicate (TEOS) are then added all at once under the meniscus of the reaction and the final mixture is stirred for 5 hours. Subsequently, 1.75 mL of TEOS are added and the reaction mixture is stirred overnight under an argon atmosphere. Following this procedure, particles of $R \sim$ 110 nm are obtained. Such particles are further used as seeds to synthesize bigger particles by means of growing a silica shell onto them. To do so, in a round-bottom flask equipped with 2 inlets, 51 mL of ethanol, 17 mL of water, 3.4 mL ammonia (25% in water) and 4 mL of the seed suspension (solid content 13.6 mg seeds/mL of suspension) are mixed. Through one of the inlets, a mixture of 5 mL of TEOS with 10 mL of ethanol is pumped with a peristaltic pump at 1.7 mL/hour. Through the other inlet a second mixture consisting of 1.34 mL ammonia (25% in water), 10.25 mL of ethanol and 3.4 mL of water is also pumped with the same flow rate. After all the reactants are added, the resulting suspension of silica colloids (of $R \sim$ 220 nm) is washed and stored in ethanol.

Colloids are post-functionalized with the NVOC-C_{11}-OH linker following a general method described by van Helden. [40] Briefly, 10 mg of the dried silica colloids ($R \sim$ 110 nm in radius) are dispersed by sonication in 1 mL of ethanol together with 30 mg of the NVOC-linker. [41] Subsequently, the ethanol is removed by evaporation using and argon stream. The reaction mixture is then heated up to 180 °C during 6 hours under stirring and in argon atmosphere. The resulting functionalized particles are thoroughly washed with chloroform. The big particles ($R \sim$ 220 nm) are functionalized following the same procedure but using a 1:9 stearyl alcohol:NVOC-linker molar ratio. NVOC-functionalized particles are further dispersed in chloroform and irradiated for 1 h in a UV-oven (UV-A, λ = 354 nm, 12.25 $\pm$ 0.5 mW/cm^2) under continuous stirring in order to cleave off the NVOC group, yielding hence amine-functionalized particles. The coupling of the PALM dyes is proceeded by adding 2 μL of a stock solution of 10 mM of the PALM dye in DMSO and 20μL of Et_3N to the dispersion. The system is kept under stirring overnight and particles are subsequently washed with chloroform. The resulting suspension of silica colloids is stored in ethanol.

Silica particles are characterized by SEM using a FEI Quanta 600F ESEM. Figures 6.13a and 6.13b show the SEM images of the big and small colloids, respectively. The insets depict the size distribution obtained from image analysis of more than 100 particles, using Image J: $\langle R \rangle$ = 214 $\pm$ 17 nm for the big and $\langle R \rangle$ = 115 $\pm$ 14 nm for the small colloids.

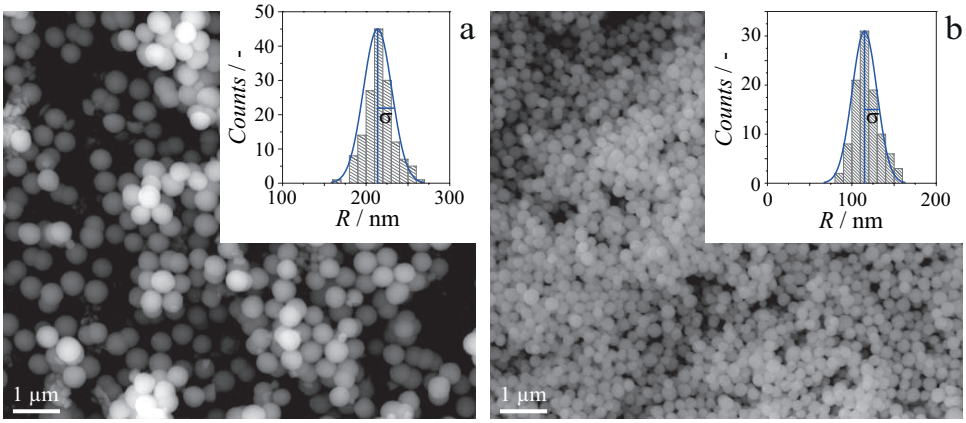

Figure 6.13: SEM characterization of silica colloids. SEM pictures of plain silica beads of $R \sim 220$ nm (a) and $R \sim 110$ nm (b). The insets illustrate the size distribution of the two batches taking into account over 100 beads for each distribution.

6.4.3 Microscopy

PALM images are acquired using a Nikon N-STORM system equipped with ∼160.0 mW/cm^2 ($\lambda = 405$ nm), ∼488 mW/cm^2 ($\lambda = 561$ nm) and ∼1335 mW/cm^2 ($\lambda = 647$ nm) laser lines configured for *quasi* total internal reflection fluorescence (*quasi*-TIRF) imaging. The excitation inclination was tuned to maximize the signal-to-noise ratio. Fluorescence is collected by means of a Nikon 100×, 1.4 NA oil immersion objective and passed through a quad-band pass dichroic filter (97335 Nikon). All timelapses are recorded onto a 256 × 256 pixel region (pixel size 170 nm) of an EMCCD camera (ixon3, Andor) at a rate of 47 frames/s. 15×10^3 frames are acquired in each experiment; the Cage-552 moieties are photo-activated with a 405 nm UV laser (0.5% power) and excited with a $\lambda = 561$ nm laser (100% power), conversely the Cage-635 moieties are photo-activated with a 405 nm UV laser (0.5% power) and excited with a $\lambda = 647$ nm laser (100% power). Single molecule localization movies are analyzed with NIS-element Nikon software. 3D PALM measurements are performed using the astigmatism method. [42] The *z*-position in 3D PALM experiments on dispersions is computed using a calibration curve made with fluorescent TetraSpeck™ microspheres ($R = 50$ nm, Life-technologies, Molecular Probes®) that relates the ellipticity of the fluorescence signal of single molecules to their *z*-position.

6.4.4 Image analysis

The image analysis procedure for PALM measurements is outlined in figure 6.14. First, the raw image (fig. 6.14a) is corrected for the background signal from a small amount of fluorescent dyes adsorbed on the glass coverslip (fig. 6.14b). The background signal removal (implemented in the NIS element Nikon software) is density-based: the algorithm looks for data points having at least *n* other data points within a certain range δ, and removes those localizations which do not fulfill the set parameters (n=10, δ=100 nm in fig. 6.14b). Next, single beads are identified (fig. 6.14c), and the localizations of single molecules corresponding to the individual beads are saved in a separate file for further analysis of particle size and size distribution (fig. 6.14d). Mean particle sizes are determined using the three-dimensional fitting routine entitled 'Sphere Fit' in Matlab. This 3D fitting routine uses the three-dimensional data set collected for each single bead that is identified and computes the center coordinates (x_c, y_c, z_c) and the sphere radius, R (fig. 6.14e). Here, $\sum[(x^2 - x_c^2)^2 + (y^2 - y_c^2)^2 + (z^2 - z_c^2) - R^2]^2$ is minimized.

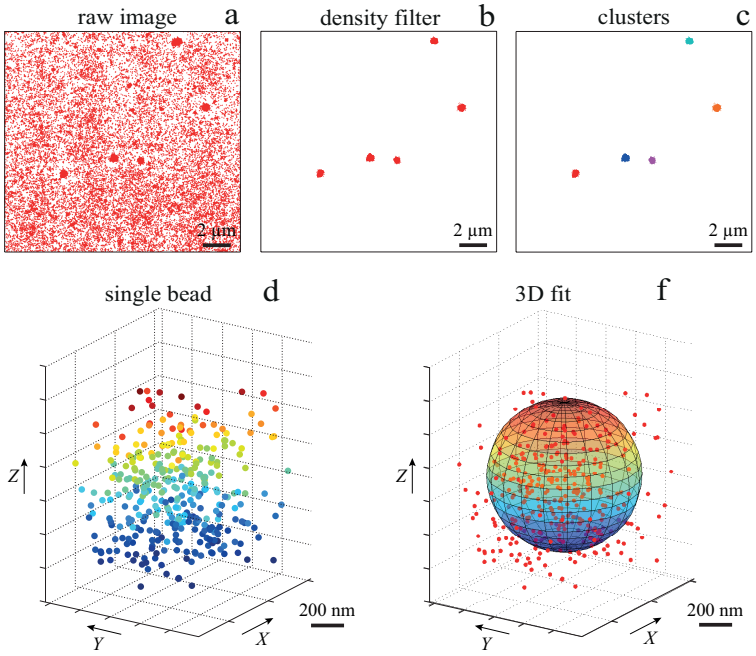

Figure 6.14: PALM data analysis routines. Representative PALM image of silica beads of $R \sim 220$ nm (a) before and (b) after background removal. (c) Identification of each individual bead; clustered beads are not taken into account in further data analysis steps. (d) Three dimensional PALM image of a single bead. (e) Three-dimensional fit of a sphere to all single molecule localizations of the entire bead shown in d to find the bead center and radius.

The size distributions of silica colloids of $R \sim 220$ nm (fig. 6.15a) and $R \sim 110$ nm

(fig. 6.15b) have been determined by PALM imaging in chloroform, methanol, acetonitrile, cyclohexane and toluene, as described in section 6.4.4. All size distributions agree well with the SEM size distribution, except for the small $R \sim 110$ nm colloids in toluene. This is because the perfect focus system (PSF) of the microscope, which provides a real time focus correction of the sample from the drift, is incompatible with toluene. Therefore, an alternative method, which relies on the brightness of the pixels in the low-resolution image, is used to image the $R_{green} \sim 220$ nm and $R_{red} \sim 110$ nm particles in toluene. Subsequent analysis of this data set follows the two-dimensional fitting routine 'Circle Fit' in Matlab. This 2D fitting routine uses the two-dimensional data set collected for each single bead that is identified and computes the center coordinates (x_c, y_c) and the circle radius, R. Here, $\sum[\,(x^2 - x_c^2)^2 + (y^2 - y_c^2)^2 - R^2]^2$ is minimized. This method works well for large objects, such as the $R \sim 220$ nm colloids in toluene (fig. 6.15a), but is suboptimal for small objects, such as the $R \sim 110$ nm particles in toluene (fig. 6.15b), when the uncertainty related to the focus determination is comparable to the size of the particles. Thus, a small error in the determination of the focal plane leads to a visible shift of the size distribution to lower $\langle R \rangle$.

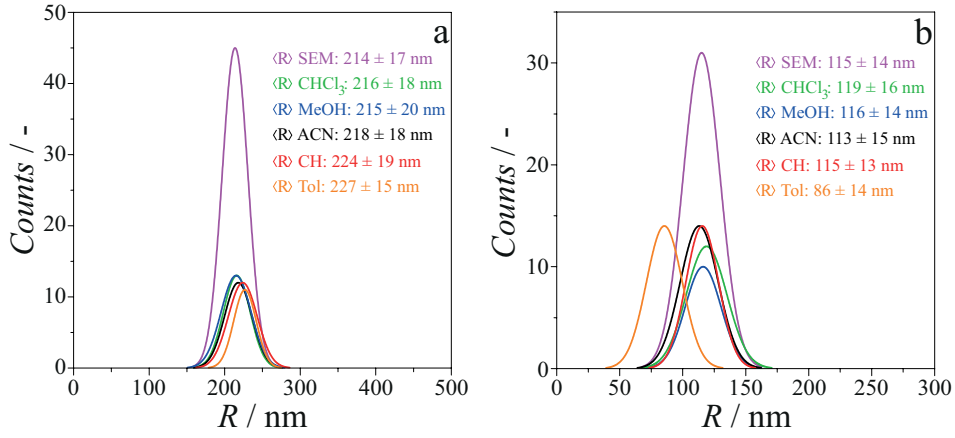

Figure 6.15: Size distribution of large and small silica colloids. Size distributions of silica beads of (a) $R \sim 220$ nm labelled with Cage-552 and (b) $R \sim 110$ nm labelled with Cage-635 obtained from three-dimensional fits (for chloroform, methanol, acetonitrile and cyclohexane), and a two-dimensional fit (for toluene) on all single molecule localizations of the entire beads as described in figure 6.14.

6.4.5 Sample preparation

Sample chambers are made from a coverslide (Menzel Gläser, 76×26 mm, thickness 1 mm) onto which a coverslip (Menzel Gläser, No. 1.5, 24×24 mm, thickness 170 μm) is glued with double-sided tape. Prior to assembly of the chamber, the coverslip is cleaned to remove impurities and to reduce background fluorescence as follows: the coverslip is consecutively

immersed and sonicated for 10 minutes in acetone, isopropanol and MilliQ water (18.2 MΩ), followed by piranha etching, extensive rinsing with MilliQ water and finally drying with a N_2 stream.

6.4.5.1 Silica particles

PALM samples are prepared by application of few drops of the colloidal dispersion onto a coverslip, followed by drying in a N_2 stream after which the sample chamber is closed and a solution of organic solvent is introduced.

6.4.5.2 BTA fibers

A solution containing 5% (molar concentration) of Cage-552-BTA in non-functionalized BTA at a final concentration of 5×10^{-5} M in methylcyclohexane is prepared by mixing the appropriate amounts of stock solutions (200 μM in methylcyclohexane). The new solutions are heated to 70 °C for 5 min in a water bath to equilibrate the supramolecular structure. The mixed fibers are spin-casted (2000 rpm, 60 sec) on a cleaned coverslip which is used to close the sample chamber. Cyclohexane (with 2% v/v isopropanol) is fluxed in before imaging.

Bibliography

[1] Betzig, E.; Patterson, G.H.; Sougrat, R.; Lindwasser, O.W.; Olenych, S.; Bonifacino, J.S.; Davidson, M.W.; Lippincott-Schwartz, J.; Hess, H.F. *Science* **2006**, *313*, 1642.

[2] Hofmann, M.; Eggeling, C.; Jakobs, S.; Hell, S.W. *Proc. Natl. Acad. Sci. U. S. A.* **2005**, *102*, 17565.

[3] Huang, B.; Babcock, H.; Zhuang, X. *Cell* **2010**, *143*, 1047.

[4] Grotjohann, T.; Testa, I.; Leutenegger, M.; Bock, H.; Urban, N.T.; Lavoie-Cardinal, F.; Willig, K.I.; Eggeling, C.; Jakobs, S.; Hell, S.W. *Nature* **2012**, *478*, 204.

[5] Eggeling, C.; Willig, K.I.; Sahl, S.J.; Hell, S.W. *Q. Rev. Biophys.* **2015**, *48*, 178.

[6] Heilemann, M.; van de Linde, S.; Schüttpelz, M.; Kasper, R.; Seefeldt, B.; Mukherjee, A.; Tinnefeld, P.; Sauer, M. *Angew. Chem., Int. Ed.* **2008**, *47*, 6172.

[7] Shi, Y. *Cell* **2014**, *159*, 995.

[8] Wüthrich, K. *J. Biol. Chem.* **1990**, *265*, 22059.

[9] Bai, X.-C.; McMullan, G.; Scheres, S.H.W. *Trends Biochem. Sci.* **2015**, *40*, 49.

[10] Lakadamyali, M.; Babcock, H.; Bates, M.; Zhuang, X.; Lichtman, J. *PLoS One* **2012**, *7*, e30826.

[11] Wang, W.; Li, G. W.; Chen, C.; Xie, X.S.; Zhuang, X. *Science* **2011**, *333*, 1445.

[12] Dempsey, G.T.; Vaughan, J.C.; Chen, K.H.; Bates, M.; Zhuang, X. *Nat. Methods* **2011**, *8*, 1027.

[13] Aida, T.; Meijer, E.W.; Stupp, S.I. *Science* **2012**, *335*, 813.

[14] Matson, J.B.; Stupp, S.I. *Chem. Commun.* **2012**, *48*, 26.

[15] Albertazzi, L.; van der Zwaag, D.; Leenders, C.M.A.; Fitzner, R.; van der Hofstad, R.W.; Meijer, E.W. *Science* **2014**, *344*, 491.

[16] Boott, C.E.; Laine, R.F.; Mahou, P.; Finnegan, J.R.; Leitao, E.M.; Webb, S.E.D.; Kaminski, C.F.; Manners, I. *Chem. - Eur. J.* **2015**, *21*, 18539.

[17] Harke, B.; Ullal, C.K.; Keller, J.; Hell, S.W. *Nano Lett.* **2008**, *8*, 1309.

[18] Friedemann, K.; Turshatov, A.; Landfester, K.; Crespy, D. *Langmuir* **2011**, *27*, 7132.

[19] Schermelleh, L.; Heintzmann, R.; Leonhardt H.J. *Cell Biol.* **2010**, *190*, 165.

[20] van de Linde, S.; Sauer, M. *Chem. Soc. Rev.* **2014**, *43*, 1076.

[21] Rust, M.J.; Bates, M.; Zhuang, X. *Nat. Methods* **2006**, *3*, 793.

[22] van de Linde, S.; Kasper, R.; Heilemann, M.; Sauer, M. *Appl. Phys. B* **2008**, *93*, 725.

[23] van de Linde, S.; Löschberger A.;, Klein, T.; Heidbreder, M.; Wolter, S.; Heilemann, M.; Sauer, M. *Nat. Protoc.* **2011**, *6*, 991.

[24] Belov, V.N.; Wurm, C.A.; Boyarskiy, V.P.; Jakobs, S.; Hell, S.W. *Angew. Chem., Int. Ed.* **2010**, *49*, 3520.

[25] Grimm, J.B.; Sung, A.J.; Legant, W.R.; Hulamm, P.; Matlosz, S.M.; Betzig, E.; Lavis, L.D. *ACS Chem. Biol.* **2013**, *8*, 1303.

[26] Lord, S.J.; Conley, N.R.; Lee, H.-L. D.; Samuel, R.; Liu, N.; Twieg, R.J.; Moerner, W.E. *J. Am. Chem. Soc.* **2008**, *130*, 9204.

[27] Belov, V.N.; Mitronova, G.Y.; Bossi, M.L.; Boyarskiy, V.P.; Hebisch, E.; Geisler, C.; Kolmakov, K.; Wurm, C.A.; Willig, K.I.; Hell, S.W. *Chem. - Eur. J.* **2014**, *20*, 13162.

[28] Suppan, P.J. *Photochem. Photobiol., A* **1990**, *50*, 293.

[29] Resch-Genger, U.; Rurack, K. *Pure Appl. Chem.* **2013**,*85*, 2005.

[30] Gelles, J.; Schnapp, B.J.; Sheetz, M.P. *Nature* **1988**, *331*, 450.

[31] Ogi, S.; Sugiyasu, K.; Manna, S.; Samitsu, S.; Takeuchi, M. *Nat. Chem.* **2014**, *6*, 188.

[32] Korevaar, P.A.; George, S.J.; Markvoort, A.J.; Smulders, M.M.J.; Hilbers, P.A.J.; Schenning, A.P.H.J.; De Greef, T.F.A.; Meijer, E.W. *Nature* **2013**, *481*, 492.

[33] Kang, J.; Miyajima, D.; Mori, T.; Inoue, Y.; Itoh, Y.; Aida, T. *Science* **2015**, *347*, 646.

[34] Cantekin, S.; De Greef, T.F.A.; Palmans, A.R.A. *Chem. Soc. Rev.* **2012**, *41*, 6125.

[35] Mes, T.; Cantekin, S.; Balkenende, D.W.R.; Frissen, M.M.M.; Gillissen, M.A.J.; De Waal, B.F.M.; Voets, I.K.; Meijer, E.W.; Palmans, A.R.A. *Chem. - Eur. J.* **2013**, *19*, 8642.

[36] Roosma, J.; Mes, T.; Leclère, P.; Palmans, A.R.A.; Meijer, E.W. *J. Am. Chem. Soc.* **2008**, *130*, 1120.

[37] Liu, Y.; Pauloehrl, T.; Presolski, S.I.; Albertazzi, L.; Palmans, A.R.A.; Meijer, E.W. *J. Am. Chem. Soc.* **2015**, *137*, 13096.

[38] Stöber, W.; Fink, A.; Bohn, E.J. *Colloid Interf. Sci.* **1968**, *26*, 62.

[39] Giesche, H. *J. Eur. Ceram. Soc.*, **1994**, *14*, 189.

[40] van Helden, A.K.; Jansen, J.W.; Vrij, A.J. *Colloid Interf. Sci.* **1981**, *81*, 354.

[41] Vilanova, N.; de Feijter, I.; Voets, I.K., *J. Vis. Exp.* **2016**, *110*, e53934.

[42] Huang, B.; Wang, W.; Bates, M.; Zhuang, X. *Science* **2008**, *319*, 810.

Chapter 7

Perspectives in single-molecule localization microscopy

Exemplary applications of iPAINT and PALM microscopy in material science and supramolecular chemistry have been presented in the previous chapters. One of the major advantages of iPAINT is the versatility of its labelling strategy: photo-activatable dyes are introduced in a non-covalent fashion through physical adsorption, instead of *via* chemical modifications of the material under scrutiny. In this chapter, we first showcase the general applicability of iPAINT in two additional studies on supramolecular fibers (Part I) and nanoparticles-liposomes mixtures (Part II). We use two-colour iPAINT microscopy to validate by direct visualization spectroscopic measurements on supramolecular copolymers, which indicate the formation of block-like architectures. The presence of these blocks and their stability over time is investigated. Next, we use a combination of PAINT and iPAINT microscopies to investigate the recruitment of drug carriers by nanoparticles. We study the structural integrity of the carriers upon recruitment by the nanoparticles, and we quantify the clearance efficiency of the nanoparticles. In Part III we report on the preliminary characterization of a new rhodamine spirolactam dye for super-resolution microscopy. In stark contrast to most of the commercially available photo-activatable dyes, this new dye enables iPAINT in both aqueous and organic solvents, irrespective of pH, polarity and addition of co-solvents.

Part of this work has been submitted as:
Part I: Adelizzi, B.; Aloi, A.; Markvoort, A.J.; ten Eikelder, H.M.M.; Voets, I.K.; Palmans, A.R.A.; Meijer, E.W. & Aloi, A.*; Adelizzi, B.*; van Zee, N.J.; Palmans, A.R.A.; Meijer, E.W.; Voets, I.K.;
Part II: Aloi, A.*; van Onzen, A.H.A.M.*; Jacobs, I.; Versteegen, R.M.; Janssen, H.M.; Milroy, L.G.; Robillard, M.S.; Brunsveld, L.; Voets, I.K.
Part III: Vargas Jentzsch, A; Aloi, A.; Voets, I.K.; Anderson, H.L.

Part I

Thermodynamically stable supramolecular copolymers visualized by single-molecule localization microscopy

7.1 Introduction

The widespread implementation of nanotechnology and micro-engineered devices calls for a rapid development of high-performance (ordered) nanostructured materials. Since homopolymers and random copolymers can rarely be used to prepare such ordered topologies, controlling the monomer sequence within polymers is of crucial importance. In conventional polymers, wherein monomers are covalently bonded, block-wise arrangements are routinely produced [1] by tuning the reactivity kinetics of the monomers, [2] or *via* living polymerization. [3] In supramolecular polymers with non-covalently bound monomers, sequence control necessitates insights over the molecular recognition and assembly pathways of the constituents. Aiming to build-up supramolecular block copolymers, B. Adelizzi designed and synthesized two chiral molecules (fig. 7.1a, and 7.1b) with similar geometry: tri(pyrid-2-yl)amine tricarboxamide (*S*-1), and triphenylamine tricarboxamide (*S*-2), and the equivalent achirals (*A*-1, *A*-2).

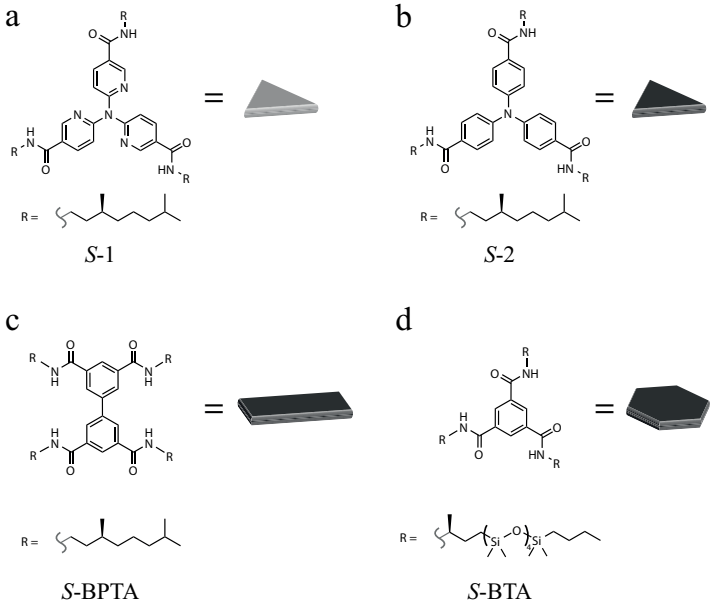

Figure 7.1: Different supramolecular monomers capable of hydrogen-bond mediated assembly. (a) Tri(pyrid-2-yl)amine tricarboxamide (*S*-1). (b) Triphenylamine tricarboxamide (*S*-2). (c) N3,N3',N5,N5'-Tetrakis((S)-3,7-dimethyloctyl)-[1,1'-biphenyl]-3,3',5,5'-tetracarboxamide (*S*-BPTA). (d) N1,N3,N5-tris((R)-3,7-dimethyloctyl)benzene-1,3,5-tricarboxamide (*S*-BTA).

These monomers have been proven already to have analogous propensity to self-assemble into uni-dimensional fibers, [4] with interesting applications in water splitting solar cells. [5] Preliminary light scattering, spectroscopic studies and theoretical modeling on mixtures of *S*-1 and *S*-2, in a 1:1 ratio, indicate the presence of block-like architectures in the self-

assembled fibers. However, conclusive experimental evidence is lacking. Here, we report on the imaging of stable supramolecular block copolymers in organic solvents by two-colour iPAINT measurements. Moreover, we study the stability of these blocks over time.

7.2 Results and discussion

Aiming to test the feasibility of single-molecule localization microscopy experiments to visualize supramolecular fibers of *S*-1 and *A*-1, *S*-2 and *A*-2, *S*-BPTA and *S*-BTA, we first perform single colour iPAINT experiments on the supramolecular homopolymers. These reveal bundling of fibers of *A*-1, which we attribute to the low solubility of the system. Next, we image supramolecular copolymers in two-colour, which demonstrates an unusual block-like organization, in support of the spectroscopic data. Finally, we report on the kinetic stability over several days of the block-like constructs obtained.

7.2.1 Supramolecular homopolymers imaged by iPAINT microscopy

First, we evaluate whether the recently developed technology iPAINT [6] can be extended to image supramolecular polymers in organic solvents. To this end, we prepare a 200 μM solution of each monomer (*S*-1, *S*-2, *S*-BPTA, and *S*-BTA) in methylcyclohexane, and we allow the system to self-assemble into uni-dimensional fibers. Then we add 1% v/v of isopropanol (see chapter 6 for details), [7] and dissolve $\sim$0.5-1% v/v of the caged dye (Cage-552 or Cage-635) in the solutions. Here, the 'staining' is achieved through a non-covalent interaction between the dyes and the supramolecular homopolymer. The advantage of this strategy is that it circumvents the need for time-consuming synthesis of chromophore-tagged molecules. It does, however, necessitate additional control experiments. Since the dyes are not permanently bound to the monomers, they might influence the self-assembly process as well. It is worth to note that due to the non-covalent labelling of the fibers, the dye molecules might desorb from the aggregates or migrate along the fibers. Hence, it is of crucial importance to prove the correspondence between the localizations of the dye and the monomer, such that the dye reports on the localization of the monomer. This is particularly important in the two-colour iPAINT experiments (described in the next section), in which we probe the block-like organization along the supramolecular fibers.

Figure 7.2 illustrates exemplary images of supramolecular homopolymers which are several μm long. The poly(*S*-1) fibers are stained with Cage-635 (fig. 7.2a), while the poly(*S*-2) (fig. 7.2b), poly(*S*-BPTA) (fig. 7.2c) and poly(*S*-BTA) (fig. 7.2d) fibers are stained with Cage-552. Most of these single-component fibers are linear, occasionally we find poly(*A*-1)

branched fibers.

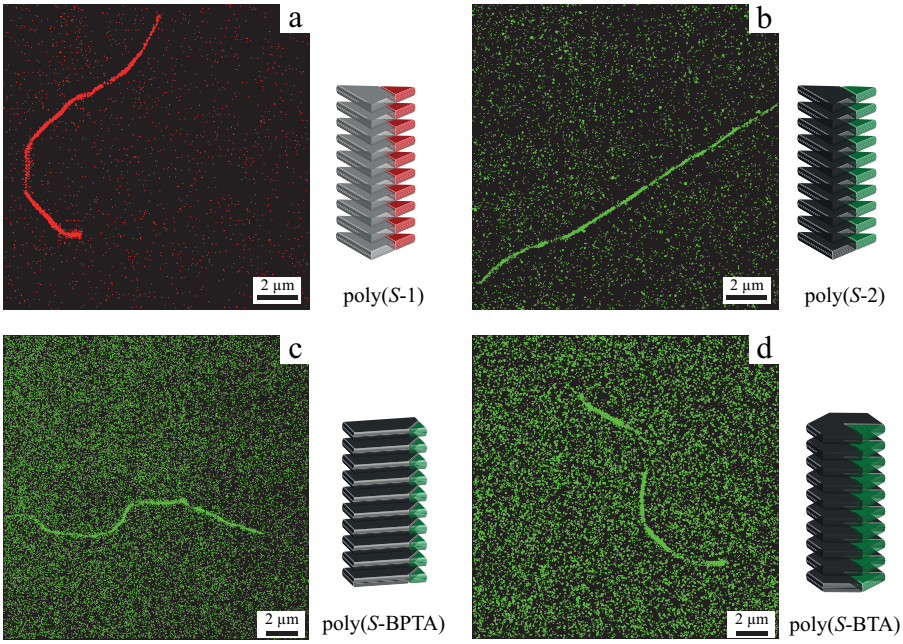

Figure 7.2: iPAINT images of four different hydrogen-bonded supramolecular polymers. (a) Tri(pyrid-2-yl)amine tricarboxamide (poly(*S*-1)) supramolecular fiber stained with Cage-635. (b) Triphenylamine tricarboxamide (poly(*S*-2)) supramolecular fiber stained with Cage-552. (c) N3,N3',N5,N5'-Tetrakis((S)-3,7-dimethyloctyl)-[1,1'-biphenyl]-3,3',5,5'-tetracarboxamide (poly(*S*-BPTA)) supramolecular fiber stained with Cage-552. (d) N1,N3,N5-tris((R)-3,7-dimethyloctyl)benzene-1,3,5-tricarboxamide (poly(*S*-BTA)) supramolecular fiber stained with Cage-552. Imaging carried out in methylcyclohexane, with 0.5% v/v in (a-b) and 1% v/v in (c-d) of caged dye, 10 mM in DMSO, plus 1% v/v isopropanol.

We examine bundling of the poly(*A*-1) fibers more closely, by studying the thickness of the fibers (fig. 7.3). A multi-branched aggregate is visible in wide-field, with protrusion of several μm's in length (fig. 7.3a). As upper limit for their mean thickness, we take the full width at half maximum (FWHM) from the intensity profile *vs.* pixel position. We obtain comparable values for three exemplary branches (fig. 7.3a): 458 nm, 529 nm and 418 nm (fig. 7.3c-e). Hence, the branches appear to have a similar upper bound thickness, which may be because their thickness is comparable, or because it is much smaller than the diffraction limit. The same analysis on the super-resolved image (fig. 7.3b) unveils finer thickness with up to 6-fold difference in width.The thinnest reconstructed fiber is 26 nm wide, and the thickest 120 nm. The 26 nm cross-section of the thinnest fiber compares well with the 25 nm width reported for BTA fibers previously reported in our group by STORM microscopy. [8] Once again, this is due to the resolution limit of both microscopy methods. We attribute the bundling observed by iPAINT of poly(*A*-1) to the scarce solubility of the compound, already observed macroscopically.

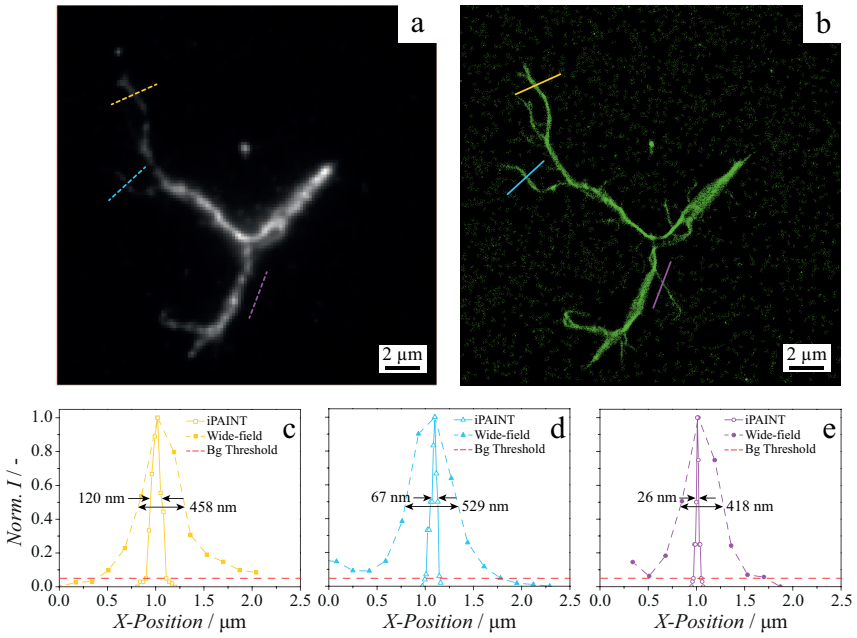

Figure 7.3: iPAINT imaging and thickness analysis of a supramolecular polymers. (a) Wide-field image and (b) relative super-resolved image of poly(*A*-1). The thickness analysis has been carried out on different branches highlighted with yellow, cyan and purple lines in (a) and (b). The thickness measured in wide-field are reported for thick bundles, and a single fiber with closed symbols and dashed line in (c-e), while the open symbols and solid lines are the respective thicknesses obtained from the super-resolved image.

7.2.2 Supramolecular copolymers made out of μm-long blocks

The poly(*S*-1) and poly(*S*-2) homopolymers described above have very similar planar geometry handedness (in a range of temperature between 7 °C and 70 °C) and act as a donor-acceptor couple when the two are in close proximity. It is therefore of interest to study their arrangement within mixed supramolecular fibers. Circular dichroism (CD) on 1:1 poly(*S*-1):poly(*S*-2) mixtures (data not shown) revealed fiber formation, which was further studied in so-called "sergeant and soldiers" (S&s) experiments to test the interaction between the monomers. In a typical S&s on mixed fibers, the chiral "sergeant" *S*-1 monomer imposes its helicity to achiral "soldiers" *A*-2 monomers. For *S*-1/*A*-2, the S&s experiment revealed such chiral transfer, which was found to be temperature dependent. Below 5 °C, no chirality transfer was observed, suggesting completely self-sorted fibers. At elevated temperature, the presumably self-sorted fibers started to interact, which gave rise to a different fingerprint in the spectra. These CD experiments were supported by UV-vis spectra (data not shown) also performed by B. Adelizzi, which suggested intercalation of *S*-1 and *S*-2. However, none of these techniques can be used to provide direct evidences for the monomer

arrangement within the poly[(*S*-1)-co-(*S*-2)] fibers, which may be block-like or random. Hence, two-colour iPAINT microscopy experiments were performed aiming to clarify by direct visualization whether *S*-1/*S*-2 are arranged in a random or block-wise fashion within mixed fibers. To this end, we stain poly(*S*-1) fibers with Cage-635 and poly(*S*-2) fibers with Cage-552 in separate vials, and add 1% v/v iso-propanol to the solutions. Subsequently, we mix the two pre-stained supramolecular homopolymers in a 1:1 ratio at 40 °C, where the fibers have the same handedness, and adsorb the fibers on the microscope coverslip to anneal their structures. Distinct block-like architectures as visible in two-colour iPAINT images (fig. 7.4). The (predominantly) di- and tri-block copolymers have blocks with a mean length of roughly ∼3-4 μm.

We have stained the individual fibers prior mixing aiming to identify poly(*S*-1) blocks as red (Cage-635) and poly(*S*-2) blocks as green (Cage-552). But, since the dyes are not covalently attached to the monomers, we need to confirm that Cage-635 reports on *S*-2 and Cage-552 on *S*-1, *i.e.*, that the location of the dyes indeed corresponds to the location of the monomers throughout the experiments. In the following we describe a series of experiments performed to exclude imaging artifacts (section 7.2.3), desorption of the dye and its migration along the fibers (section 7.2.4, 7.2.5), specific dye-fiber (section 7.2.6) or dye-monomer interactions (section 7.2.7).

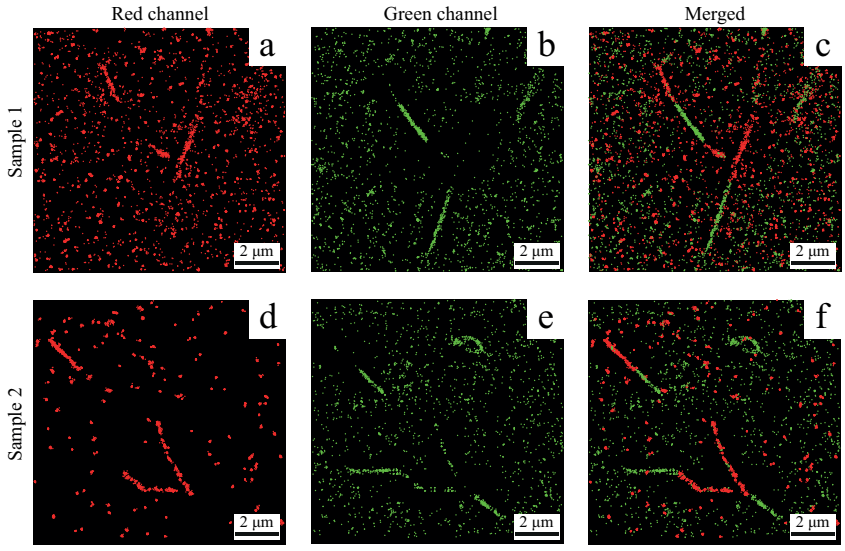

Figure 7.4: iPAINT imaging of supramolecular copolymer poly[(*S*-1)-co-(*S*-2)]. Copolymer obtained adding poly(*S*-2) stained with 1% v/v Cage-552, 10 mM in DMSO, to poly(*S*-1) stained with 0.5% v/v Cage-635, 10 μM in DMSO, and 1% v/v isopropanol at 40 °C.

7.2.3 Quantification of spectral overlap in two-colour iPAINT imaging

In a typical two-colour iPAINT experiment the sample is illuminated by a UV laser ($\lambda = 405$ nm) to photo-activate the dyes, and two read-out beams ($\lambda = 561$ nm and $\lambda = 647$ nm) to excite the photo-activated dyes, in an alternate fashion. When the $\lambda = 561$ nm laser line is ON, the imaging software registers all the single molecules localized in that frame in the 'green' channel. Alternatively, the molecules are registered as 'red' when the illumination of the sample is operated by $\lambda = 647$ nm laser line. The alternation between green and red illumination in subsequent frames leads to the distinction between green and red dyes. This is needed since all the single molecules are localized on a single greyscale EMCCD camera without spectral filters, and not on separated detectors. To localize solely Cage-552 when the green laser is ON, the absorption of the red fluorescent tag Cage-635 at $\lambda = 561$ nm should be zero. The same holds for the green molecules when the $\lambda = 647$ nm laser line is ON. Conversely, if the green (red) dye has a non-negligible absorbance at $\lambda = 647$ nm ($\lambda = 561$ nm), a small amount of green (red) molecules will be excited and localized in the red (green) frame as red (green) molecules. We refer to this incorrect attribution as false positives or crosstalk between two subsequent frames.

The absorption spectra of the open (uncaged) forms of Cage-552 and Cage-635 are reported in figure 7.5a, together with the excitation laser lines $\lambda = 561$ nm and $\lambda = 647$ nm. A non-negligible spectral overlap is clearly visible between the two dyes (fig. 7.5a). When Cage-552 molecules ($\lambda_{max}^{abs} = 552$ nm) are excited at $\lambda = 647$ nm, roughly 3% of the dye is absorbing (green circle in fig. 7.5a). In the case of Cage-635, the spectral overlap is higher, and upon excitation at $\lambda = 561$ nm more than 20% of the molecules absorb (red circle in fig. 7.5a). To demonstrate the effect of the spectral overlap on the imaging of supramolecular fibers, we prepare single-colour stained homopolymers and image them in wide-field with $\lambda = 561$ nm and $\lambda = 647$ nm laser lines. A solution of poly(*S*-2) is stained with Cage-552, whereas a solution of poly(*S*-1) homopolymer is stained with Cage-635. Figure 7.5b shows the wide-field image of Cage-552-stained poly(*S*-2) collected in the green frame upon illumination of $\lambda = 561$ nm, and in the red frame upon $\lambda = 647$ nm excitation. The contour of the fiber is visible under both illuminations. In the case of the Cage-635-stained fiber (fig. 7.5b, bottom row) the poly(*S*-1) is completely visible in wide-field in both the green and red frames.

Given the observed spectral overlap, we need to quantify which percentage of the localizations corresponds to false positives in a two-colour iPAINT experiment. To this end, iPAINT imaging of the single-colour stained homopolymers has been carried out, illuminating the fibers with $\lambda = 561$ nm and $\lambda = 647$ nm, as done before for the wide-field microscopy.

Figure 7.6a illustrates the reconstruction of a poly(*S*-2) fiber stained with Cage-552. The

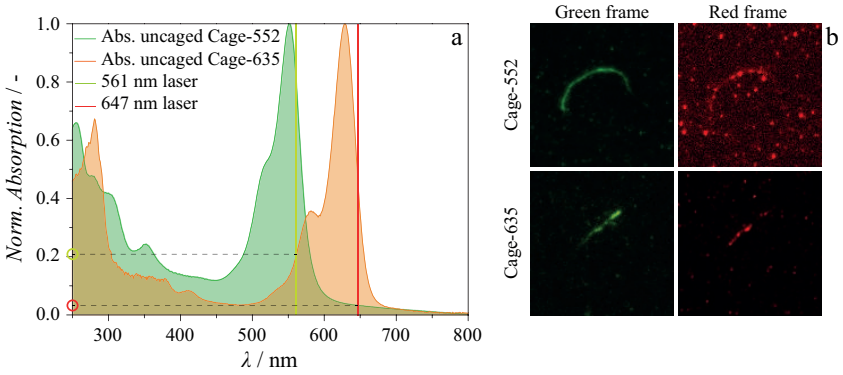

Figure 7.5: Absorption spectra of the open (uncaged) form of Cage-552 and Cage-635. (a) Spectral overlap in Cage-552 (green spectrum) and Cage-635 (orange spectrum) when excited by $\lambda = 561$ nm (green solid line) and $\lambda = 647$ nm (red solid line) lasers. (b) Green-stained fiber visualized in the green and red frames (top row), and red-stained fiber visualized in the green and red frame (bottom row).

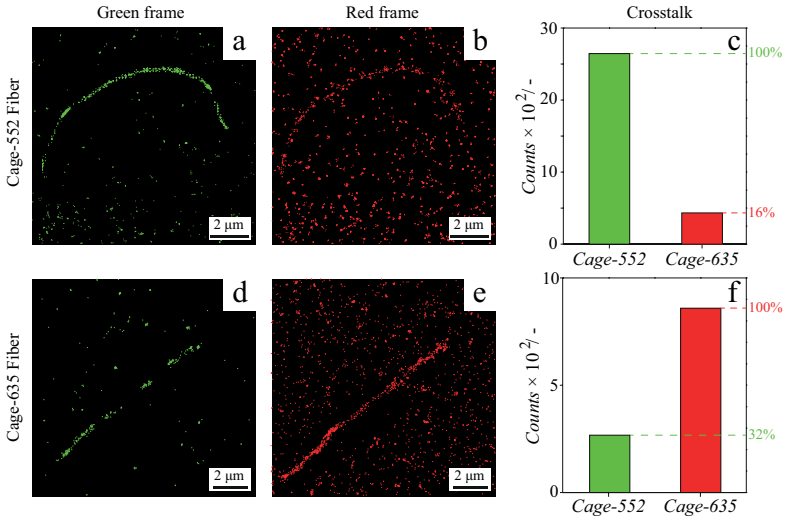

Figure 7.6: Exemplary single-colour stained supramolecular homopolymers. (a-b) Poly(*S*-2) stained with Cage-552, and (d-e) poly(*S*-1) stained with Cage-635 both excited by $\lambda_{ex} = 561$ nm and $\lambda_{ex} = 647$ nm. The false positive localizations on the (c) green and (f) red fibers amount to 16% and 32%, respectively.

amount of false positives calculated in the red frames (fig. 7.6b) is 16% compared to the single-molecule localized in the green frames (fig. 7.6c). We perform the same measurement on poly(*S*-1) homopolymer stained with Cage-635. Here, 32% of the red molecules have been localized also in the green frame (fig. 7.6f), in line with the higher spectral overlap reported in figure 7.5a.

It is worth to note that, the spectral overlap is not the only factor causing false positives in two-colours iPAINT imaging. The uncaging mechanism of the caged dyes plays a role as well. In fact, we assume that photo-activation, excitation and emission of a single molecule

occurs within a single frame (∼20 ms). However, a small fraction of molecules can have slower reactions to the illumination, due to the stochasticity of the uncaging process, to their local environment, or the position in the focal plane. This effect contributes to the spectral overlap of the dyes, increasing the number of false positives in the single-molecule measurements compared to the crosstalk percentage calculated from the absorption spectra.

Next, we compare the number of green localizations in the predominantly red blocks, and *vice versa*, the number of red localizations in the green blocks, within the poly[(*S*-1)-co-(*S*-2)] (fig. 7.4) with the crosstalk percentages (fig. 7.6). In the two-colour experiment, we find that 11.3% of all localizations in the red block are registered as green, while 18.4% of all single-molecule localizations in the predominantly green block are recorded as red (fig. 7.4). These values are comparable to the calculated crosstalk in the single-colour homopolymers (fig. 7.6). Hence, we attribute these to crosstalk due to spectral overlap of the dyes. This means that upon mixing the green blocks observed in figure 7.4 are stacks of poly(*S*-2), while the red blocks are stacks of *S*-1 monomers.

7.2.4 The dye on the fibers does not exchange with the bulk reservoir

One of the main advantages of iPAINT microscopy is the non-covalent labelling of the structure of interest. The high concentration of dye free in solution during iPAINT imaging allows for continuous labelling and hence long and more accurate localizations, as described in chapter 2. In the case of supramolecular block copolymers, instead, the desorption and re-adsorption of free dye in solution would be detrimental for the imaging, since the dye-monomer correspondence would be lost. Hence, we now evaluate whether the dyes remain on the fiber during the imaging time (∼3 min), or whether they exchange with the free dye in solution.

To this end, we image single-colour stained poly(*S*-1) and poly(*S*-2) and determine the number of single-molecule localizations along the fibers within the imaging time. Figure 7.7a illustrates a poly(*S*-2) fiber stained with Cage-552, and the counts of single molecules localized as a function of time. The number of localizations clearly decreases exponentially in time. This suggests that the dye adsorbed on the fiber is not exchanging with the free dye in solution. The same behaviour is observed for the poly(*S*-1) fibers stained with Cage-635 (fig. 7.7b). After ∼200 s, no more Cage-552 molecules are localized, while Cage-635 shows a faster decreasing rate, since after ∼80 s no more red dyes are localized.

The absence of exchange between the dye on the fiber and the dye in the bulk reservoir may have several origins. The interaction between the fiber and the dye could be fairly strong, hence preventing the dye to leave the surface of the fibers, or the dye in the reservoir

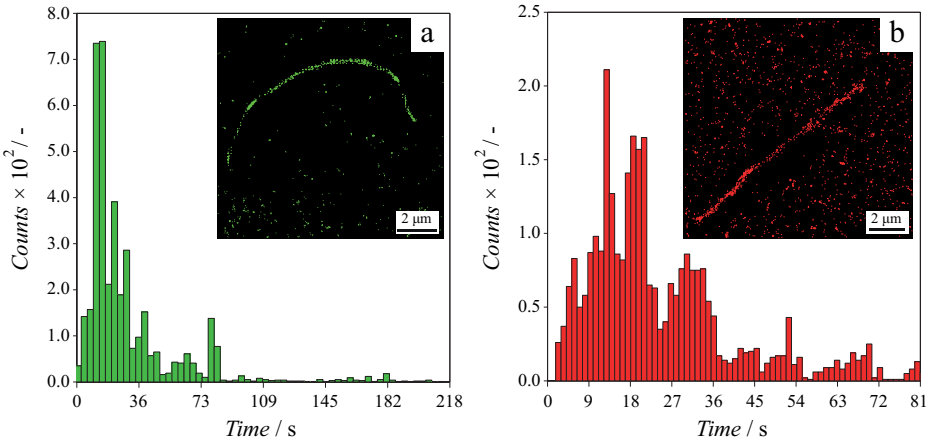

Figure 7.7: Decay of single-molecule localizations in supramolecular homopolymers. (a) Single molecule localized in time along the poly(*S*-2) stained with Cage-552. (b) Single molecule localized in time along the poly(*S*-1) stained with Cage-635. An exponential decay is observed for the localizations of both dyes, suggesting no exchange with the dye free in solution is taking place.

is depleted by strong adsorption on the coverslip. The latter would result in a high localization density on the coverslip. We register a mean value of ∼500 localizations/μm^2 in the two-colour iPAINT experiment in this chapter. In iPAINT experiments where the exchange between the adsorbed dyes and the bulk reservoir has been observed (chapter 2), we find roughly 5 times less localizations. Hence, the depletion of the dye molecules from the bulk reservoir is an important contributor to the absence of exchange in the experiments presented in this chapter. We attribute this to the low solubility of the dye in the organic solvents relatively to water (chapter 2). This is in line with the observation that UV-vis spectra of Cage-552 and Cage-635 could not be collected in cyclohexane/iso-propanol mixtures due to its poor solubility, as reported in chapter 6.

In summary, the depletion of the dye from the bulk reservoir enables to maintain the dye-monomer correspondence throughout the iPAINT experiments, by preventing exchange between the dyes adsorbed on the fiber and those in solution.

7.2.5 No migration of the dye is observed along the fibers

In the above we demonstrated that the small amount of red localizations in the green blocks, and *vice versa*, is due to spectral overlap between the dyes used, and there is no exchange between the dye adsorbed on the fibers and the free dyes in solution, because most dyes are either bound to the fibers or coverslip. Another mechanism through which dye-monomer correspondence could be lost is the migration of the dye along the fibers within the acquisition time.

To investigate potential dye diffusion along the backbone of the supramolecular block copolymers, we monitor the number of single-molecule localizations in the red and green block of a selected poly[(*S*-1)-co(*S*-2)] architecture shown in figure 7.8a as a function of time. We compare the (normalized) single-molecule counts detected in the red and green channels for the red block (fig. 7.8b and 7.8d) and green block (fig. 7.8c and 7.8e) as a function of time. Evidently, the rates at which the two signal originating from the same block decay are highly similar. This suggests there is little or no dye migration along the fiber, since this would reduce the correlation between the two signals.

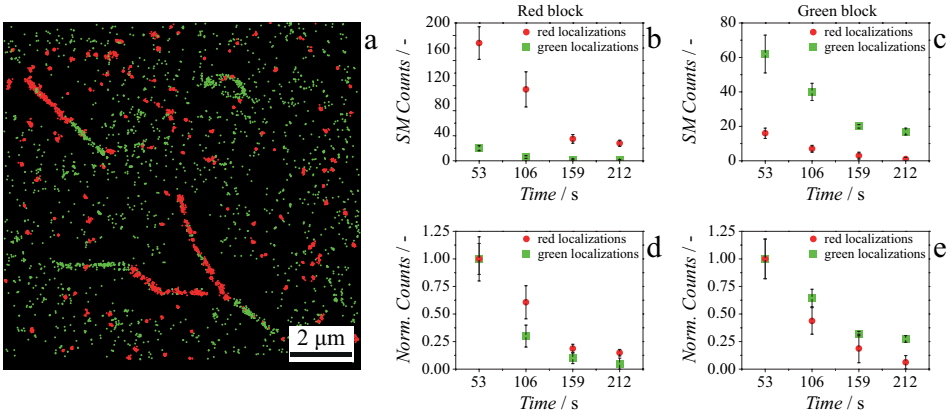

Figure 7.8: Migration of iPAINT probes along supramolecular copolymers. (a) Illustrative example of supramolecular copolymers poly[(*S*-1)-co-(*S*-2)] pre-stained with Cage-552 and Cage-635. Evolution of green and red localizations within (b) red and (c) green blocks in time. Normalized decay of red and green single-molecule localizations within (d) red and (e) green blocks in time. The error bars are the standard deviations calculated over several fibers.

7.2.6 Two-colour blocks are not induced by preferential dye-fiber interactions

Next, we aim to verify that the block-wise architecture is not due to a tendency of the Cage-552 and Cage-635 dyes to segregate, nor that they hinder monomer mixing. To this end we first image poly(*S*-1) fibers stained with both dyes. If the dyes induce the formation of block-like structures, we should obtain blocks even if the supramolecular polymer is composed of exclusively *S*-1 monomers. We prepare the poly(*S*-1) homopolymers upon direct mixing of two solutions of preformed poly(*S*-1) fibers, one stained with Cage-552 and the other with Cage-635, at 40 °C (fig. 7.9a). iPAINT imaging is performed on an aliquot of the sample taken immediately after mixing (fig. 7.9b and 7.9c). The image reconstructions from the red (fig. 7.9b) and green channel (fig. 7.9c) are seemingly identical, indicating that the fibers are more or less randomly stained with red and green dyes. Hence, fast exchange of

monomers and dyes between the originally red and green poly(*S*-1) fibers must have taken place within the few tens of seconds between mixing and sample preparation, since monomer and dye exchange are prevented once the fibers are adsorbed on the coverslip (see section 7.2.4). This simple experiment clearly demonstrates that the dyes do not tend to phase separate along the poly(*S*-1) fibers, nor do they hamper mixing of *S*-1 monomers within the fibers. In a complementary experiment, we first heat to 90 °C and subsequently cool back to room temperature the mixed solution of poly(*S*-1) fibers assembled at 40 °C and stained with either Cage-552 or Cage-635. As the fibers disintegrate at 90 °C leading to a molecular solution of *S*-1 monomers and free dyes, the supramolecular fibers now reform upon cooling in the presence of both dyes. The iPAINT images obtained from these samples again display more or less identical fibers in both channels with again seemingly randomly incorporation of the dyes along one-dimensional objects. Next, we repeat both sets of experiments for poly(*S*-2) (fig. 7.9f-j) and again, observe in both cases, randomly stained red and green fibers. Finally, we further substantiate the qualitative interpretation of the iPAINT images presented in figure 7.9 by quantification of the single-molecule localizations (insets in fig. 7.9). We find that the amount of red and green localizations along the fiber is equal within the experimental errors. These findings prove that the block-wise architectures observed in the poly[(*S*-1)-co-(*S*-2)] copolymers are neither induced by the dyes nor a result of the dyes inhibiting monomer mixing.

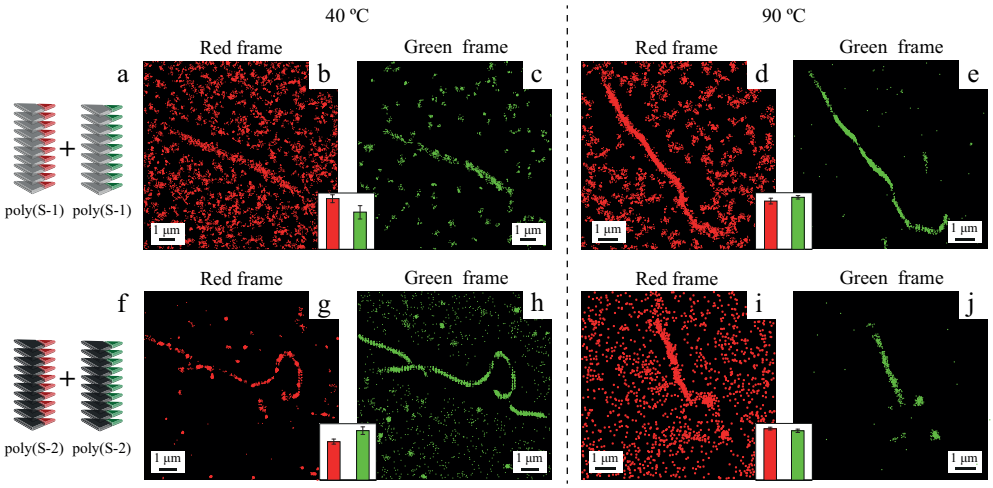

Figure 7.9: Two-colour homopolymer supramolecular fibers. Schematic illustrations of (a) poly(*S*-1) and (f) poly(*S*-2) stained with red and green dyes. (b-c) Poly(*S*-1) stained with Cage-552, mixed with poly(*S*-1) stained with Cage-635 at (b-c) room temperature, and (d-e) after heating at 90 °C. Poly(*S*-2) stained with Cage-552, mixed with poly(*S*-2) stained with Cage-635 at (g-h) room temperature, and (i-j) after heating at 90 °C. Both cases report fibers randomly stained along their backbone, as shown by the red and green histograms in the insets. The error bars are the standard deviations calculated over several fibers.

7.2.7 Dye-monomer correspondence in block copolymers is lost upon heating-cooling cycle

From the above it is clear that the arrangement of *S*-1 and *S*-2 monomers in the poly[(*S*-1)-co-(*S*-2)] supramolecular block copolymers can be reliably detected in the two-colour iPAINT images as long as the dyes remain colocalized with the monomers. Indeed, iPAINT images of copolymers prepared upon direct mixing at 40 °C of two solutions of preformed poly(*S*-2) fibers stained with Cage-552 and poly(*S*-1) fibers stained with Cage-635 (fig. 7.10b and 7.10c), display block-like structures. An illustrative example of a tri-block copolymer is shown in figure 7.10b and 7.10c, with the midblock visible in the red channel and the two outer *S*-2 blocks visible almost exclusively in the green channel. Next, we subject the copolymers to the same heat treatment as the homopolymers imaged in section 7.2.6.

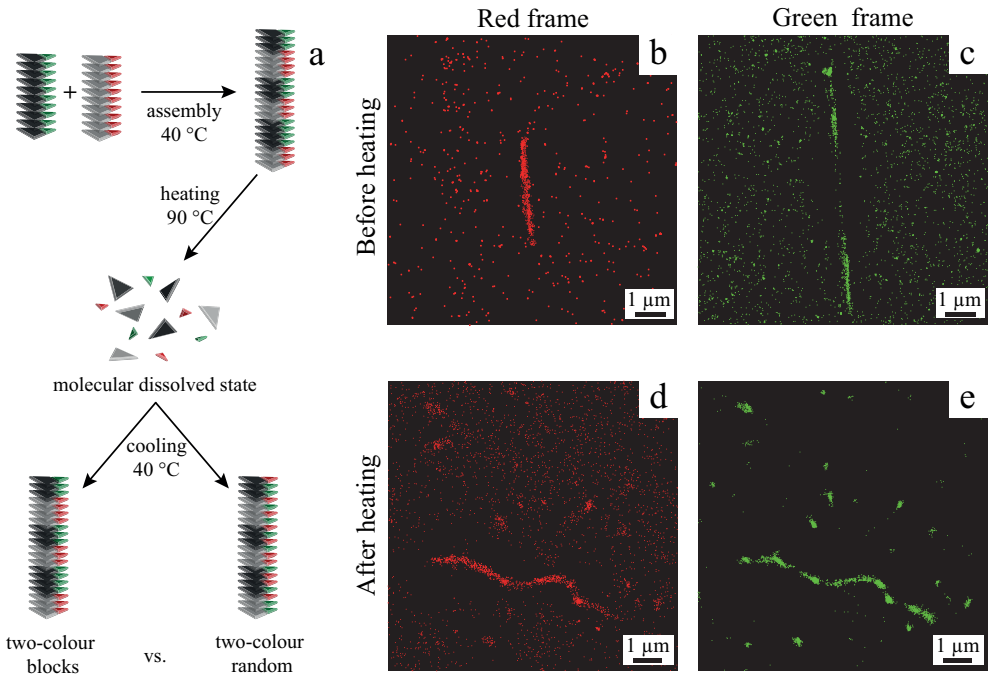

Figure 7.10: Imaging of supramolecular copolymers before and after assembly-disassembly cycle. (a) Schematic representation of assembly of supramolecular homopolymers stained with green and red dyes into supramolecular block copolymers, followed by disassembly through heating and subsequent re-assembly by cooling. (b-c) Poly[(*S*-1)-co-(*S*-2)] obtained via step-wise addition of poly(*S*-2) stained Cage-552 to poly(*S*-1) stained with Cage-635 imaged in the (b) red and (c) green frames. Upon heating to 90 °C the system is brought back to the molecular dissolved state. By cooling the solution the supramolecular assembly takes place. (d-e) iPAINT image of supramolecular polymer after heating and cooling steps imaged in the (d) red and (e) green frames.

From CD and UV-vis spectroscopy, we know that the same block-like arrangement is obtained upon reassembly of the fibers from the molecular dissolved state at 90 °C. This

is because the fibers have the same spectroscopic fingerprint before and after the heating-cooling cycle. However in the iPAINT images obtained after the heating-cooling cycle we no longer observe a block-wise arrangement. This is because the monomer-dye correspondence is lost in the molecular dissolved state at 90 °C. As the dyes do not preferentially adsorb on *S*-1 or *S*-2 monomers, they are randomly adsorbed on the copolymer chains that reform in the presence of both dyes.

In sum, iPAINT cannot be used to study the formation of poly[(*S*-1)-co-(*S*-2)] block copolymers from the molecular dissolved state at 90 °C when the monomers assemble into the copolymer upon cooling in the presence of both dyes, since they do have a similar affinity for both monomers. But, the iPAINT can reliably detect the formation of copolymers upon direct mixing of red and green fibers assembled in the presence of either one of the dyes.

7.2.8 Stability of the supramolecular block copolymers

Despite the similarity in geometry and handedness of *S*-1 and *S*-2 packing within the supramolecular fibers, the contact between *S*-1 and *S*-2 has a specific activation energy barrier which has to be overcome to favor the copolymerization. CD and UV-vis spectroscopy suggests that at temperatures below 5 °C the interaction is unfavored, leading to self-sorted poly(*S*-1) and poly(*S*-2) fibers, while at higher temperatures block-like structures form, since thermal energy promotes interactions and the enthalpic cost of a terminal monomer is reduced. To validate this interpretation of the spectroscopy data, we aim to capture the transition from self-sorted fibers to block-like architectures by iPAINT microscopy. To this end, we image the system immediately after mixing the pre-stained poly(*S*-1) and poly(*S*-2) at 5 °C. Figure 7.11a-c clearly shows that this results in self-sorted red and green fibers. A quantitative analysis of the false positives (fig. 7.11d) yields a crosstalk percentage that is similar to what has been measured for homopolymers in section 7.2.3. Next, we first allow the sample to equilibrate at room temperature and image aliquotes taken from the mixed solutions at certain time intervals (1 hour, 8 hours, and 3 days after mixing). Block-wise structures are visible from 1 hour after mixing (fig. 7.11e-g), which remain visible for at least 8 hours (fig. 7.11i-k), up to 3 days (fig. 7.11m-o). Once again, the false positives localizations (figure 7.11h, 7.11l and 7.11p) calculated for each image at different mixing times support the block-like nature of the fibers, since all the red localizations in the green block, and *vice versa*, are within the crosstalk values. After 1 week, however, we observe instead randomly mixed fibers, as illustrated by figure 7.11q-s. The red and green counts within the same fiber are now comparable (fig. 7.11t). This is in contrast with the results from CD and UV-vis spectra, which do not show any time evolution, suggesting that the block-like arrangement is still present after 1 month. Hence, we can affirm that up to 3 days, the dye-monomer correspondence is preserved, such that the block-wise arrangement

can be visualized directly in two-colour iPAINT experiments. However, this correspondence is lost sometime between 3-7 days after mixing, which means that iPAINT no longer depicts the supramolecular arrangement of the block copolymers.

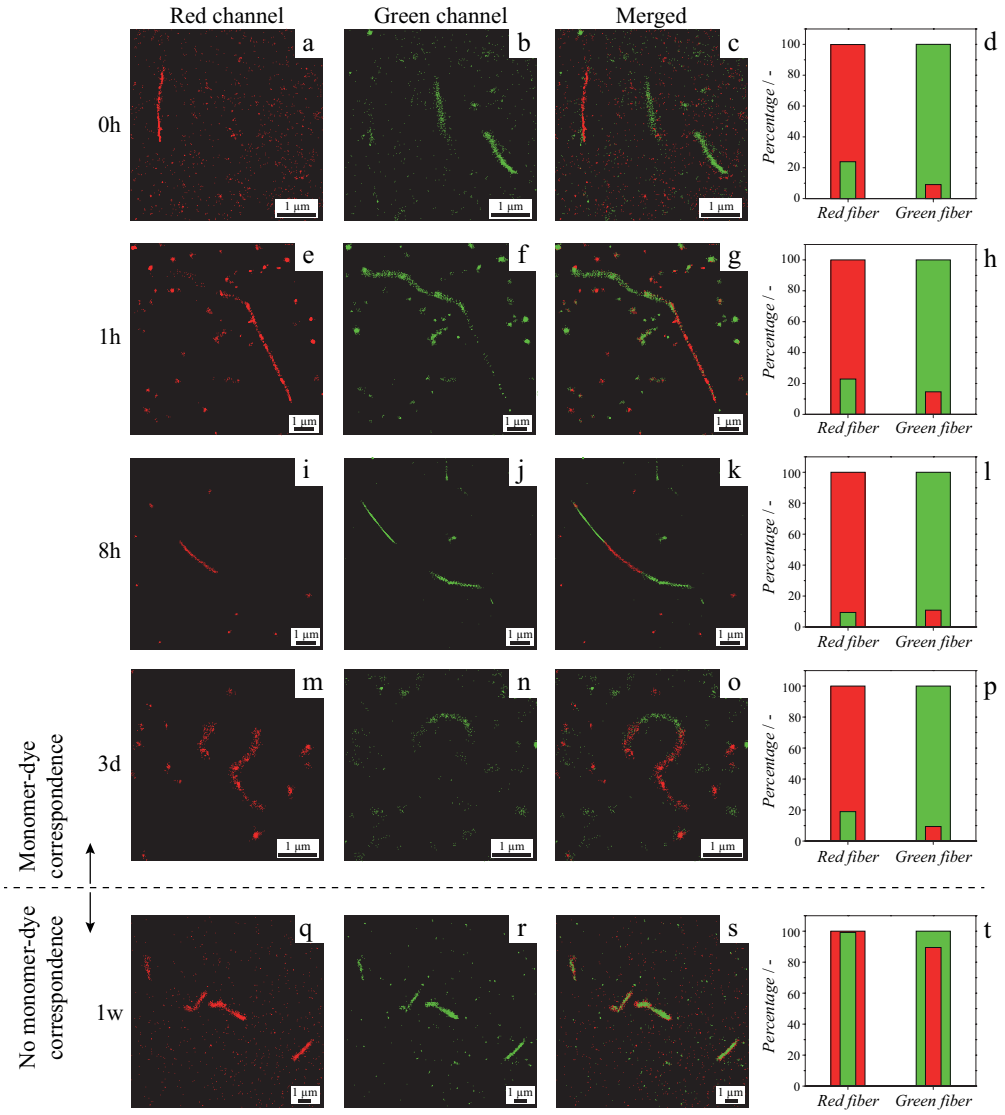

Figure 7.11: Self-sorting of supramolecular homopolymers and kinetics evolution towards supramolecular copolymers. Solution obtained by mixing poly(**S-2**) stained with 0.5% v/v Cage-552, 10 mM in DMSO, with poly(**S-1**) stained with 0.5% v/v Cage-635, 10 mM, at 5 °C in methylcyclohexane with 1% v/v isopropanol. iPAINT imaging was carried out at different time-lapses at 20 °C. (a) Red and (b) green self-sorted fibers are observed right after the mixing. (d-f) supramolecular block copolymers are observed 1h after mixing, and result stable over (g-l) 3 days.

7.3 Conclusions

We report on the visualization of uni-dimensional self-assembled aggregates of poly(*S*-1), poly(*S*-2), poly(*S*-BPTA) and poly(*S*-BTA), with a resolution down to ∼20 nm, without the incorporation of covalently bound dyes. By iPAINT microscopy we study the arrangement of *S*-1 and *S*-2 monomers within supramolecular copolymers. We demonstrate the presence of a block-like architecture, implicitly suggested by spectroscopy measurements. We finally investigate the kinetics of mixing and the stability of the observed blocks. We follow the evolution of the system from the self-sorted state to the assembly into copolymers. Hence, we successfully extend the scope of iPAINT to organic solvents. This is important since we can now visualize complex supramolecular structures with high spatial resolution in their native environment, by simple non-covalent staining without any further chemical modification. Exploiting this advantage of iPAINT microscopy, the interpretation of spectroscopic data can be further substantiated in a straightforward fashion by iPAINT microscopy.

7.4 Experimental

The synthesis of Tri(pyrid-2-yl)amine tricarboxamide (*S*-1), and Triphenylamine tricarboxamide (*S*-2) has been carried out by B. Adelizzi. The synthesis of N3,N3',N5,N5'-Tetrakis((S)-3,7-dimethyloctyl)-[1,1'-biphenyl]-3,3',5,5'-tetracarboxamide (*S*-BPTA) has been carrried out by dr. N. Van Zee. The synthesis of N1,N3,N5-tris((R)-3,7-dimethyloctyl)benzene-1,3,5-tricarboxamide (*S*-BTA) has been carried out by dr. G. Vantomme.

7.4.1 Microscopy

iPAINT images are acquired using a Nikon N-STORM system equipped with $\sim$ 160 mW/cm^2 (λ = 405 nm), $\sim$ 488 mW/cm^2 (λ = 561 nm) and $\sim$ 1.3 W/cm^2 (λ = 647 nm) laser lines configured for total internal reflection fluorescence (TIRF) imaging. The angle at which the inclined excitation is performed is finely tuned to maximize the signal-to-noise ratio. The fluorescence emission is collected by means of an oil immersion objective (Nikon 100×, 1.49 NA). A quad-band pass dichroic filter (97335 Nikon) is used to separate the excitation light from the fluorescence emission. Time-lapses of 15×10^3 frames are recorded onto a 256 × 256 pixel region (pixel size 170 nm) of an EMCCD camera (ixon3, Andor) at a rate of 47 frames/sec. Two different photo-activatable dyes are used to perform two-colour iPAINT measurements: Cage-552 and Cage-635 (Abberior®). These caged rhodamines reside in a dark, non-fluorescent state; upon UV irradiation (λ = 405 nm) the photolysis of the photo-activatable moiety is carried out, leading to an open (fluorescent) form through the Wolff rearrangement. [9] Upon excitation with the proper wavelength (λ = 561 nm for Cage-552, λ = 647 nm for Cage-635), the fluorescence of the dyes is collected. To perform single-molecule experiments, a low UV laser light power (<1% power) is used. In this way a small amount of dyes per frame is uncaged, statistically ensuring a spatial separation greater than the diffraction limit of light ($\lambda/2NA \simeq$ 200 nm). Subsequently, the sample is irradiated with a 100% power laser at λ = 561 nm and λ = 647 nm to excite the single molecules previously photo-activated. The high power lasers also bleach the excited molecules, so that a new subset of molecules can be photo-activated, excited and localized with high accuracy. The localization of single molecules in iPAINT image iscarried out by NIS-element Nikon software.

7.4.2 Sample preparation

The sample chamber used to perform iPAINT imaging is made from a coverslide (Menzel Gläser, 76×26 mm, thickness 1 mm) and a coverslip (Menzel Gläser, no. 1.5, 24×24 mm, thickness 0.17 mm) hold together by double-side tape, creating a chamber volume of ∼30 μL. Prior to assembly of the sample chamber, the coverslip is cleaned by piranha etching,

followed by rinsing and 10 min sonication in acetone, isopropanol, MilliQ-water (18.2 MΩ), and finally blown-dry with nitrogen. To perform super-resolution imaging in organic solvents, 1% v/v of iso-propanol is added to 200 μM solution of supramolecular polymer dissolved in methylcyclohexane. Subsequently, 0.5% v/v of a 10 mM solution of caged dye in DMSO is added in to the mixture, to stain the fibers. The mixture is then inserted in the sample chamber, and subsequently imaged.

Part II

Illuminating the interaction between PLGA-particles and liposomes by iPAINT

7.5 Introduction

Tumor cells can nowadays be targeted using antibody-drug conjugates, which are extremely potent biopharmaceutical molecules that bind to specific receptors on the cell surface through antibodies. The advantage of such systems is that drugs nanocarriers can be employed to selectively reach the tumor cell and release their cargo. [10] One of the most suitable drug nanocarriers are liposomes, since both hydrophobic and hydrophilic drugs can be stored either in the lipid bilayer or in the inside shell. [11] Although liposomes can accumulate in the tumor *via* enhanced permeability and retention effect, [12] the massive loading, *i.e.*, the high concentration required to defeat solid tumors, often results into liposomes physisorbing on healthy parts of the body. In this case, a recruitment system can be designed to gather and help the body to expel the excess of liposomes which did not meet their targets. Herein, we present a recruitment mechanism based on the reaction between *trans*-cyclooctene (TCO) and tetrazine (tz) molecules. The reaction is based on an inverse-electron-demand Diels-Alder mechanism, and is reported in figure 7.12a. [13] The recruiters are tetrazine-coated biodegradable poly(lactic-*co*-glycolic acid) (PLGA) based particles with radius $R \sim 250$ nm (fig. 7.12b, top row). PLGA particles are interesting recruiters since these are made out of biodegradable materials used for sutures, implants and drug-delivery systems, [14] covered with poly(ethylene-*alt*-maleic acid) (PEMA) as stabilizer. [15] The carriers are liposomes of radius R $\sim$ 50 nm composed of DPPC (1,2-Dipalmitoyl-*sn*-glycero-3-phosphocholine), 10% of which is labelled with a TCO moiety (fig. 7.12b, bottom row)

Herein, we use a combination of super-resolution microscopy (SRM) techniques to investigate the recruitment of liposomes by PLGA particles. We visualize the liposomes by PAINT (Point Accumulation for Imaging in Nanoscale Topography) microscopy using Nile red as probe. [18] Here, the hydrophobicity of the liposomes acts as a trigger to switch on the Nile red molecules whenever they adsorb onto their surfaces. The fluorescence signal is interrupted when the dye leaves the surface of the liposome. The PLGA particles are imaged by iPAINT microscopy (interface Point Accumulation for Imaging in Nanoscale Topography), [6] using a construct, namely PEG-635, which is a polymeric chain (poly ethylene glycol - PEG) end-functionalized with a photo-activatable moiety [9] (Cage-635, Abberior®). We are particularly interested in the amount of recruited liposomes per particle, and the shape of the liposomes upon binding. The liposomes should remain intact upon binding, since they would otherwise release their cargo, resulting in adverse side-effects. We select SRM since iPAINT does not require chemical modification of the liposomes of PLGA particles for visualization with high precision. Furthermore, traditional methods as electron microscopy (EM) and light scattering (LS) failed to provide conclusive evidences.

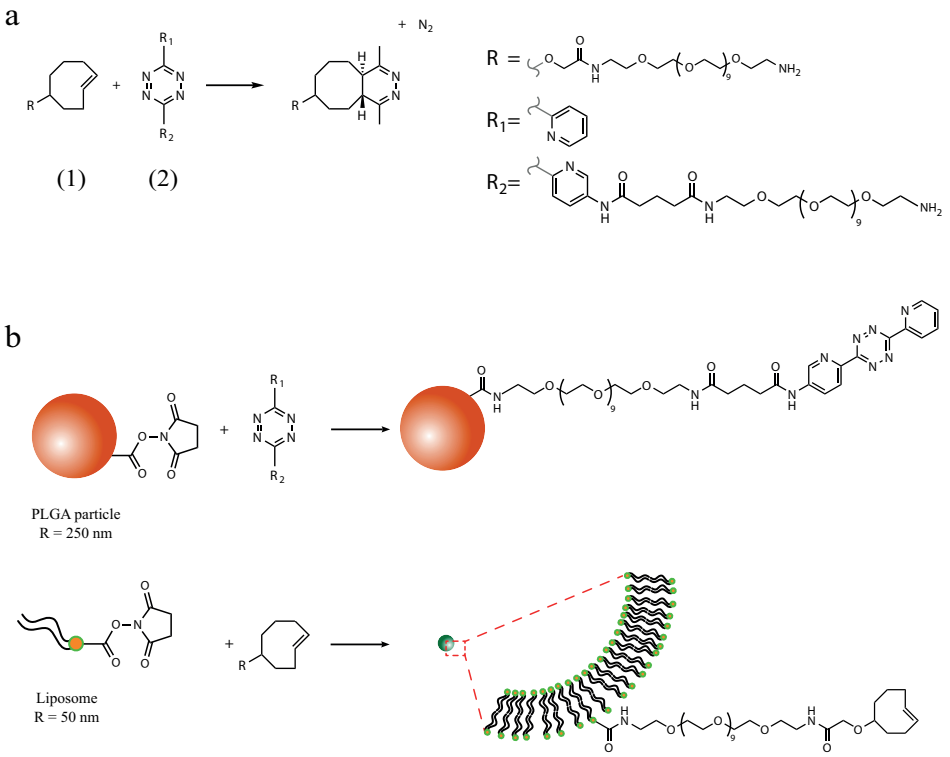

Figure 7.12: Click chemistry reaction between PLGA-tetrazine functionalized particle and *trans*-cyclooctene (TCO)-functionalized liposome. (a) Inverse Diels-Alder reaction mechanism between TCO (1), and bismethyl-tetrazine (2). [16,17] (b) Reaction path for PLGA particles functionalization with tetrazine by NHS-amine coupling (top row), and liposomes labelling with TCO moiety by NHS-amine coupling (bottom row). [13]

7.6 Results and discussion

To verify whether SRM is able to resolve with high spatial resolution the shape and dimensions of the liposomes and the PLGA particles we set out to image PLGA particles with iPAINT and subsequently the liposomes with PAINT microscopy. The DPPC liposomes are immobilized on the microscope coverslip and reversibly labelled with Nile red molecules. The liposomes are hardly visible in the wide-field image in figure 7.13a as they are smaller than the diffraction limit. But, the transient binding of Nile red molecules allows for single molecule localization, which yields the super-resolution image in figure 7.13b and 7.13c, in which liposomes are resolved with an accuracy of ∼19 nm. Zooming-in on the liposomes, we observe uniform spherical structures, with a mean radius $\langle R_{liposome} \rangle = 60 \pm 17$ nm over <100 liposomes analized (green distribution in fig. 7.13g). The size distribution obtained from PAINT images is in good agreement with dynamic light scattering data ($\langle R_{liposome} \rangle = 56 \pm 16$ nm).

The PLGA particles are imaged by iPAINT microscopy. To this end, the sample chamber is loaded with a dispersion of PLGA particles, followed by an injection of the iPAINT probe solution. Wide-field imaging shows an inhomogeneous fluorescence signal over the field of view. Sub-μm bright spots are hinting at the position of particles, but these are not accurately resolved (fig. 7.13e). An illustrative iPAINT image of the same field of view is given in figure 7.13f. This shows the reconstruction of PLGA particles with a localization accuracy of <20 nm. From the contours of ∼100 particles we determine their radii, obtaining a mean value of $\langle R_{PLGA} \rangle = 230 \pm 58$ nm (red distribution in fig. 7.13g). The size distribution obtained by iPAINT is in good agreement with dynamic light scattering data ($\langle R_{PLGA} \rangle = 269 \pm 64$ nm) and SEM imaging over ∼100 particles ($\langle R_{PLGA} \rangle = 241 \pm 63$ nm, fig. 7.17a). [13]

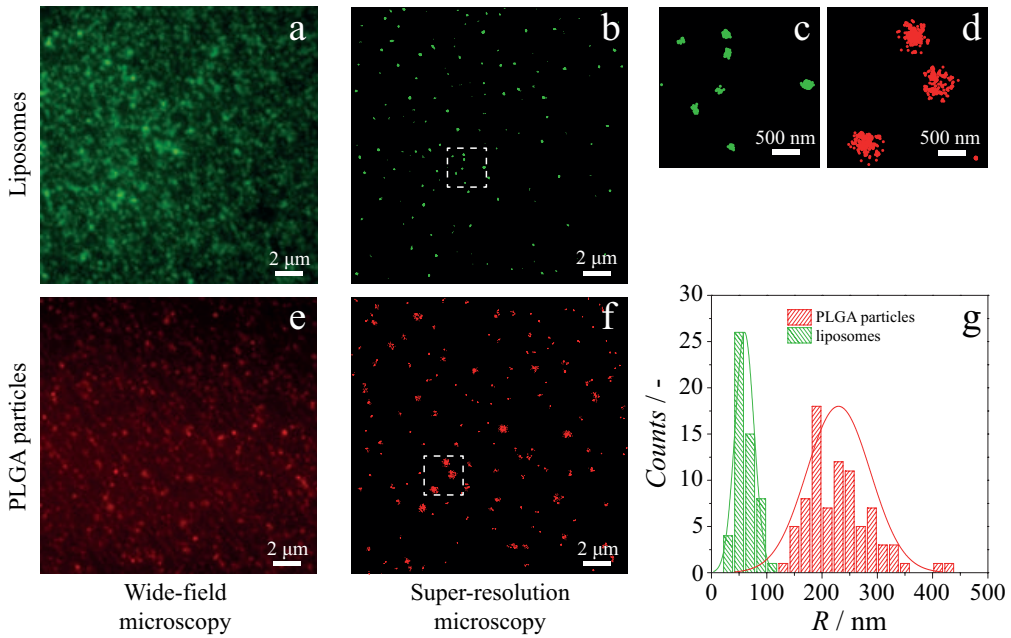

Figure 7.13: Imaging and of liposomes and PLGA particles by super-resolution microscopy. (a and e) Diffraction limited image, and (b and f) corresponding super-resolved images of liposomes (PAINT technique - Nile red was used as fluorescent probe), and PLGA particles (iPAINT technique - PEG-635 construct was used as fluorescent probe). (c and d) Zoom-ins of liposomes and PLGA particles, respectively, in b and f, highlighted by white dashed squares. (g) Radii distribution of the identified and reconstructed liposomes (green histogram) and PLGA particles (red histogram); $\langle R_{liposome} \rangle = 60 \pm 17$ nm, $\langle R_{PLGA} \rangle = 230 \pm 58$ nm.

7.6.1 PLGA particles recruit liposomes

Having established that PAINT and iPAINT are suitable techniques to visualize the liposomes and the PLGA particles, we now report on the recruitment of the liposomes by PLGA particles. To do so we prepare two samples to image: *i)* tz-PLGA particles mixed with liposomes that are not carrying the TCO tag, and hence defined as 'inactive'; *ii)* tz-PLGA particles mixed with TCO-liposomes. We start off by imaging inactive liposomes, to quantify the amount of aspecific interactions between PLGA particles and liposomes (fig. 7.14a). We consider a liposome 'recruited' by the PLGA particle if their centre-to-centre distance is comparable or smaller than the particle radius (∼250 nm). Roughly 10% of the 'inactive' liposomes are <250 nm separated from PLGA particles, and hence considered bound. We attribute this to physisorption and sedimentation of the liposomes onto the microscope coverslip in areas both with and without previously adsorbed particles.

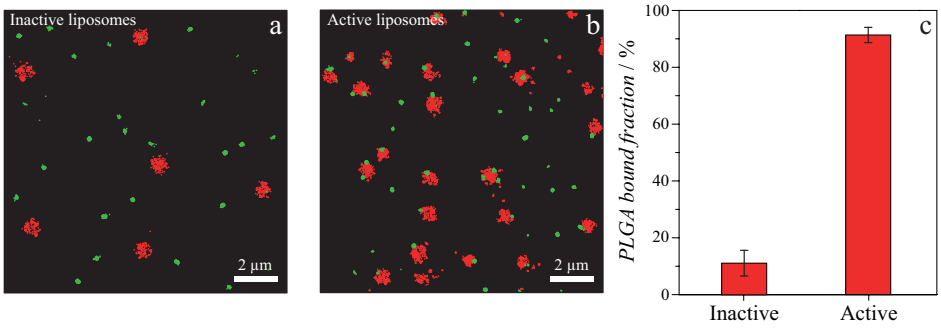

Figure 7.14: Visualization of PLGA particles recruiting activity. (a) Liposomes without TCO molecule (inactive liposomes) mixed with PLGA particles carrying a tetrazine moiety. No clear interaction between the two species is observed in the super-resolution image. (b) Active liposomes functionalized with TCO molecule interacting with PLGA particles through an inverse-electron-demand Diels-Alder reaction. The liposomes are bound to the PLGA particles without altering their spherical shapes. (c) Quantification of PLGA particles fraction bound to liposomes in the inactive and active states. The error bars are the standard deviations calculated over several experiments.

Next, we image liposomes carrying the TCO groups on the surface (10% surface coverage), and a clear recruitment of the liposomes is observed (fig. 7.14b) through the presence of green and red localizations within a radius of ∼250 nm. More than 90% of the PLGA particles are imaged in presence of one or more liposomes. From figure 7.14a and 7.14b we can conclude that the presence of the TCO binding domain is of crucial importance to the recruitment of the liposomes.

7.6.2 Liposome sphericity upon binding

To investigate whether the liposomes remain intact upon binding to the PLGA particles, we compare the size of (in)active liposomes, and quantify their sphericity. To this end, we

calculate the mean radii of more than 100 inactive and active liposomes as the radius of the circumference which includes 95% of the single-molecule localizations (red circle in fig. 7.15a and 7.15b). We obtain a mean radius $\langle\varphi_{inactive}\rangle = 54 \pm 18$ nm for the inactive liposomes (fig. 7.15a), and $\langle\varphi_{active}\rangle = 46 \pm 12$ nm for the active species (fig. 7.15b). Hence, no significant differences in their sizes are observed. Furthermore, to investigate the shape of the liposomes, we study the morphological distribution of single molecules in polar coordinates centered in the pointcloud's center of mass. The radial distribution of the localizations of both inactive and active liposomes are symmetric with respect to their centers of mass (fig. 7.15a and 7.15b).

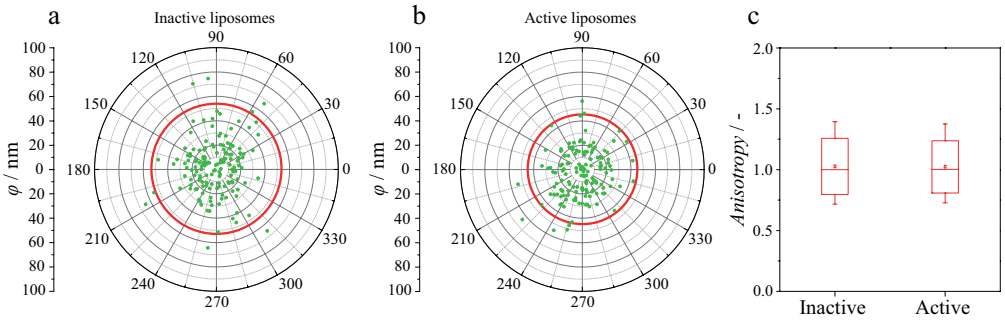

Figure 7.15: Evaluation of the liposomes sphericity. Distribution of single molecule localizations of inactive (a) and active (b) liposomes in polar coordinates. The red circle includes 95% of localization, and determines the mean radius of the liposome. $\langle\varphi_{inactive}\rangle = 54$ nm; $\langle\varphi_{active}\rangle = 46$ nm. (c) Radial anisotropy for inactive and active liposomes. Dots indicate the mean, the horizontal line within the box is the median, the boxes are the 25^{th} and 75^{th} percentiles, the whiskers denote the 5^{th} and 95^{th} percentiles.

To evaluate the degree of anisotropy within the cluster of localizations we divide the mean radius calculated in each sector ($\langle\varphi_\theta\rangle$) by the mean radius in the opposite sector ($\langle\varphi_{\theta+180^\circ}\rangle$) in figures 7.15a and 7.15b. Interestingly, no significant differences are reported (fig. 7.15c). The inactive liposomes have an anisotropy of 1.05 $\pm$ 0.33, while we obtain a value of 1.08 $\pm$ 0.43 for the active species. This confirms that the binding of liposomes to PLGA particles does not affect their sizes nor their shapes. We can thus exclude any fragmentation and/or wrapping of the lipid bilayer around the PLGA particles.

7.6.3 Quantification of PLGA particle clearance

We now take a closer look at the recruitment of liposomes by PLGA particles, aiming to quantify the number of liposomes bound per particle. To this end 30 μL of 0.1 mg/mL suspension of PLGA particles is fluxed in the sample chamber with the iPAINT probes. Subsequently, 30 μL of a 2.68 μM solution of active liposomes stained with Nile red is added. After equilibration ($\sim$5 min) the system is imaged. The majority of PLGA particles recruits only one liposome, as revealed by the percentage of singlets which exceeds 60% (fig.

7.16). About 20% of all analyzed particles bind two liposomes, while almost 9% is carrying three liposomes. Surprisingly, just ∼7% of all analyzed particles bind four or more liposomes, which are indicated as 'several' in figure 7.16.

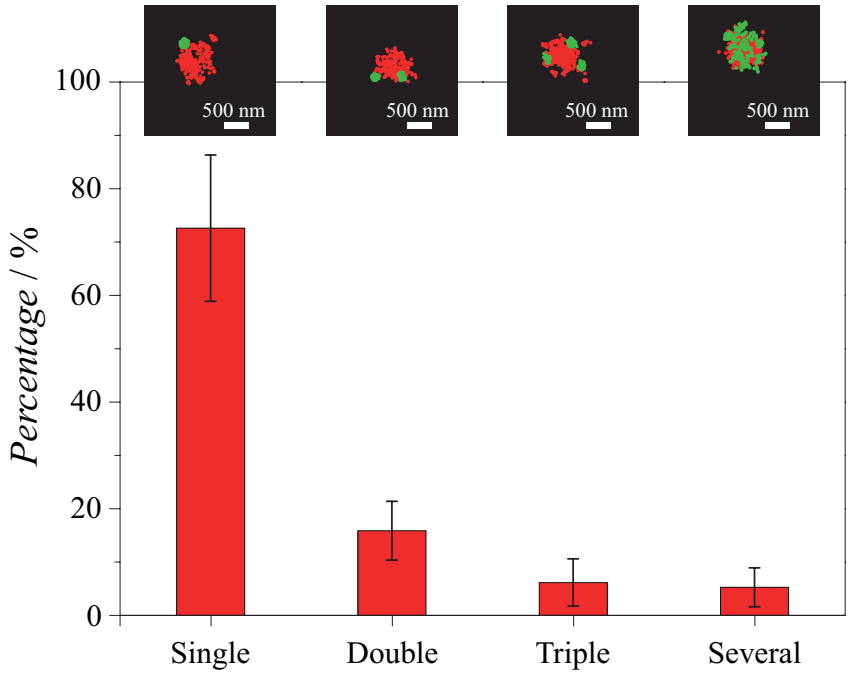

Figure 7.16: Quantification of liposomes bound to PLGA particles. The histogram quantifies the number of active liposomes interacting with single PLGA particles in single, double, triple and several bonds. A 1:1 ratio between particles and liposomes occurs most of the time (>60% occurrence), whereas higher binding events decay exponentially. The insets upon the bars are representative images of the single, double, triple and several bonds between a PLGA particle and TCO-liposomes. The error bars are the standard deviations over several experiments.

This result can be rationalized as follows: *i)* the PLGA particles, and/or the liposome surface coverage of active binding sites is not high enough to ensure multiple binding; *ii)* a single but strong bond between a liposome and a PLGA particle is preferred over multiple weak bindings. Future experiments at various degree of surface coverage of TCO and tetrazine, are required to elucidate the cause of this low binding percentage, even though the observed clearance is extremely high.

7.7 Conclusions

In conclusion, we report on a recruitment system based on PLGA particles carrying a tetrazine moiety which can selectively react with *trans*-cyclooctene. This fast reaction allows the PLGA particles to bind TCO-marked liposomes. Using a combination of PAINT and iPAINT super-resolution microscopy we characterize the interactions between the two species. First, we detect the binding between PLGA particles and liposomes in a two-colour experiment by a direct comparison of active *vs.* inactive liposomes. We quantify the bound fraction to be higher than 90%, demonstrating the high clearance achievable with this approach. Next, we investigate the morphology of the liposomes. No significant changes in the sphericity of liposomes in the active and inactive states are observed, suggesting that the liposomes remain intact after recruitment. Finally we look specifically at the clearance characteristics, quantifying the number of liposomes per PLGA particle. The majority of the samples analyzed shows a single liposome per particle, while less than 40% overall shows multiple bindings.

7.8 Experimental

The synthesis of the biodegradable poly(lactic-*co*-glycolic acid) (PLGA) based particles and the DPPC (1,2-Dipalmitoyl-*sn*-glycero-3-phosphocholine) based liposomes has been carried out by dr. A.H.A.M. van Onzen.

7.8.1 Synthesis of PEG-635 probes

1 mg of poly(ethylene glycol) bis(amine) (M_W 20kDa) is purchased by Sigma-Aldrich and dispersed in 1 mL of sodium bicarbonate buffer 0.1 M (pH 8.5) without further purification, to react with 20 μL of N-hydroxysuccinimide ester activated rhodamine, Cage-635 (Abberior®) in DMSO (10 mM). The reaction mixture is stirred overnight at room temperature, under protection from UV light, and subsequently purified by dialysis (Spectra/Por®7 dialysis membrane, pre-treated RC tubing, molecular weight cutoff: 8 kDa) to remove the unreacted dye molecules.

7.8.2 Sample preparation

For iPAINT/PAINT imaging PLGA particles are first dispersed in TRIS buffer and fluxed in the sample chamber. Once the particles sediment on the coverslip, the chamber is fluxed with TRIS buffer to remove the unbound particles. Right after the iPAINT probe solution is added, and incubated for 1 min. Subsequently, the iPAINT solution is replaced by liposomes stained with Nile red. The latter is prepared beforehand dispersing liposomes ($\sim$0.27 mM) in a solution 0.43 μM of Nile red in TRIS buffer.

The samples hereby investigated are imaged in a sample chamber made of a microscope coverslip (Menzel Gläser, no. 1.5, 24$\times$24 mm, thickness 0.17 mm) hold together with a microscope coverglass (Menzel Gläser, 76$\times$26 mm, thickness 1 mm) by double-side tape, creating an inner volume of $\sim$30 μL. Prior to chamber assembly, the coverslips are etched using a piranha solution, followed by thorough rinsing and sonication in acetone, isopropanol and MilliQ-water. Finally the coverslips are blown dry in a nitrogen stream, and used to close the sample chamber as described before.

7.8.3 Microscopy

PAINT and iPAINT images are taken using a Nikon N-STORM system equipped with a 488.0 mW/cm^2 green laser ($\lambda = 561$ nm), a 1335.0 mW/cm^2 red laser ($\lambda = 647$ nm), and a 160.0 mW/^{2} UV laser ($\lambda = 405$ nm). The laser lines are coupled into an optical fiber and focused onto the specimen through the microscope objective (100$\times$, 1.49 NA oil immersion) in a

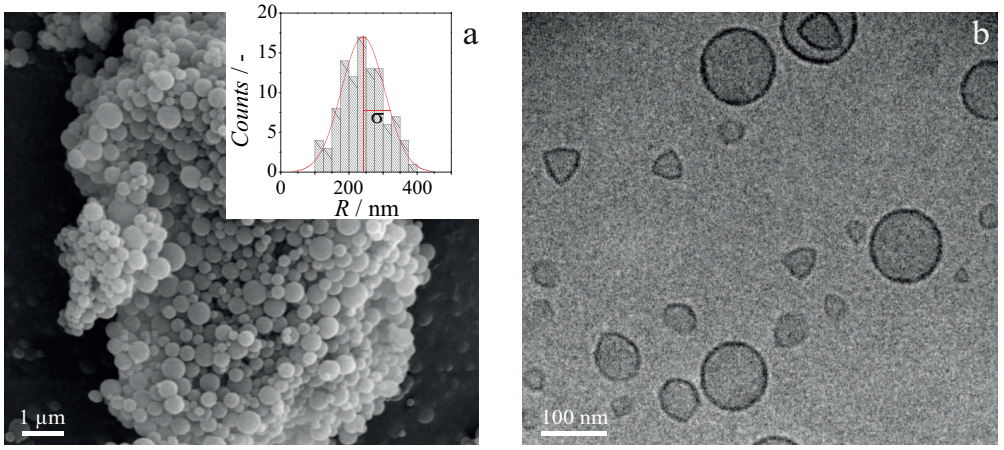

Figure 7.17: SEM and cryo-TEM characterization of PLGA particles and liposomes, respectively. (a) SEM picture of PLGA particles, the inset illustrates the size distribution of the particles calculated over more than 100 beads. (b) Cryo-TEM image of liposomes.

quasi-total internal reflection fluorescence (TIRF) illumination. The TIRF angle is chosen to maximize the signal-to-noise ratio during the image acquisition. The outcoming fluorescence signals are filtered using a quad-band pass dichroic filter (97335 Nikon). The time lapses are recorded on a EMCCD camera (ixon3, Andor) with a frame rate of 97 frames/sec on a field of view 128 $\times$ 128 pixels (170 nm pixel size). Unless stated otherwise, 2×10^4 frames are acquired for each experiment. A solution of 4.3 μM of Nile red in MilliQ-water (18.2 MΩ) is used to stain the liposomes and perform PAINT super-resolution imaging. Single-molecule imaging is achieved by using 561 nm laser (100% power), through the blinking of the fluorophores upon binding to the liposomes. Conversely, the imaging of PLGA particles was performed by iPAINT, using a combination of photo-activation (0.5% power UV laser, λ = 405 nm), and excitation/bleaching (100% power red laser, λ = 647 nm) of the PEG-635 probes (5×10^{-5} M in MilliQ-water). In both cases, single-molecule analyzed by NIS-element Nikon software. The analysis procedure consists of the following steps: a) identification of diffraction limited fluorescence peaks based on pixel intensities; b) fitting procedure of each peak by a two-dimensional Gaussian function, to switch from pixels to (x,y) coordinates; c) correction for drifting in the acquired images based on Nikon software; d) background signal removal, by filtering the single-molecule localizations by density.

Part III

Consequences of a sulphur atom - from spirolactam to spirothiolactam rhodamines

7.9 Introduction

In the past decade super-resolution microscopy (SRM) advanced as a promising tool to characterize nanostructures, capturing details finer than the diffraction limit. The main advantages of SRM are all related to the use of fluorescence as a means to image: negligible invasiveness, low radiation energy, high selectively (red-shift), and a wide range of colours to identify specific targets *via* (non-)covalent tagging with distinct dyes. The two families of SRM are structured illumination (STED, SIM, *etc.*) methods, and stochastic approaches (PALM, STORM, PAINT, *etc.*), both of which exploit the interconversion of fluorescent emitters between two different states. [19] Such switching is achieved optically (photoswitching, photoactivation) [20–28] or non-optically (chemical environment, ligand binding). [18,29–32] Optical photoswitchers can be further classified as genetically encoded or organic fluorophores. The former is desired for targeting specific biological structures. The latter offers the advantages of bright emission and small size, as their are >10 times brighter, [33] and >20 times smaller [34] than (large) fluorescent proteins. Here we report on the photophysical properties (absorption and emission spectra, single-molecule localizations) of a new class of optical photoswitchers, rhodamine spirolactams, and the impact of the modification of a single atom in their structures on their applicability for single-molecule imaging.

7.10 Results and discussion

7.10.1 Rhodamine spirolactam - spontaneous blinking

Rhodamine spirolactams have been thoroughly investigated as potential photo-controllable organic fluorescent dye molecules for SRM. [35,36] This specific class of rhodamines presents a non-fluorescent 'closed' form, and a bright fluorescent 'open' state, which is obtained upon UV light exposure (fig. 7.18a). The absorption of the closed form is limited to the UV region (ε = 15-20 $\times$ 10^3 M^{-1} cm^{-1} for 250 $< \lambda <$ 325 nm), with a small tail extending up to $\lambda \sim$ 350 nm ($\varepsilon < 10^3$ M^{-1} cm^{-1}). [27] The open isomer has an emission at λ_{em} = 580 nm. [27] The simplified Jablonski diagram in figure 7.18b describes the relevant electronic transitions. The closed form can be excited at $\lambda <$ 350 nm to reach its S_1 state (solid purple arrow). Subsequently, the molecule can either decay non-radiatively to the S_0 ground state (solid grey arrow), or, instead, switch to its open fluorescent form through ring opening of the closed form (dashed black arrow). The stability of the S_1 state of the open isomer is limited, which thus rapidly returns to the closed form by thermal relaxation (dashed grey arrow). Alternatively, it can be excited by visible light and brought to its excited state S_1 (solid green arrow), from which it may photobleach (dotted black line) or return to its ground state. The latter process can occur either in a non-radiative fashion, or by emitting

a red-shifted radiation (solid red arrow). The thermal relaxation between the open and closed isomers typically occurs on the millisecond timescale and depends on the polarity of the solvent used. [37] Hence, spontaneous blinking can be exploited for single-molecule measurements.

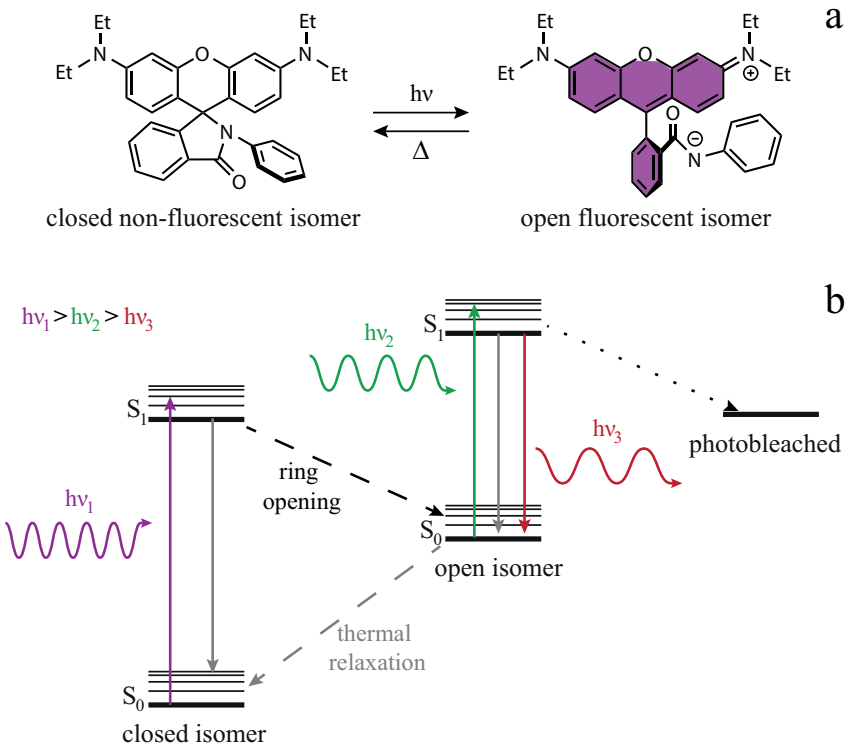

Figure 7.18: Photo-switching mechanism of rhodamine spirolactam. (a) Closed (non-fluorescent) and open (fluorescent) forms of a rhodamine spirolactam dye. (b) Simplified Jablonski diagram of electronic transitions in closed and open forms of rhodamine spirolactams.

Aiming to red-shift the absorption as far as possible, various chemical modifications of rhodamine spirolactams have been reported. [27] This would be advantageous for imaging with this optical photoswitcher in biological environments, as it would lower the phototoxicity in live cell imaging and allow for excitation at wavelengths commonly used in standard microscopes. To date, the absorption of spirolactams has been red-shifted beyond $\lambda = 450$ nm by increasing the conjugation of the substituents attached to the rhodamine core. [27]

7.10.2 Rhodamine spirothiolactam - the effect of a sulphur atom

Our approach to develop a single-molecule microscopy enabling rhodamine spirolactam is based on the prior knowledge that the single atom substitution of oxygen into sulphur in amides (*i.e.*, from a lactam to a thiolactam) extends its absorption into visible spectrum. We anticipate that this approach is more generally applicable beyond rhodamine spirolactams to develop suitable PALM dyes from molecules presently deemed unfit for microscopy due to their low activation wavelengths. The photoswitching mechanism of the spirothiolactam is illustrated in figure and the absorption spectra of the closed spirolactam (black line), the closed spirothiolactam (green line) and the open spirothiolactam (red line) are shown in figure 7.19.

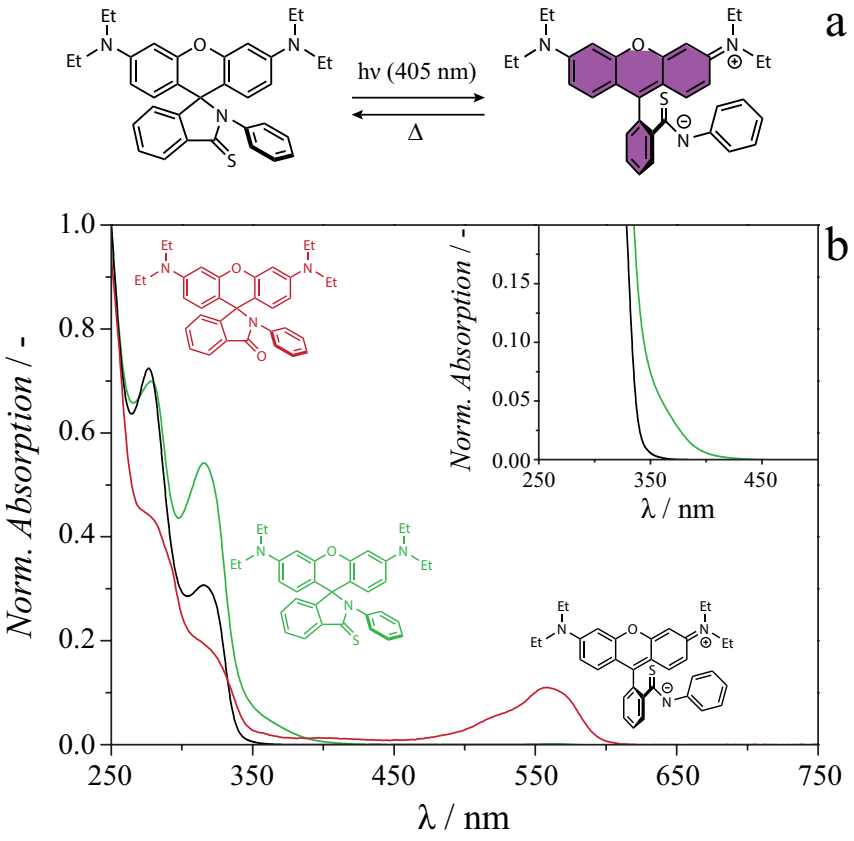

Figure 7.19: Absorption spectra of rhodamine spiro(thio)lactam. The absorption spectrum of the closed form of rhodamine spirolactam (black curve) acquired in chloroform (10^{-5} M), is broadened by the addition of a suphur atom (green curve) towards the visible region. A tail with non-negligible absorbance appears in the spectrum at $\lambda > 400$ nm. The red curve is the absorption spectrum of the open form of the rhodamine spirothiolactam.

Conversion from the closed into the open state is achieved upon illumination with $\lambda =$ 405 nm, while the reverse process takes place due to thermal relaxation (fig. 7.19a). The absorption spectra in figure 7.19b demonstrate that the substitution of the oxygen by the sulphur atom extends the short absorption tail up to $\lambda = 450$ nm (inset), albeit with low molar absorption coefficient (< 1000 M^{-1} cm^{-1}). The open form of the spirothiolactam has an absorption maximum at $\lambda_{abs} = 565$ nm, which represents a red shift of 25 nm with respect to the parent molecule, rhodamine B. This shift is highly advantageous in view of the availability of $\lambda = 561$ nm lasers in most microscopes.

7.10.3 Single-molecule photo-activation and localization

To evaluate whether the rhodamine spirothiolactam is suitable for single-molecule measurements, we embed spiro(thio)lactams at a dye concentration of 10^{-8} M into a poly(vinyl alcohol) (PVA) mesh and image both in water. Fig 7.20 shows the fluorescence images (fig. 7.20a and 7.20c) and the single-molecule localizations (fig. 7.20b and 7.20d) of spirolactam (fig. 7.20a and 7.20b) and spirothiolactam (fig. 7.20c and 7.20d) into PVA meshes.

A clear increase in fluorescence signal upon irradiation with UV light ($\lambda = 405$ nm, $\sim$16 mW/cm^{-2}), and continuous irradiation with a green laser line ($\lambda = 561$ nm, $\sim$488 mW/cm^{-2}) is observed for rhodamine spirothiolactam relative to the fluorescence before and after photo-activation (fig. 7.20a). Conversely, no fluorescence bursts are visible upon 'uncaging' of the spirolactams (fig. 7.20c). Indeed, approximately 70 single rhodamine spirothiolactam molecules are localized per photo-activated cycle of $\sim$250 frames within a 256 $\times$ 256 pixels area, while the number of single-molecules localizations is reduced approximately to 30 in between 4 consecutive cycles with only green excitation laser on (fig. 7.20b). This is in stark contrast with rhodamine spirolactam, for which no more than 4 molecules are localized at any moment in time throughout the photo-activation cycles. Now that uncaging and excitation of the open isomer of the rhodamine spirothiolactam has been demonstrated, we turn to a quantitative analysis of the observed single-molecules. We use continuous photo-activation and excitation at 1% and 100% laser power, respectively, to ensure sparse localizations over an area 40 $\times$ 40 μm^2. Gratifyingly, we find that most molecules reside in the fluorescent state for a single frame of $\sim$20 ms (fig. 7.21), which ensures sufficient temporal separation to localize two different photo-activated molecules in subsequent frames. Less than 5% of the molecules appears to be fluorescent for longer than a frame (at most 4 frames). This slower decay to the ground state may hint at a difference in thermal relaxation pathways. The mean number of photons emitted per molecule is $\sim$1500 (see section 7.12.2 for further details), resulting in a localization precisition of $<$20 nm.

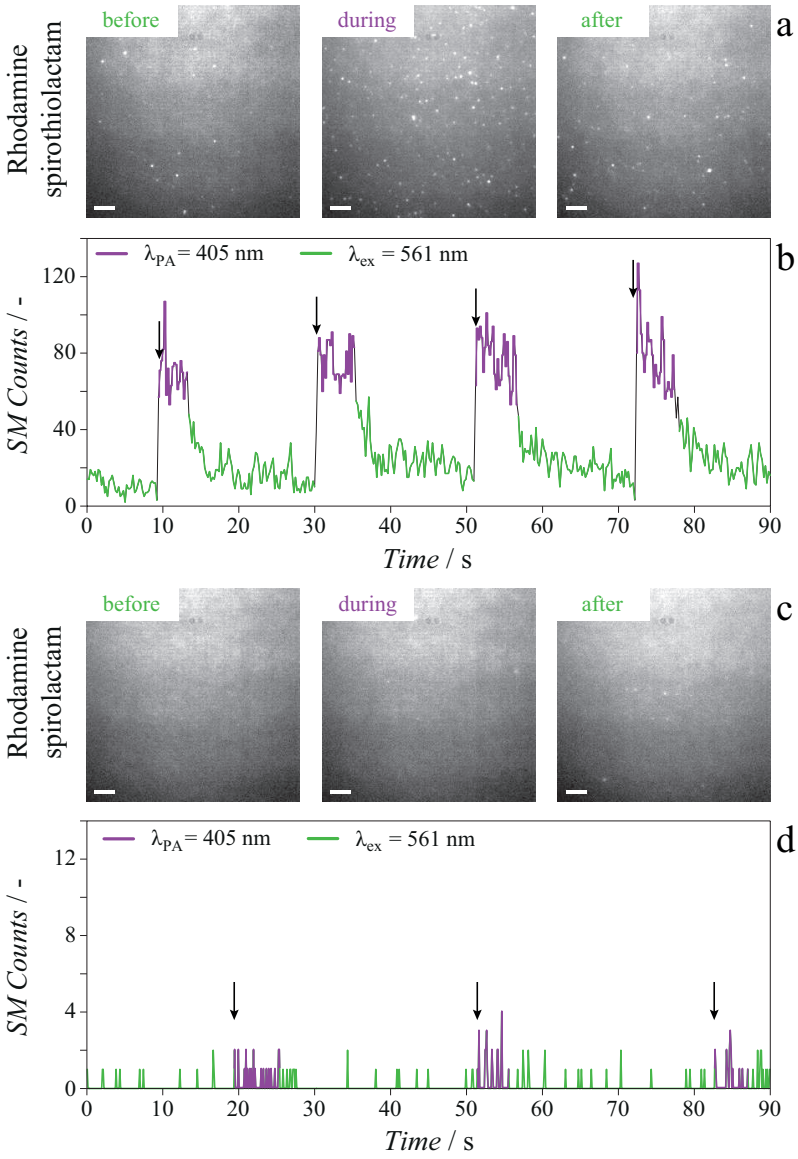

Figure 7.20: Photo-activation of single molecules embedded into a polymer film. (a) Rhodamine spirothiolactam molecules embedded in a poly(vinyl alcohol) matrix. Upon $\lambda_{PA} = 405$ nm several single molecules are photo-activated. Scale bars 4 μm. (b) Counts of single-molecule localizations upon photo-activation with $\lambda_{PA} = 405$ nm and excitation with $\lambda_{ex} = 561$ nm as a function of time. (c) Rhodamine spirolactam molecules embedded in a poly(vinyl alcohol) matrix. Scale bars 4 μm. No/little fluorescence is observed upon photo-activation. (d) Counts of rhodamine spirolactam single-molecule localizations upon irradiation with $\lambda_{PA} = 405$ nm and $\lambda_{ex} = 561$ nm as a function of time. Arrows indicate the photo-activation with $\lambda_{PA} = 405$ nm.

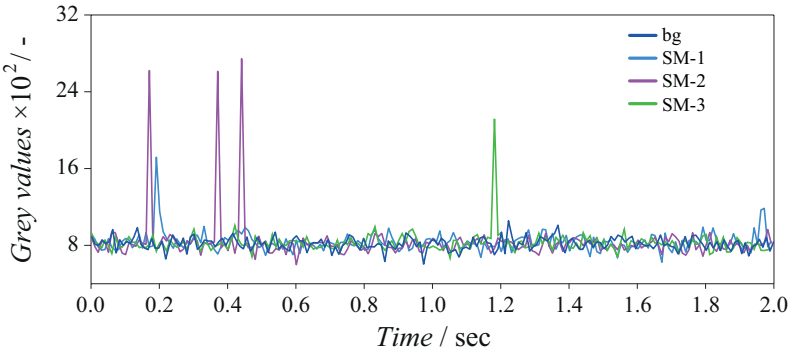

Figure 7.21: Single-molecule traces of rhodamine spirothiolactam (cyan, purple and green lines) compared to the background signal (blue line) collected under continuous excitation $\lambda = 561$ nm (100% power) and constant photo-activation $\lambda = 405$ nm (1% power).

In future work, we aim to synthesize an amine-reactive N-Hydroxysuccinimide (NHS) rhodamine spirothiolactam for covalent coupling to biological and synthetic structures via primary amines.

7.11 Conclusions

We report on the synthesis of a new class of rhodamine spirothiolactams able to interconvert between a 'closed' non-fluorescent state and an 'open' fluorescent form. A single atom substitution from oxygen to sulphur, extends the absorption of the closed form towards the visible region, allowing the photo-activation at $\lambda = 405$ nm, and excitation at $\lambda = 561$ nm. Furthermore, they spontaneously blink due to the thermal relaxation to the more stable closed form in the millisecond timescale, in both water and in organic solvents. This paves the way for single-molecule localization microscopy in aqueous and organic environments without additives, at any desired pH value. Hence, in contrast with virtually most of commercially available dyes, these rhodamine spirothiolactams do not impose any restriction on the imaging medium, offering unprecedented freedom in the design of single-molecule localization microscopy experiments.

7.12 Experimental

7.12.1 Synthesis of spirothiolactams

The synthesis of rhodamine spirothiolactam has been carried out by dr. A. Vargas Jentzsch.

7.12.1.1 3',6'-bis(diethylamino)-2-phenylspiro[isoindoline-1,9'-xanthene]-3-thione

3',6'-bis(diethylamino)-2-phenylspiro[isoindoline-1,9'-xanthen]-3-one (200 mg, 0.386 mmol) and Lawessons's reagent (117 mg, 0.290 mmol) are dispersed in 50 mL of toluene and the reaction mixture is heated to reflux (110 °C) overnight. Although the TLC shows starting material, the reaction is stopped. The solvent is evaporated under reduced pressure and the residue purified by column chromatography (pure DCM, the product is pink on silica) to yield the pure product as light yellow solid (520 mg, 77%). ^{1}H-NMR (399 MHz, $CDCl_3$) δ 8.25 (m, 1H), 7.57 (m, 2H), 7.12-7.25 (m, 4H), 6.59 (d, 2H, J = 8.8 Hz), 6.49 (m, 2H), 6.33 (dd, 2H, J = 8.8 Hz, J = 2.6 Hz) 6.18 (d, 2H, J = 2.6 Hz), 3.32 (m, 8H), 1.14 (t, 12H, J = 7.0 Hz). ^{13}C-NMR (100 MHz, $CDCl_3$) δ 153.7, 150.0, 149.3, 139.0, 138.1, 132.8, 129.03, 128.8, 128.8, 128.7, 128.3, 125.8, 123.8, 108.2, 104.9, 97.9, 77.5, 77.4, 77.2, 76.8, 44.5, 12.6. Maldi-TOF-MS: (m/z) calc for $C_{34}H_{35}N_3OS$ 533.25, found 534.29 $[M+H]^+$.

7.12.2 Microscopy

The photoactivation of spirothiolactam molecules is performed in a Nikon N-STORM system equipped with a ∼488.0 mW/cm^2 green laser (λ = 561 nm) and a ∼160.0 mW/^{2} UV laser (λ = 405 nm). The laser lines are coupled into an optical fiber and focused onto the specimen through the microscope objective (100×, 1.49 NA oil immersion) in a quasi-total internal reflection fluorescence (TIRF) illumination. The TIRF angle is chosen to maximize the signal-to-noise ratio during the image acquisition. A quad-band pass dichroic filter (97335 Nikon) is used to filter the outcoming fluorescence signals from the excitation light. The time lapses are recorded on a EMCCD camera (ixon3, Andor) with a frame rate of 47 frames/sec on a field of view 256 × 256 pixels (170 nm pixel size). Single-molecule blinking is observed by using 561 nm laser (100% power), after 10% power photo-activation with UV laser, λ = 405 nm. Single-molecule are analyzed by NIS-element Nikon software through the identification of diffraction limited fluorescence peaks. Each peak is subsequently filtted by a two-dimensional Gaussian function.

A film of PVA is prepared by spin-coating a solution of the polymer in water (1% w/w) containing a solution of the photoswitcher (10^{-8} M) onto a glass slides.

Figure 7.22 shows the number of mean photons detected per on-cycle of the spirothiolactam molecules embedded in the PVA film, upon UV ($\lambda = 405$ nm, $\sim$16 mW/cm^{-2}) irradiation. The mean number of photons detected is $\sim$1500, which allows for a theoretical accuracy of $\sim$15 nm in a super-resolved image, comparable with other commercially available dyes.

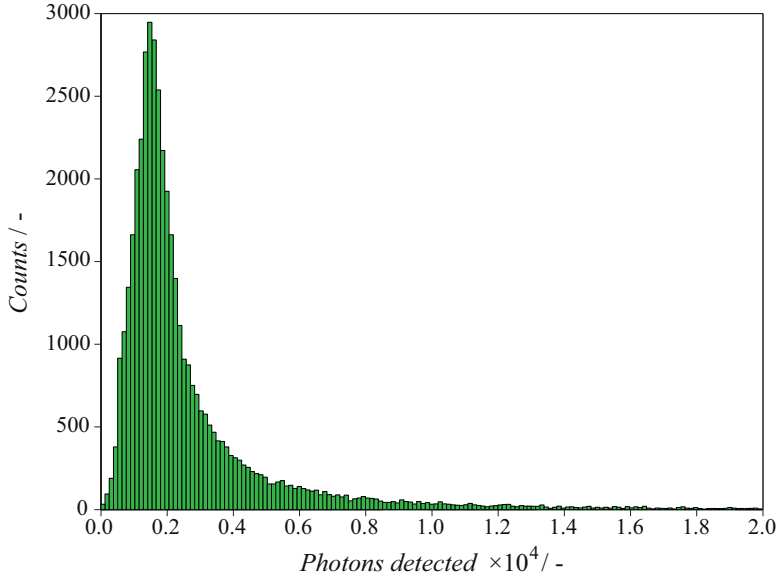

Figure 7.22: Number of photons detected upon UV irradiation ($\lambda = 405$ nm) of spirothiolactam. The mean value of photons detected is $\sim$1500.

Bibliography

[1] van Genabeek, B.; de Waal, B.F.M.; Gosens, M.M.J.; Pitet, L.M.; Palmans, A.R.A.; Meijer, E.W. *J. Am. Chem. Soc.* **2016**, *138*, 4210.

[2] Badi, N.; Lutz, J.-F. *Chem. Soc. Rev.* **2009**, *38*, 3383.

[3] Moad, G.; Mayadunne, R.T.A.; Rizzardo, E.; Skidmore, M.; Thang, S.H. *Macromol. Symp.* **2003**, *192*, 1.

[4] Adelizzi, B.; Filot, I.A.W.; Palmans, A.R.A.; Meijer, E.W. *Chem. Eur. J.* **2017**, *23*, 6103.

[5] Mtangi, W.; Tassinari, F.; Vankayala, K.; Vargas Jentzsch, A.; Adelizzi, B.; Palmans, A.R.A.; Fontanesi, C.; Meijer, E.W.; Naaman, R. *J. Am. Chem. Soc.* **2017**, *139*, 2794.

[6] Aloi, A.; Vilanova, N.; Albertazzi, L.; Voets, I.K. *Nanoscale* **2016**, *8*, 8712.

[7] Aloi, A.; Vargas Jentzsch, A.; Vilanova, N.; Albertazzi, L.; Meijer, E.W.; Voets, I.K. *J. Am. Chem. Soc.* **2016**, *138*, 2953.

[8] Albertazzi, L.; van der Zwaag, D.; Leenders, C.M.A.; Fitzner, R.; van der Hofstad, R.W.; Meijer, E.W. *Science* **2014**, *344*, 491.

[9] Belov, V.N.; Mitronova, G.Y.; Bossi, M.L.; Boyarskiy, V.P.; Hebisch, E.; Geisler, C.; Kolmakov, K.; Wurm, C.A.; Willig, K.I.; Hell, S.W. *Chem. Eur. J.* **2014**, *20*, 13162.

[10] Polakis, P. *Pharmacol. Rev.* **2016**, *68*, 3.

[11] Alavi, M.; Karimi, N.; Safaei, M. *Adv. Pharm. Bull.* **2017**, *7*, 3.

[12] Kneidl, B.; Peller, M.; Winter, G.; Lindner, L.H.; Hossann, M. *Int. J. Nanomedicine* **2014**, *9*, 4387.

[13] van Onzen, A.H.A.M. *Doctoral dissertation* **2016**. Retrieved from TU/e Repository.

[14] Davidsen, J.; Jørgensen, K.; Andresen, T.L.; Mouritsen, O.G. *Biochim. Biophys. Acta BBA - Biomembr.* **2003**, *1609*, 95.

[15] van Elk, M.; Deckers, R.; Oerlemans, C.; Shi, Y.; Storm, G.; Vermonden, G.; Hennink, W.E. *Biomacromolecules* **2014**, *15*, 1002.

[16] Versteegen, R.M.; Rossin, R.; ten Hoeve, W.; Janssen, H.M.; Robillard, M.S. *Angew. Chem. Int. Ed.* **2013**, *52*, 14112.

[17] Rossin, R.; van Duijnhoven, S.M.J.; ten Hoeve, W.; Janssen, H.M.; Kleijn, L.H.J.; Hoeben, F.J.M.; Versteegen, R.M.; Robillard, M.S. *Bioconjugate Chem.* **2016**, *27*, 1697.

[18] Sharonov, A.; Hochstrasser, R.M. *Proc. Natl. Acad. Sci. U.S.A.* **2006**, *103*, 18911.

[19] van de Linde, S.; Sauer, M. *Chem. Soc. Rev.* **2014**, *43*, 1076.

[20] Fölling, J.; Belov, V.; Kunetsky, R.; Medda, R.; Schönle, A.; Egner, A.; Bossi, M.; Hell, S.W. *Angew. Chem. Int. Ed.* **2007**, *46*, 6266.

[21] Heilemann, M.; Dedecker, P.; Hofkens, J.; Sauer, M. *Laser Photon. Rev.* **2009**, *3*, 180.

[22] Marriott, G.; Mao, S.; Sakata, T.; Ran, J.; Jackson, D.K.; Petchprayoon, C.; Gomez, T.J.; Warp, E.; Tulyathan, O.; Aaron, H.L.; Isacoff, E.Y.; Yan, Y. *Proc. Natl. Acad. Sci. U.S.A.* **2008**, *105*, 17789.

[23] Uno, K.; Niikura, H.; Morimoto, M.; Ishibashi, Y.; Miyasaka, H.; Irie, M. *J. Am. Chem. Soc.* **2011**, *133*, 13558.

[24] Uno, S.-N; Kamiya, M.; Yoshihara, T.; Sugawara, K.; Okabe, K.; Tarhan, M.C.; Fujita, H.; Funatsu, T.; Okada, Y.; Tobita, S.; Urano, Y. *Nat. Chem.* **2014**, *6*, 681.

[25] Subach, F.V.; Patterson, G.H.; Manley, S.; Gillette, J.M.; Lippincott-Schwartz, J.; Verkhusha, V.V. *Nat. Methods* **2009**, *6*, 153.

[26] Lord, S.J.; Conley, N.R.; Lee, H.-D.; Samuel, R.; Liu, N.; Twieg, R.J.; Moerner, W.E. *J. Am. Chem. Soc.* **2008**, *130*, 9204.

[27] Lee, M.K.; Rai, P.; Williams, J.; Twieg, R.J.; Moerner, W.E. *J. Am. Chem. Soc.* **2014**, *136*, 14003.

[28] Nevskyi, O.; Sysoiev, D.; Oppermann, A.; Huhn, T.; Wöll, D. *Angew. Chem. Int. Ed.* **2016** *55*, 12698.

[29] Schwering, M.; Kiel, A.; Kurz, A.; Lymperopoulos, K.; Sprödefeld, A.; Kramer, R.; Herten, D. *Angew. Chem. Int. Ed.* **2011**, *50*, 2940.

[30] Vogelsang, J.; Cordes, T.; Forthmann, C.; Steinhauer, C.; Tinnefeld, P. *Proc. Natl. Acad. Sci. U.S.A.* **2009**, *106*, 8107.

[31] Lee, M.K.; Williams, J.; Twieg, R.J.; Rao, J.; Moerner, W.E. *Chem. Sci.* **2013**, *4*, 220.

[32] Lee, S.F.; Vérolet, Q.; Fürstenberg, A. *Angew. Chem. Int. Ed.* **2013**, *52*, 8948.

[33] Lord, S.J.; Lee, H.D.; Moerner, W.E. *Anal. Chem.* **2010**, *82*, 2192.

[34] Gahlmann, A.; Moerner, W.E. *Nat. Rev. Microbiol.* **2014**, *12*, 9.

[35] Fölling, J.; Polyakova, S.; Belov, V.N.; van Blaaderen, A.; Bossi, M.L.; Hell, S.W. *Small* **2008**, *4*, 134.

[36] Belov, V.N.; Bossi, M.L.; Fölling, J.; Boyarskiy, V.P.; Hell, S.W. *Chem. Eur. J.* **2009**, *15*, 10762.

[37] Willwohl, H.; Wolfrum, J.; Gleiter, R. *Laser Chem.* **1989**, *10*, 63.

Summary

On the edge:
Imaging soft interfaces by single-molecule localization microscopy

In the past decade super-resolution microscopy has gained ground as a versatile, non-invasive method for sub-μm visualization of fluorescently tagged nanostructures. Multi-colour labelling, target specificity and high spatial resolution make single-molecule localization microscopy (SMLM) an attractive method complementary to well established techniques, such as electron and atomic force microscopy. However, material science and supramolecular chemistry have scarcely profited from the development of SMLM. This thesis aims to broaden the scope of SMLM techniques to the visualization of synthetic soft matter in (non-)aqueous environments, with minimal perturbation of the sample under investigation. In this thesis, we present a new strategy in SMLM: interface Point Accumulation for Imaging in Nanoscale Topography (iPAINT), and extend the use of photo-activated localization microscopy (PALM) and iPAINT to organic solvents.

Chapter 1 introduces the transition from diffraction limited imaging to super-resolution microscopy, giving a general overview on the different strategies to achieve nanometer resolution in optical microscopy. We highlight selected achievements in biology accomplished using SMLM which exploit the high spatial resolution, chemical specificity, minimal invasiveness, and multi-colour labelling. Next, we describe applications of SMLM in supramolecular chemistry, polymer and colloidal science. We offer a detailed description of how SMLM has been of crucial importance in clarifying the structure and the exchange dynamics in uni-dimensional supramolecular co-polymers. We present the characterization by SMLM of how colloidal nanoparticles, microgels and block co-polymers react to external stimuli. We finish with a brief overview of new dyes specifically designed for application of SMLM in supramolecular chemistry and material science.

In **chapter 2** we describe a new strategy in SMLM based on the Point Accumulation for

Imaging in Nanoscale Topography (PAINT) approach. We exploit the non-covalent staining of PAINT and combine it with photo-activatable dyes to reconstruct in a non-invasive fashion three-dimensional solid-liquid-air interfaces, with a spatial resolution below 20 nm. We coin this method interface Point Accumulation for Imaging in Nanoscale Topography (iPAINT). The iPAINT strategy relies on the continuous physisorption and desorption of a poly(ethylene oxide)-tagged caged rhodamine, which prevents the need for covalent labelling of the object under study. This is of crucial importance since it allows to characterize samples in their native state, without further chemical modifications, and enables imaging of dynamic interfaces such as liquid-air. Three exemplary studies are presented to evaluate the possibilities and limitations of iPAINT. We study dispersions of silica nanoparticles, oil-in-water and water-in-oil emulsions, and air nanobubbles, characterizing their sizes and contact angles. Our results show excellent agreement with SEM and AFM data, validating the applicability of iPAINT to visualize (deformable) interfaces in a minimally invasive manner through non-covalent labelling with photo-activatable dyes.

Chapter 3 is devoted to the morphological characterization of complex coacervate core micelles (C3Ms) by iPAINT microscopy. These polymeric micelles form through electrostatically driven co-assembly of oppositely charged co-polymers and are visualized without any further chemical modification. We directly image C3Ms composed of PF and P2MVP$_{29}$-*b*-PEO$_{204}$. Under these conditions conventional methods, such as small X-ray scattering, electron microscopy and AFM are unsuccessful due to the high water content of the micelles, their low electron density, and low concentration. Instead, iPAINT allows to clearly resolve the morphology of micelles as a function of their concentration. This reveals a transition from spherical to more elongated architectures upon an increase in C3M concentration. We quantify the emergence of C3Ms anisotropy at the single-micelle level. We further show a broadening of the size distribution upon an increase in C3M concentration, as the morphology gradually evolves from spherical to elliptical. We attribute this unusual morphological transition to the intrinsic stiffness of the anionic PF within the micellar core.

In **chapter 4** we utilize iPAINT microscopy to study the position of single spherical colloidal particles adsorbed at a fluid interface. We demonstrate how iPAINT microscopy enables simultaneous visualization of the nanoparticles and the fluid interfaces. This enables accurate measurements of the single-particle contact angles of isotropic hydrophilic and hydrophobic particles at a water-octanol interface. We calculate their mean contact angles and the related distributions using one- and two-colour iPAINT imaging. We find narrower contact angle distributions than what has been reported to date by other single-particle methods such as the gel trapping technique and FreSCa microscopy. This is because

iPAINT is an *in-situ* approach, which greatly simplifies sample handling, and minimizes external perturbations. Furthermore, we identify a size dependence in the contact angle distributions, which we attribute to the presence of line tension effects at the interface with an estimated magnitude of $\sim 10^{-9}$ N.

Encouraged by the results obtained in the previous chapter, we utilize the same experimental design in **chapter 5** to investigate the position and orientation of anisotropic colloidal particles straddling two immiscible liquids. For the first time, ellipsoidal particles oriented normal, parallel and oblique to the water-decane interface have been observed. We quantify their orientations in terms of contact and polar angles. The mean values of these angles and the related distributions are subsequently computed, resulting in a spread which is broader for the oblique orientation than for the parallel configuration. Being able to visualize the particle position and the fluid interface, we study the deformation of the latter induced by the anisotropy of the particles. We trace the profile of the interface around a single particle oriented in an oblique fashion at the interface, showing a dipolar deformation. Subsequently, we determine the deformation around a single particle laying flat at the interface, which appears to be quadrupolar. Finally, we calculate the pair-interaction potential for ellipsoids with different arrangements, namely side-by-side and tip-to-tip, which appears to be more attractive for the former than for the latter.

Chapter 6 presents the first *in-situ* use of PALM microscopy in organic solvents. We measure the absorption and emission spectra of the closed (non fluorescent) and open (fluorescent) forms of two photo-activatable caged rhodamines in several solvents. We chose to study the uncaging mechanism in solvents spanning a wide range of dielectric constants, commonly used in organic and supramolecular chemistry. We clarify the mechanism of photo-activation, and how to enhance the ON-OFF switch by adding a small percentage of alcohol in the solvent mixture. This enables the imaging in two colours of two-dimensional self-assemblies of colloidal nanoparticle in cyclohexane. We then turn to the imaging of supramolecular aggregates that are μm long and nm wide. In this way, we pave the way to SMLM imaging of complex synthetic materials in organic solvents.

Finally, **chapter 7** highlights two new exemplary applications of iPAINT microscopy and the development of a novel class of dyes for SMLM. Exploiting the versatility of the non-covalent labelling in iPAINT microscopy, we describe studies on supramolecular fibers (Part I) and nanoparticles-liposomes mixtures (Part II). We use two-colour iPAINT microscopy to directly visualize supramolecular block co-polymers, and infer their stability over time. Next, resorting to PAINT and iPAINT microscopies, we quantify the recruitment of liposomes utilized as drug carriers by nanoparticles. We characterize the structural integrity of the

liposomes upon recruitment by the particles and measure the clearance efficiency of this strategy. Part III reports on the preliminary characterization of a rhodamine spirothiolactam dye for super-resolution microscopy. Here, we show that this new dye enables SMLM in both aqueous and organic solvents, irrespective of pH, polarity and addition of co-solvents.

Curriculum vitae

Antonio Aloi was born on the 23rd of January 1987 in Terlizzi (Italy). After completing high school in 2005, he obtained his bachelor degree in Material Science at the University of Bari in 2010. In his bachelor thesis he investigated the generation and detection of terahertz radiation in time domain spectroscopy. In 2013 he obtained his master degree in Material Science and Technology, defending the thesis on femtosecond transient absorption in synthetic eumelanin solutions. After graduating *cum laude* at the University of Bari, in 2013 he started his Ph.D. project within the SOMATAI European network, as a Marie Curie fellow, at the Institute for Complex Molecular Systems (ICMS), at the University of Technology of Eindhoven. Under the supervision of dr. ir. I.K. Voets and prof. dr. O.J. Luiten, and in the research group of Organic Molecular Chemistry of prof. dr. E.W. Meijer, Antonio developed a new method in super-resolution imaging to specifically investigate deformable interfaces in soft matter and supramolecular chemistry. The most significant results of his research are presented in this dissertation.

List of publications

- Aloi, A.; Guibert, C.; Olijve, L.L.C.; Voets, I.K. "Morphological evolution of complex coacervate core micelles revealed by iPAINT microscopy", *Polymer*, **2016**, *107*, 450.
- Aloi, A.; Vilanova, N.; Albertazzi, L.; Voets, I.K. "iPAINT: a general approach tailored to image the topology of interfaces with nanometer resolution", *Nanoscale*, **2016**, *8*, 8712.[1]
- Aloi, A.; Vargas Jentzsch, A.; Vilanova, N.; Albertazzi, L.; Meijer, E.W.; Voets, I.K. "Imaging nanostructures by single-molecule localization microscopy in organic solvents", *J. Am. Chem. Soc.*, **2016**, *138*, 2953.
- Oude Vrielink, A.S.; Aloi, A.; Olijve, L.L.C.; Voets, I.K. "Interaction of ice binding proteins with ice, water and ions", *Biointerphases*, **2016**, *11*, 018906-1.
- Van Zee, N.J.; Adelizzi, B.; Meng, X.; Aloi, A.; Zha, R.H.; Lutz, M.; Filot, I.A.W.; Palmans, A.R.A.; Meijer, E.W. "Potential enthalpic energy of water in oils exploited to control supramolecular helicity", *Nature*, *under review*.
- Adelizzi, B.; Aloi, A.; Markvoort, A.J.; ten Eikelder, H.M.M.; Voets, I.K.; Palmans, A.R.A.; Meijer "Supramolecular block copolymers under thermodynamic control", *J. Am. Chem. Soc.*, *submitted*.
- Aloi, A.*; Adelizzi, B.*; Van Zee, N.J.; Palmans, A.R.A.; Meijer, E.W.; Voets, I.K. "Painting supramolecular polymers in organic solvents by super-resolution microscopy", *ACS Nano*, *submitted*.[2]

[1] This article is part of themed collection: *"2016 Hot Articles in Nanoscale"*, and selected article for the *"Nanoscale blog"*: "iPAINT: brushing-up on super resolution microscopy", by dr. Lee Barrett.

[2] * These authors contributed equally.

- Aloi, A.; Voets, I.K. "Nanoscopy on soft matter", *Curr. Opin. Colloid Interface Sci.*, *submitted*.
- Aloi, A.*; van Onzen, A.H.A.M.*; Jacobs, I.; Versteegen, R.M.; Janssen, H.M.; Milroy, L.G.; Robillard, M.S.; Brunsveld, L.; Voets, I.K. "Super-resolution microscopy reveals the interaction between lipids and solid particles", *in preparation*.[3]
- Aloi, A.; Vilanova, N.; Isa, L.; Voets, I.K. "*In-situ* visualization of nanoparticles adsorbed at liquid-liquid interfaces by iPAINT microscopy", *in preparation*.

other publications of the author are:

- Aloi, A.; Tommasi, R. "Raman Spectroscopy and Application", InTech, book chapter: *Inverse Raman scattering in femtosecond broadband transient absorption experiments*, **2017**, ISBN 978-953-51-2908-0.
- Triggiani, L.; Brunetti, A.; Aloi, A.; Comparelli, R.; Curri, M.L.; Agostiano, A.; Striccoli, M.; Tommasi, R. "Colloidal TiO_2 Nanorods for Photocatalysis: a Femtosecond Transient Absorption Study", Conference paper - X INSTM CONFERENCE **2015**.
- Aloi, A.; Burnetti, A.; Perna, G.; Lasalvia, M.; Capozzi, V.; Tommasi, R. "Ultrafast transient absorption of eumelanin suspensions: the role of inverse Raman scattering", *Biomed. Opt. Express*, **2015**, *6*, 4000.
- Arciuli, M.; Brunetti, A.; Fiocco, D.; Zacchino, V.; Centoducati, G.; Aloi, A.; Tommasi, R.; Santeramo, A.; De Nitto; E.; Gallone, A. "A multidisciplinary study of the extracutaneous pigment system of European sea bass (Dicentrarchus labrax L.). A possible relationship between kidney disease and dopa oxidase activity level", *Fish and Shellfish Immunology*, **2015**, *42*, 184.
- Triggiani, L.; Brunetti, A.; Aloi, A.; Comparelli, R.; Curri, M.L.; Agostiano, A.; Striccoli, M.; Tommasi, R., "Excitation-Dependent Ultrafast Carrier Dynamics of TiO_2 Nanorods Dispersed in Organic Solvent", *J. Phys. Chem. C*, **2014**, *118*, 25215.

[3]* These authors contributed equally.

Acknowledgments

By definition an 'end' is the concluding part, a point that indicates the full extent of something. 'End' is an outcome, a result. Someone, many actually, sees the end of this long journey called PhD as the finish line so long sought after. Instead, the way I see it, this is a story to tell, a full paragraph of a life lasted 4 years, which barely fits in the margin of these (too many) pages. A text full of ideas, trials, mistakes, corrections, re-written words. The pages are those 1616 days, give or take, which brought me here, in this very room to defend this story. Many the names and faces of people who walked with me during this journey, to whom i'm deeply thankful. Let's start with some order. First, *Ilja*, a supervisor and a mentor. Thanks for your attitude to push me out of my comfort zone and let me explore all the possibilities around. I still remember your answer when i naively asked you when i could have started working in the lab a couple of months after my beginning: 'Were you waiting for my green light?! Just go, try, and have fun!'. That was also the very moment when the PhD project arranged within the Marie Curie Network drifted away from the original plan, and led us to unexpected, thrilling, and colorful microscopy images of everything else but ice crystals. *Jom*, I'm grateful to you being involved in this project, bringing a more physical point of view in this sea of chemistry. *Bert*, despite my background so far from your everyday topics, you still welcomed me with enthusiasm and looking forward to what could have been the outcome of such collaboration. Sincerely many thanks for this opportunity. Dr. *Albertazzi*, dear *Lorenzo*, the man who intiated me to microscopy and thought me most of the things i know now about SMLM. Thanks for the time you spontaneously dedicated to me, and for the time i somehow manage to steal you. The coupling reaction of NH_2 to the NHS-ester will be always with me, the only one though. I would like to express my gratitude to all the committee members, especially to prof. *J. Vermant*, dr. *S. Manley*, dr. *A. de Jong*, who took part to my defence and gave the start to constructive and fruitful discussions. A big thanks goes to all the people involved in the microscopy meeting, Peter Zijlstra *in primis*, who shared passion, troubleshooting and tips.

As I was saying earlier, every story has a beginning, mine started applying for a project

on anti-freeze proteins in a country 2000 km far from home. It was for fun, no many thoughts involved, just to see how it goes. 'Surely it won't involve chemistry', you say to yourself, 'they look for someone who likes to play with lasers afterall', and you do! You fly to this place, 'Eindhoven? Never heard of it'. Look around to find the way to the university, end up in this green campus; follow the chimney. In the first meeting, Ilja started crying because of a misplaced contact lens, and you think 'Oh gods, this sounds like the perfect start, you didn't even begin to talk and already made this woman cry!'. You speak with the big boss of the department and he asks you 'How can you apply this third-order susceptibility in chemistry?' and you mumble words hoping they make some sense. At the end of the day you find yourself liking the place, the people you've talked to so far are nice, the building brand new and you think: 'I can do this! I really want to stay here for my next 4 years!'. Sitting here in this room now proves that everything turned out well, and you find yourself a couple of months after signing a contract appointed in the organic chemistry department headed by one of the big names of supramolecular chemistry. Well guys, no matter which kind of things you'll promise to yourself, Fate is a moody woman, and she'll always find the way to make a fool out of you.

In these 4 years I've met many people, some at their goodbye parties, some others left after a year, right when the connections were becoming stronger, others walked with me till halfway. Some did the whole path, and finally the new generation is starting. This is the *SMO family*! A big melting-pot of cultures, knowledge, ideas, projects floating out from a huge bucket overloaded where everyone leaves something, most of the time good memories. Thanks you all guys for making these years fantastic, with our retreats, Christmas dinners, unofficial dinners, SMO beers and cakes.

Of course, some people remains in your heart more than others, they are elective affinites, as Goethe used to say. *Isja* and *Neus*, the dearests above all. We started sharing an office, and we ended up sharing much more than that. Our talks were endless, the dinners (home-made and not) cosy, the crocketje blanket warm, the drinks many, the love even more. Having you there for me has been a blessing, our paths crossed once to remain entagled more and more as time goes by.

Bea, your coming in Bert's group had the perfect timing. Your tough look is just a shield in this world, the softness, care, love and passion you are capable of are boundless. 'Do you know Rise Against?' – 'Yes' – 'No wait, not the Rage Against the Machine, the Rise Against!' – 'I told you, yes!' – 'You are my friend now!'. The support you gave and still give has the touch of a delicate caress and the stability of a massive rock.

Ghislaine, I've learn a lot from you in these last two years, both at a personal and working level. Your dedication to work is commendable and yet, the energy and enthusiasm you put in your everyday life seems untouched by the amount of time you spend in the lab. Keep on

doing what you like above all!

Andreas, we started talking about time-resolved spectroscopy and we finished enjoying climbing and bouldering more than everything else. The cheesecakes brought in the office during your last months were amazing. The moments shared, the tips had, your being direct and still caring are all treasures i'll keep jealously.

The beads boys: *Daan* and *Sjors*, having you in Ceres (or nearby) was a continuous source of inspiration. I've been lucky to discuss with you about microscopy, Matlab, and everything else chemistry related.

José, The inside man in Helix, thanks for your help with the GPC columns, and all the unknown chemistry left out (still black magic for me).

A big thanks goes to the members of the *ICMS animation studio*, an amazing group of guys ready to put chemistry on a paper as beautiful and colorful cartoons.

Sheen thanks for taking care of the lab, the meetings and especially the cookies.

The ICMS coudn't be the place it is without the great help, the efforts and the passion of three amazing ladies: *Carla*, *Wendy* and *Cindy*. Thanks for the time and all the energies you put in here everyday. *Carla*, a special mention to you, the eye that everything sees, the ear ready to listen, the pure energy I've only seen few times in people.

The Voets group: *Dylan* (who needed to check twice our group before taking a decision... M8, it was a match since the beginning with you and your fluffy weird friday t-shirts – riiiiiiiiiiiibs!), *Emma* (kindness and attention, thanks for all the 'should we go for an hypothetical?', the samasthiti and namastè), *Hande* (HANDEEEEEEE! Since your coming your smile has been a light in our open-space!), *Marieke* (t-t-t taratata t-t-t taratata still in mind! The Biffy Clyro won't be happy with that cover, but hey, we had fun!), *Lisa* (vitality and braids), *Romà* (with Munchkin 2.0, and the WTF - whiskey tasting fridays - with Dylan in the office), *Phil* (the calm one), *Maja* (and the talks on phylosophical concepts along with Louis CK), all the students: *Nicki*, *Danny*, *Rob*, *Haifei*, *Anne*, *Shidong*, *Christian*, *Thijs*, *Katja* and *Patrick* (I like to think the two of you made me more patient and prone to listen, thanks for this!), and the former members: *Anneloes*, *Luuk*, *Clement* (Monsieur! The DLS is not for me...), *Marleen*. I'm sure all of you guys will have a successful life. Just go for it!

The *SOMATAI* guys and girls. Being in a Marie Curie Network is not only a great opportunity to set up collaborations and travel each three-four months, but as I found out also to meet nice people and go partying till the day after in the most beautiful capitals of Europe, taking part to conferences held on sunny beaches in Crete and even get the chance to laser shoot your supervisors at the laser-quest! that was fun guys, thanks for those great moments.

When an Italian moves to a foreign country for his first time, he doesn't know (yet)

that he will find an entire Italian family there, or alternatively, he will create one. Well, the italian clustering algorithm works 100%! The Italian crew, a family in Edh has been and still is the big cornerstone, people who cuddles you while in the storm, with who you share the feelings, dinners, the 'all we can fry', sunny sunday coffees, rainy sunday coffees, the 'oh shit! She is vegetarian! Remove the meat from the dish...', cards against humanity (and the jaaaaaaaaar), and much much more: *Alberto* (a mom for every lost soul in this country, the wide shoulder i could always count on), *Arianna* (kind, strong, caring), *Valerio* (Zì! Your energy is comparable only to the many drinks you can handle, read G&T at the Berlin...), *Sasa* (your skills in the kitcken made all our gatherings more and more enjoyable), *Tommy* (Potscho! The tender with a big heart, 'it's just a potscho afterall' but we like you the way you are), *Johanna* (Potscha! The sport, the bone-cells, and the amazing cakes), *Ben* (the welsh accent and the rugby matches at the irish pub), *Francesco* (the Bear with a special taste for music, beautiful records and IPA), *Bea* (you've got already your section :p), *Jaba* (with your hidden tenderness showing up at home whenever, and always welcoming), *Mayla* (A:'Tetteeeeeeee' M: 'Peloooooo', the lasagne in Den Haag and the overflowing non-sense), *Alessandro* (the coffees at metaforum and the tamarro compilations), *Nate* (last entry but with the right attitude to enjoy this big mess of people), *Valerio* (piccolo, le focacce alla barese yummy! and the take-it-slow life style). All of you guys enriched my life, made me feel at home even if far away!

BAGS! What are the chances to find Brilliant, Awesome, Genius, Smart people in a small town in the middle of the Black Forest? Well, you guys are the proof that this can happen. Our roughly-every-six-months meetings were so good moments, ready to be turned in a big laugh, from Kiel to Rome, from Bisceglie to Eindhoven. Waiting for another 'just one' (maybe in Siberia).

A PhD doesn't come without some level of nerdyness all along. This happened weekly playing Risk!, D&D, Catan and much more with *Gianmarco* 'I have to read the entire manual to check if we are doing it correctly', *Tommy* 'I need to take into account the rotation of the Earth while i roll my dice, don't push me', *Fabio* 'I will help you (but you know i'll backstab you as soon as i will have the opportunity)', *Bea* 'I rolled a 19 to check for traps, rolled a 2 to escape from it', *Alberto* 'the dark master', and those who joined our controlled madness once in a while. We laughed till tears while the pizza kept coming out from the oven, those were unforgettable nights!

One of the very first things Ilja thought me wasn't science related, it was: bouldering is amazing! It became a requirement to join our group, but most of all was a way to release stress, enjoy nice beers, share time with people and spend a lot of money in gears and shoes.

The Monk! Such a beautiful place. We started in many: *Andreas*, *Andreas*, *Thijs*, *Ilja*, *Ghislaine*, *Rachel*, *Helen*, *Greg*; and I tried to learn as many tricks as possible from you guys. The climbing in Berdorf and the bouldering in Fountaine Bleau were unesplicable amazing days! Now, the group is smaller with *Bea*, *Nate*, and *Valerio* but the fun going monking, the satisfaction after finishing a route and the frustration at each fall are still there! Allez-up!

Irene, the neverending skype calls kept a piece of me always home in all these years, surrounded by all the warmth and the sweetness you are capable of. Thanks.

Ciro and *Daniele*, Fire and Karma. Brothers given by the Fate, arms to lift up (again and again), feet to walk through life, eyes to look far, lungs to breath deeply, heart to feel. Still much to say that words won't cover it all, too much to live together to limit it by simple definitions.

E alla fine di tutto, *Mamma* e *Papà*, chi ha sempre creduto, sperato, lottato, ha incassato rabbia ingiustificata, ha insegnato, ha avuto pazienza, ha pianto e soprattutto sorriso per tutto ciò. Insieme a *Daniele* e *Fabio*, siete i miei meridiani nel mondo, non linee da superare ma guide per sapere dove mi trovo, chi sono, a qualsiasi latitudine.

KNULP